Abstract

Title of Dissertation: Outflows in Infrared-Luminous Galaxies:
Absorption-Line Spectroscopy
of Starbursts and AGN

David S. Rupke, Doctor of Philosophy, 2004

Dissertation directed by: Professor Sylvain Veilleux
Department of Astronomy

Large-scale galactic outflows, better known as superwinds, are driven by the powerful energy reservoirs in star forming and active galaxies. They play a significant role in galaxy formation, galaxy evolution, and the evolution of the intergalactic medium. We have performed a survey of over 100 infrared-luminous galaxies in order to address the exact frequency with which they occur in different galaxy types, the dependence of their properties on those of their host galaxies, and their properties in the most luminous starburst and active galaxies. Most of our sample consists of ultraluminous infrared galaxies (ULIRGs), and we use moderate-resolution spectroscopy of the Na I D interstellar absorption feature (which directly probes the neutral gas phase).

We find superwinds in the majority of these galaxies at typical maximum, deprojected velocities of $500 - 700$ km s^{-1}. The detection rate increases with star formation rate (SFR) in starbursts, while the mass outflow rate appears constant with SFR, contrary to theoretical expectations. The resulting mass entrainment efficiencies in ULIRGs are quite low, of order a few percent of the star formation rate. There is some dependence of outflow velocity on host galaxy properties; the outflow velocities in LINERs are higher than those in H II galaxies, and the highest

column density gas in each galaxy may have an upper envelope in velocity that increases with SFR.

Outflows in most galaxies hosting a dominant AGN have very similar properties to those in starbursts, so discerning their power source is difficult. The velocities in Seyfert 2 outflows may be slightly higher than those in starbursts, and the fraction of neutral gas escaping Seyfert 2s is higher than that in starbursts ($\sim 50\%$ vs. $\lesssim 20\%$). The outflows in our Seyfert 1 galaxies have extreme velocities of up to $\sim 10^4$ km s^{-1}, and two of three Seyfert 1s with outflows possess broad absorption lines.

Finally, we find that spectroscopy of a few galaxies at very high spectral resolution does not reveal unresolved narrow components. The mass outflow rates at very high resolution are thus comparable to those from our large sample of moderate-resolution spectra, demonstrating the reliability of our moderate-resolution data.

Outflows in Infrared-Luminous Galaxies: Absorption-Line Spectroscopy of Starbursts and AGN

by

David S. Rupke

Dissertation submitted to the Faculty of the Graduate School of the
University of Maryland at College Park in partial fulfillment
of the requirements for the degree of
Doctor of Philosophy
2004

Advisory Committee:

Professor Sylvain Veilleux, advisor
Professor Jordan Goodman
Professor Glenn Mason
Professor Stacy McGaugh
Professor Chris Reynolds
Professor Gregory Sullivan

soli Creator gloria

Acknowledgements

There are many things I could say here but I will be brief. Those listed here are not necessarily in order of importance.

Many thanks to my advisor, Sylvain Veilleux, for his willingness to invest substantial amounts of time, travel funding, and other resources into my education. Thanks also to him for allowing me the latitude to explore astronomical problems with true academic freedom, and for providing advice when appropriate. I am grateful to the teaching faculty of the Physics and Astronomy departments for academic discussions and advice, and to the staff for processing my travel requests, making sure I was paid, keeping the computers running, cleaning my office, and answering questions. I am also quite grateful to the time allocation committees of various telescopes for providing copious amounts of observing time, and to the observatory support staffs, who have the enviable job of taking care of the instruments and telescopes we used. Finally, thanks to the students and faculty of the Astronomy Department for welcoming an

outsider (me) and making the last two-thirds of my graduate education an enjoyable one.

Since my vocation as an astronomer is only one facet of my life (though admittedly an important one), there are others who have provided support and encouragement. My life during graduate school has been a learning experience in more than just an academic sense, mostly due to the influence of good friends and my church community. I am grateful for much fun and laughter in these contexts, and for the richness of a life lived in community. I can think of many people to mention here, and a few handfuls that are especially important to me (perhaps more good friends than one person deserves), but I will refrain from making a list and I look forward to thanking each of these people in person.

Finally, I'm grateful for my family. Thanks go to them for instilling in me a confidence to learn without bounds and in my own gifts. Their unconditional love and acceptance would give anyone the strength to do about anything.

Contents

List of Tables

List of Figures

Chapter 1

Introduction

1.1 SUPERWINDS

The fingerprints of galaxy formation and evolution are seen in the dynamics of stars and gas, both inside of galaxies and in their environs. The processes that shape the structure and content of these entities can often be identified by the unique kinematic signatures they leave, in contrast to typical behavior (e.g., the rotation of a disk). The standard picture of galaxy formation is that of small accumulations of gas and stars merging to form bigger clumps, which in turn merge to form larger ones, and so on. One of the kinematic tracers of this process is radial infall. In constrast to infall, gas is often observed to flow outward from galaxies, on various scales and as the result of a number of processes.

Galaxy-scale outflows of gas, sometimes called 'superwinds,' have been known for some time to be a ubiquitous phenomenon in galaxies undergoing intense and spatially concentrated star formation (i.e., starburst galaxies). Outflows are also observed in galaxies that host an accreting supermassive black hole (an 'active galactic nucleus,' or AGN), but these sometimes have characteristics that distinguish them from outflows in starbursts, such as relativistic ($\sim 0.1c$) velocities or variability. The cause of these outflows is, generally speaking, the deposition of a large amount of energy in a short period of time into the interstellar medium of a galaxy. In the case of starburst galaxies, this energy comes from the cumulative effect of the deaths of many massive stars in the form of supernova explosions. In the case of galaxies with AGN, it may be a result of collimated jets, hot winds, intense radiation fields, or even magnetic fields. Regardless, the result is a bulk outward motion of the gas on scales comparable to the scale of the galaxy (i.e., kiloparsec scales).

These winds may play a number of roles in the evolution of galaxies and the surrounding inter-galactic or intra-cluster medium in which they are embedded. They may also resolve a number of issues in cosmology (e.g., problems with galaxy formation scenarios). They are often used in numerical simulations of galaxy formation and evolution, but seldom in a way that is fully motivated by observations.

The observational data set on outflows is steadily increasing, both in quality and quantity, but in many ways is still quite limited. Over most of cosmic history, the frequency and impact of superwinds remains unquantified. We also know very little about how the properties of superwinds depend on the properties of their host galaxies. Observations have typically focused on dwarf galaxies or edge-on disk galaxies with moderate star formation rates (as a well as a set of high-redshift galaxies with as yet uncertain properties).

In this chapter, we discuss the current theoretical and observational picture of superwinds in some detail, in order to motivate our work and place it in context. We also summarize our survey in preparation for the detailed explanation of the following chapters.

1.2 SUPERWIND MODELS AND PHYSICS

1.2.1 Basic model of starburst-driven outflows

The theory behind the evolution of superwinds derives ultimately from the consideration of well-studied phenomena. Blast wave evolution has been understood since mid-century, as described by Taylor (1950) and Sedov (1959). The 'Taylor-Sedov' solution is self-similar (it can be scaled up to describe astrophysical phenomena) and is often applied to supernova blast waves, which have a single burst of energy injection (though it was originally used to describe the explosion of a thermonuclear weapon).

The evolution of bubbles in the interstellar medium that are blown up by stellar winds is similar to that of a supernova, but in this case the injection of energy is continuous. The evolution of a wind-blown bubble happens in several stages: (a) adiabatic expansion of a free wind; (b) radiative losses of material swept up by the wind cause this collected gas to cool into a thin shell (the 'snowplow' phase); and finally (c) the dissipation of the shell into the surrounding ISM (Castor, McCray, & Weaver 1975; Weaver et al. 1977). This picture was first applied to the more specific case of a starburst-driven superwind in M82 by Chevalier & Clegg (1985), who flesh out the physical model of the energy source and apply their analytic model to observations of M82.

In a starburst, rapid, concurrent, and coincident star formation produces massive stars quickly. As these stars have short lifetimes, they quickly yield hot winds and supernova blast waves which propagate into the surrounding interstellar medium on timescales of millions of years from the beginning of the starburst. These winds and supernovae collide with one another, the shock of these collisions produces hot gas,

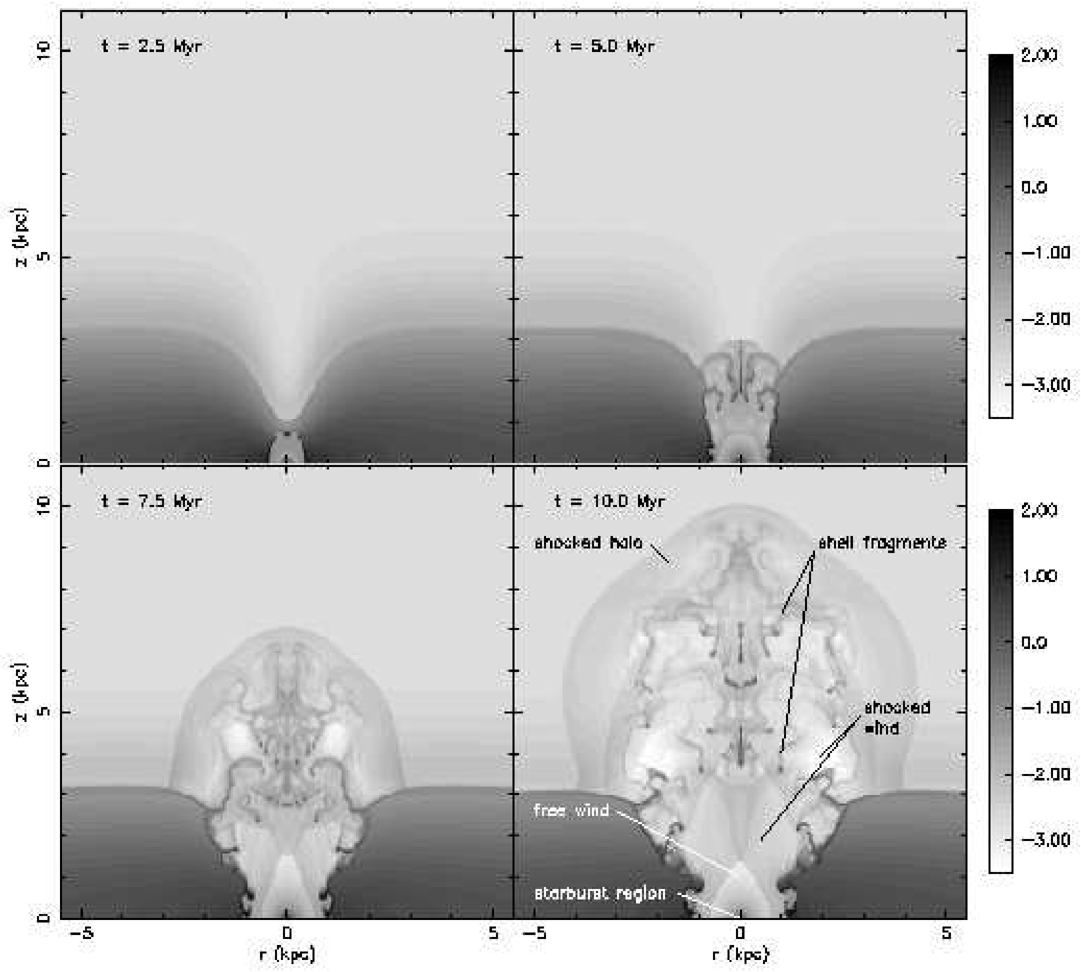

Figure 1.1: Hydrodynamic simulations of the structure and evolution of a starburst-driven superwind. The grayscale levels show logarithmic density variations, with dark being high density and light being low. The four panels represent times after the onset of the starburst (2.5 – 10 Myr). Each panel is 11 kpc on a side. Reprinted from Strickland & Stevens (2000).

and their equally hot ($\sim 10^7$ K) interiors combine to produce a thermalized bubble that expands radially outward due its overpressure with respect to the surrounding gas.

Hydrodynamic simulations detail the evolution of the wind in the specific environment of a galactic disk (see Figure 1.1; Tomisaka & Ikeuchi 1988; Mac Low, McCray, & Norman 1989; Suchkov et al. 1994; Strickland & Stevens 2000). In this case, the expanding superwind is collimated by the density gradient between the galactic disk and its halo, which produces a bipolar structure along the minor axis of the galaxy (i.e., perpendicular to the disk). In order of approximately increasing radius, this structure consists of (a) a central starburst of size up to a kpc; (b) a hot ($T \sim 10^7$ K), freely-expanding wind surrounding the starburst region; (c) wind material that has been shocked as it reaches the outer shell; (d) disk gas entrained by the wind; (e) a shell of post-shock halo gas that has been swept up by the wind and is now cooling; (f) shocked halo gas; and finally (g) undisturbed halo material.

Most of the mass in the superwind is not in the original gas expelled by the supernova blast waves from the starburst but rather in the entrained disk and halo gas. For instance, in the dwarf NGC 1569, Martin, Kobulnicky, & Heckman (2002) estimate that there is 9 times as much entrained gas as there is gas in the free wind. In NGC 1569, this gas is 'mass-loaded' into the wind: the hot free wind destroys clumps of cooler gas via evaporation by thermal conduction or ablation by hydrodynamic processes (Strickland & Stevens 2000). Entrainment does not just imply cloud destruction, however, as the mass of cold, neutral and warm, ionized material observed in superwinds is significant (and may dominate the mass budget; Heckman, Armus, & Miley 1990).

An important stage in superwind evolution is the fragmentation of the shell of swept-up halo and disk gas. Assuming a stratified halo, at large radius the ambient gas reaches low enough density that the superbubble can accelerate. Hydrodynamic Rayleigh-Taylor instabilities then arise between the shell and the surrounding low-density halo gas. The shell fragments into clumps and filaments (see Figure 1.1) and the hot wind fluid is free to expand into the outer halo of the galaxy. This is one mechanism by which the hot free wind, enriched by metals from the supernovae that power the wind, can escape the galaxy and enrich the intergalactic medium.

1.2.2 Winds in AGNs

Outflows in galaxies with active galactic nuclei, powered by the energy from an accreting supermassive black hole, display a variety of properties. They appear to occur in the form of both highly-collimated and loosely-collimated outflows (i.e., jets and wide-angle winds) on a range of scales. Relativistic jets with small opening angles are found in radio-loud AGN at small and large scales. Weaker jets may also be common in radio-quiet Seyfert galaxies (e.g. Ulvestad & Wilson 1984; Kukula et al. 1999). Wide-angle winds are found in nearby Seyferts on large scales (Colbert et al. 1996a,b, 1998), and may also be found near the accretion disk.

These small-scale outflows are generated by the energy produced by matter accreting onto the central black hole. The detailed physics by which this occurs are not understood, however. Crenshaw, Kraemer, & George (2003) summarize various models, which include (1) the expanding coronae of accretion disks that are heated by Compton scattering; (2) radiation pressure from dust opacity, ‘line driving,’ or ionization; (3) centrifugal forces from rotating magnetic fields; or (4) some combination of the above. A phenomenological model involving an outflow along the sides of a bipolar cone has been proposed to synthesize many of the current observations (Elvis 2000).

On kiloparsec scales, the physics of outflows powered by AGN is also uncertain, especially given the similarity of the outflow characteristics to starburst-driven superwinds (e.g., extended optical and X-ray emission-line nebulae near the galaxy minor axis). Possible mechanisms have been discussed extensively in the literature, and include extension of a nuclear wide-angle wind or the injection of energy from a jet; for the detailed discussion of individual objects, see (for example) Veilleux, Shopbell, & Miller (2001, NGC 2992) and Veilleux et al. (1999a, NGC 4388) and references therein.

1.3 COSMOLOGICAL IMPLICATIONS

The number of theoretical papers incorporating galactic winds has grown sharply in recent years. Superwinds have been invoked to explain a myriad of issues relating to contemporary cosmology (for a recent review, see Veilleux & Rupke 2004). Here, we cover a handful of the most important implications of winds, especially in the high-redshift universe.

Numerous observations of absorption systems in quasar sightlines through the intergalactic medium (IGM) have shown that the space between galaxies is enriched with metals to a small fraction of solar metallicity. One way for these metals to reach the outskirts of galaxies and into the IGM is via galactic superwinds. Numerical simulations incorporating winds have shown that these levels can be reached (e.g., Aguirre et al. 2001a,b; Madau, Ferrara, & Rees 2001). However, the results may depend sensitively on the distribution of gas in each galaxy and the intergalactic pressure (Silich & Tenorio-Tagle 2001).

Many of these metals may arise in the form of clumps of gas that absorb light along quasar sightlines. A number of authors suggest that some non-negligible fraction of these absorbers are produced by winds, and that some of these may be distinguished by their kinematic signatures or ionization state (Nulsen, Barcons, & Fabian 1998; Bond et al. 2001; Furlanetto & Loeb 2001; Schaye 2001; Theuns et al. 2001; Simcoe, Sargent, & Rauch 2002; Theuns et al. 2002).

If galaxies do expel significant amounts of metals, does the mass of the galaxy affect how much is ejected? High mass ellipticals and bulges are observed to have higher metallicity than lower-mass objects, and this discrepancy could be explained if high mass galaxies retain metals more easily due to their deeper gravitational potentials (Larson 1974; Vader 1986; Kauffmann & Charlot 1998).

Due to their vigorous redistribution of gas, superwinds could also affect galaxy formation scenarios, especially in relation to low-mass galaxies. By preferentially reducing the mass of low-mass galaxies, superwinds can suppress their relative number densities (Dekel & Silk 1986; Scannapieco, Ferrara, & Broadhurst 2000; Scannapieco, Thacker, & Davis 2001; Theuns et al. 2002). They may do this by simply removing gas, but they can also inhibit accretion and strip or heat nearby acculumations of gas (Scannapieco et al. 2000, 2001; Theuns et al. 2002).

1.4 PREVIOUS OBSERVATIONS

1.4.1 Absorption-line spectroscopy

Absorption lines have frequently been used to discern the presence and diagnose the properties of outflows in both starbursts and AGN. Strong absorption lines arising in interstellar gas occur primarily in the (rest-frame) UV and X-ray regions of the electromagnetic spectrum. However, there are a few prominent lines visible in the rest-frame optical, as well, including Na I D and Ca II H & K. Absorption-line spectroscopy is a very common technique for studying AGN-driven outflows. More recently, it has also been used to study starburst-driven winds.

Outflowing gas is probed over a range of scales by absorption-line studies of bright Seyfert galaxies (e.g., Crenshaw et al. 2003) and distant quasars, and the physical model that describes them is a work in progress. For simplicity, absorption lines in AGN are typically broken into several phenomenological classes. In 60%

of $z < 0.1$ Seyfert 1 galaxies with moderately-bright AGN, *intrinsic absorbers* are seen in the UV and X-rays, with velocities relative to systemic of $\Delta v = -2400 - +200$ km s^{-1}and absorber component widths of $20 - 500$ km s^{-1} FWHM (Crenshaw et al. 1999). The frequency of occurrence of these lines decreases with ionization potential (down to 6% for Mg II absorbers), and they have global covering fractions of $C_g \gtrsim 50\%$, which may imply a wide-angle wind (Crenshaw et al. 1999). In quasars (i.e., higher-luminosity, more distant AGN), we observe *associated absorption lines (AALs)*, which have widths of a few hundred km s^{-1} and velocities relative to systemic of up to -5000 km s^{-1}. We also see *broad absorption lines (BALs)* in quasars, which have widths up to 10000 km s^{-1} and velocities up to -50000 km s^{-1}($= -0.17c$) and occur with a frequency of $10 - 15\%$ (Reichard et al. 2003).

A number of absorption-line studies of individual starburst galaxies have been conducted. The observation of narrow, blueshifted Na I D, coupled with redshifted Na I D in emission, in the inclined spiral galaxy NGC 1808 is intepreted as evidence of outflow (Phillips 1993). Outflowing warm ionized ($T \sim 10^{4-5}$ K) gas was observed using UV transitions in NGC 1705 (Heckman & Leitherer 1997; Sahu & Blades 1997). Lyman-α absorption, probing H I gas, is blueshifted (and the emission is redshifted) with respect to systemic in several nearby dwarfs (Lequeux et al. 1995; Kunth et al. 1998). Finally, O VI $\lambda\lambda1032, 1038$ absorption is blueshifted with respect to systemic in NGC 1705, which shows that hot, coronal ($T \sim 10^{5-6}$ K) gas is outflowing (Heckman et al. 2001).

1.4.2 Surveys of superwinds

The local universe

Previous large surveys of local starburst galaxies have shown that evidence for superwinds is common. Lehnert & Heckman (1995, 1996) detail an imaging and spectroscopic survey of ~ 50 edge-on galaxies with $L_{\rm IR} < 10^{12}\ L_{\odot}$and $cz < 15000$ km s^{-1}. Evidence for superwinds in these galaxies includes (along the minor axis): extended/excess line emission, shock-like line ratios, broad emission lines, velocity shear, blue emission line asymmetries, and decreasing gas pressure with radius. Several of these properties also show a positive correlation with infrared activity ($= L_{\rm IR}/{\rm L}_{\rm opt}$), including minor axis gas excess, line width, and [N II]/Hα line ratio. Lehnert & Heckman (1996) also suggest an average (deprojected) outflow speed for these galaxies of 170^{150}_{-80} km s^{-1}.

Using the complementary technique of optical absorption-line spectroscopy, Heckman et al. (2000) recently studied a sample of 32 infrared-luminous galaxies with $z \lesssim 0.1$. Their survey includes 5 ULIRGs, and they also find a substantial superwind fraction. Heckman et al. (2000) also show that these outflows are dusty, and measure outflow velocities up to $400-600$ km s^{-1}; however, they do not measure an individual mass outflow rate for each galaxy and fit only a single velocity component to each observed absorption line.

High redshift

As discussed above, superwinds at high redshift ($z \gtrsim 1$) may play important roles in galaxy formation and the evolution of the IGM. Studying these winds at such distances is difficult, and possible only using deep observations of bright or gravitationally-lensed galaxies.

One of the best-studied high-redshift galaxy populations is the Lyman-break galaxies (LBGs). These galaxies are detected in broad-band photometry by their rapid drop in flux at the Lyman break, where the ultraviolet ionizing luminosity is absorbed by dust and gas. These galaxies have been studied in large numbers at $z \sim 3$, and appear to be UV-bright, massive star-forming galaxies with modest (a few to a few tens of $\mathrm{M}_{\odot}$ yr^{-1}) star formation rates (Steidel et al. 1996; Pettini et al. 2001).

Extensive spectroscopic observations of LBGs have shown that most of them host high-velocity outflows (Pettini et al. 2001; Shapley et al. 2003; Adelberger et al. 2003). Nebular emission lines from interstellar gas in starbursts are not common in the UV, and the low resolution of these observations is typically not enough to distinguish stellar and interstellar absorption. To detect these outflows, the velocity of Lyman-α emission is compared to that of the UV absorption lines. The Lyman-α emission is redshifted (perhaps due to resonant scattering on the receding half of the outflow), while the absorption lines are blueshifted due to interstellar absorption in the outflow. The average offset of the two is 614 km s^{-1} (Adelberger et al. 2003), implying that an average (deprojected) outflow velocity is approximately 600 km s^{-1}. Tentative evidence suggests that these outflows are quite large ($r \lesssim 500$ kpc) and are metal-enriched (Adelberger et al. 2003), though this needs confirmation.

A recent survey of a handful of gravitationally-lensed objects also reveals evidence for winds at high z. Five galaxies in Frye, Broadhurst, & Benítez (2002) show an offset between the Lyα and UV absorption lines in the range $360 - 830$ km s^{-1}, consistent with the results from LBGs.

1.5 OUR WORK

1.5.1 Starbursting infrared galaxies

To complement and extend the current state of knowledge of superwinds, we have taken the largest survey to date of massive outflows in infrared-luminous galaxies. Our survey extends over a broad redshift range from $z = 0$ to $z = 0.5$. We have included starburst galaxies with a range of host properties and, for the first time, searched for superwinds in a large number of ultraluminous infrared galaxies (ULIRGs), defined as galaxies with $L_{\rm IR} > 10^{12}\ L_{\odot}$. These are massive galaxies which are the result of binary mergers of roughly equal-mass gas-rich spirals. Our pilot study of 11 ULIRGs (Rupke, Veilleux, & Sanders 2002) showed that winds occur with high frequency in these galaxies.

The size and makeup of our sample allows us to look for statistical properties of these winds as a function of host galaxy properties and redshift over a large dynamic range. Our technique, absorption-line spectroscopy of the Na I D doublet in the optical, also allows us to estimate the mass flux rate of the wind. This quantity, when normalized by star formation rate (SFR), is a good measure of the relative efficiency with which these winds entrain of interstellar gas clouds. It has been estimated for some local galaxies of small-to-moderate size to be approximately unity (Martin 1999; Heckman et al. 2000). Globally, this 'mass entrainment efficiency' (also called 'reheating efficiency,' though the former is more accurate given that the mass of superwinds is dominated by entrained gas) is somewhat difficult to estimate given the uncertainty in the contribution of different phases of the ISM to the wind mass budget, but in a given gas phase it is relatively straightforward.

1.5.2 AGN-dominated infrared galaxies

In parallel with our survey of absorption-line gas in infrared-selected, starbursting galaxies, we have compiled a large sample of infrared-selected galaxies with AGN that dominate the energy budget of the galaxy and taken spectra of the Na I D feature. This allows us to compare the detection rate and properties of outflows in each sample, looking especially for distinguishing characteristics of AGN-powered outflows. We separate the galaxies into Seyfert 1s and 2s and compare them.

1.5.3 High-resolution observations

Finally, we have observed a handful of galaxies at very high spectral resolution. This allows us to search for narrow absorbing components that are unresolved by the moderate-resolution spectra. If unresolved, these components have the potential to cause us to underestimate the actual column densities along the line of sight and the resulting mass outflow rates of neutral gas.

1.5.4 Method

The existence of outflows can be inferred from the presence of absorption lines that are blueshifted with respect to the systemic velocity of the host galaxy. We apply this technique using the Na I D doublet and measure individual outflow properties such as absorbing column density and outflow velocity. Figure 1.2 shows the energy levels of Na I D; the D doublet is an electronic transition from the ground-state $3s$ to the excited $3p$ state whose levels are split by fine structure. The ratio of probabilities of an electron absorbing a D_2 photon vs. a D_1 photon is the ratio of their oscillator strengths divided by the ratio of their wavelengths:

$$\frac{P(D_2)}{P(D_1)} = \frac{f_2}{f_1} \times \frac{\lambda_1}{\lambda_2} = 2.0093, \tag{1.1}$$

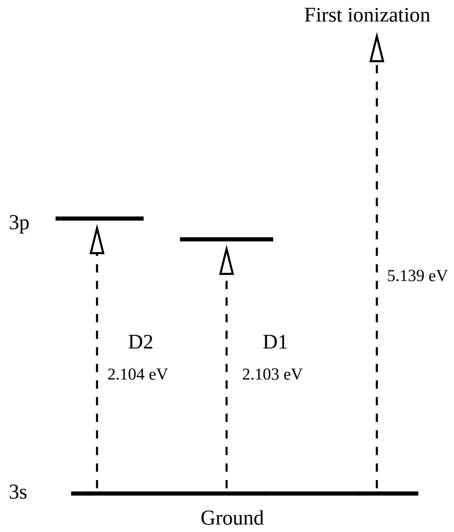

Figure 1.2: Grotrian diagram of the D doublet energy levels in Na.

where $\lambda_2 = 5891.58$ Å(in vacuum), $f_2 = 0.6311$, $\lambda_1 = 5897.56$ Å, and $f_1 = 0.3180$ (Morton 1991).

Absorption in Na I D atoms occurs both in the interstellar media of galaxies and in the atmospheres of stars. In each case, a background source, either the background starlight of the galaxy or an individual star, loses some light at the wavelength of the transition due to the absorption of a photon by the Na atom, which is then re-emitted isotropically. Na I D emission can be produced by resonance scattering of continuum photons at the periphery of a gas cloud. In high density environments, Na I D can be collisionally excited and produces photons via radiative de-excitation, for instance in high-density broad-line regions around a supermassive black hole. However, if the density is too high (on the order of a million particles per cm^{-3}) collisional de-excitation will dominate over radiative processes.

We analyze the line profiles by means of a χ^2 minimization fitting algorithm that allows for non-Gaussian intensity profiles, multiple absorbing components, and a covering fraction that is less than unity. Assuming that all absorption components that are blueshifted more than ~ 50 km s^{-1} are outflowing, a simple model of a mass-conserving free wind then yields the corresponding mass outflow rates.

1.6 OUTLINE

The structure of this thesis is as follows. In Chapter 2, we discuss the observations and data reduction common to all our data. We also summarize techniques for analyzing absorption lines, especially blended doublets, and our line-fitting routines. In Chapter 3, we introduce the sample of starburst-dominated infrared galaxies, show the results of our work on this sample, and interpret it. We present the sample of AGN-dominated infrared galaxies and our high-resolution observations in Chapters 4 and 5, respectively. Finally, in Chapter 6, we summarize and conclude.

For all calculations, we assume present-day values for the cosmological parameters of $H_0 = 75$ Mpc^{-1} and the standard $\Omega_m = 0.3$, $\Omega_\Lambda = 0.7$ cosmology (where Ω_m and Ω_Λ are the matter and 'dark energy' densities relative to the critical density). All wavelengths quoted are vacuum wavelengths (except those used as labels for spectral lines) and are generally taken from the NIST Atomic Spectra Database[1].

---

[1] http://physics.nist.gov/cgi-bin/AtData/main_asd

Chapter 2

Observations, Data Reduction, and Analysis

2.1 INTRODUCTION

In this chapter, we discuss the details of our experiment. This project is relatively straightforward, because it uses well-tested observational, data reduction, and analysis techniques. However, we are applying these well-tested techniques in a few unique ways.

Our spectroscopic methods are traditional ones. The ‘long slit’ technique uses a dispersing element in a single diffraction order to spread out one dimension in space into a second dimension in wavelength (or equivalently, velocity). Echelle spectroscopy uses two dispersing elements; one ‘cross-disperses’ the light from the other and allows multiple orders to be viewed at once. To get the appropriate amount of velocity information about our sources, we have used a resolution that is moderately high for typical galaxy surveys (i.e., in the range $60 - 90$ km s^{-1}); this high resolution is made possible by large, $8 - 10$m class telescopes. We have also carried out very high resolution spectroscopy (with an instrumental FWHM $\Delta v \sim 13$ km s^{-1}) of a few targets. This degree of resolution is very atypical for non-quasar extragalactic sources, and thus represents a non-traditional application of a traditional technique.

The data reduction procedures we use are those typically used for processing astronomical spectra. The size of the survey and the complexity of the echelle data has necessitated a higher degree of automation in this procedure, which is in turn made possible by fast computers and specifically tailored pipeline software. As large surveys with complex, high-quality data become the norm in astrophysics, pipeline reduction is on the rise, and this thesis reflects some of that tendency.

The primary component of our analysis is the (multi-parameter, non-linear) function fitting we use to derive the parameters of the Na I D absorption feature. Optimization is a developing field, but rather than using state-of-the-art commercial procedures, we employ a simple iterative minimization routine to fit the data. However, we have attempted to apply this fitting to *blended* multiplet transitions in a physical way, and there is little precedent for this. This has required us to better develop the theory behind it.

2.2 OBSERVATIONS

2.2.1 Survey data

The data for our moderate-resolution observations of starburst- and AGN-dominated sources were taken over the course of many observing runs at three different facilities. These observing runs are listed in Table 2.1 as runs $1-13$ and 15.

For the most distant (and faintest) targets, we used the Echellette Spectrograph and Imager (ESI; Sheinis et al. 2002) on the 10m Keck II in echellette mode (an

Table 2.1. Observing Runs

Run (1)	UT Dates (2)	Telescope (3)	Instrument (4)	CCD (5)	Seeing (6)
1	2001 Jan 23-24	Keck II	ESI	MITLL	0″.8−1″.1
2	2001 Feb 27-28	Keck II	ESI	MITLL	0″.6−1″.1
3	2001 Oct 07-09	KPNO 4m	R-C Spec.	T2KB	1″.4−1″.6
4	2002 Jan 16-17	Keck II	ESI	MITLL	0″.8−1″.5
5	2002 Feb 16	Keck II	ESI	MITLL	1″.2−1″.5
6	2002 Mar 15	Keck II	ESI	MITLL	0″.8
7	2002 Jul 10-13	KPNO 4m	R-C Spec.	T2KB	1″.3
8	2002 Dec 27-30	KPNO 4m	R-C Spec.	T2KB	1″.4−3″.0
9	2002 Dec 31- 2003 Jan 01	MMT	Red Channel Spec.	UA/ITL	1″.4−2″.0
10	2003 Jan 06	Keck II	ESI	MITLL	0″.7
11	2003 May 30- 2003 Jun 02	KPNO 4m	R-C Spec.	T2KB	0″.9−1″.5
12	2003 Jun 03-04	MMT	Red Channel Spec.	UA/ITL	1″.0−1″.5
13	2003 Sep 24-29	KPNO 4m	R-C Spec.	T2KB	0″.7−1″.0
14	2003 Dec 25	Keck I	HIRES	Tek	0″.7−0″.8
15	2004 Apr 12-16	KPNO 4m	R-C Spec.	T2KB	0″.9−1″.6

echellette grating operates at lower cross-dispersed orders than a true echelle spectrograph). This spectrograph is a sensitive instrument with wide spectral coverage (3900 − 11000 Å) over 10 cross-dispersed orders (orders 6 − 15). With a 1″.0 slit width, we obtained a constant spectral resolution of $R \sim 4600$ for our observations, which corresponds to 65 km s^{-1}. We used a 20″ slit length. The associated CCD is a 2k×4k MIT-LL.

For some of our median-redshift data, we used the Red Channel Spectrograph on the 6.5m Multiple Mirror Telescope with an echellette grating. This instrument is less sensitive than ESI and has a smaller wavelength coverage ($\sim$ 5000 Å over $\sim$ 7 orders, with the actual range dependent on the setup). For our observations, we tried two different setups, one including orders 6 − 13 (with only a small portion of order 13), the other using orders $7-13$ (with more of order 13). A single setup is difficult to replicate, as it is changed by manually loosening the dewar mounting screws, shifting the instrument by hand, and re-tightening the mounting screws. We found that we had some difficulty with the stability of the wavelength calibration over the course of a night and with image quality (though this was at least partly due to windy conditions!). With a $1\farcs0 \times 20''$ slit, we obtained a spectral resolution that varied from order to order but averaged around $R \sim 3400$, or 87 km s^{-1}. The Red Channel detector is fairly small, only 1200×800 pixels.

For the nearest (and brightest) targets, we used the R-C Spectrograph on the Kitt Peak 4m. The R-C Spec. is a well-used facility instrument, with many available gratings, deckers, and slit sizes. We used the KPC-18C grating in 1st order, which is a compromise between high resolution and good wavelength coverage. The latter is important so that (a) we can observe Na I D and bright emission lines ([O I]λ6300, Hα, [N II]λ6583, and [S II]$\lambda\lambda6716,6731$) in a single observation and (b) we can use the same grating tilt for multiple targets. We typically chose an 'open' decker, which maximizes the slit length at $\sim 5\farcm4$. The slit width varied between $1\farcs0$ and $1\farcs5$. The dispersion of the spectrograph depends on a number of factors, including wavelength, choice of focus, and the slit width. We calculate an average spectral resolution at 6300 Å of $R \sim 3500$, or ~ 85 km s^{-1} FWHM, with a variation of $10-15$ km s^{-1} around this value. The blocking filters we used (typically the GG-475 or GG-495) have a cut-off near 5000 Å to remove higher orders from the data.

For the ESI and R-C Spec. observations, we generally observed our flux standard stars with large apertures, $\sim 6''$. However, MMT does not allow multiple slit widths in echellette mode, and we were forced to observe with a small slit and correct the resulting flux for the seeing. This sometimes worked fine, but not always.

Most observations were made in photometric conditions. We achieved a median signal-to-noise ratio of 27 per Å and a range from $7 - 194$ per Å. The seeing ranged from a spectacular $0\farcs6$ to a miserable $3\farcs0$, though it was generally good (with variations depending both on the site and on transient weather conditions). The values listed in Table 2.1 are representative but not exhaustive.

2.2.2 High-resolution observations

Our high-resolution observations were obtained during a single night, listed as run 14 in Table 2.1. We used the HIRES echelle spectrograph (Vogt et al. 1994) on Keck I. The wavelength settings for this spectrograph are fully adjustable in two dimensions, so that an observer may select the desired orders and center them properly on the detector (the format of which limits the range of each order that is available). We used a different set-up for each galaxy observed, in order to optimally align the Na I D feature and prominent emission lines on the detector. We also used the GG-475 blocking filter and the red collimator. The slit size was $1\farcs722 \times 14''$ (the D4 decker), which yields a spectral resolution of $R \sim 23000 = 13$ km s^{-1}. The current CCD for HIRES is an engineering-grade Tek 2k × 2k (soon to be upgraded to a more sensitive large-format detector).

2.3 DATA REDUCTION

Standard data processing techniques were used to reduce our data. In each case, Poisson error spectra were propagated in parallel with the data, since these errors are necessary for profile fitting (§2.5).

For our long slit data, the following steps were performed:

- subtraction of the variable 1-dimensional overscan bias and the constant 2-dimensional bias

- correction for illumination variations along the slit, using a twilight flatfield
- subtraction of the (wavelength-dependent) sky background, typically with a 2nd- or 3rd-order polynomial extrapolation along the slit at each wavelength
- extraction of spectra, summing the data over a given range along the slit at each wavelength
- wavelength calibration, including finding the dispersion solution, correcting for zero-point shifts with sky lines, converting to vacuum wavelengths from air wavelengths, and shifting to a heliocentric reference frame
- flux calibration

Note that the long slit data were not flatfielded, in order to retain the statistical weights of the raw data.

For the MMT echellette data, the same basic procedures were followed, modulo the following steps: the data were flatfielded to remove fringing and other defects, which were severe in the reddest orders; the curved echelle orders were traced with one of the standard stars before extraction; and the spectral extraction was performed using either 1- or 2-dimensional 'optimal' extraction (Horne 1986; Marsh 1989).

For the ESI echellette data, we performed the initial data processing using MAKEE[1]. MAKEE performs the following automatically: bias subtraction, flat-fielding, order-tracing, sky subtraction, object extraction (optimal), and wavelength calibration (including an air-to-vacuum wavelength conversion and a heliocentric velocity correction).

---

[1] `http://www2.keck.hawaii.edu/inst/common/makeewww/index.html`

HeNeAr lamps were used to wavelength-calibrate the long slit and MMT data; CuAr, HgNe, and Xe lamps were used simultaneously for the ESI data; and ThAr was used for HIRES. A number of standard stars were used for flux calibration; the most effective ones are those with smooth continua free of metal absorption lines, such as G191-B2B and Feige 34 (which are both hot dwarf stars). Because the ESI data is finely sampled and of moderately high resolution, the flux standards chosen should have closely-spaced wavelength points, and any absorption features must be carefully avoided. The HIRES data was not flux-calibrated due to the inherent difficulty in flux-calibrating very high resolution data.

We generally extracted as much of the galaxy continuum light as possible. In some cases faint continuum or emission-line spatial extensions are present in the spectra, especially for the nearest galaxies, but we did not extract these regions if it seriously harmed the signal-to-noise of the extracted spectrum. For this program, it would have been desirable to use a constant linear aperture for each galaxy in order to fix this variable and to gauge the properties of the gas at a given size scale (both in determining the properties of potential outflows and in computing nuclear spectral types for galaxies). Practically, this was not possible due to the large redshift range in our sample, as well as other factors like variations in seeing. The result is that the linear size probed in each galaxy is different, depending on the light distribution and redshift of the galaxy and the seeing.

Before fitting the Na I D feature, we divided the continuum by a Legendre polynomial fit (of order $2-6$) of 100 Å of data on either side of the He I-Na I D complex. Where necessary, cosmic rays were removed from the data by hand.

2.3.1 Spectral types

In this study we use the four basic optical spectral types (e.g., Veilleux & Osterbrock 1987): H II-region-like, LINER (low-ionization nuclear emission-line region), Seyfert 1, and Seyfert 2. For those objects where nuclear optical spectral types are not available from previous data (mostly galaxies from our hi-z subsample), we determine them using optical line ratios and the diagnostic diagrams of Veilleux & Osterbrock (1987). There are four galaxies for which the spectral type is ambiguous because either Hα or [O III]λ5007 are unobserved or absorbed by resonance lines in the atmosphere, but there is sufficient evidence in each case to effectively rule out a dominant AGN.

Seyfert 1s are distinguished from Seyfert 2s largely by the presence of strong, broad (FWHM $>$ 2000 km s^{-1}) emission line components in the recombination lines. Many Seyfert 1s also possess bright Fe II emission-line complexes. However, there are many other signs of AGN activity, and these can lead to intermediate classifications (e.g., Seyfert 1.9 in the case of a faint broad line in Hα). For the purpose of this study we stick to the Seyfert 1 and 2 classes, with no intermediate stages.

The primary uncertainty in our spectral type measurements is increasing aperture size with redshift. The aperture is rectangular, with one side being the slit width $\sim 1\farcs0$ and the other the extraction size along the slit. As we have chosen to extract most of the galaxy continuum along the slit, we are taking in part of the galaxy's extended (i.e., extra-nuclear) light, and at $z \sim 0.4$, a $1\farcs0$ slit is equivalent to 5 kpc. Thus, the host galaxy could dilute the light from the nucleus and hide an AGN (especially weak broad-line regions). For this reason, the spectral types in our hi-z subsample should be considered somewhat uncertain.

2.3.2 Redshifts

For each galaxy, we compute the redshift ($z \equiv (\lambda_{observed} - \lambda_{rest})/\lambda_{rest}$) from emission and absorption lines in the optical spectrum. Stellar absorption lines are preferable in that they are more likely to trace the systemic velocity of the galaxy; however, in many cases these lines are not present in our spectra or have too low S/N, and we must resort to using emission lines. In both cases we average over as many strong lines as possible. Where possible, we use redshifts measured from H I emission or absorption lines (Mirabel & Sanders 1988; Hutchings 1989; Martin et al. 1991; van Driel, Gao, & Monnier-Ragaigne 2001), which is available for ~ 20 of the nearest galaxies in our sample. In a very few cases, we use the emission-line redshift from a rotation curve instead of the H I velocity.

In many galaxies, the optical emission lines show a double-lobed profile indicative of rotation in the 1-D spectrum and apparent rotational tilt in the 2-D image. For these galaxies, the emission-line redshift equals the average redshift of the two emission lobes. Other profiles show a single lobe. The sizes of the core and wings of the profiles vary greatly, and some profiles show asymmetries. The ULIRGs tend to show the most complex and broadest profiles (see Chapter 3).

To de-blend adjacent lines (e.g., Hα/[N II] or [S II] $\lambda\lambda 6716, 6731$), we fit a Gaussian, Lorentzian, or Voigt profile to the line, which generally provides a flux-averaged redshift. In complex profiles where two lobes are not obvious, there is no rotational tilt in the 2-D spectrum, and the profile is too irregular to fit with an analytic function, we have generally used the redshift of the peak of the line.

2.4 PHYSICAL INTERPRETATION OF ABSORPTION LINES

Absorption lines in astronomical spectra originate in a variety of contexts. The properties of an absorption line can be used to derive physical quantities about the absorbing gas independent of the specific context. However, the derived quantities achieve their final significance only after being folded into the relevant astronomical situation. Here, we discuss the unique difficulties behind the interpretation of a particular class of absorption lines.

Absorption line profiles can be classified in a number of ways that affect the choice of analysis technique:

- **Optical depth and covering fraction.** Is the line optically thin or optically thick? Is the covering fraction of the absorbing gas less than unity?

- **Instrumental Resolution.** Is the line resolved or unresolved by the spectrograph?

- **Number of transitions.** How many transitions of a given atomic or molecular state are available? If there are multiple transitions, are they blended or unblended?

- **Velocity distribution.** Can the velocity distribution be described by a simple function like a Gaussian (i.e., the 'curve-of-growth' assumption)? Is it symmetric or asymmetric? Can it be described by overlapping components of a simple function?

For a single line, the distribution of the average optical depth along the line-of-sight can be computed exactly as a function of wavelength (i.e., velocity) if the covering fraction of the gas is unity (in other words, if the absorbing gas completely covers the background source). This is generally the case for quasar or stellar sight lines through the intergalactic and interstellar media, respectively, since the background light source in each of these cases is a point source. This analysis can also be done for blended doublet, triplet, or multiplet lines by solving a set of linear equations, Gaussian fitting, or 'regularization' methods (Arav et al. 1999b).

However, in the case of an extended background light source, such as a nuclear galaxy starburst, or gas very near a continuum source (like clouds in the broad-line region near a quasar), the covering fraction is not in general unity. In this case there is a degeneracy between optical depth and covering fraction for a single line. This degeneracy is typically resolved by observing two or more atomic transitions with the same lower level, whose relative optical depths can be computed exactly from atomic physics.

2.4.1 Multiple unblended transitions

In the ultraviolet region of the spectrum, there are a number of strong stellar and interstellar absorption lines which possess multiple transitions in the same ionic species (e.g., C IV $\lambda\lambda 1548, 1550$). Typically, these lines are observed at high enough resolution that they are resolved and unblended.

For the case of multiple resolved, unblended lines in the same ion that arise from the same energy level, it is trivial to calculate both optical depth and covering fraction as a function of velocity. This is independent of the assumption of a Maxwellian, or Gaussian, velocity distribution (the 'curve-of-growth,' or COG, assumption), since the relative optical depths of the lines are determined a priori from atomic physics. One caveat for the case of two lines (a doublet) is that this optical depth ratio should be substantially different from unity.

The techniques for extracting τ and C_f in this case are discussed in a number of papers on intrinsic quasar absorption lines in the UV (e.g., Barlow & Sargent 1997; Hamann et al. 1997; Arav et al. 1999a,b). Note that the optical depths and covering fractions determined this way are still subject to uncertainties, since they are averages along the line-of-sight and across the continuum source. Furthermore, the covering fraction determined in this way also accounts for light scattered into the line of sight. (Other subtleties of interpretation exist, but are beyond the scope of this discussion.)

The classic alternative to this for two unresolved (but still unblended lines) is the doublet ratio method (Nachmann & Hobbs 1973). The equivalent width for a single line is given by

$$W_{eq} = \int_0^\infty [1 - I(\lambda)] d\lambda. \tag{2.1}$$

For a partial covering fraction and optical depth that depend on velocity, the general expression for the intensity of an absorption line, assuming a continuum level of unity, is

$$I(\lambda) = 1 - C(\lambda) + C(\lambda) e^{-\tau(\lambda)}. \tag{2.2}$$

Under the curve-of-growth (COG) assumption (i.e., a Maxwellian velocity distribution), the optical depth τ can be expressed as

$$\tau(\lambda) = \tau_0 e^{-(\lambda-\lambda_0)^2/(\lambda_0 b/c)^2}, \tag{2.3}$$

where τ_0 and λ_0 are the central optical depth and central wavelength in the line and b is the width of the line (specifically, the Doppler parameter $b = \sqrt{2}\sigma = \mathrm{FWHM}/[2\sqrt{\ln 2}]$).

The ratio of the equivalent widths of the two lines of the doublet, $R \equiv W_{eq,2}/W_{eq,1}$, is independent of C_f as as long as C_f is independent of velocity (i.e., a constant across the absorption line profile). If we can measure the equivalent widths for the doublet lines from the measured spectra, then under the COG assumption, the equivalent width ratio R is a monotonic function of the central optical depth of one of the lines (see Table 2.1 in Spitzer 1968). We can thus determine the central optical depth from the measured equivalent widths and compute the total gas column density (Spitzer 1968). Again, this holds even if the covering fraction is less than unity, as long as it is constant with velocity (since it appears under the integral for W_{eq}).

In the case of a non-Gaussian velocity distribution, however, the doublet-ratio method can underestimate the true optical depth. Nachmann & Hobbs (1973) explore the case of a 2-component profile (i.e., two overlapping Gaussian profiles in a single transition). Narrow, saturated components that carry a small fraction of the actual line-of-sight mass but dominate the equivalent width of the line can cause this underestimate.

There are generic cases in which a superposition of components can accurately mimic the behavior of the Maxwellian COG, however (Jenkins 1986). A few superposed components do not mimic a standard COG well. But a combination of many components, even if a few are mildly saturated (with optical depth $\tau \sim 5 - 10$), can produce good results (i.e., the ratio of computed to actual column densities $N_{experimental}/N_{true} \sim 0.84 - 1.00$). This is true whether or not the components actually overlap in velocity space. However, it assumes that the individual components are approximately Gaussian and that the distributions of their parameters (Doppler parameter b and optical depth τ) are not too strange (Jenkins 1986).

2.4.2 Multiple blended transitions

In cases where the lines in a doublet or other multiplet are blended together, extracting the properties of the absorbing gas becomes much more difficult, both in technique and physical interpretation. As discussed previously, apparent optical depth can be measured in this case by a variety of techniques (Arav et al. 1999b), but no information on covering fraction is available. If we are interested in solving for optical depth and covering fraction directly, we must make simplifying assumptions. In the following discussion, we limit ourselves to a doublet, for simplicity and because it is relevant to this work.

One method is to fit simple functional forms (such as Gaussian or Voigt profiles) to the intensity as a function of wavelength, measure the resulting equivalent widths, and use the doublet ratio to determine the optical depth of the line. Recall that the doublet ratio method assumes a Gaussian in optical depth, which only translates into a Gaussian in intensity in the case of optically thin gas. Recall also that the doublet ratio is independent of covering fraction only as long as C_f is constant with velocity. With knowledge of the optical depth, the covering fraction then follows from the residual intensity of the doublet lines.

If fitting Gaussian intensity profiles leads to a high optical depth, one of the assumptions of this method is incorrect. Possible explanations include: (a) a non-Gaussian optical depth distribution that mimics a COG (e.g., a superposition of many components; Jenkins 1986); or (b) a (possibly saturated) profile that is modulated by velocity variation in the covering fraction, rather than in the optical depth. In the latter case, the doublet ratio method overestimates the optical depth, as can be seen in Figure 2.1 (see also Arav et al. 1999a, 2003). If (a) is true, then this method may still yield correct results (see Jenkins 1986, for more details). However,

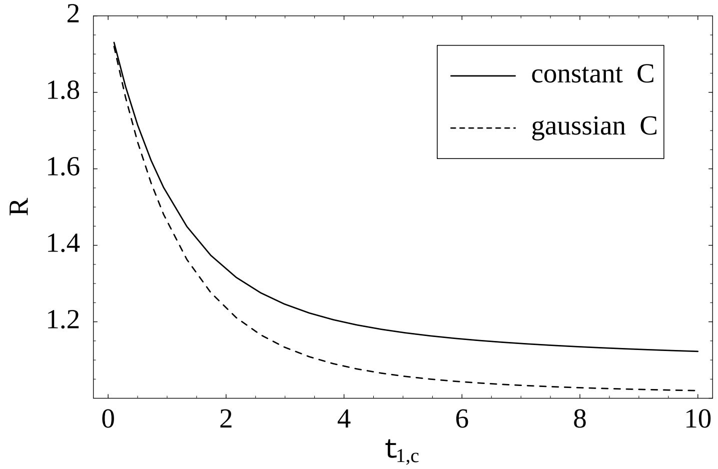

Figure 2.1: Equivalent width ratio of the Na I D doublet, $R \equiv W_{eq}(D_2)/W_{eq}(D_1)$, as a function of the central optical depth of the red line, $\tau_{1,c}$. We assume a Gaussian in optical depth (COG assumption) and a constant covering fraction C_f (solid line) or a Gaussian $C(\lambda)$ with the same width as $\tau(\lambda)$ (dashed line). The case of a Gaussian intensity profile and a high optical depth as measured from the doublet ratio R is self-contradictory, since the intensity profile should not be Gaussian for a high optical depth under the COG assumption. The covering fraction in this case may vary with velocity (perhaps as a Gaussian), which means that the normal curve-of-growth severely overestimates τ for $R \lesssim 1.2$.

if (b) is the case, then this method fails. Unfortunately, it may be impossible to distinguish among these two cases and the nominal case unless we have independent information about either the optical depth or the covering fraction.

A second method is to allow more complex intensity profiles, which are functions of physical parameters. The obvious benefit of this is that the profile shape is readily understood in terms of these physical parameters, and the optical depth and covering fraction distributions can be chosen independently. Furthermore, different assumptions about these distributions can be tried. However, it has the same drawback of the first method of requiring SOME assumption about the form of these.

The Na I D lines are generally blended together in our data into a single feature, and some have a covering fraction less than unity. We choose to use the second analysis method described above. For simplicity, we assume a curve of growth. To treat the covering fraction, we can then take one of the two following approaches:

1. **Constant C_f.** Assume a covering fraction that is independent of velocity within a given component; this implies that the absorbing atoms in a given component are spatially coincident (see below).
2. **Non-constant C_f.** Allow the covering fraction to vary as a function of velocity, perhaps as a Gaussian with the same width as the optical depth profile. Assume that the absorbing atoms in a given component follow case (3) for a blended doublet (see below).

In the current analysis we have restricted ourselves to a constant covering fraction, for simplicity. However, exploring the second approach in future work would be interesting and useful.

2.4.3 Multiplet blending and geometry

Decomposing blended profiles correctly requires an assumption about geometry. Consider the following three cases, discussed in the context of the Na I D doublet as a specific example. Note that at a given wavelength, the atoms producing the D_1 line are separated by 6 Å ~ 300 km s^{-1} from the atoms producing the D_2 line. However, at a given velocity, we expect them to have (a) relative optical depths determined by atomic physics and (b) the same covering fraction.

1. **Co-spatial atoms.** Suppose that the atoms at all velocities are essentially coincident–that is, located at the same position in the plane of the sky relative to the background continuum source. This is likely to be true if the broadening of the lines is due to local physics. (If the broadening is due to large-scale

physics and wind geometry, widely-separated velocities will probably not be co-spatial.) We can then assume a covering fraction that is independent of velocity, such that at a given wavelength the atoms producing the D_1 and D_2 lines have the same covering fraction (even though their velocities differ by 300 km s^{-1}). The correct expression for the combined intensity of two separate velocity components (each with optical depth τ_i) is then given by

$$I(\lambda) = 1 - C + Ce^{-\tau_1(\lambda)-\tau_2(\lambda)}. \tag{2.4}$$

2. **Non-co-spatial atoms.** Suppose that at any wavelength, the atoms producing the D_1 and D_2 lines have no spatial overlap in the plane of the sky. Then the covering fraction is velocity-dependent, and the total intensity is given by

$$I(\lambda) = 1 - C_1(\lambda) - C_2(\lambda) + C_1(\lambda)e^{-\tau_1(\lambda)} + C_2(\lambda)e^{-\tau_2(\lambda)} = I_1(\lambda) + I_2(\lambda) - 1, \tag{2.5}$$

   where I_i is the total intensity for a single absorbing component, as given in Eq. 2.2. In this case, the total covering fraction at any wavelength is then

$$C_{total} = C_1 + C_2 \leq 1. \tag{2.6}$$

3. **Partial overlap.** A ‘middle-ground’ assumption is that there is overlap between the atoms producing the doublet lines at a given wavelength, and that the covering fraction describes the fractional coverage of both the continuum source and also of the atoms producing the other line. The correct expression is then

$$I(\lambda) = [1 - C_1(\lambda) + C_1(\lambda)e^{-\tau_1(\lambda)}] \times [1 - C_2(\lambda) + C_2(\lambda)e^{-\tau_2(\lambda)}] = I_1(\lambda)I_2(\lambda). \tag{2.7}$$

> This formulation also allows for a covering fraction that varies with velocity. It contains the expression for our second case plus a cross term involving the product C_1C_2. In this case, the total covering fraction of the continuum source at a given wavelength is
>
> $$C_{total} = C_1 + C_2 - C_1C_2. \tag{2.8}$$

We have chosen the case of 'partial overlap' for our analysis. The 'co-spatial' assumption is probably the simplest in this case; however, it is unlikely to be physical, given that the lines in these galaxies are very broad, with widths that are dominated by large-scale physics that will not keep the absorbing atoms in the same place. We find the other extreme to also be unlikely.

2.5 LINE FITTING TECHNIQUES

2.5.1 Mathematical background

There is an enormous amount of mathematical literature on 'optimization,' which is the umbrella under which the practical problem of fitting functional forms to scientific data falls.[2] Our problem is classified as a non-linear minimization problem with simple bound constraints. It is non-linear because the functional dependence on the parameters is not linear, and there are upper and lower bounds on some parameters (e.g., the covering fraction, $0 < C_f < 1$).

The particular technique that we choose is the Levenberg-Marquardt method

---

[2] An excellent resource is the 'Optimization Technology Center,' found on-line at `http://www.ece.northwestern.edu/OTC/`, which classifies and describes the optimization problem according to various criteria. It also offers links to or descriptions of various solvers, both open-source and commercial.

(Marquardt 1963), which is a trust-region method for solving unconstrained nonlinear problems. 'Trust-region' implies that new iterations are restricted to stay in a certain phase-space neighborhood of previous ones. Levenberg-Marquardt methods are a hybrid of the straightforward steepest-descent method and the Gauss-Newton method.

Steepest descent (ascent) operates by assuming that the minimum (maximum) lies in the direction where the gradient is lowest (highest). We then move in this direction by some amount, re-calculate the gradient, and iterate.

Newtonian methods approximate the function to be fit by expanding it in terms of the first and second derivatives, which includes a quadratic dependence on the function. This is equivalent to assuming the function is near the minimum (or maximum) and can be approximated as a parabola. We can then solve for the minimum of this parabola right away. To do this, we need to know the Jacobian and Hessian matrices (the first and second derivatives, respectively, with respect to the parameters to be fit). Gauss-Newton methods approximate the Hessian by its first term (the product of the Jacobian with its transpose) and throw away the term involving the second derivative.

Each of these methods has drawbacks. Steepest descent methods can get stuck in local minima and are not as efficient near the minimum, while the assumption of parabolic shape is invalid far from the minimum. Levenberg-Marquardt is a hybrid of these two methods using a Lagrange multiplier λ that, when large, governs the steepest descent step size; for small λ, Levenberg-Marquardt is equivalent to Gauss-Newton. The magnitude of λ is changed depending on whether the minimum is getting closer (use Gauss-Newton $\Rightarrow$ smaller λ) or farther away (use steepest descent $\Rightarrow$ larger λ).

2.5.2 Code

The particular L-M implementation that we use is taken from Numerical Recipes (Press et al. 1992). We have modified this routine to include bound constraints, and we have wrapped it in a loop structure. As long as the χ^2 value is decreasing, the routine continues. However, as soon as the magnitude of the change in χ^2 between iterations dips below a certain tolerance (10^{-5} in our fitting) and χ^2 is no longer decreasing (i.e., $\Delta\chi^2 > 0$), the routine outputs the result as the minimum. The danger is that this will leave us decreasing χ^2 indefinitely as we approach the minimum, but the nature of the parabolic approximation near the minimum ameliorates this difficulty. We also reset λ to its initial value (0.001) if χ^2 has increased for 7 straight iterations; this generally is not important, but sometimes prevents the routine from getting stuck in steepest descent.

Levenberg-Marquardt is technically not equipped to deal with constraints. One option would be to incorporate so-called 'active set' methods. However, given that we are only constrained by simple boundaries we have used a straightforward recipe that simply pulls the solution back to the phase-space boundary of acceptable values if it crosses it.

Because the L-M algorithm is a local optimizer (it doesn't search all of phase space!), the number of components we choose and the initial parameter values are of some importance. We generally fit $1 - 3$ velocity components, as this seems to be the maximum number that is well-constrained by our data. Adding more components has a tendency to either create components with very high or very low optical depths.

We determine by eye the initial parameter values for input to the fitting routine. The final solution is in general not strongly sensitive to these initial guesses. However, in the instances that it is, the tendency is for the solution to increase toward high optical depths ($\tau \gg 1$). This sometimes shows up as long tails in the simulated optical depth distributions (§2.5.5) in cases where the best-fit optical depth is only $\sim$ a few. For most of these cases we set the optical depth and corresponding mass outflow rate as a lower limit to the true value. The most important boundary constraint is thus the optical depth upper limit, which we generally set to be ~ 5 (as the fitting is insensitive to changes in optical depth above this value because of the minimal change in the profile shape). However, the high-resolution data permits better sensitivity to τ, and we can relax this limit somewhat.

2.5.3 Comparison to SPECFIT

The interactive fitting package SPECFIT[3] is commonly used in optical spectroscopy, since it is bundled with IRAF and has a range of analytic functions that can be fit to the data (Kriss 1994). In Rupke et al. (2002), we used SPECFIT and added an analytic function for an absorbing doublet with partial (but constant) covering fraction.

We compared our finished code to SPECFIT, since the latter is a frequently used and already tested code. SPECFIT has four fitting algorithms that it can use to converge to a best-fit value, including versions of (1) a downhill simplex and (2) a Levenberg-Marquardt (L-M) routine, (3) alternation between these two, and (4) a basic parameter grid search. It has inputs for lower and upper bounds on parameters, and is written in SPP (an IRAF programming language). We find that our code converges much more quickly, but the resulting parameters are similar to those obtained with SPECFIT.

On close inspection we discovered some minor problems with SPECFIT, primar-

---

[3] `http://www.pha.jhu.edu/~gak/specfit.html`

ily in how it treats parameter boundaries. (1) If the solution is across a parameter boundary after a predetermined number of iterations, SPECFIT automatically fixes the value of this parameter at the boundary and stops varying it. This can artificially constrain the parameter before the minimum is reached. (2) The L-M algorithm enforces the parameter limits after each iteration (which in parameter phase space corresponds to moving the solution back to or across the boundary in one dimension) at the wrong time, such that the computed χ^2 applies to the position across the boundary, not the corrected position. (3) The L-M algorithm makes a stepwise numerical approximation to the first derivative using central differences; while some approximation to the Hessian should be made to avoid singularities, the exact first derivative is easy to compute from the model function and not computationally expensive. Finally, (4) the 'step' parameter in the algorithm is used to control more than one variable (and its use is not adequately explained in the accompanying documentation).

2.5.4 Instrumental smearing

Ideally, our fitting technique should convolve the expected profile shape with the instrumental resolution. This convolution adds computation time to the routine; however, with a fast Fourier transform (FFT) and at most a few hundred iterations this is not much of an issue (the fitting time might change from a few seconds to a few minutes at most).

Unfortunately, the instrumental response function for our data is not always Gaussian, especially for the data with slit widths comparable to or larger than the spectral resolution (e.g., our high-resolution Keck data). For these set-ups, the intrinsic profile tends to be flat-topped. Accurately measuring this profile should be possible with a sufficient number of sky lines.

We find that instrumental smearing has little impact on our data, however. In Figure 2.2, we show profiles with and without instrumental smearing included. This figure illustrates that the difference is minimal when the error bars on our data are considered. In some cases this difference could artificially inflate the best-fit χ^2 value; however, we do not anticipate that it causes measurable changes in the best-fit parameters.

2.5.5 Parameter errors

To determine errors in the fitted parameters, we used Monte Carlo simulations. To do this, we first assumed the fitted parameters represent the 'real' parameter values. We then created multiple statistical realizations of this by using Poisson errors estimated from the signal-to-noise of the data. We fitted the resulting spectrum in each realization, yielding a distribution of fitted parameters for each galaxy. The distributions in wavelength, λ, and Doppler parameter, b, are generally Gaussian, which is consistent with the assumptions of the fitting procedure. Fits to these Gaussians yield 1σ errors.

This method was chosen as an alternative to estimating errors directly from the covariance matrix that is output by the fitting algorithm or from two-dimensional χ^2 contours. Given the large number of parameters involved, some of which are not completely independent of each other, it would be uninformative to simply quote one-dimensional errors.

The covariance matrix output from our fitting routine shows that in general the covering fraction and optical depth are anti-correlated in the fit of a given velocity component. Because of this, we examined the distribution of the product $C_f \times \tau$, rather than of C_f or τ separately. In the case of high S/N data, $C_f\tau$ is typically distributed as a Gaussian. However, for most components, this product has a tail

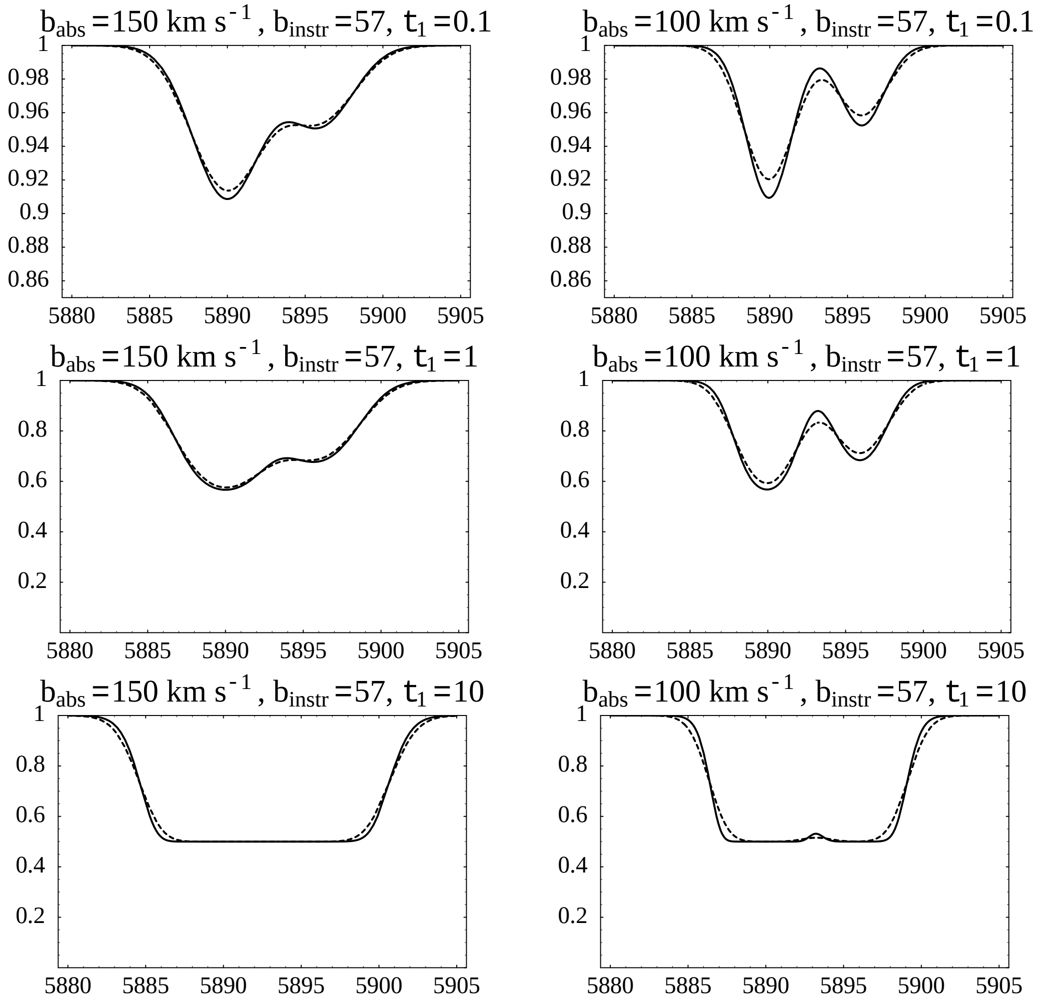

Figure 2.2: Plots of the Na I D doublet with (dashed lines) and without (solid lines) instrumental smearing, for three optical depths ($\tau = 0.1, 1, 10$) and two intrinsic linewidths ($b_{abs} = 100, 150$ km s^{-1}). These linewidths correspond approximately to the mean and lower limits in our data. The instrumental linewidth $b_{instr} = 57$ km s^{-1} corresponds to FWHM = 95 km s^{-1}, which is approximately the lowest instrumental resolution in our observations.

to high values, of varying length. Instead of fitting a Gaussian to the distribution in $C_f\tau$, we compute 68%-confidence errors both above and below the mean. When propagating these errors to other quantities, we assume that the percent error is split evenly between C_f and τ.

Nearby stellar features

The spectral region near Na I D is a zoo of weak stellar lines, illustrated in Figure 2.3 using the high-resolution solar atlas of Beckers, Bridges, & Gilliam (1976). We convolve these lines with Gaussians of width $\sigma = 100 - 300$ km s^{-1} to imitate the effects of instrumental smearing and galactic rotation/dispersion. The resulting spectra show that the nearby stellar features will introduce complications into our analysis that affect continuum normalization, identification of blueshifted features, and fitting of the Na I D lines.

The best solution is to fit stellar synthesis models or convolved stellar spectra to our data and remove this component. However, our spectra are in general not of high enough signal-to-noise to do this reliably.

In fitting the continuum, we have generally avoided the strongest stellar features blueward of Na I D (the nearest of which blends slightly with He I λ5876). Avoiding the redward features is difficult, however, and we have not attempted this.

The strongest nearby stellar feature is located 33 Å ($\sim$ 1700 km s^{-1}) blueward of the D_2 line, centered at $\sim$ 5857.5 Å. There is variation in its strength among our spectra, and in general it is too weak to be noticeable without heavy smoothing and too far to the blue to mimic anything but very high velocity outflowing gas. Smoothing does in general reveal the presence of this feature, however. In Figure 2.4 we show examples of two galaxies where we boxcar smooth by $\sim$ 350 km s^{-1} and overlay the $\sigma = 300$ km s^{-1} convolved solar spectrum from Figure 2.3 in order

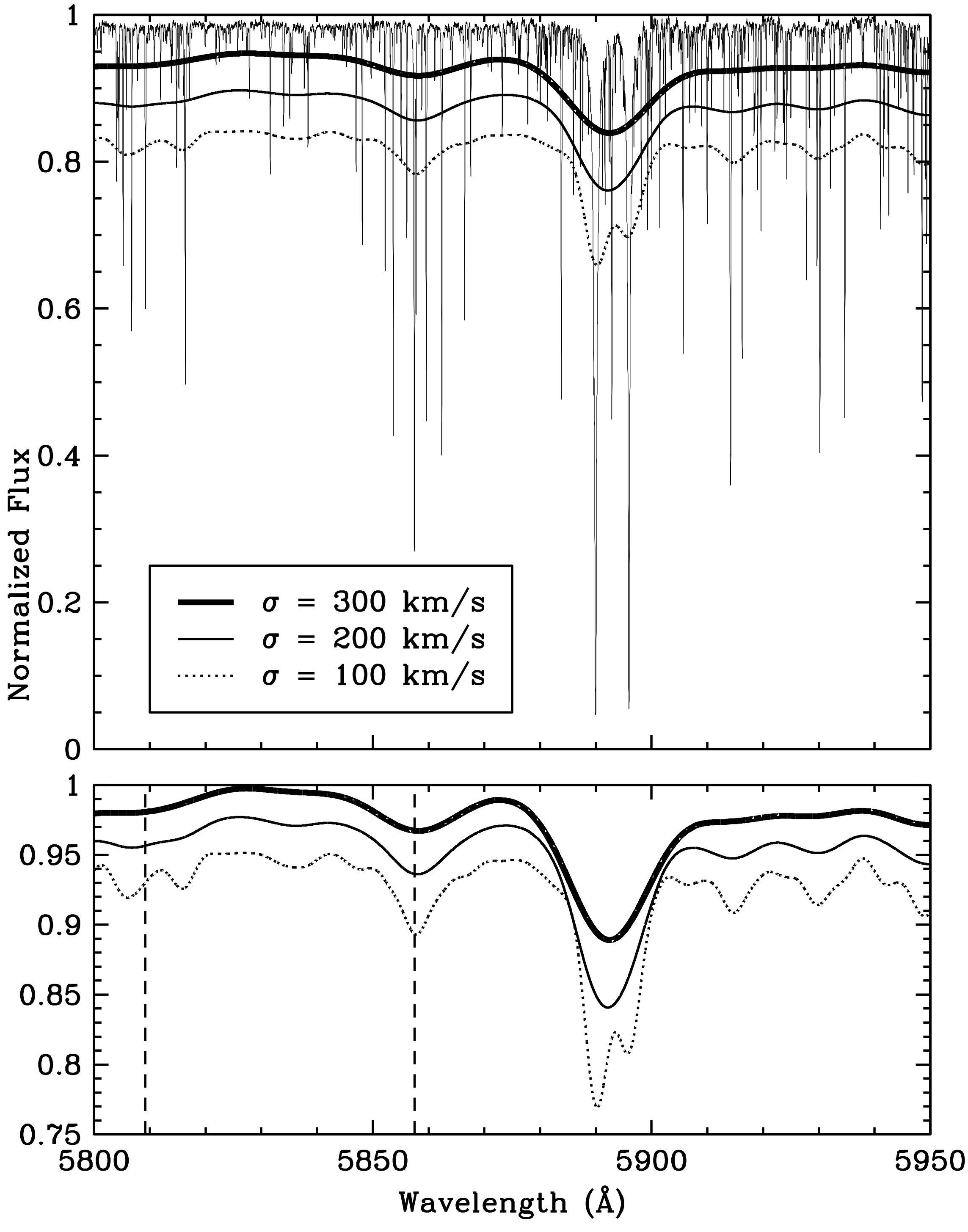

Figure 2.3: (a) High-resolution solar spectrum from Beckers et al. (1976), both raw and convolved with Gaussians of width $\sigma = 100 - 300$ km s^{-1}. The convolved spectra have offsets applied for better viewing. (b) Close-ups of the convolved spectra. The lower two spectra have slight offsets applied for better viewing. Note the zoo of weak stellar lines which combine to make a relatively strong feature blueward of Na I D in the convolved spectra.

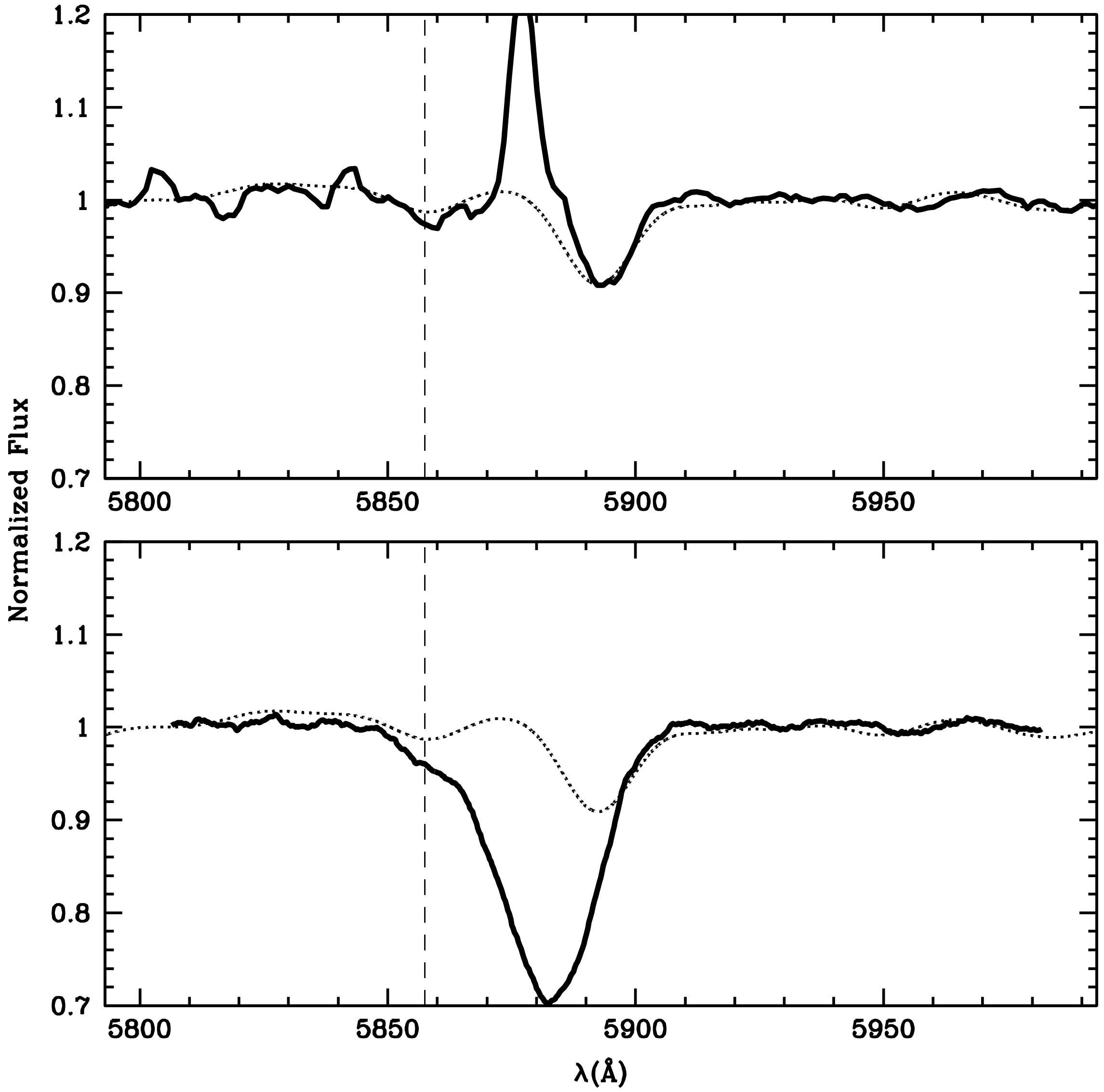

Figure 2.4: Spectra for two galaxies (F15549+4201 and F10378+1108) in the region of Na I D, boxcar smoothed by $\sim$ 350 km s^{-1} to bring out weak stellar features. The strong stellar feature blueward of Na I D is marked with a vertical dashed line. The solar spectrum convolved with a $\sigma = 300$ km s^{-1} Gaussian (see Figure 2.3) is overlaid as the dotted line.

to highlight the weak stellar features.

The weak absorption lines in the solar spectrum correspond fairly well to those in each galaxy (though there are some discrepancies, probably due to the use of a G-type star as a template). In the first (F15549+4201, z = 0.0348), the Na I D absorption is purely stellar (consistent with our fitting but not with the Mg I b diagnostic; see Chapter 3). In the second (F10378+1108, $z = 0.1367$), the absorption is mostly interstellar, but there is some stellar contribution. We are able to fit a weak, optically thick line at this position, plus three blueshifted interstellar components, though this fit is not well-constrained enough to use in the actual analysis. The blue stellar feature blends slightly with the most blueshifted interstellar component, but this contribution is small and we ignore it. The rest of our sample is somewhere in between these two cases in terms of stellar contribution to Na I D, and the blue stellar feature blends slightly with blueshifted Na I D in at most a few cases.

Chapter 3

Outflows in Starburst-Dominated Infrared-Luminous Galaxies

3.1 INTRODUCTION

The primary phenomenon of interest in this work is outflows from starbursting galaxies. Starbursts come in a variety of sizes and flavors, so to narrow down the search further we initially focussed on the most massive starbursts. Assuming a conversion from supernova mechanical energy into the thermal energy of the wind (and then back into bulk kinetic energy as gas is accelerated) that is the same in dwarfs and 'super-starbursts,' these galaxies have the most energy available to power winds. However, this assumption may be invalid, and there is likely to be other important physics. For instance, the size of the gravitational potential affects the escape velocity, and the gaseous environment can absorb energy and provide a confining pressure.

Infrared emission is an excellent indicator of starburst activity. Stars are formed in dense molecular environments which have a similarly high dust density, and this dust absorbs the ultraviolet light from the starburst and re-emits it as blackbody radiation, primarily at infrared wavelengths (implying dust temperatures of several tens of K). This is especially true of galaxies that are the most luminous in the infrared, which contain copious amounts of molecular gas and dust. These galaxies have infrared luminosities which are equal to their bolometric luminosities within a factor of 2 or less. In other words, essentially all of the stellar luminosity is reprocessed by the dust and turned into infrared emission. The infrared luminosity and star formation rate are then directly proportional to each other (Kennicutt 1998):

$$\mathrm{SFR} = \frac{L_{\mathrm{IR}}}{5.8 \times 10^9\ L_\odot}. \tag{3.1}$$

As we discuss below, an active galactic nucleus can contribute to L_{IR}, so in some cases we include a downward correction α in this formula.

Infrared-selected galaxies are classified into several classes according to their luminosities. These classifications vary with author, but the most common is based on the $8 - 1000\mu$m luminosity. The classes are

- **LIRG** ≡ luminous infrared galaxy, with $11 \leq \log(L_{\mathrm{IR}}/L_\odot) < 12$
- **ULIRG** ≡ ultraluminous infrared galaxy, with $12 \leq \log(L_{\mathrm{IR}}/L_\odot) < 13$
- **HyLIRG** ≡ hyperluminous infrared galaxy, with $\log(L_{\mathrm{IR}}/L_\odot) \geq 13$

For an observational definition of $L_{\mathrm{IR}}(8-1000\mu\mathrm{m})$ (based on a two-temperature dust model), see Sanders & Mirabel (1996) or Perault (1987).

The ultraluminous infrared galaxies have unique properties (Sanders & Mirabel 1996). They are typically massive starbursts, but may also have significant AGN activity (Veilleux, Kim, & Sanders 1999b; Veilleux, Sanders, & Kim 1999c; Lutz, Veilleux, & Genzel 1999; Genzel et al. 1998). The frequency of occurrence of AGN activity in ULIRGs increases with increasing infrared luminosity (Veilleux et al. 1999b). Most are late mergers of two gas-rich spirals that are evolving into moderate-size elliptical galaxies (Kim, Veilleux, & Sanders 2002; Veilleux, Kim, & Sanders 2002; Genzel et al. 2001; Tacconi et al. 2002), and most of those classfied as AGN are in the latest stages of merging (Veilleux et al. 2002). Their number density increases strongly with increasing redshift, evolving approximately as $(1+z)^7$ (Kim & Sanders 1998; Cowie et al. 2004). Possible counterparts are seen in deep submillimeter imaging at high redshift, further suggesting strong density evolution (Smail, Ivison, & Blain 1997; Hughes et al. 1998; Blain et al. 1999; Lilly et al. 1999; Barger, Cowie, & Sanders 1999). This redshift evolution has interesting implications for star formation and merger history, and should be nailed down firmly by observations with the Spitzer Space Telescope.

ULIRGs contain copious amounts of dense molecular gas in their cores (e.g., Sanders, Scoville, & Soifer 1991), which is available to power star formation. They also possess quasar-like bolometric luminosities, and are the most numerous high-luminosity objects at low redshifts. In fact, it is hypothesized that ULIRGs play a role in the evolution of quasars. Many ULIRGs may contain buried AGN that are hidden by dust; when this dust is removed (by radiation pressure, or perhaps the outflows studied in this work), a bright quasar is left (Sanders et al. 1988). This evolutionary process is currently under scrutiny, and is probably active in some, but not all, cases.

LIRGs possess some of the same properties of ULIRGs. They possess intense starbursts, and many are in the process of interaction with a smaller companion or equal-mass neighbor (Arribas et al. 2004; Ishida et al. 2004, in prep.). In our work, for ease of terminology we group LIRGs and some less-luminous galaxies in a single group, which we label **IRGs** (for Infrared Galaxies).

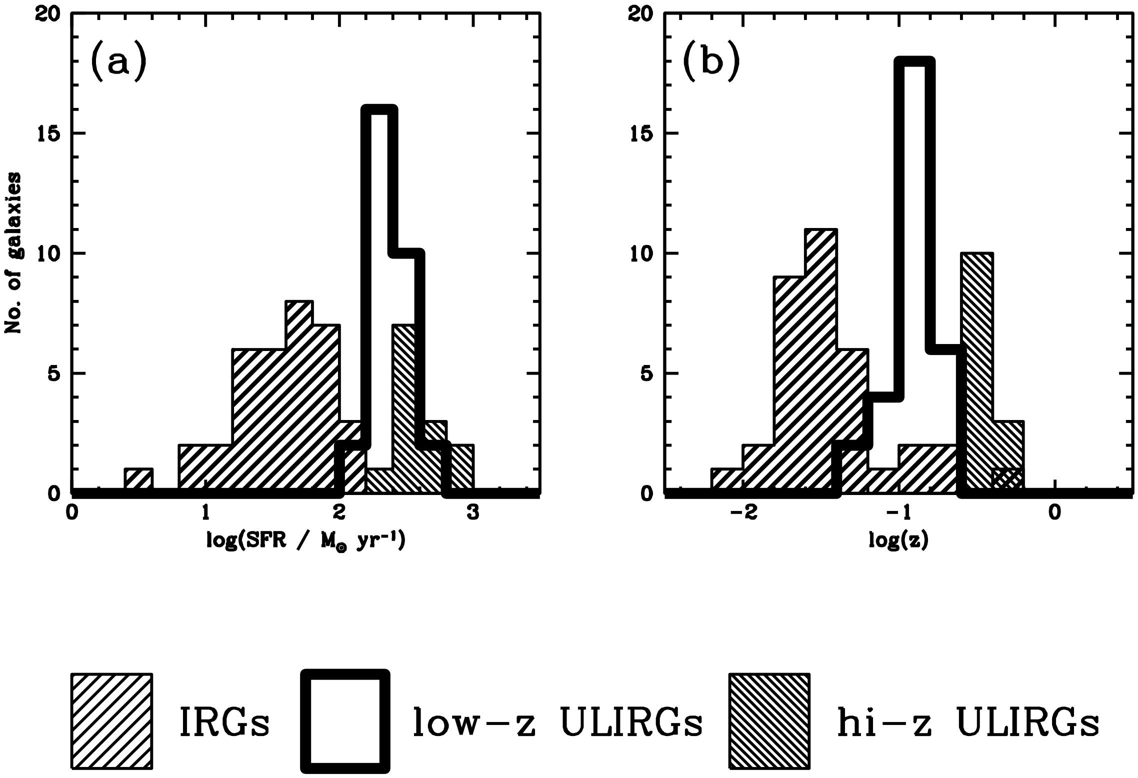

Figure 3.1: The distributions of (a) star formation rate and (b) redshift for our three subsamples (§3.2). Notice that the mean values for each subsample are different and that the distributions are largely disjoint.

3.2 SAMPLE

Our starburst-dominated sample consists of 78 galaxies with a large range of host galaxy properties, including star formation rate (SFR), morphology, redshift, mass, and size. We subdivide this sample by two primary observables, redshift and far-infrared luminosity ($L_{\rm IR} \equiv L[8-1000\ \mu{\rm m}]$). Figure 3.1 shows the distributions of redshift and SFR (computed from the infrared luminosity – see §3.3.4) for the three subsamples described below. Tables 3.1 and 3.2 show the average properties of each subsmaple and the individual properties of each galaxy, respectively.

Table 3.1. Subsample Average Properties

Quantity (1)	IRGs (2)	low-z ULIRGs (3)	high-z ULIRGs (4)
N_{gals}	35	30	13
$\langle z \rangle$	$0.031^{+0.042}_{-0.018}$	$0.129^{+0.066}_{-0.044}$	$0.360^{+0.070}_{-0.059}$
$\langle log(L_{\rm IR}/L_\odot) \rangle$	$11.36^{+0.38}_{-0.38}$	$12.21^{+0.15}_{-0.15}$	$12.45^{+0.19}_{-0.19}$
$\langle$SFR$\rangle$ ($M_\odot$ yr^{-1})	40^{+55}_{-23}	225^{+95}_{-67}	389^{+211}_{-137}
$\langle dM/dt \rangle$ ($M_\odot$ yr^{-1})	7^{+10}_{-4}	8^{+15}_{-5}	6^{+4}_{-2}
$\langle \eta \rangle$	$0.15^{+0.25}_{-0.09}$	$0.04^{+0.09}_{-0.03}$	$0.02^{+0.02}_{-0.01}$
$\langle \Delta v \rangle$ (km s^{-1})	113^{+97}_{-52}	183^{+152}_{-83}	161^{+219}_{-93}
$\langle \Delta v_{max} \rangle$ (km s^{-1})	301^{+145}_{-98}	416^{+233}_{-149}	359^{+119}_{-90}
$\langle \Delta v$[max. N(H)]$\rangle$ (km s^{-1})	104^{+80}_{-45}	176^{+131}_{-75}	161^{+219}_{-93}

Note. — For each value we include the median ± the linear 1σ dispersions under the assumption of a Gaussian distribution in the log of the quantity.

Table 3.2. Galaxy Properties

Name (1)	Other (2)	z (3)	Type (4)	$L_{\rm IR}$ (5)	$K^{(\prime)}$ (6)	SFR (7)	dM/dt (8)	η (9)	Run (10)	t_{exp} (11)	PA (12)	Refs (13)
IRGs												
F00521+2858	UGC.556	0.0155	L	10.84	-24.29	12	0.00	0.0000	8	3600	90	34
Z01092−0139	···	0.1533	H	11.65	-24.99	77	>3.96	>0.0515	13	7200	160	2
F01250−0848	Mrk.995	0.0488	H	11.68	-25.85	83	6.85	0.0822	13	2700	40	5
F01417+1651:N	III.Zw.35	0.0276	L	11.56	-24.23	63	0.00	0.0000	13	4500	15	34ab
F01417+1651:S	···	0.0271	H	···	···	···	···	···	···	···	···	34ab
F01484+2220	NGC.695	0.0323	H	11.64	-25.99	75	7.48	0.0994	13	1800	55	34
F02114+0456:SW	IC.214	0.0296	H	11.42	···	45	0.00	0.0000	13	2700	55	34
F02433+1544	···	0.0254	H	10.99	-24.43	17	>7.86	>0.4665	13	2700	140	4
F02437+2122	···	0.0234	L	11.10	-25.02	22	6.11	0.2814	8	1800	55	34
F02509+1248	NGC.1134	0.0122	···	10.85	-25.26	12	0.00	0.0000	8	2400	148	3ab
F02512+1446:S	UGC.2369	0.0315	H	11.63	···	74	6.50	0.0875	13	4500	0	34
Z03009−0213	···	0.1191	H	11.36	-25.10	40	0.00	0.0000	9	5400	0	2
F1_5	···	0.4786	H	11.85	···	122	12.87	0.1055	4	7200	0	6
F03359+1523	···	0.0357	H	11.48	-24.00	52	0.00	0.0000	13	2700	70	34a
F03514+1546	CGCG.465-012	0.0222	H	11.15	-24.82	24	5.71	0.2346	8	3600	55	34b
F04097+0525	UGC.2982	0.0179	H	11.13	-25.11	23	0.00	0.0000	8	4800	55	34
F04315−0840	NGC.1614	0.0159	H	11.60	-25.20	69	9.52	0.1387	8	900	30	34b
F04326+1904	UGC.3094	0.0247	···	11.44	-25.58	48	0.00	0.0000	8	3600	180	3
F05187−1017	···	0.0285	L	11.23	-24.30	29	0.00	0.0000	13	2700	100	34
F08354+2555	NGC.2623	0.0182	L	11.55	-23.92	61	0.00	0.0000	8	4800	180	34
F08498+3513	···	0.1895	L	11.75	-25.70	97	0.00	0.0000	9	7200	0	2
F09120+4107	NGC.2785	0.0085	H	10.70	-23.88	9	0.00	0.0000	8	3600	120	34
F09320+6134	UGC.5101	0.0395	L	11.96	-25.92	157	0.00	0.0000	15	10800	90	34
F10015−0614	NGC.3110	0.0166	H	11.31	-25.24	35	>5.28	>0.1501	8	2400	170	34
F13532+2517	CGCG.132-048	0.0293	L	10.99	-24.26	17	34.03	2.0194	11	2400	20	-
F13565+3519	MCG+06-31-036	0.0347	H	11.33	-25.25	37	0.00	0.0000	11	2400	130	-

Table 3.2 (cont'd)

Name (1)	Other (2)	z (3)	Type (4)	L_{IR} (5)	$K^{(\prime)}$ (6)	SFR (7)	dM/dt (8)	η (9)	Run (10)	t_{exp} (11)	PA (12)	Refs (13)
F15364+3320	CGCG.194-012	0.0222	H	10.21	-23.42	3	1.06	0.3803	11	2400	90	4
F15386+3807	···	0.1828	H	11.62	-25.61	72	35.37	0.4921	12	7200	270	2
F15549+4201	UGC.10099	0.0348	H	11.10	-24.79	22	0.00	0.0000	11	3600	130	4
F16130+2725	···	0.0459	H	10.68	···	8	0.00	0.0000	13	4800	60	4
F16504+0228	NGC.6240	0.0243	L	11.86	-25.02	125	>9.73	>0.0779	15	7200	90	34
F21484−1314	···	0.0768	H	11.50	-25.48	55	0.00	0.0000	13	3600	100	1
F21549−1206	···	0.0511	L	11.19	-24.90	27	0.00	0.0000	13	4800	125	4
F22213−0238	···	0.0566	H	11.33	-24.86	37	0.00	0.0000	13	3600	110	4
F22220−0825	···	0.0604	H	11.40	-24.73	44	18.66	0.4263	13	4800	35	4
F22338−1015	···	0.0623	H	11.36	-24.99	40	0.00	0.0000	13	4800	25	4
low-z ULIRGs												
F00188−0856	···	0.1283	L	12.38	-25.30	333	13.55	0.0407	3	5400	0	1
F01298−0744	···	0.1361	H	12.35	-23.94	308	16.48	0.0536	10	1800	15	1
F02411−0353:SW	···	0.1434	H	12.25	-25.35	243	0.00	0.0000	3	5400	25	1
F02411−0353:NE	···	0.1441	H	···	···	···	···	···	···	···	···	1
F03250+1606	···	0.1290	L	12.13	-25.50	185	67.92	0.3679	2	1800	0	1
F08231+3052	···	0.2478	L	12.32	-25.96	288	0.00	0.0000	9	5400	0	2
F08474+1813	···	0.1454	L	12.22	-23.72	230	0.00	0.0000	10	900	130	1
F08591+5248	···	0.1574	···	12.24	-25.57	241	7.43	0.0308	3	3600	80	1
F09039+0503	···	0.1252	L	12.10	-24.75	173	21.96	0.1271	2	1800	0	1
F09116+0334	···	0.1454	L	12.18	-25.80	211	5.77	0.0273	1	1200	0	1
F09539+0857	···	0.1290	L	12.13	-23.94	187	16.77	0.0896	2	1800	0	1
F10091+4704	···	0.2451	L	12.64	-25.38	597	4.27	0.0072	9	5400	0	1
F10190+1322:W	···	0.0766	H	11.99	-25.45	136	0.00	0.0000	2	900	0	1
F10190+1322:E	···	0.0759	L	···	···	···	···	···	···	···	···	1
F10378+1108	···	0.1363	L	12.32	-24.94	291	>49.56	>0.1703	2	1800	0	1
F10494+4424	···	0.0919	L	12.17	-24.67	203	>7.15	>0.0352	8	5400	10	1

Table 3.2 (cont'd)

Name (1)	Other (2)	z (3)	Type (4)	$L_{\rm IR}$ (5)	$K^{(\prime)}$ (6)	SFR (7)	dM/dt (8)	η (9)	Run (10)	t_{exp} (11)	PA (12)	Refs (13)
F10565+2448	⋯	0.0430	H	12.04	-25.58	151	44.11	0.2917	8	2700	53	34b
F11028+3130	⋯	0.1986	L	12.43	-24.13	368	0.00	0.0000	9	6300	0	1
F11387+4116	⋯	0.1489	H	12.20	-25.05	219	23.13	0.1054	2	1800	0	1
F11506+1331	⋯	0.1274	H	12.33	-24.95	297	4.07	0.0137	12	7200	43	1
F11582+3020	⋯	0.2234	L	12.60	-24.88	544	3.22	0.0059	9	7200	0	1
F14060+2919	⋯	0.1169	H	12.10	-25.21	173	>10.53	>0.0608	11	5400	48	1
F14197+0813	⋯	0.1305	L	12.16	-24.96	197	2.47	0.0125	12	7200	124	1
F15206+3342	⋯	0.1254	H	12.20	-25.17	218	8.41	0.0387	11	5400	80	1
F16333+4630:W	⋯	0.1908	L	12.43	-25.42	367	0.00	0.0000	12	3600	74	1
F16333+4630:E	⋯	0.1908	H	⋯	⋯	⋯	⋯	⋯	⋯	⋯	⋯	1
F16474+3430:S	⋯	0.1121	H	12.19	-26.18	213	4.04	0.0190	11	7200	164	1
F16474+3430:N	⋯	0.1126	H	⋯	⋯	⋯	⋯	⋯	⋯	⋯	⋯	1
F16487+5447:W	⋯	0.1038	L	12.15	-24.69	194	>1.52	>0.0078	11,13	9000	68	1
F16487+5447:E	⋯	0.1038	L	⋯	⋯	⋯	⋯	⋯	⋯	⋯	⋯	1
F17068+4027	⋯	0.1794	H	12.38	-24.80	334	0.00	0.0000	12	3600	0	1
F17207−0014	⋯	0.0428	L	12.35	-25.60	306	>36.66	>0.1197	11	2400	96	3
I20046−0623:W	⋯	0.0840	H	12.09	⋯	169	>3.16	>0.0187	12	1800	70	-
I20046−0623:E	⋯	0.0847	H	⋯	⋯	⋯	⋯	⋯	⋯	⋯	⋯	-
F20414−1651	⋯	0.0872	H	12.32	-24.22	290	4.47	0.0154	11,13	6000	170	1
F23234+0946:W	⋯	0.1279	L	12.11	-25.25	178	13.03	0.0730	10	2100	113	1
F23234+0946:E	⋯	0.1277	L	⋯	⋯	⋯	⋯	⋯	⋯	⋯	⋯	1
high-z ULIRGs												
F01462+0014	⋯	0.2797	L	12.34	-25.86	302	0.00	0.0000	10	3600	53	2
Z02376−0054	⋯	0.4104	L	12.64	-26.13	595	0.00	0.0000	4	5400	0	2
Z03151−0140	⋯	0.2653	L	12.15	-26.12	195	4.93	0.0253	10	1800	0	2
F04313−1649	⋯	0.2672	L	12.66	-24.54	626	0.00	0.0000	2	2400	0	1
F07353+2903	⋯	0.3348	L	12.36	-25.91	316	6.15	0.0195	4,6	7200	0	2

Table 3.2 (cont'd)

Name (1)	Other (2)	z (3)	Type (4)	$L_{\rm IR}$ (5)	$K^{(\prime)}$ (6)	SFR (7)	dM/dt (8)	η (9)	Run (10)	t_{exp} (11)	PA (12)	Refs (13)
F07449+3350:W	···	0.3571	L	12.75	-26.27	776	0.00	0.0000	2,4,10	8400	127,0	2
F07449+3350:E	···	0.3571	L	···	···	···	···	···	2,10	6000	127	2
F08136+3110	···	0.4070	H	12.46	-26.30	398	2.11	0.0053	4,6,10	9240	0	2
F08143+3134	···	0.3606	···	12.38	-25.99	329	9.57	0.0291	10	3600	140	2
F08208+3211	···	0.3955	H	12.49	-25.83	426	0.00	0.0000	4,10	7200	0	2
F09567+4119	···	0.3605	L	12.45	-26.49	389	3.60	0.0093	10	1800	118	2
F10156+3705	···	0.4895	H	12.82	-26.08	908	0.00	0.0000	4	3600	0	2
F10485+3726	···	0.3559	L	12.34	-25.26	303	0.00	0.0000	4,10	6600	0	2
F16576+3553	···	0.3710	L	12.38	-24.97	331	7.05	0.0213	5,6	7200	0	2

References. — (1) Kim & Sanders 1998; Veilleux et al. 1999b; (2) Stanford et al. 2000; (3) Sanders et al. 2003; (4) Kim et al. 1995; Veilleux et al. 1995; (5) Kewley et al. 2001; (6) Clements, Desert, & Franceschini 2001; (a) Lehnert & Heckman 1995, 1996; (b) Heckman et al. 2000.

Note. — Col.(1): IRAS Faint Source Catalog label, plus nuclear ID. Only 1 object is not found in the FSC. Col.(2): Another name. Col.(3): Heliocentric redshift, in vacuum. Col.(4): Optical spectral type. Col.(5): Infrared luminosity, in logarithmic units of $L_\odot$ (§3.2). Col.(6): K- or K′-band absolute magnitude (Stanford et al. 2000; Kim et al. 2002; Jarrett et al. 2003; NICMOS refs; 2MASS). 2MASS magnitudes are 'total.' Col.(7): Star formation rate, computed from the infrared luminosity and a correction for AGN contribution to $L_{\rm IR}$ (§3.3.4). Col.(8): Total mass outflow rate, in $M_\odot$ yr^{-1}. Col.(9): Mass entrainment efficiency; $\eta = dM/dt/$SFR. Col.(10): Observing run (from Chapter 2). Col.(11): Total exposure time in seconds. Col.(12): Position angle. Col.(13): Reference.

Most of the objects in our sample are single-nucleus galaxies. However, given that ULIRGs are the late stages of equal-mass mergers (Veilleux et al. 2002), we would expect multiple nuclei in some of these galaxies. In fact, there are 10 objects in our sample which have well-resolved double nuclei, 8 of which are ULIRGs. In most cases we have taken spectra of both nuclei. However, there are other cases where there may be multiple nuclei with very small separation (not resolved in our spectra), such as the well-known case F16504+0228 (NGC 6240).

3.2.1 $z < 0.25$ ULIRGs

Most of these galaxies are taken from the IRAS 1 Jy survey (Kim & Sanders 1998). This dataset is a complete sample, down to a flux level of $f_\nu(60\ \mu\mathrm{m}) = 1$ Jy, of 118 ULIRGs with Galactic latitude $|b| > 30°$ and declination $\delta > -40°$. These objects have redshifts of $z = 0.02 - 0.27$ and are the brightest sources with luminosities in the range $\log(L_{\mathrm{IR}}/L_\odot) = 12.01 - 12.84$. We have slightly increased the published infrared luminosities to correspond to the standard cosmology.

We also include three nearby ULIRGs that are not part of the 1 Jy survey: F10565+2448, F17207−0014, and IRAS 20046−0623. The latter two are excluded due to their low Galactic latitude, while the first is excluded because its luminosity is slightly lower using older fluxes. A single object from the FIRST/FSC survey (Stanford et al. 2000) is also part of the low-z subsample.

We selected galaxies which have H II-region-like or LINER optical spectral classifications based on low-dispersion spectroscopy (Kim, Veilleux, & Sanders 1998; Veilleux et al. 1999b). These galaxies have infrared luminosities that are likely to be dominated by star formation rather than active galactic nuclei, as suggested by mid-infrared diagnostics of ULIRGs (Genzel et al. 1998) and the good correspondence of optical and mid-infrared spectral classifications (Lutz, Veilleux, & Genzel 1999).

Six of the galaxies in this subsample were observed in the mid-infrared with ISO and are classified as starbursts; one other has an AGN classification (F17068+4027) (Lutz et al. 1999). Ten galaxies (including F17068+4027) were observed in the near-infrared and show no evidence of broad-line regions. Note, however, that some LINERs may contain buried (but not energetically dominant) AGN; for instance, VLA observations show compact radio cores in a number of ULIRG LINERs (Nagar et al. 2003).

3.2.2 $0.25 < z < 0.5$ ULIRGs

These galaxies were selected from the FIRST/FSC survey (Stanford et al. 2000). The FIRST/FSC survey is a cross-correlation of 60 μm and 100 μm point sources from the IRAS Faint Source Catalog (FSC) with 1.4 GHz point sources in the VLA FIRST database. This technique yields distant infrared-luminous galaxies because of the tight radio/far-infrared flux relationship for galaxies (Condon, Anderson, & Helou 1991). The resulting sample consists of 108 sources with $\langle z \rangle = 0.31$. We selected targets from the FIRST/FSC catalog that have redshifts in the desired range and have high infrared luminosities.

Since in most cases the 12 and 25 μm fluxes of these galaxies are too faint to be measured by IRAS, L_{IR} cannot be calculated using the usual formula (though the contribution of the 12 and 25 μm fluxes to L_{IR} is small; Perault 1987). For many of these sources, infrared luminosities were calculated by including radio fluxes in the SED fitting and using the radio/infrared correlation (Blain, Barnard, & Chapman 2003; Andrew Blain, private communication). Where these luminosities are not available, we have used the 60 and 100 μm fluxes and scalings to the 12 and 25 μm fluxes (Kim & Sanders 1998) to compute the infrared luminosity. The difference between these two methods is generally small when both are available.

One object from the 1 Jy survey (Kim & Sanders 1998) also falls in this subsample.

3.2.3 IRGs

To study trends in outflow properties over a large range of SFR, we observed infrared-selected galaxies with infrared luminosities in the range $\log(L_{\mathrm{IR}}/L_{\odot}) = 10.2 - 12.0$ (median 11.36). (Hereafter we refer to these galaxies as IRGs, rather than LIRGs, since some have lower luminosities than LIRGs). The bulk of our galaxies were culled from the IRAS Revised Bright Galaxy Sample (RBGS; Sanders et al. 2003) and the Warm Galaxy Survey (WGS; Kim et al. 1995). We chose objects with measured optical spectral types (of HII-region-like or LINER). We also selected relatively distant objects to minimize aperture- and distance-related measurement biases (the median redshift is $z = 0.032$).

Two of the galaxies in this subsample, F09320+6134 (UGC 5101) and F16504+0228 (NGC 6240), were observed in the mid-infrared with ISO and are classified as starbursts (Lutz et al. 1999).

We also observed one object at $z = 0.479$ from a 12 μm ISO survey (Clements et al. 1999; Clements, Desert, & Franceschini 2001). The infrared luminosity for this object, F1_5, is extrapolated from the 12 μm luminosity assuming a starburst SED and is thus uncertain.

As we discuss below (§3.4.5), the morphologies of these galaxies, as determined from DSS2 and 2MASS images, are varied. For the most distant objects, the shallowness of these surveys prevents a detailed morphological analysis.

3.3 OUTFLOW PROPERTIES

3.3.1 Spectra

Figures 3.2 − 3.4 display the spectra and line fits for our three subsamples. The data are binned in ~ 35 km s^{-1} bins for the echelle data and slightly larger bins ($50-60$ km s^{-1}) for the KPNO data, in each case using variance weighting. The horizontal axis shows the velocity relative to systemic of the D$_2$ λ5890 line.

Figures 3.5 − 3.7 show the same spectra again, this time alongside the emission-line profiles of the forbidden lines [N II]$\lambda\lambda6548, 6583$ and [O III]λ5007. Since the former straddle Hα to either side and are often blended with it, we plot the red half of λ6583 and the blue half of λ6548 (scaled appropriately to match the λ6583 line; the fluxes of these lines are set by atomic physics in the ratio ∼3:1 for λ6583 and λ6548, respectively, but we simply match the lines at the intersection). These figures also show the spatial variation of Hα line emission along the spectrograph slit. We discuss these figures in more detail below.

Tables 3.1 − 3.3 list the average outflow properties for our three subsamples, the measured outflow properties of each individual galaxy, and the fitted parameters of each velocity component, respectively.

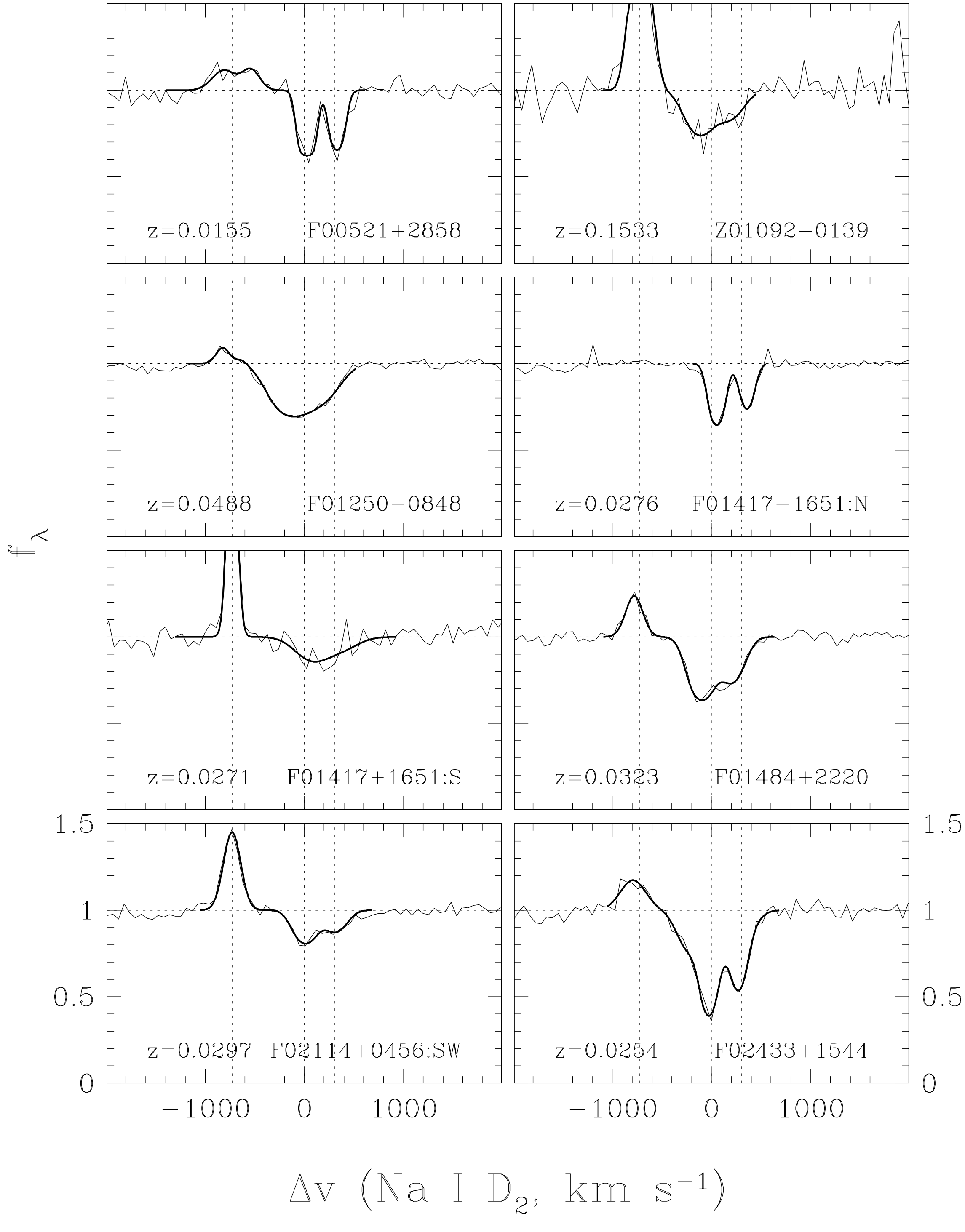

Figure 3.2: Spectra of the Na I D line in our IRG (low L_{IR}) subsample. The thin lines are the original spectra (slightly smoothed) and the thick lines are the fits to the data. The vertical dotted lines locate the Na I D$\lambda\lambda5890, 5896$ doublet and He I $\lambda5876$ emission line in the rest frame of the galaxy. The diagonal hashed lines locate atmospheric absorption from O_2, when present.

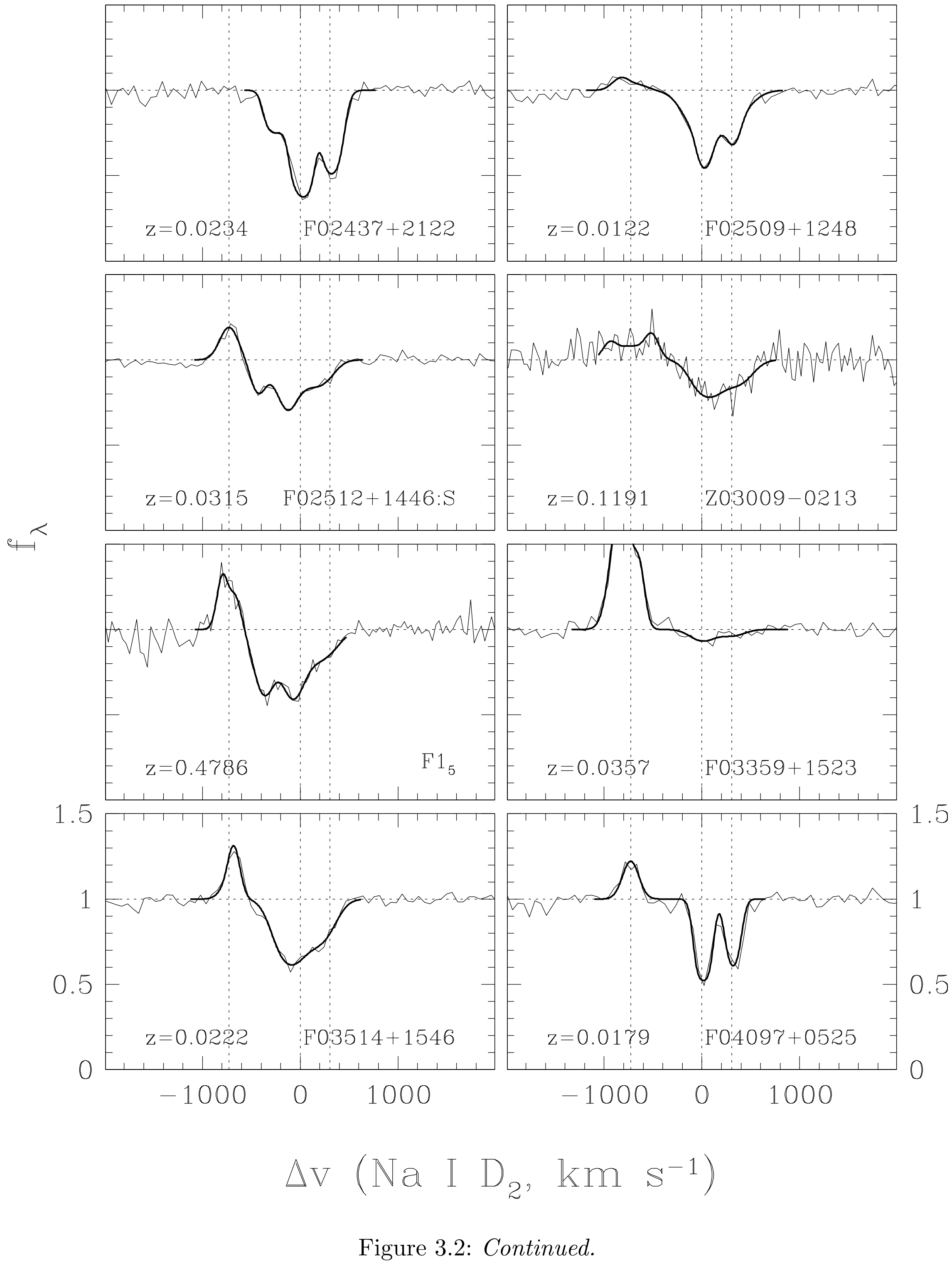

Figure 3.2: *Continued.*

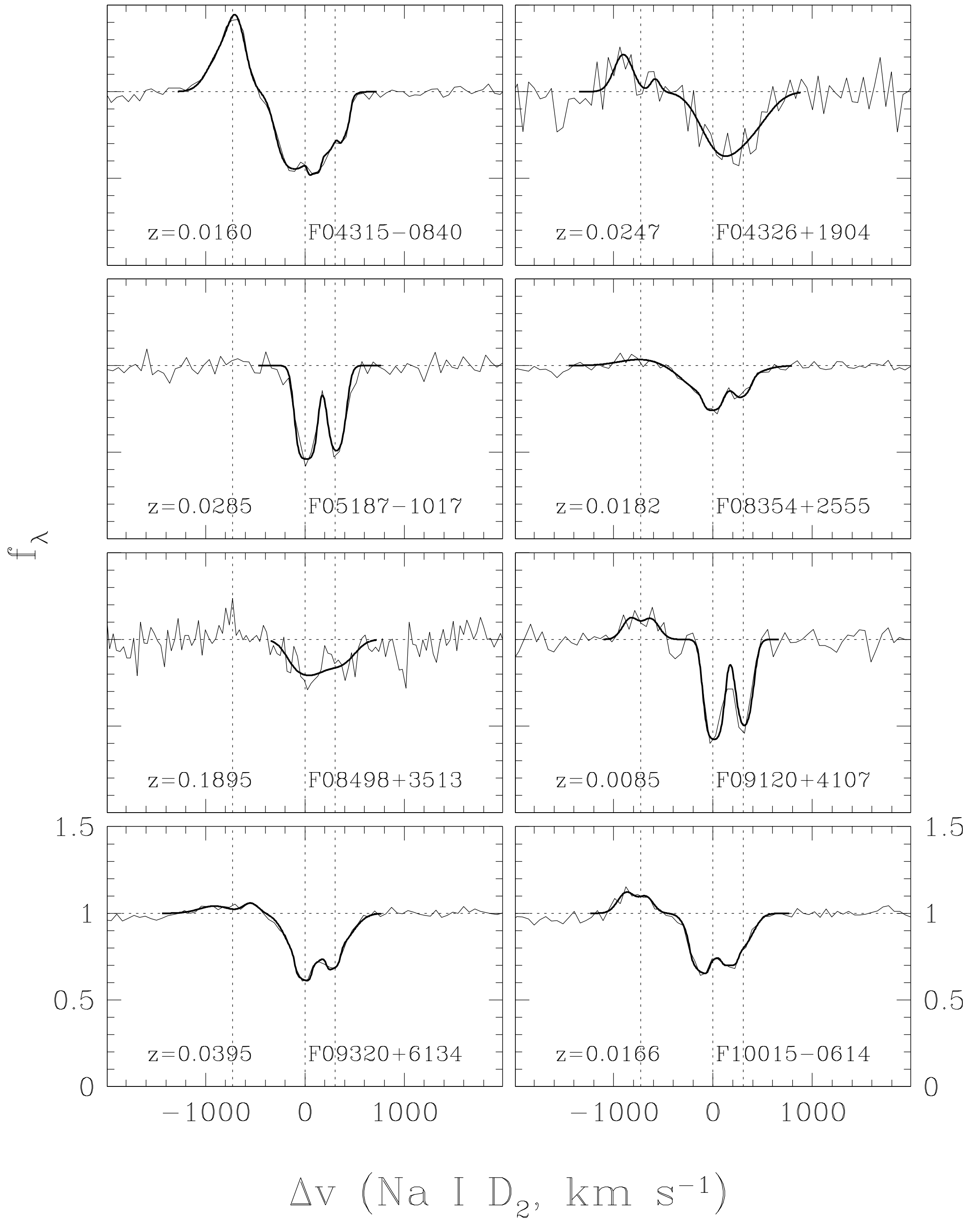

Figure 3.2: *Continued.*

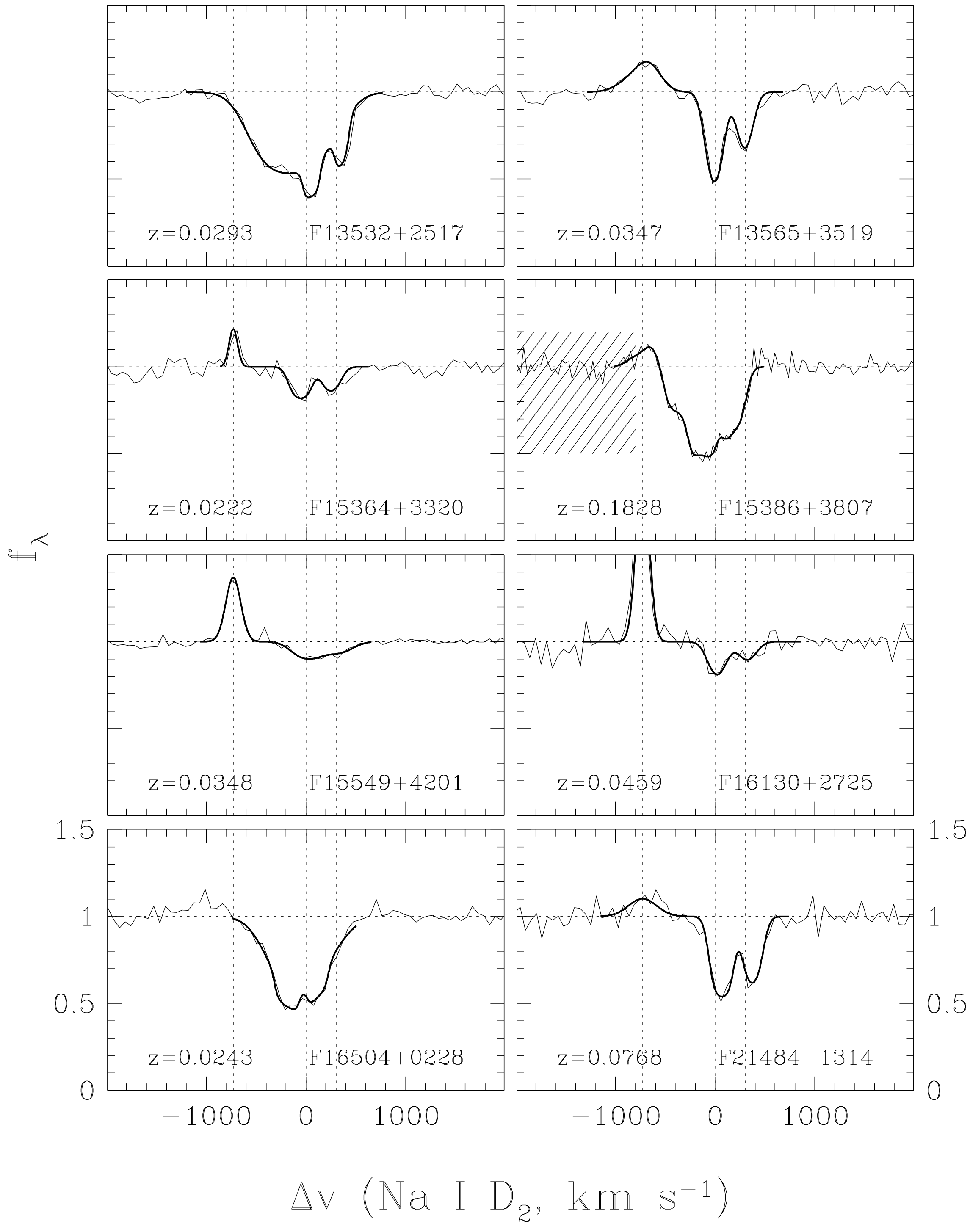

Figure 3.2: *Continued.*

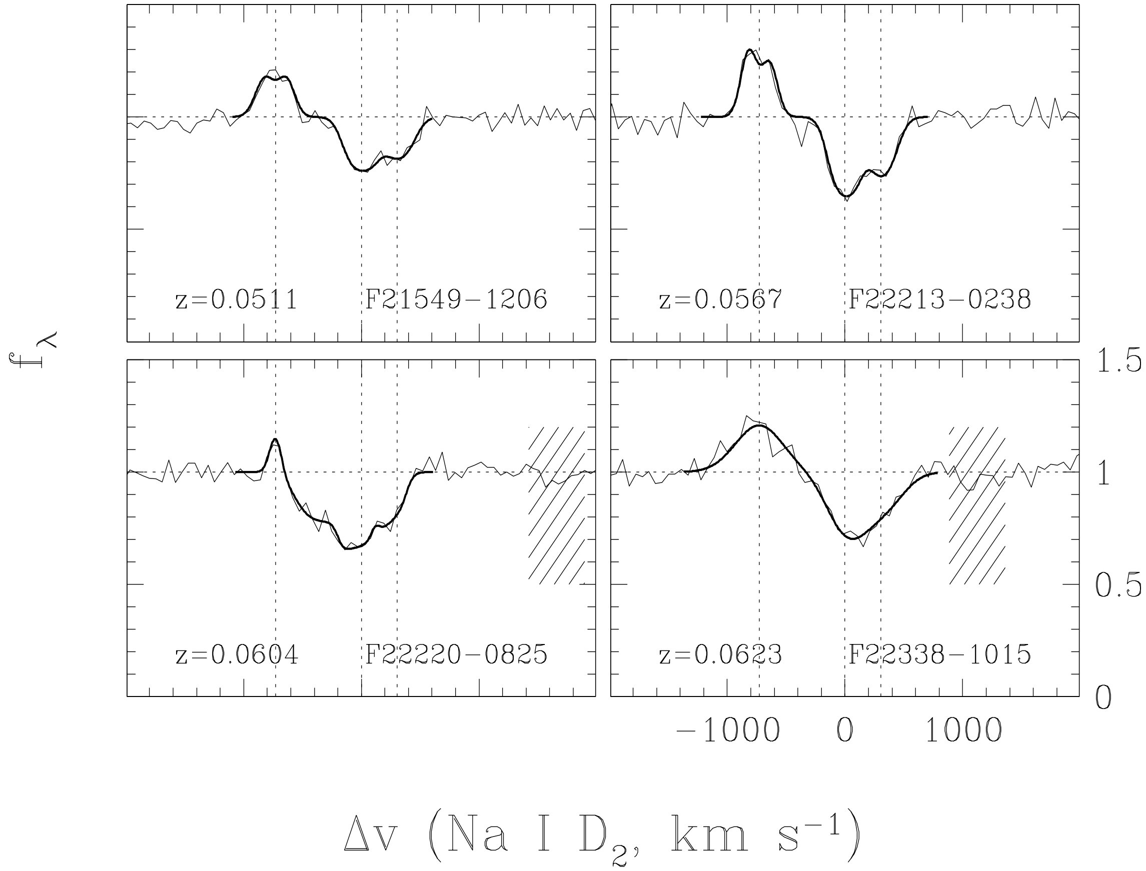

Figure 3.2: *Continued.*

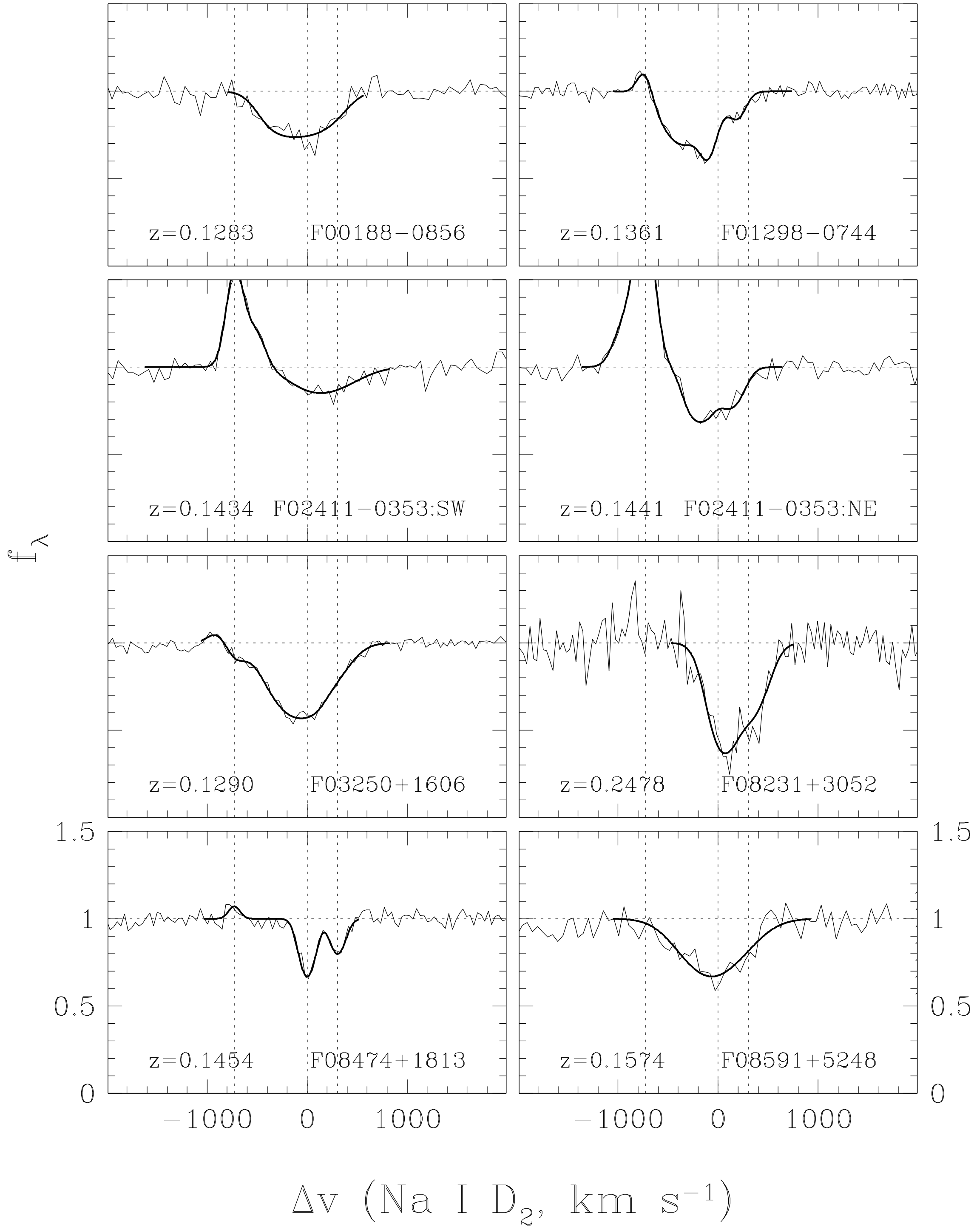

Figure 3.3: Spectra of the Na I D line in our $z < 0.25$ ULIRG subsample. See Figure 3.2 for more details.

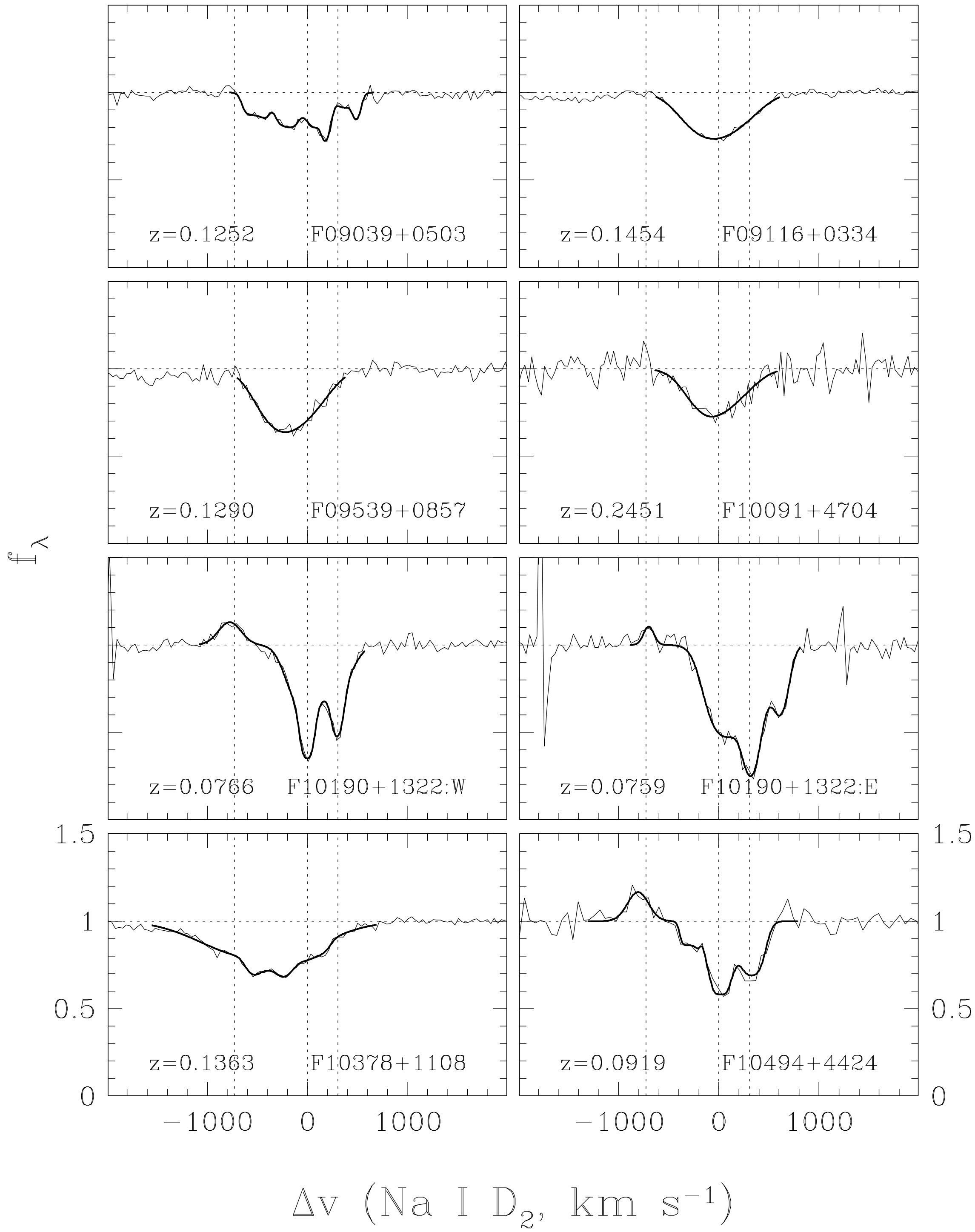

Figure 3.3: *Continued.*

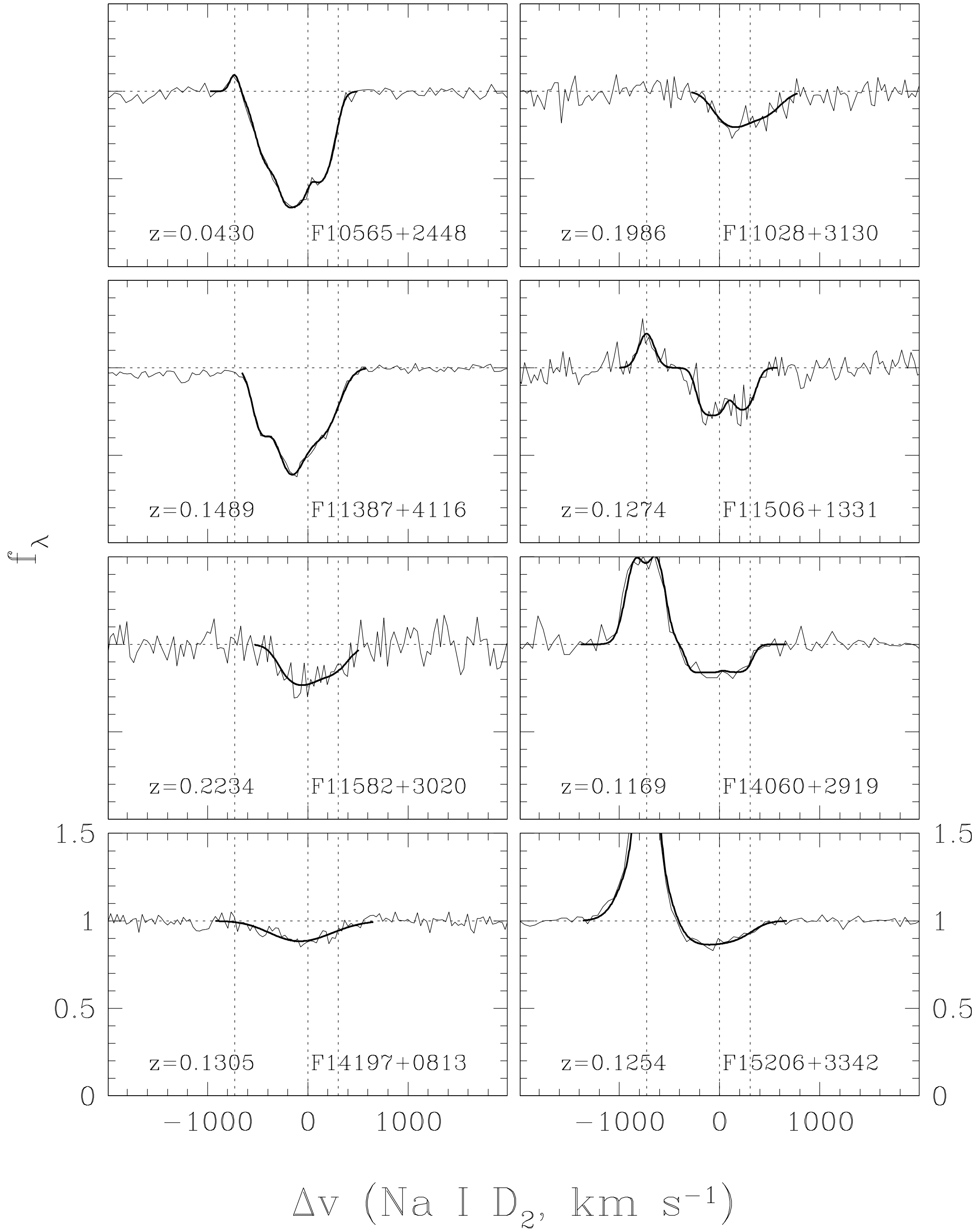

Figure 3.3: *Continued.*

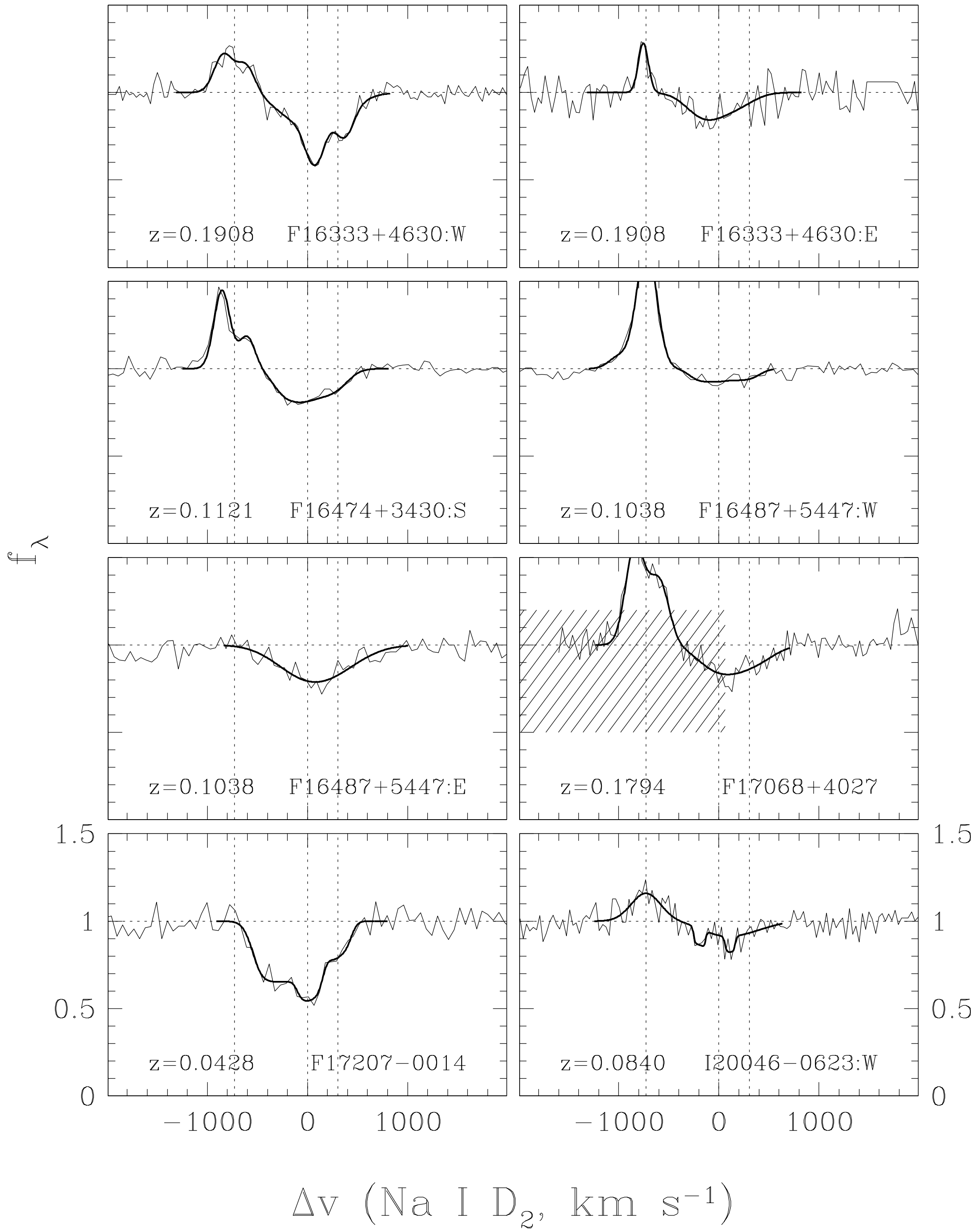

Figure 3.3: *Continued.*

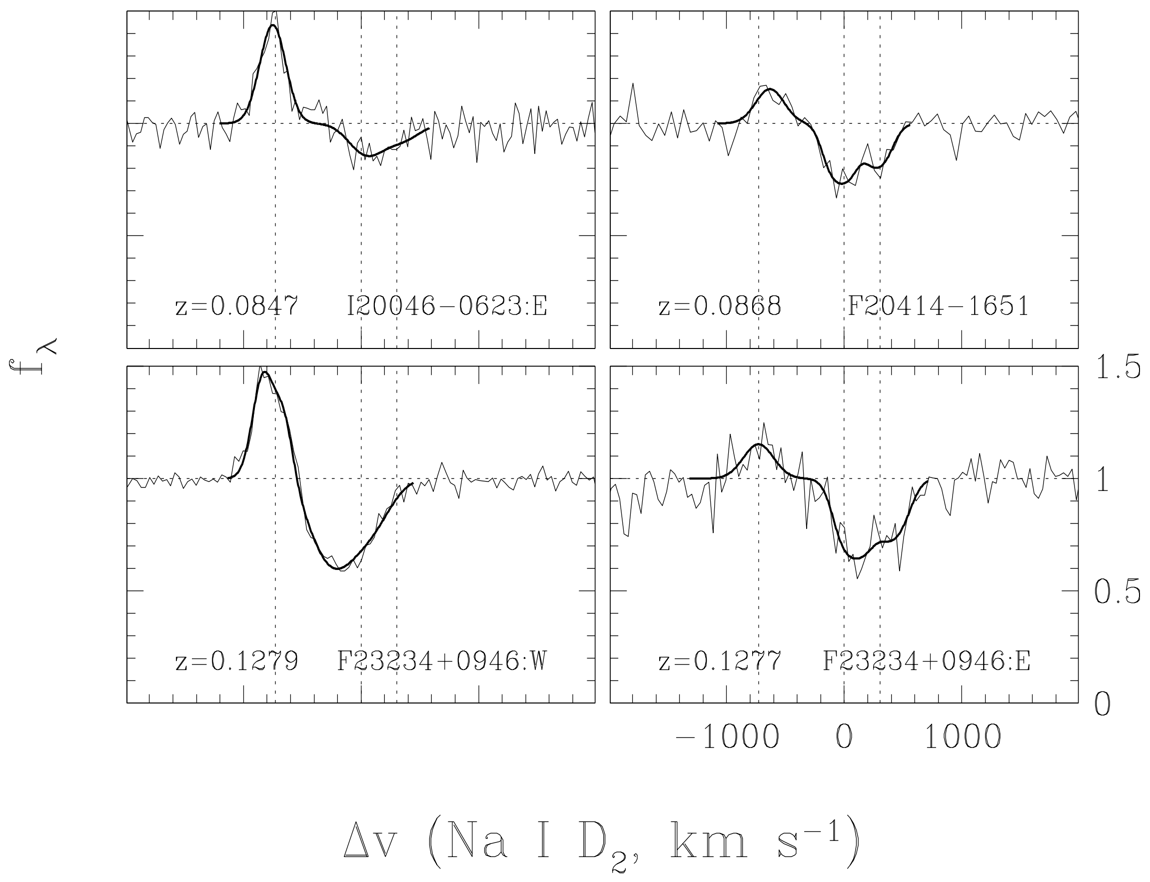

Figure 3.3: *Continued.*

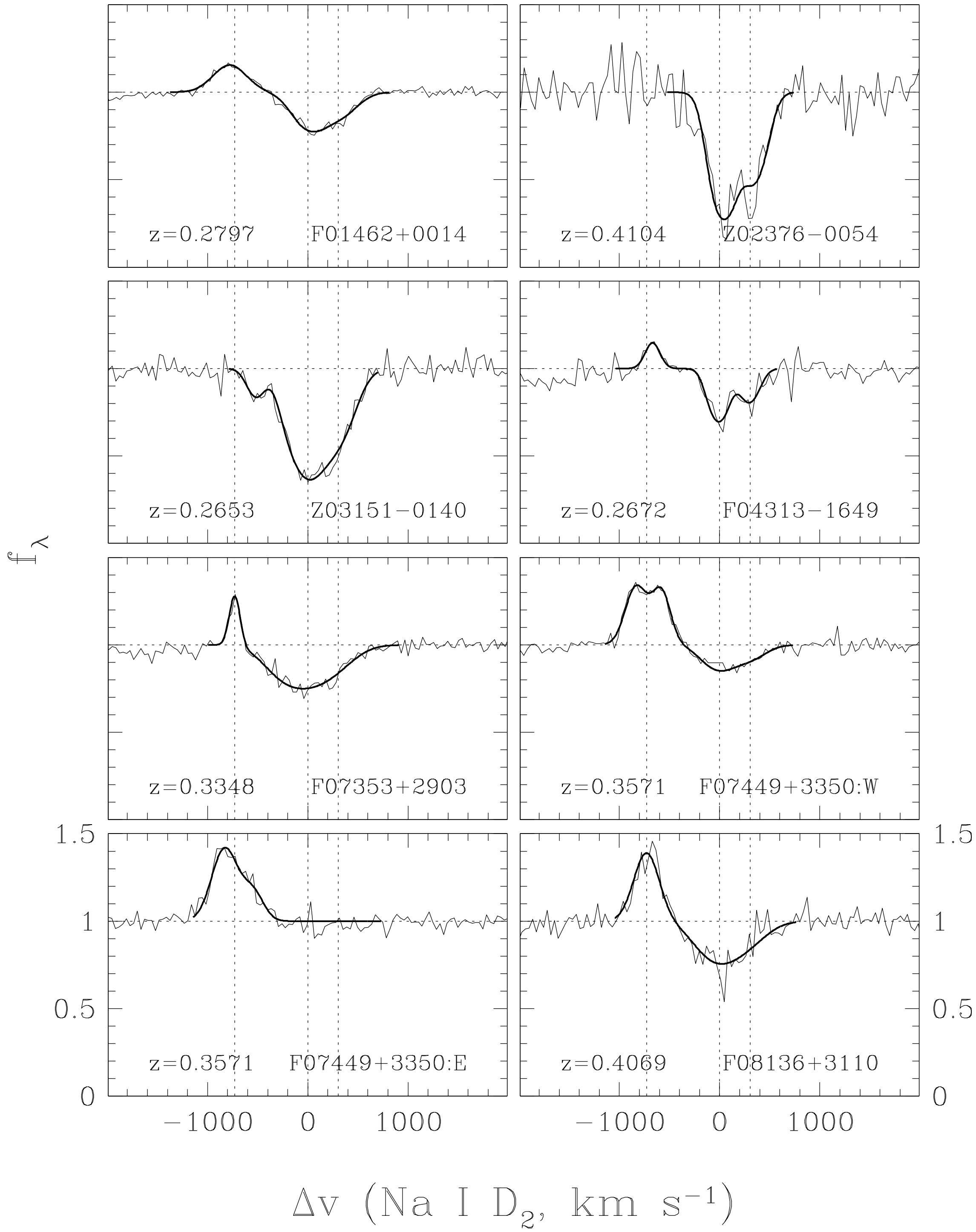

Figure 3.4: Spectra of the Na I D line in our $z > 0.25$ ULIRG subsample. See Figure 3.2 for more details.

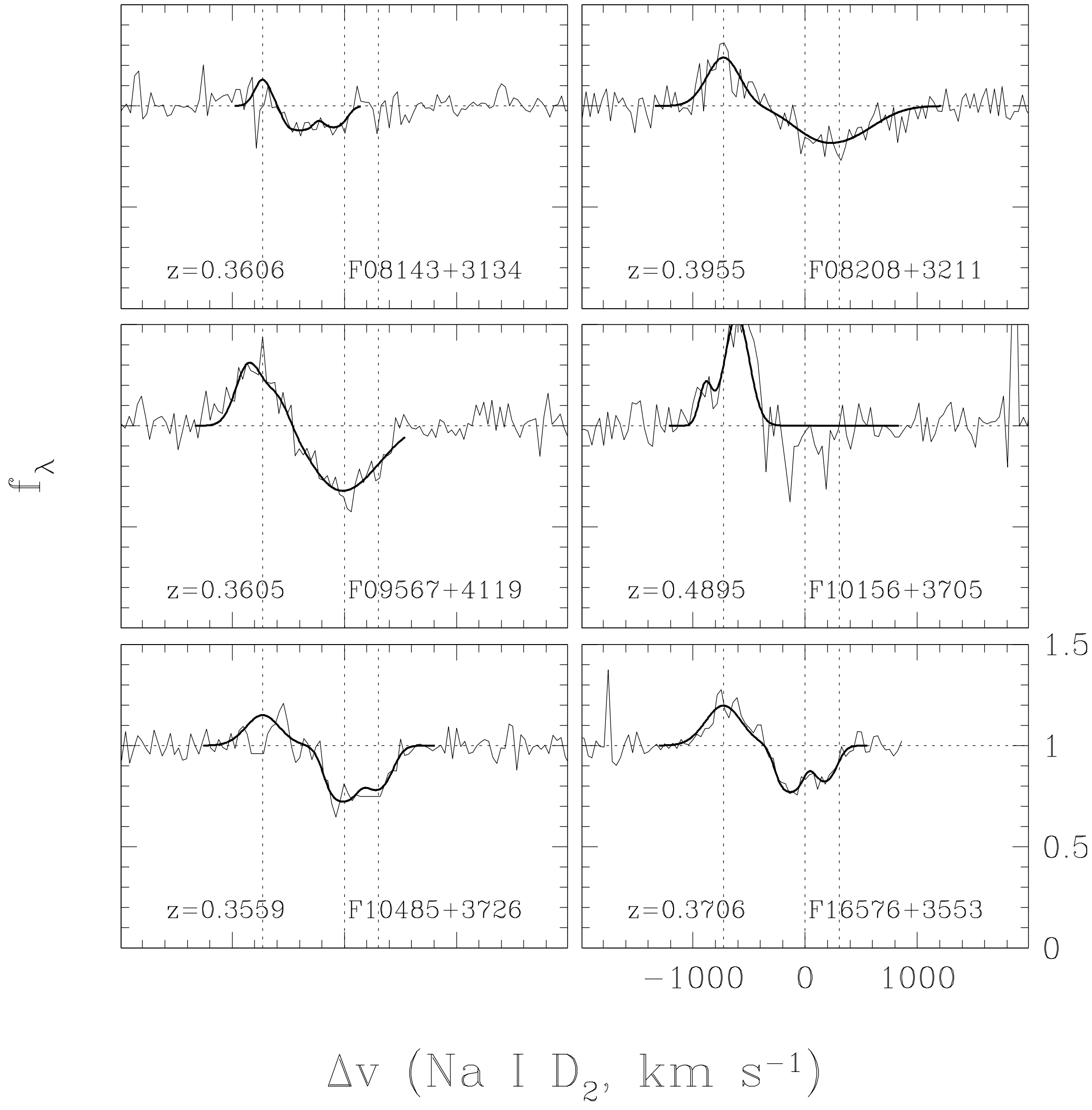

Figure 3.4: *Continued.*

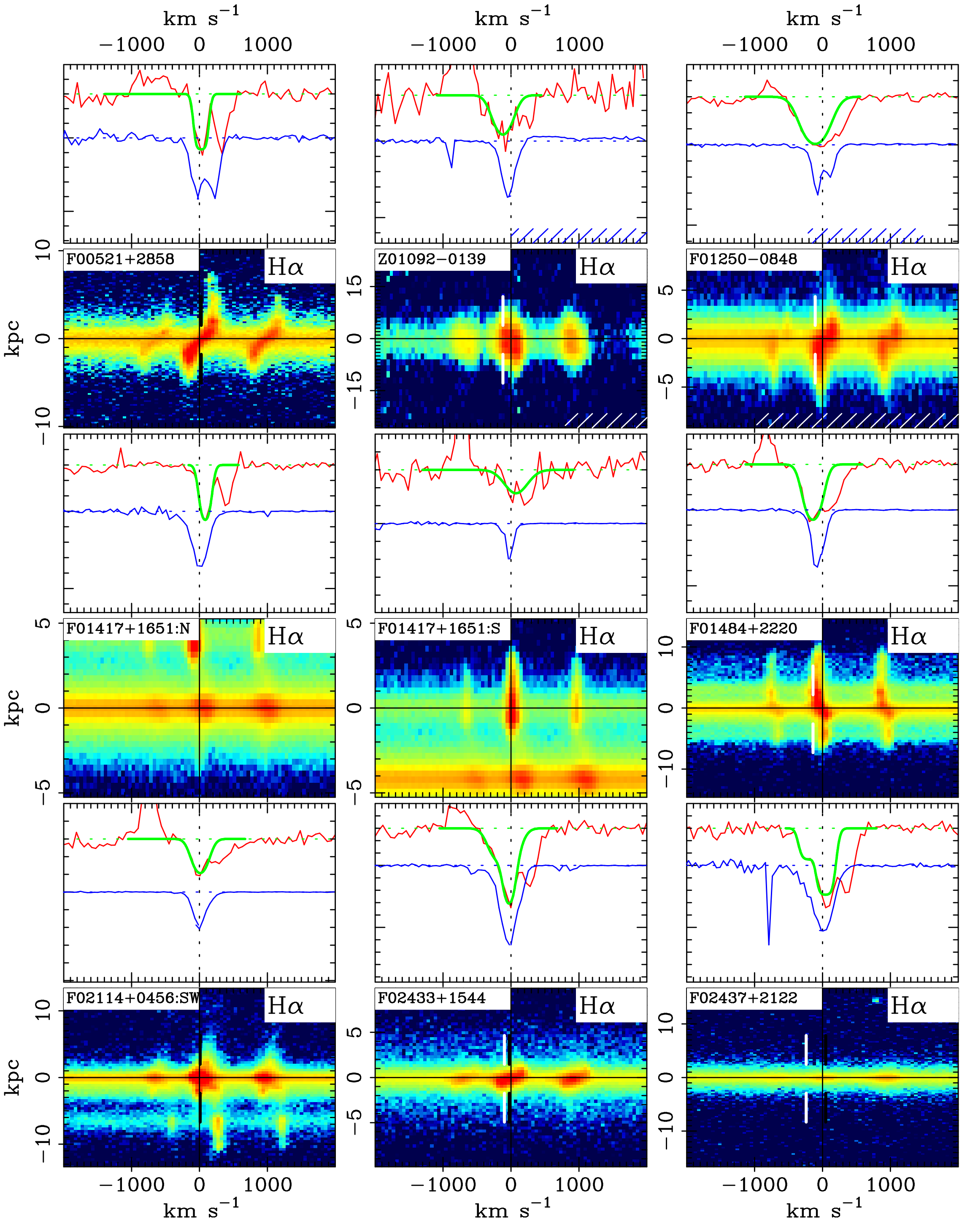

Figure 3.5: Smoothed spectra of Na I D, [N II]$\lambda\lambda 6548, 6583$, and [O III]$\lambda 5007$ from our IRG (low $L_{\rm IR}$) subsample. Below these we plot the spatial distribution of Hα for each galaxy. In the 1-dimensional spectra, red is the observed Na I D profile, green is a singlet realization of this profile at the expected location of Na I D$_2$, blue is the observed [N II] profile, and orange is the [O III] profile. (*Continued*)

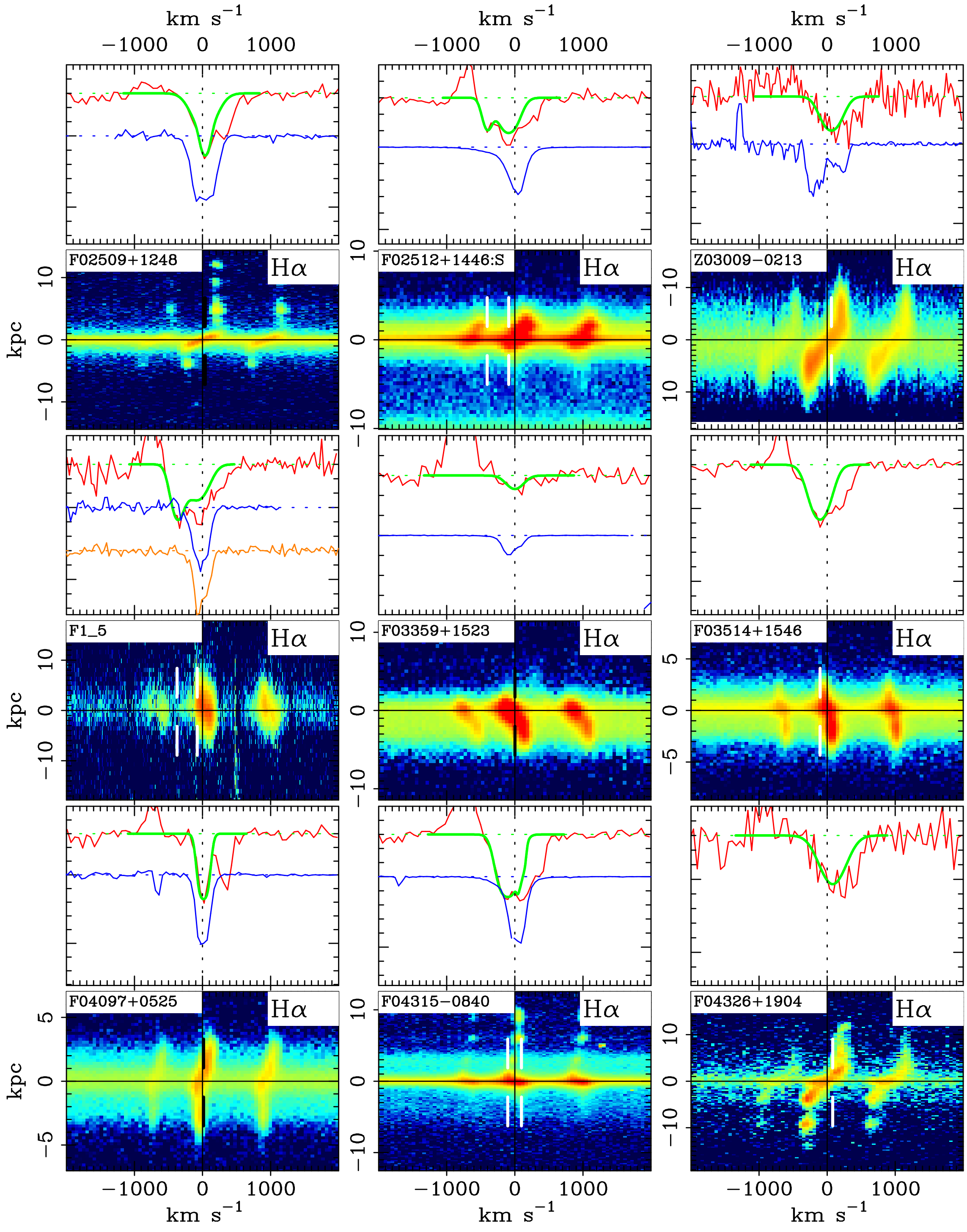

Figure 3.5: The hashed lines locate atmospheric absorption from O_2 and are color coded to match the appropriate line. In the 2-dimensional spectra, the vertical dashed lines locate the fitted velocity components in Na I D. Black represents components within 50 km s^{-1} of systemic, and white represents components blue- or red-shifted at least 50 km s^{-1} from systemic. The sense of direction is such that for a slit with PA = 0°, north is down and south is up.

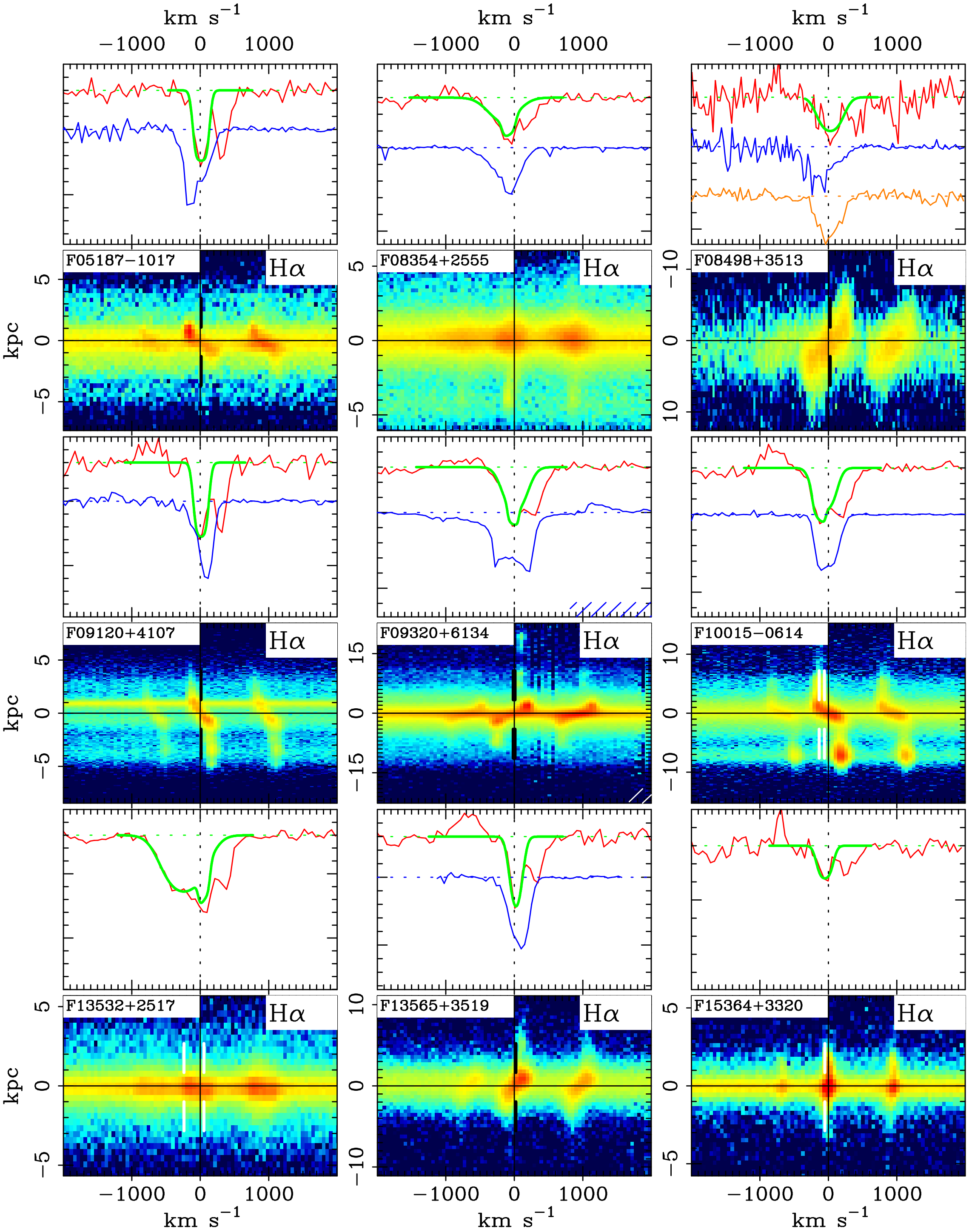

Figure 3.5: *Continued.*

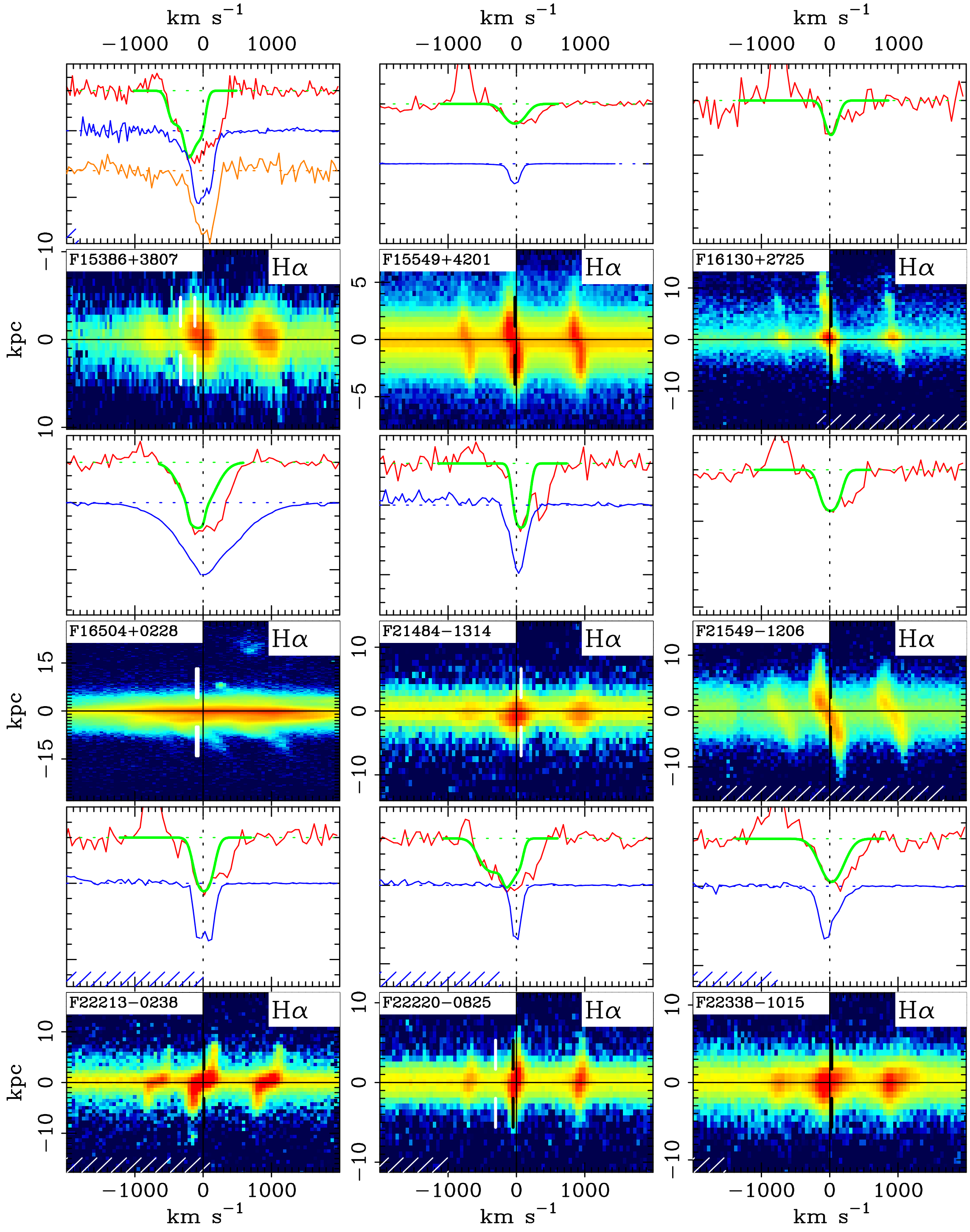

Figure 3.5: *Continued.*

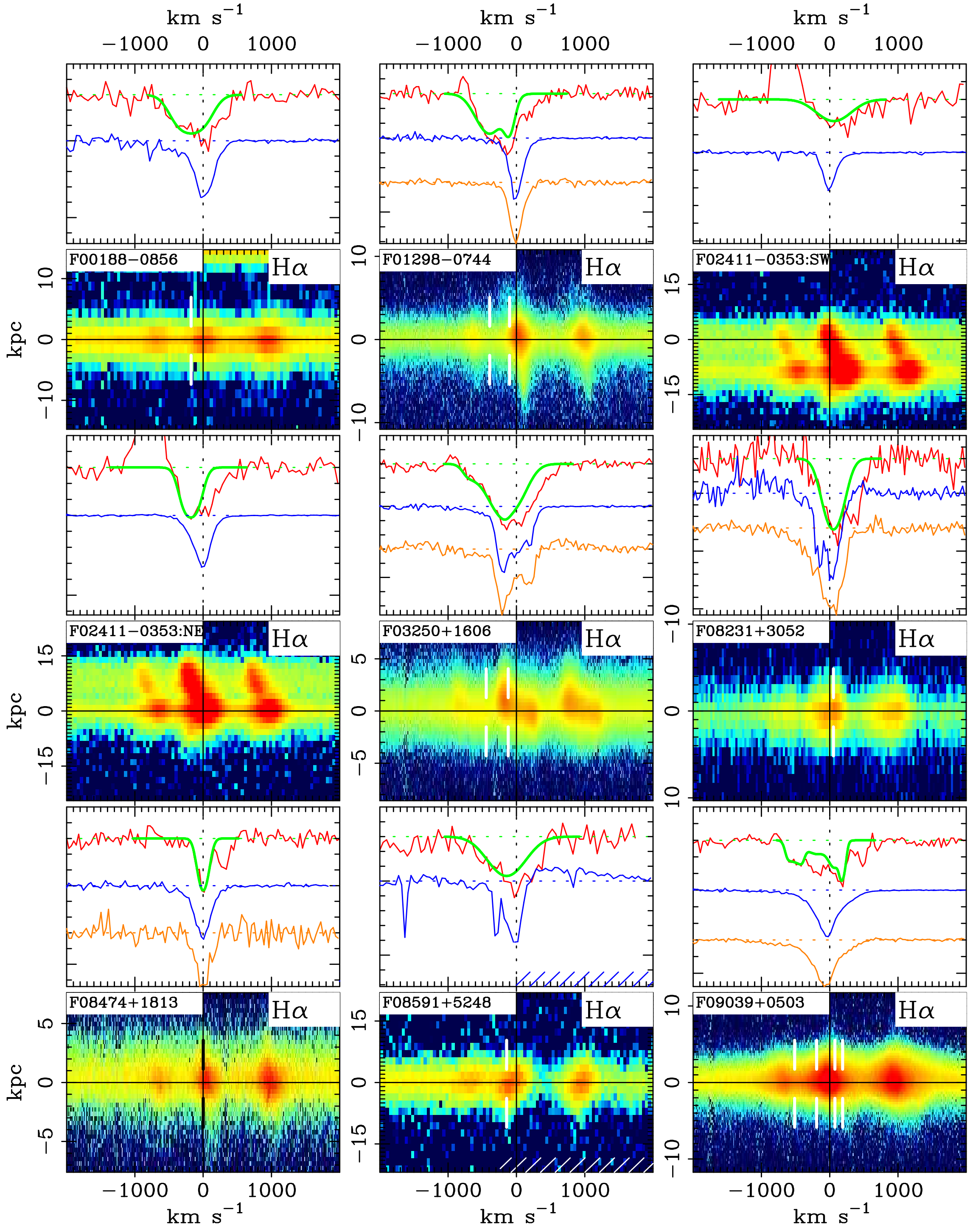

Figure 3.6: The same as figure 3.5, but for our low-z ULIRGs subsample.

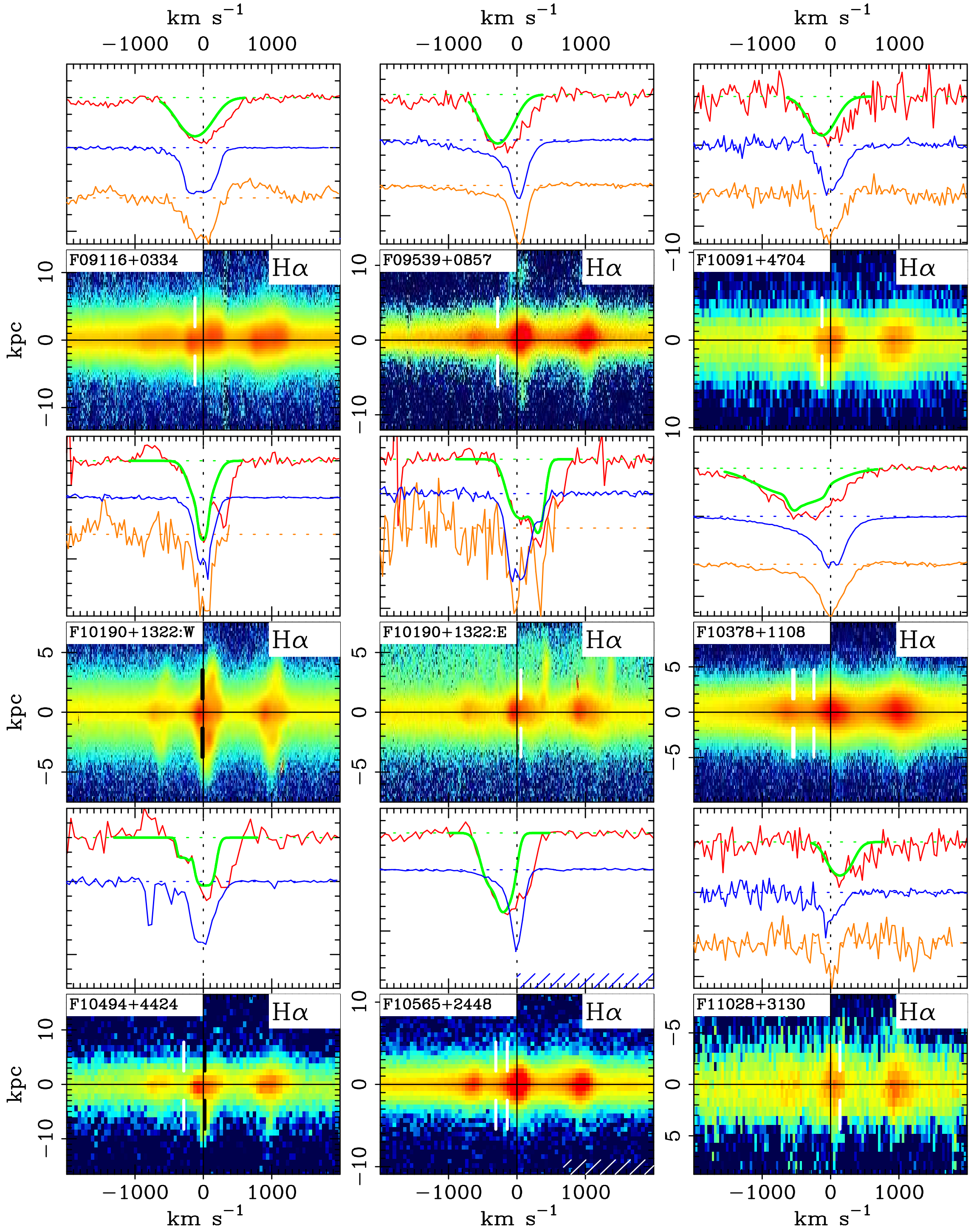

Figure 3.6: *Continued.*

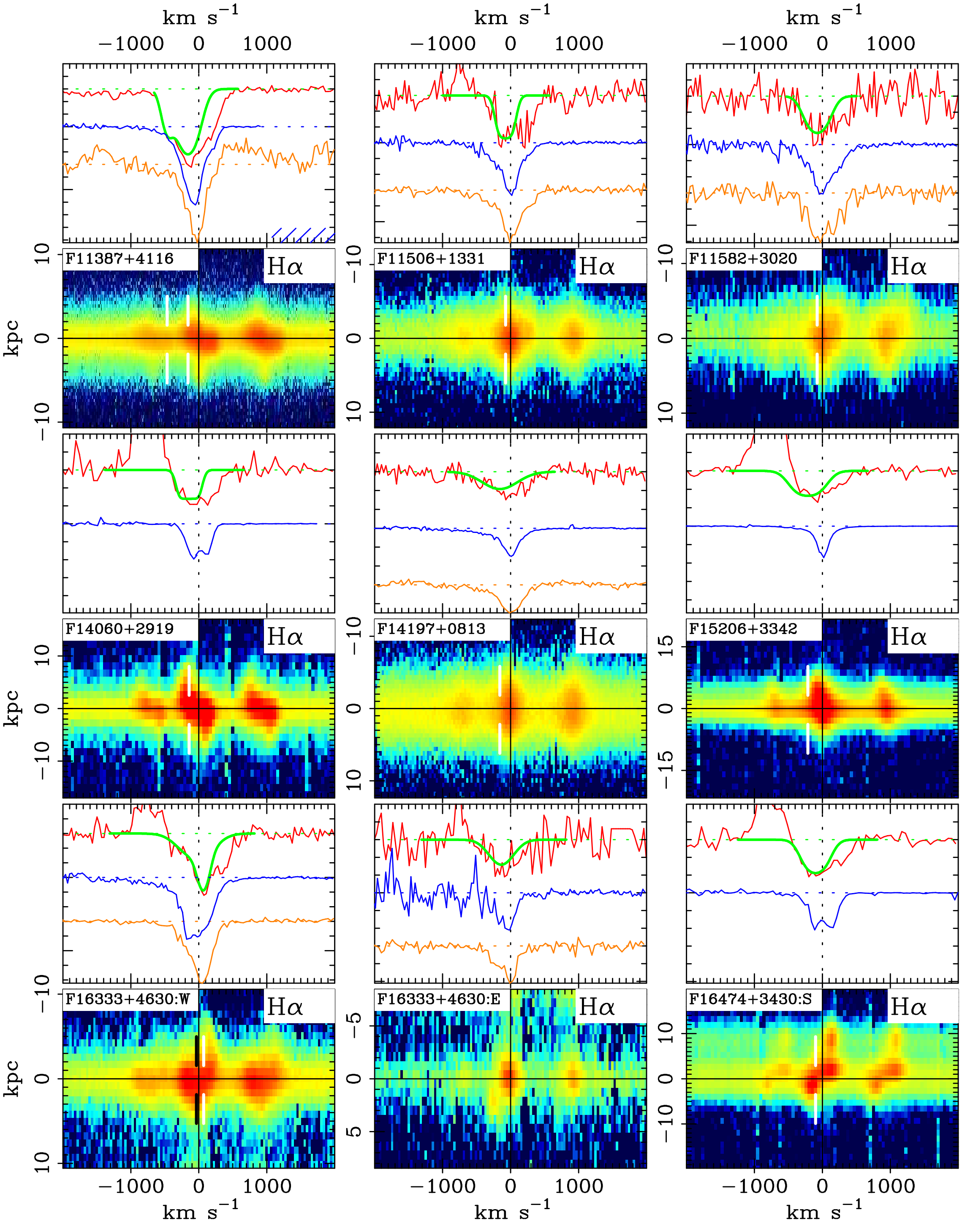

Figure 3.6: *Continued.*

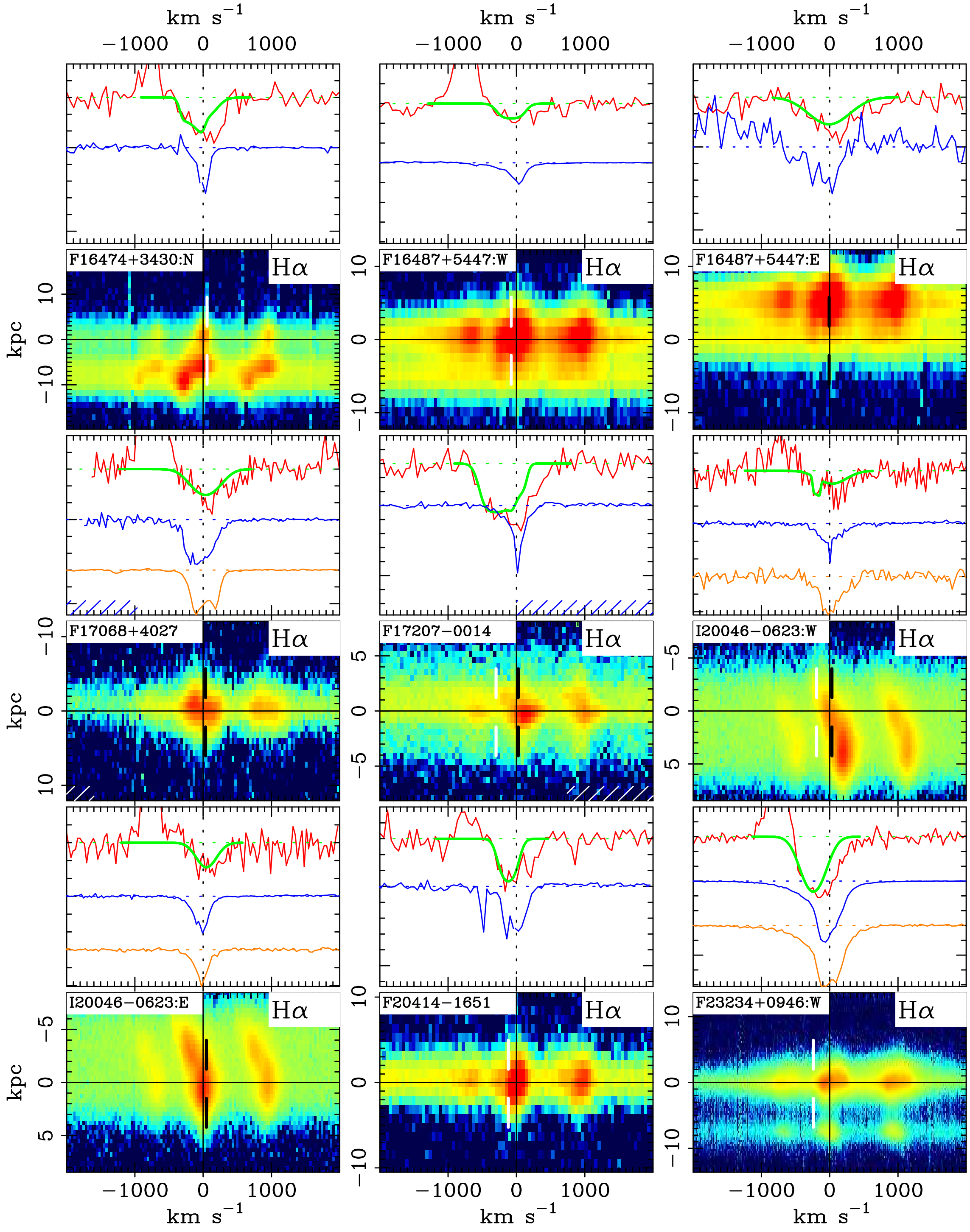

Figure 3.6: *Continued.*

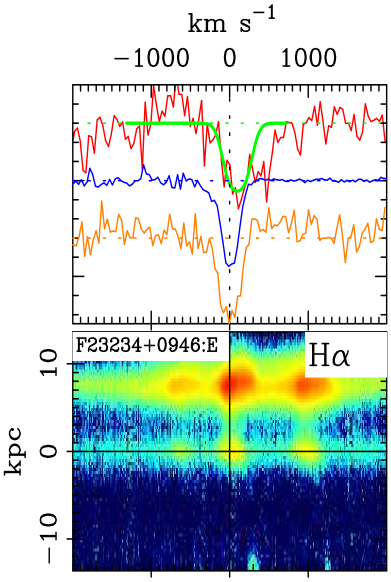

Figure 3.6: *Continued.*

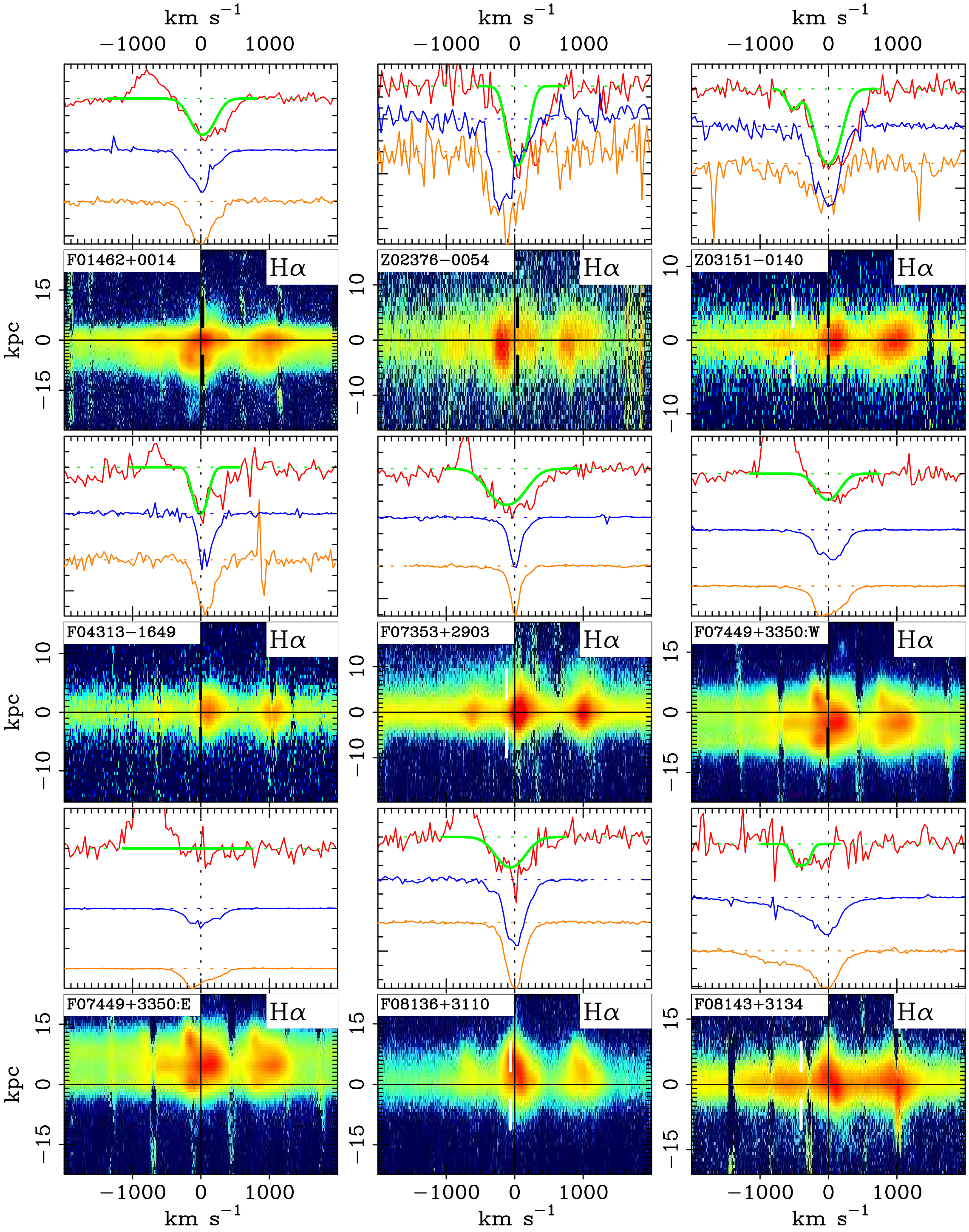

Figure 3.7: The same as figure 3.5, but for our high-z ULIRGs subsample.

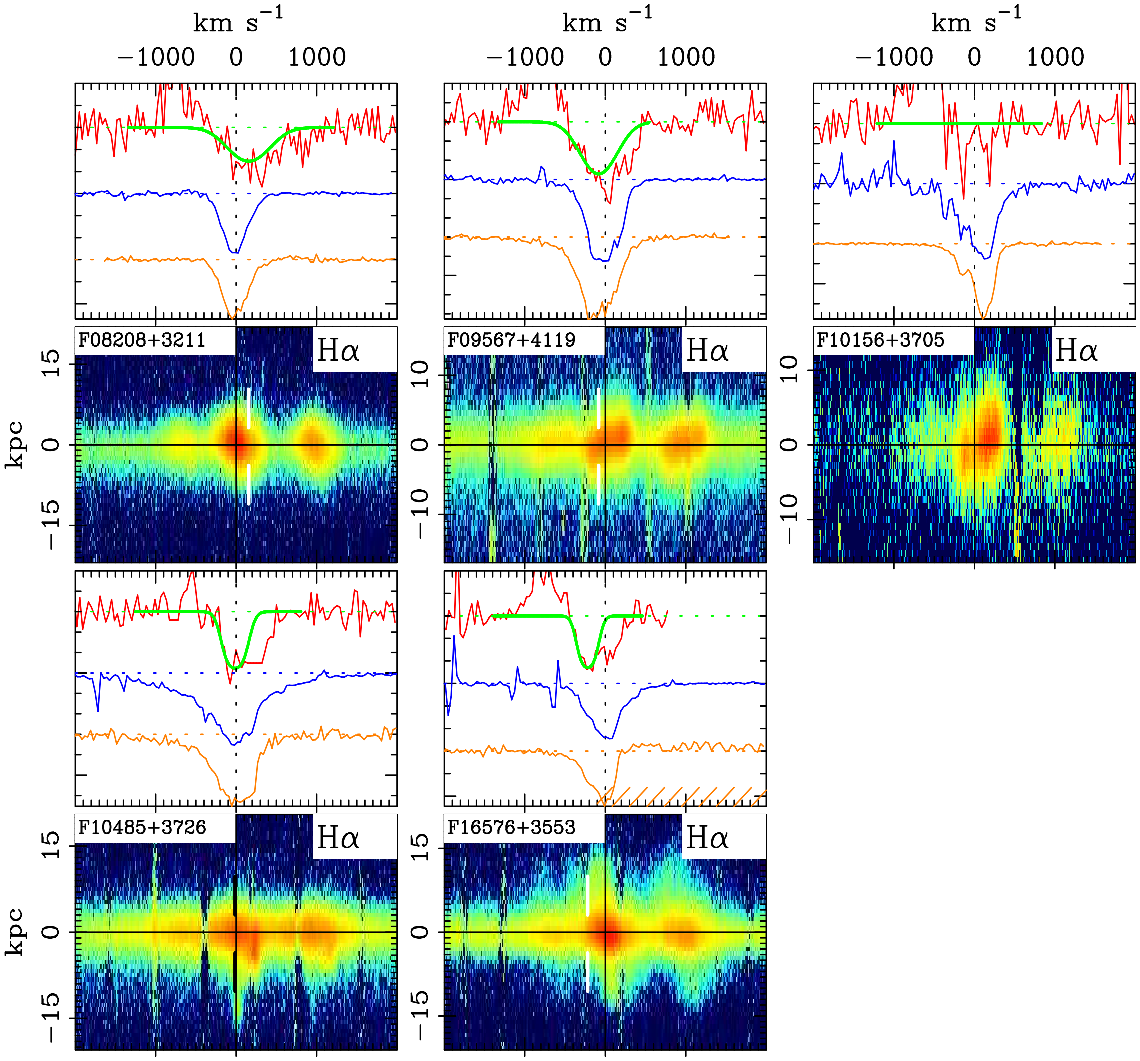

Figure 3.7: *Continued.*

Table 3.3. Outflow Component Properties

Name (1)	$\lambda_{1,c}$ (2)	Δv (3)	b (4)	$\tau_{1,c}$ (5)	C_f (6)	log[N(Na I)] (7)	log[N(H)] (8)	dM/dt (9)
IRGs								
F00521+2858	5989.36	26	67	2.36	0.38	13.75	21.39	0.00
Z01092−0139	6798.96	-119	172	0.56	0.38	13.53	21.17	3.96
F01250−0848	6182.55	-107	233	0.83	0.36	13.84	21.48	6.85
F01417+1651:N	6061.11	87	75	1.03	0.41	13.44	21.08	0.00
F01417+1651:S	6058.93	74	226	0.07	1.00	12.75	20.39	0.00
F01484+2220	6086.31	-139	145	0.94	0.43	13.69	21.33	7.48
F02114+0456:SW	6072.63	11	136	0.65	0.26	13.50	21.14	0.00
F02433+1544	6045.41	-97	192	1.66	0.28	14.06	21.70	7.86
···	6046.84	-26	84	0.72	0.61	13.33	20.97	0.00
F02437+2122	6030.17	-240	82	1.26	0.27	13.57	21.21	6.11
···	6035.94	46	100	2.34	0.54	13.92	21.56	0.00
F02509+1248	5969.77	27	227	0.22	0.77	13.24	20.88	0.00
···	5970.04	41	65	0.72	0.30	13.22	20.86	0.00
F02512+1446:S	6074.37	-406	85	0.24	0.48	12.86	20.50	3.61
···	6080.78	-90	168	0.77	0.27	13.66	21.30	2.89
Z03009−0213	6601.33	62	183	0.60	0.31	13.59	21.23	0.00
F1_5	8709.25	-374	122	0.31	0.76	13.14	20.78	9.96
···	8717.86	-78	198	0.56	0.37	13.60	21.24	2.92
F03359+1523	6108.41	1	159	0.21	0.20	13.07	20.71	0.00
F03514+1546	6026.55	-103	188	0.60	0.54	13.60	21.24	5.71
F04097+0525	6003.31	15	70	1.52	0.50	13.58	21.22	0.00
F04315−0840	5989.48	-104	154	1.37	0.47	13.88	21.52	9.52
···	5993.50	98	48	3.24	0.16	13.74	21.38	0.00
F04326+1904	6044.87	80	252	0.22	0.93	13.29	20.93	0.00
F05187−1017	6065.92	14	74	2.32	0.54	13.79	21.43	0.00
F08354+2555	6003.41	-164	286	0.08	1.00	12.89	20.53	3.30
···	6005.12	-79	56	2.17	0.11	13.64	21.28	0.95
F08498+3513	7015.80	28	180	0.95	0.24	13.78	21.42	0.00
F09120+4107	5948.10	12	74	1.82	0.59	13.68	21.32	0.00
F09320+6134	6130.18	-16	11	>5.00	0.12	>13.30	>20.94	0.00
···	6130.73	11	194	0.57	0.43	13.59	21.23	0.00
F10015−0614	5993.01	-134	36	>5.00	0.11	>13.80	>21.44	>2.35
···	5994.56	-57	150	1.29	0.29	13.84	21.48	2.94
F13532+2517	6065.67	-238	321	0.94	0.52	14.03	21.67	34.03
···	6071.60	54	38	2.33	0.30	13.50	21.14	0.00
F13565+3519	6102.13	24	95	0.51	0.80	13.24	20.88	0.00
F15364+3320	6027.39	-51	95	1.20	0.20	13.61	21.25	1.06
F15386+3807	6967.94	-331	123	2.58	0.26	14.06	21.70	24.90
···	6972.80	-122	97	2.62	0.37	13.96	21.60	10.47
F15549+4201	6103.24	-21	174	0.58	0.14	13.56	21.20	0.00
F16130+2725	6168.90	20	111	0.23	0.52	12.95	20.59	0.00
F16504+0228	6037.14	-99	59	>5.00	0.18	>14.03	>21.67	>4.98
···	6037.66	-74	292	0.27	0.88	13.45	21.09	4.75

Table 3.3 (cont'd)

Name (1)	$\lambda_{1,c}$ (2)	Δv (3)	b (4)	$\tau_{1,c}$ (5)	C_f (6)	log[N(Na I)] (7)	log[N(H)] (8)	dM/dt (9)
F21484−1314	6352.18	69	92	1.57	0.48	13.71	21.35	0.00
F21549−1206	6199.08	11	138	1.20	0.26	13.77	21.41	0.00
F22213−0238	6231.88	11	132	1.05	0.40	13.69	21.33	0.00
F22220−0825	6247.30	-305	213	1.35	0.23	14.01	21.65	18.66
···	6252.63	-49	91	2.95	0.17	13.98	21.62	0.00
F22338−1015	6265.48	30	227	0.16	1.00	13.11	20.75	0.00
low-z ULIRGs								
F00188−0856	6650.32	-176	271	1.09	0.28	14.02	21.66	13.55
F01298−0744	6691.47	-392	264	0.19	0.85	13.26	20.90	15.38
···	6697.95	-101	99	0.12	1.00	12.63	20.27	1.10
F02411−0353:SW	6744.62	60	333	0.16	0.46	13.27	20.91	0.00
F02411−0353:NE	6743.34	-180	151	1.03	0.36	13.74	21.38	9.18
F03250+1606	6648.54	-442	197	7.22	0.10	14.71	22.35	59.29
···	6655.69	-120	280	0.57	0.49	13.76	21.40	8.62
F08231+3052	7360.30	54	191	0.47	1.00	13.51	21.15	0.00
F08474+1813	6755.09	1	97	0.46	0.55	13.20	20.84	0.00
F08591+5248	6822.55	-144	366	0.15	1.00	13.30	20.94	7.43
F09039+0503	6624.59	-513	83	4.24	0.12	14.10	21.74	20.15
···	6631.69	-192	224	0.12	0.40	12.97	20.61	1.81
···	6637.60	75	111	0.08	1.00	12.49	20.13	0.00
···	6640.13	190	35	0.72	0.24	12.95	20.59	0.00
F09116+0334	6752.32	-122	313	0.39	0.43	13.63	21.27	5.77
F09539+0857	6652.08	-282	283	0.38	0.61	13.58	21.22	16.77
F10091+4704	7339.99	-125	266	0.16	0.85	13.19	20.83	4.27
F10190+1322:W	6348.87	-21	188	0.79	0.46	13.72	21.36	0.00
···	6349.24	-3	55	1.32	0.48	13.41	21.05	0.00
F10190+1322:E	6346.41	58	196	0.98	0.60	13.84	21.48	0.00
···	6351.99	322	94	0.41	1.00	13.13	20.77	0.00
F10378+1108	6689.05	-553	665	0.26	0.42	13.78	21.42	35.73
···	6689.46	-534	83	0.59	0.16	13.24	20.88	3.95
···	6695.96	-243	113	>5.00	0.08	>14.31	>21.95	>9.87
F10494+4424	6433.40	-286	40	>5.00	0.14	>13.85	>21.49	>7.15
···	6440.05	24	106	2.88	0.33	14.03	21.67	0.00
F10565+2448	6144.99	-309	181	1.41	0.49	13.96	21.60	35.07
···	6148.43	-141	106	1.54	0.43	13.77	21.41	9.04
F11028+3130	7072.03	137	199	0.66	0.27	13.67	21.31	0.00
F11387+4116	6765.18	-466	112	0.19	1.00	12.87	20.51	8.96
···	6772.13	-158	196	0.75	0.67	13.72	21.36	14.18
F11506+1331	6647.26	-74	108	1.99	0.28	13.89	21.53	4.07
F11582+3020	7213.24	-76	195	0.85	0.28	13.77	21.41	3.22
F14060+2919	6583.86	-142	113	4.47	0.16	14.25	21.89	10.53
F14197+0813	6663.68	-158	354	0.06	0.84	12.86	20.50	2.47
F15206+3342	6632.17	-213	244	1.19	0.15	14.01	21.65	8.41
F16333+4630:W	7022.00	-35	311	0.34	0.34	13.57	21.21	0.00

Table 3.3 (cont'd)

Name (1)	$\lambda_{1,c}$ (2)	Δv (3)	b (4)	$\tau_{1,c}$ (5)	C_f (6)	$\log[N(\mathrm{Na\ I})]$ (7)	$\log[N(\mathrm{H})]$ (8)	dM/dt (9)
···	7024.49	71	103	0.29	0.63	13.02	20.66	0.00
F16333+4630:E	7019.62	-136	240	0.12	0.64	13.03	20.67	2.37
F16474+3430:S	6556.65	-101	200	1.01	0.22	13.86	21.50	4.04
F16474+3430:N	6558.10	-158	103	>5.00	0.14	>14.27	>21.91	>10.23
···	6562.81	57	189	0.12	0.49	12.92	20.56	0.00
F16487+5447:W	6508.07	-76	160	1.75	0.08	14.00	21.64	1.52
F16487+5447:E	6509.55	-8	408	0.09	1.00	13.11	20.75	0.00
F17068+4027	6956.41	36	265	0.43	0.27	13.61	21.25	0.00
F17207−0014	6143.74	-298	177	2.16	0.35	14.13	21.77	36.66
···	6150.41	27	85	1.83	0.20	13.74	21.38	0.00
I20046−0623:W	6388.88	-191	37	>5.00	0.10	>13.82	>21.46	>3.16
···	6393.67	33	285	0.06	0.62	12.80	20.44	0.00
I20046−0623:E	6398.11	48	197	0.09	0.87	12.78	20.42	0.00
F20414−1651	6408.99	-119	133	1.00	0.31	13.68	21.32	4.47
F23234+0946:W	6646.53	-240	235	0.33	0.77	13.44	21.08	13.03
F23234+0946:E	6653.00	97	159	1.13	0.40	13.81	21.45	0.00
high-z ULIRGs								
F01462+0014	7547.80	27	223	0.35	0.42	13.44	21.08	0.00
Z02376−0054	8319.04	41	159	0.87	0.88	13.69	21.33	0.00
Z03151−0140	7449.29	-518	120	0.09	1.00	12.57	20.21	4.93
···	7462.07	-4	221	0.59	0.87	13.67	21.31	0.00
F04313−1649	7473.20	-7	125	0.58	0.44	13.41	21.05	0.00
F07353+2903	7868.96	-118	319	0.52	0.34	13.77	21.41	6.15
F07449+3350:W	8003.32	-9	215	0.29	0.32	13.35	20.99	0.00
F07449+3350:E	···	···	···	···	···	···	···	···
F08136+3110	8296.23	-63	277	0.22	0.60	13.34	20.98	2.11
F08143+3134	8013.52	-400	107	2.00	0.12	13.88	21.52	9.57
F08208+3211	8234.34	156	337	0.23	0.41	13.45	21.09	0.00
F09567+4119	8021.43	-82	304	0.16	0.99	13.24	20.88	3.60
F10156+3705	···	···	···	···	···	···	···	···
F10485+3726	7996.15	-13	142	1.28	0.30	13.81	21.45	0.00
F16576+3553	8079.64	-219	115	1.22	0.25	13.70	21.34	7.05

Note. — Col.(2): Redshifted heliocentric wavelength, in vacuum, of the Na ID$_1$ λ5896 line; in Å. Col.(3): Velocity relative to systemic, in km/s. Negative velocities are blueshifted. Col.(4): Doppler parameter, in km/s. Col.(5): Central optical depth of the Na ID$_1$ λ5896 line; the optical depth of the D$_2$ line is twice this value. Col.(6): Covering fraction of the gas. Col.(7-8): Logarithm of column density of Na I D and H, respectively, in cm^{-2}. Col.(9): Mass outflow rate of the component, in M$_\odot$ yr^{-1}.

Velocity distribution

Previous surveys of winds in starbursting galaxies that show the distribution of outflow velocities include Adelberger et al. (2003) and Heckman et al. (2000). The former show that the distribution of the velocity offset between the Lyα line and interstellar absorption lines in the UV is approximately a Gaussian of mean 614 km s^{-1} and width $\sigma = 316$ km s^{-1}, including a slight upturn at $\Delta v = 0$. This implies that every $z \sim 3$ Lyman-break galaxy has outflowing gas, with an average projected outflow velocity of ~ 300 km s^{-1}.

Local galaxies do not always show such unambiguous evidence for blueshifted velocities (which is at least partly due to selection bias at high redshift). The strong-stellar-contamination subsample of Heckman et al. (2000) shows a roughly symmetric distribution around 0 km s^{-1}. The distribution of the interstellar-dominated subsample is asymmetric; it lies completely in the blue for $|\Delta v| > 100$ km s^{-1}, but is curiously skewed to the red for $|\Delta v| < 100$ km s^{-1}.

In Figure 3.8, we show the distributions of the central velocity of each component in our sample (with 2 different binnings to emphasize its symmetric and asymmetric properties). Using 100 km s^{-1} bins, we see that the distribution of velocities for IRGs is fairly symmetric around $\Delta v = 0$ but has a clear tail toward blue velocities. With 50 km s^{-1} bins, we see that there are no components with velocities more redshifted than 100 km s^{-1}, whereas the blueshifted velocities extend to 450 km s^{-1}. However, among components with $|\Delta v| < 100$ km s^{-1}, there are many more redshifted than blueshifted components.

The skew at low absolute velocities with respect to systemic for the low-z ULIRG subsample is less pronounced or absent. Furthermore, the distribution of velocities for ULIRGs above $|\Delta v| = 100$ km s^{-1} is different from that of IRGs: (1) the average velocity is higher, (2) there are higher blueshifted velocities, (3) and there are several

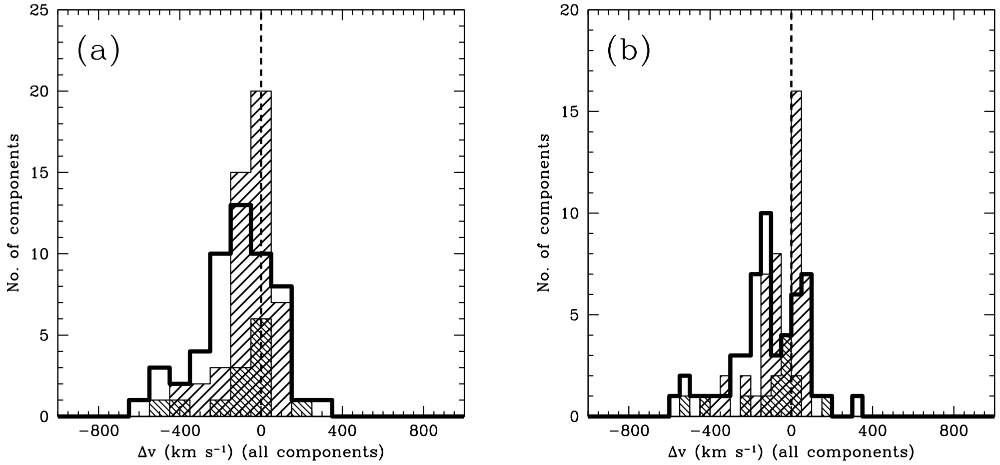

Figure 3.8: Distributions of central velocity of each component with 2 different binnings: (a) 100 km s^{-1} and (b) 50 km s^{-1}. The central bin in (a) represents components with $|\Delta v| < 50$ km s^{-1}. The distribution in velocity above $|\Delta v| = 100$ km s^{-1} is clearly skewed to the blue; however, the distribution below this value is skewed strongly to the red for the IRGs. The shading follows the pattern of Figure 3.1.

components with redshifted velocities greater than 100 km s^{-1}.

The origin of the skewness in the IRG subsample for $|\Delta v| \lesssim 100$ km s^{-1} is unclear. Possible explanations include: (1) a systematic wavelength miscalibration, (2) poor fitting, (3) there exists absorbing gas that is genuinely redshifted with respect to systemic, and/or (4) the stellar redshift of the galaxy (as traced by near-systemic Na I D) is slightly redder than the redshift from H I or optical line emission. We find (1) and (2) unlikely, but (3) and (4) are difficult to confirm or deny. The effect is slightly reduced but not removed by using H I redshifts (available for roughly 2/3 of our control sample).

The distributions of 'maximum' velocity in each galaxy ($\Delta v_{max} \equiv \Delta v$+FWHM/2) are shown in Figure 3.9(a). These distributions have median values of -300 − -416 km s^{-1} (with dispersions of 90 − 230 km s^{-1}), and truncate at -600 km s^{-1}. They also appear to have a lower envelope at -150 km s^{-1}. There is a single galaxy (F10378+1108) which has $\Delta v_{max} <$ -1000 km s^{-1}. K-S tests show that these distributions are consistent with being drawn from the same parent distribution.

The distributions of 'maximum' velocity in each galaxy ($\Delta v_{max} \equiv \Delta v$+FWHM/2) are shown in Figure 3.9(a). These distributions have median values of $300 - 416$ km s^{-1} (with dispersions of $90 - 230$ km s^{-1}), and truncate at ~ 600 km s^{-1}. They also appear to have a lower envelope at ~ 150 km s^{-1}. There is a single galaxy (F10378+1108) which has $\Delta v_{max} > 1000$ km s^{-1}. K-S tests show that these distributions are consistent with being drawn from the same parent distribution.

The distributions of the velocity of the highest column density gas in each galaxy are shown in Figure 3.9(b). These distributions have median values of $100 - 180$ km s^{-1} (with dispersions of $50 - 220$ km s^{-1}), and truncate at ~ 500 km s^{-1}. K-S tests show that the distributions of Δv[max. N(H)] for the IRGs and low-z ULIRGs are different at $> 98\%$ confidence.

It is important to note that corrections for projection effects will shift most velocities toward higher values. Assuming spherical symmetry, the average de-projection factor should be $\pi/2 \sim 1.6$. Applying this correction to the median values of Δv_{max} matches them nicely to the maximum measured velocities at $500 - 600$ km s^{-1}. Thus, the typical deprojected value of Δv_{max} is near the upper range of projected velocities rather than the median.

The Doppler widths (b = FWHM/$[2\sqrt{\ln 2}]$) of each velocity component are shown as a histogram in Figure 3.10. The range of values runs from ~ 50 km s^{-1} (the resolution limit) up to almost 700 km s^{-1}. The median value for the IRGs is ~ 150 km s^{-1}, while the average value in the low-z ULIRGs is higher at ~ 200 km s^{-1}. K-S tests show that the distributions of the different subsamples are not significantly different, however.

The large values that we measure for b imply that the broadening is due to the sum of large-scale motions in the wind, and are far above the thermal dispersion

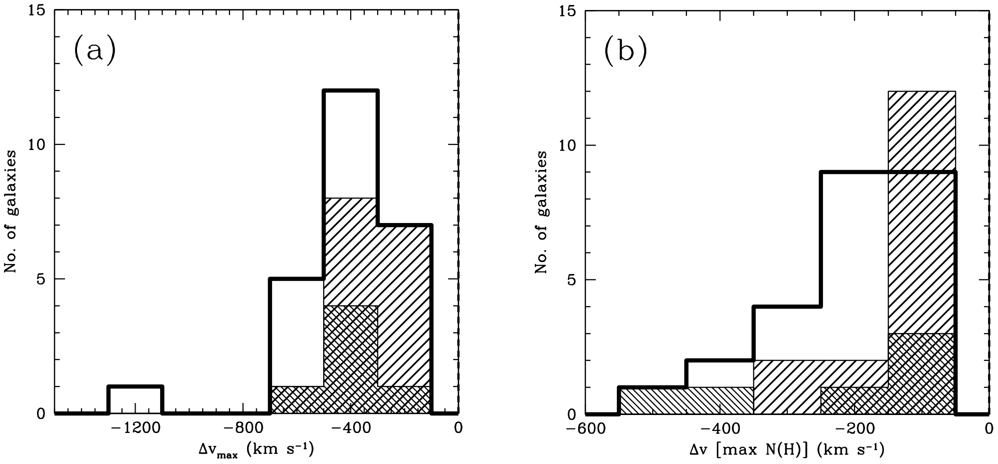

Figure 3.9: Distribution of (a) 'maximum' velocity ($\Delta v_{max} = \Delta v +$ FWHM/2) and (b) velocity of the highest column density gas in each galaxy. Note that the maximum velocities for all galaxies are $\sim$ 600 km s^{-1} or below except for F10378+1108. K-S tests show that the distributions of Δv_{max} are consistent with having the same parent distribution, but that the distributions of Δv[max. N(H)] for the IRGs and low-z ULIRGs are different at $>$ 98% confidence. The shading follows the pattern of Figure 3.1.

of warm Na gas ($\sim$ 3 km s^{-1} at $T \sim 10^4$ K). However, our spectral resolution is not enough to resolve clouds with widths $b \lesssim 50$ km s^{-1}; the wind may be a superposition of such clouds, each at a different velocity. In Chapter 5, we describe high-resolution observations designed to search for such components.

Optical depth and column density

Figure 3.11 plots the distribution of the central optical depth of the Na I D$_1$ line (the D$_2$ line has twice the optical depth). The distributions for IRGs and ULIRGs are quite similar, and K-S tests show that they are consistent with being drawn from the same parent distribution. We see that the peak of the distributions are around $\tau \sim 1$; in other words, most of the gas is moderately optically thick (if our assumptions about a constant covering fraction and a close-to-Gaussian velocity distribution are correct; see Chapter 2).

Our data constrain the amount of ground-state Na I present in the line-of-sight,

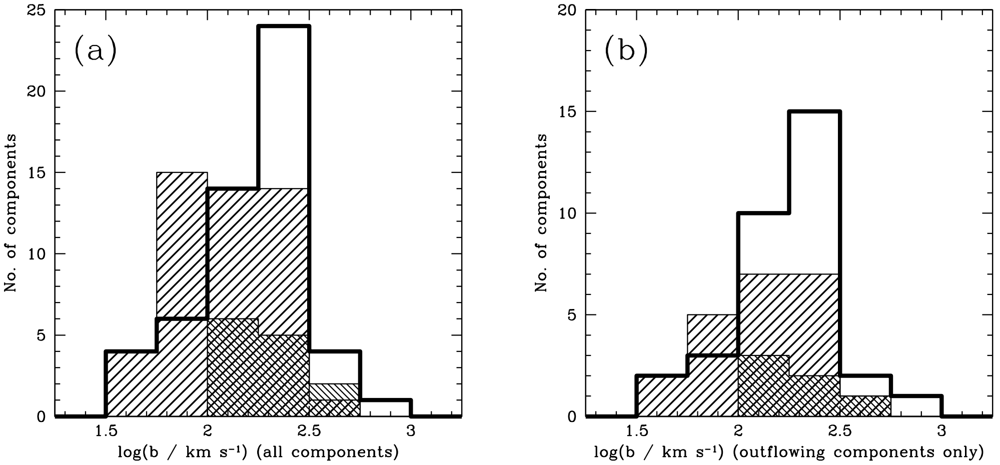

Figure 3.10: Logarithmic distributions of the Doppler parameter for (a) all and (b) outflowing components. The lines in ULIRGs appear to be slightly broader on average, though the overall differences between the IRG and ULIRG distributions are not significant. The shading follows the pattern of Figure 3.1.

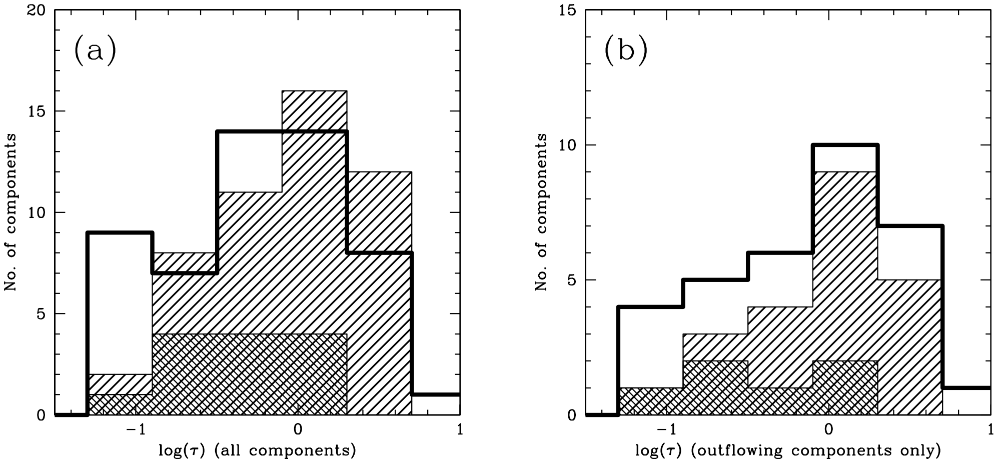

Figure 3.11: Logarithmic distributions of the central optical depth in the D_1 line for (a) all and (b) outflowing components. Notice the peak at $\tau \sim 1$. K-S tests show that the distributions of different subsamples are not significantly different from one another. The shading follows the pattern of Figure 3.1.

which for a Gaussian velocity distribution is proportional to the optical depth and the Doppler parameter b. Since we are more interested in the total amount of hydrogen, we must correct for ionization to determine the total amount of Na, and then for depletion and/or non-solar abundances to get the amount of hydrogen. One way to do this is with an empirical calibration between $\log[N(\mathrm{Na\,I})]$ and $\log[N(\mathrm{H})]$,

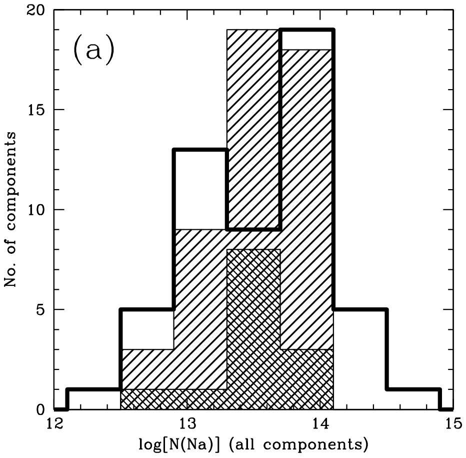

Figure 3.12: Logarithmic distributions of the Na column density for (a) all and (b) outflowing components. The distributions peak in the range $N(\mathrm{Na}) = 13.5 - 14$ and have a tail to low values. The shading follows the pattern of Figure 3.1.

taken from local Galactic lines-of-sight. This was our approach in our preliminary report (Rupke et al. 2002). However, for the full sample we have chosen to do the ionization and depletion corrections separately, for clarity. Furthermore, the physical conditions in these galaxies are extreme and are unlikely to reflect those seen in our Galaxy.

For depletion, we use the canonical Galactic value of -0.95 from Savage & Sembach (1996). The ionization state of the absorbing gas has the potential to be a significant uncertainty in converting $N(\mathrm{Na\ I})$ to $N(\mathrm{H})$. Na is easily ionized due to its low first ionization potential, 5.14 eV. Most or all of the Na in the vicinity of high-velocity shocks will be out of the ground state (see Sutherland & Dopita 1993 for the ionization structure of cooling, post-shock Na, and Dopita & Sutherland 1996 for the ionization structure of various elements in the shock and its precursor). Given the large amount of Na I that we observe, more plausible locations for the absorbing gas are either (a) the center of cold clouds/filaments that have been entrained and accelerated by the wind but not destroyed completely or (b) postshock regions where the gas has cooled sufficiently and recombined, and is no longer dominated by collisions or the hard shock radiation field. In the former case, we expect that these clouds will have ionized skins of warm and hot gas that are heated by the surrounding wind fluid.

Complicating this is the fact that without significant amounts of dust, Na may be ionized in regions where hydrogen is neutral. This occurs in Mg I (which has a slightly larger first ionization potential, 7.65 eV) because (a) it has a low first IP compared to that of hydrogen and (b) there is a decrease in recombination with the drop in electron density in regions of neutral hydrogen (de Kool et al. 2001). In fact, if significant near-UV radiation ($\lambda \lesssim 3060$ Å) penetrates to the center of the clouds/filaments or post-shock regions of the wind, Na will still be highly ionized. We do know that there is dust in these winds based on the correlation of E(B-V) and the equivalent width of Na I D seen in LIRGs and ULIRGs (Kim et al. 1998), and this dust may shield the neutral Na I D atoms and prevent total ionization.

For our galaxies, we assume modest ionization, with $N(\mathrm{Na})/N(\mathrm{Na\ I}) = 10$. This is in the middle of the range of ionization corrections set by an empirical conversion from Na to H, as determined by measurements along sightlines toward Galactic stars (Stokes 1978). The resulting column densities (and subsequent mass outflow rates) scale linearly with this assumed value for the ionization fraction.

The resulting distribution of Na column densities is shown in Figure 3.12. The distribution peaks at $\log[N(\mathrm{Na})] = 13.5 - 14$, with a longer tail to lower values than higher values. These values are larger by a factor of $10 - 100$ on average than those measured in outflows in dwarf galaxies by Schwartz & Martin (2004), who find $\log[N(\mathrm{Na})] = 11.8 - 12.5$ for 4 outflowing components (and 13.7 for a fifth). We have one galaxy in common with Schwartz & Martin (2004), NGC 1614, and our column densities match theirs within 0.25 dex (despite their much higher spectral resolution!). The difference in velocity between the red and blue components in this

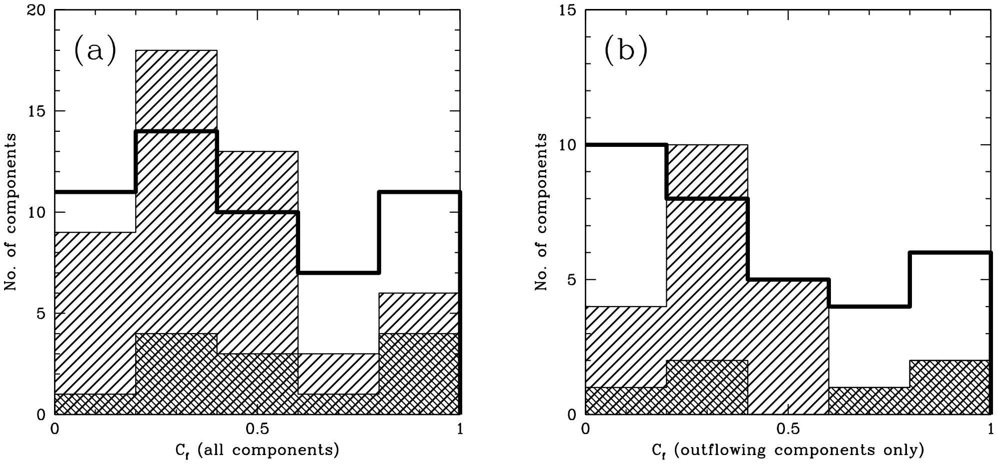

Figure 3.13: Logarithmic distributions of the covering fraction for (a) all and (b) outflowing components. In frame (b), notice the single peak at $C_f \sim 0.3$ for the IRGs and the double peak at $C_f \sim 0.1$ and 1.0 for the ULIRGs. K-S tests show that the differences between these distributions are not significant, though these tests are not as sensitive to data far from the mean (e.g. the hypothesized peak at $C_f \sim 1$). The shading follows the pattern of Figure 3.1.

galaxy in our data also match theirs ($\Delta v = 200 - 220$ km s^{-1}), but their velocities are smaller on an absolute scale by $80 - 100$ km s^{-1}. The cause of this discrepancy is unknown.

Covering fraction

In Figure 3.13, we show the distribution of covering fraction in each absorbing component. The technical aspects of the physical model behind C_f are described in detail in Chapter 2. In the superwind context, C_f may reflect (a) the clumpiness of the wind and/or (b) the global solid angle subtended by the wind with respect to the galaxy center C_Ω. In AGN, the small size of the continuum source means C_f only probes local clumpiness, but the likelihood of extended continuum sources in starbursts may allow the global covering fraction to be probed, as well. The relation of C_f to the global covering fraction must also account for the detection rate of winds; see §3.5.2 below.

For the IRGs, this distribution peaks at 0.3. The distribution of C_f in ULIRGs peaks instead at $C_f \sim 0.1$. In general the distribution for ULIRGs is flatter than that for IRGs, and it has a second peak at $C_f \sim 1$. The origin of this bimodal distribution in ULIRGs is unclear, but may reflect a different geometry for outflows in ULIRGs. K-S tests show that the differences between these distributions are not significant, though these tests are not as sensitive to data far from the mean, which is $0.34 - 0.40$ for all three subsamples.

Stellar contribution to Na I D

In galaxy spectra, Na I D has contributions due to stellar absorption from late type stars and interstellar absorption. As in Rupke et al. (2002), we can estimate the expected stellar contribution to Na I D by scaling the equivalent width of the Mg I b lines. This is possible because of the similar mechanisms by which Na and Mg are created in these stars and their similar first ionization potentials (5.14 eV for Na, 7.65 eV for Mg). There is thus a correlation between the stellar equivalent widths of Mg I b and Na I D in galaxy spectra with little interstellar contribution. Using a small sample of optically bright, nearby galaxies from Heckman, Balick, & Crane (1980), we infer that $W^{\star}_{eq}(\text{Na I D}) = 0.75\ W_{eq}(\text{Mg I b})$. However, as we illustrate in Chapter 2, and judging by the dispersion in the data used to determine the correlation, this diagnostic is not universally reliable on a galaxy-by-galaxy basis.

In Figure 3.14(a), we show the expected percentage of stellar contamination to Na I D based on this relation for a large sample of galaxies. Most are infrared-luminous galaxies from Kim et al. (1995) and Veilleux et al. (1999b), but the Heckman, Balick, & Crane (1980) data are also included. We can see from this plot that in infrared-luminous galaxies, the interstellar contribution is generally, but not always, dominant. This is expected given the large amount of gas and dust in the

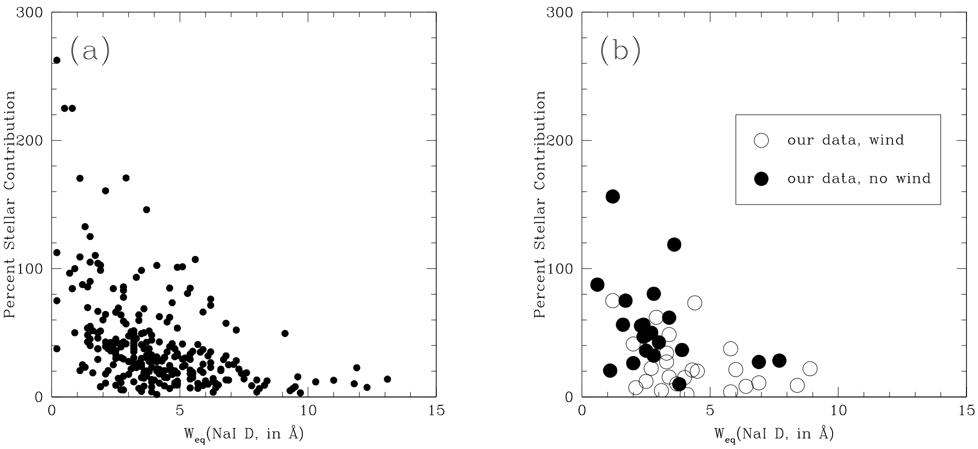

Figure 3.14: (a) Estimated percent of the equivalent width of the Na I D line that is stellar, for a large number of nearby galaxies. This is calculated using the assumption $W_{eq}^{\star}$(Na I D) = 0.75 W_{eq}(Mg I b). The interstellar contribution is generally dominant. (b) The same, but for our sample. Note that detecting winds on the basis of these diagrams alone is infeasible.

nuclei of these galaxies.

Could the relative equivalent widths of Na I D and Mg I b be a good indicator of the presence of winds in these galaxies? Heckman et al. (2000) found this to be the case, in that those galaxies where the interstellar part of Na I D dominated were more likely to host winds. Figure 3.14(b) shows the expected stellar contribution to Na I D for our sample galaxies with and without winds, for those cases where W_{eq}(Mg I b) is present in our spectra or is available from other sources. We see that those galaxies with winds tend to have smaller values of W_{eq}(Mg I b) / W_{eq}(Na I D) and larger values of W_{eq}(Na I D), but there is significant overlap, enough that it is hard to distinguish the two samples on this basis alone.

3.3.2 Rate of detection

The current survey contains over 50% more starburst galaxies than previous superwind surveys of infrared sources (Lehnert & Heckman 1995, 1996; Heckman et al. 2000). It also has a much higher number of ULIRGs (43 vs. $1-5$). We are thus in a better position to judge the frequency of occurrence of winds in ULIRGs, especially as a function of infrared luminosity.

We use a velocity cutoff of -50 km s^{-1} to delineate galaxies with superwinds, a slightly more liberal cutoff than in our pilot study (in which we used -70 km s^{-1}). Velocity components blueshifted by more than 50 km s^{-1}are assumed to be outflowing. This cutoff is chosen to avoid statistical errors in wavelength calibration, line fitting, and redshift determination. However, as our velocity distribution shows, this cutoff may include some components that are at the systemic velocity of the galaxy and are blueshifted due to rotation. Furthermore, if the red components with $|\Delta v| > 100$ km s^{-1} are mirrored on the blue side of the distribution (see Figure 3.8), some of these components are not actually outflowing gas.

Table 3.1 lists the detection rate of massive outflows in each subsample. We observe that outflows are commonly detected in each subsample, are detected in the majority of ULIRGs, and are detected more frequently in ULIRGs than in the less-luminous galaxies. There appears to be some dependence of this quantity on star formation rate (and to a lesser extent on K-band magnitude), as can be seen by looking at Figure 3.15. The detection rate seems to increase with star formation rate in the first two bins, but then dips at very high star formation rates. A similar behavior is seen for M_K. The high-z ULIRGs also show a lower detection rate than the low-z ULIRGs; we discuss this further in §3.5.6.

Applying this same cutoff to the galaxies in Heckman et al. (2000) that are

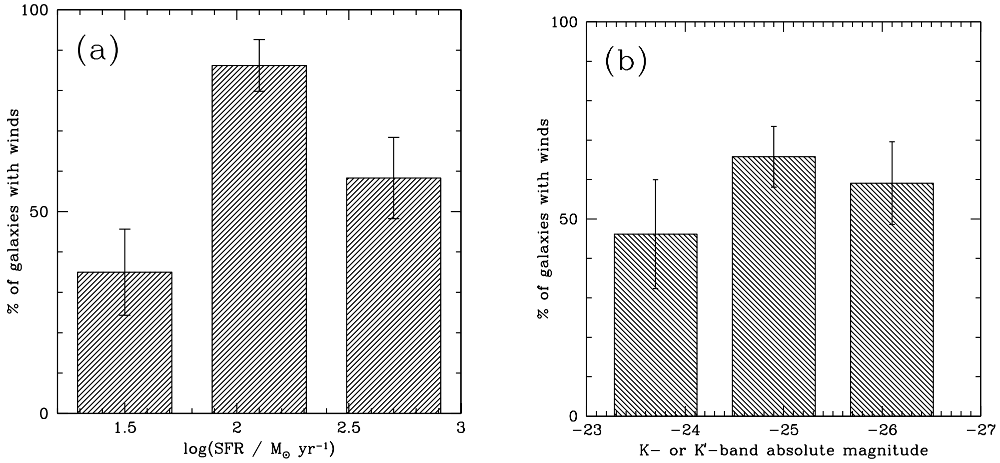

Figure 3.15: The detection rate of winds as a function of (a) star formation rate and (b) K- or K'-band magnitude. The detection rate peaks at a SFR of a few hundred, and possibly also at $M_K \sim -25.3$. The error bars represent 1σ errors, assuming a binomial distribution.

optically classified as H II galaxies or LINERs and have $L_{\rm IR} < 10^{12}\ L_\odot$, we compute a wind detection frequency of 32 ± 12% (7/22 galaxies, with a median $\log[L_{\rm IR}/L_\odot] = 11.0$). This is roughly consistent with the measurement from our control subsample. Our measurement of 43% is slightly higher than that of Heckman et al. (2000), but so is the median infrared luminosity of our subsample.

In §3.5.2, we discuss in detail the implications of this in light of the global covering fraction of the gas. However, suffice it to say for now that these detection rates are likely lower limits to the actual frequency of occurrence of outflows in these galaxies.

3.3.3 Mass outflow rate

As in our preliminary report (Rupke et al. 2002), we assume a spherically symmetric mass-conserving free wind, with a density and velocity that are independent of radius. Previously, we assumed that this wind extended from an inner radius $r_\star$ to infinity. A refinement on this model is to assume that the wind flows from some inner radius r_1 to a finite radius r_2. In this case the mass outflow rate is proportional to $r_1 r_2/(r_2 - r_1)$, rather than just $r_\star$. This dependence is more complicated in that dM/dt now depends on both the wind's radius and its thickness. A larger outer radius (r_2) and a smaller thickness (r_2/r_1) both mean an increased dM/dt. We incorporate these radial parameters as a normalization factor C_{rad}, where $C_{rad} = 1$ kpc for $r_1 = 1$ kpc and $r_2 = \infty$, and C_{rad} can range from 0 kpc to ∞. For our calculations, we assume $C_{rad} = 1$ kpc, which is true for $r_1 = 1$ kpc and for a range of outer radii r_2 from a few kpc and up to infinity. This value of r_1 is appropriate given the size of the molecular gas disks in ULIRGs (Sanders et al. 1988; Scoville et al. 1989; Downes & Solomon 1998; Sakamoto et al. 1999), where the star formation driving the wind occurs. The outer radius is motivated both by observations of local starbursts and by our own data (§3.3.5).

We include two factors, $C_\Omega \equiv \Omega/4\pi$ and C_f, which describe the global angular covering factor and the local covering factor within the wind, respectively. We assume a constant value for C_Ω of 0.4 based on measurements of local winds, and we use the measured covering fraction C_f as a substitute for the clumpiness of the gas within the wind. However, as we discuss below (§3.5.2), C_f may also include a contribution from the global angular covering factor, and this will at worst introduce a slight underestimate of dM/dt.

We also assume an average particle mass of $1.4 m_p$ to account for the contribution of He. The resulting formula is

$$dM/dt(\mathrm{H}) = 29 \left(\frac{\Omega}{4\pi}\right) C_f \, C_{rad} \left(\frac{N(\mathrm{H})}{10^{21}\ \mathrm{cm}^{-2}}\right) \left(\frac{\Delta v}{200\ \mathrm{km\ s}^{-1}}\right) M_\odot\ \mathrm{yr}^{-1}. \quad (3.2)$$

There are clearly a number of uncertainties here. The most significant is the lack of knowledge about the geometry of the wind, including radial extent, thickness, and opening angle. We can relate the wind geometry to the density of the absorbing gas by assuming a thin shell, since the shell thickness $\Delta r \sim N(\mathrm{H})/n(\mathrm{H})$. Note that

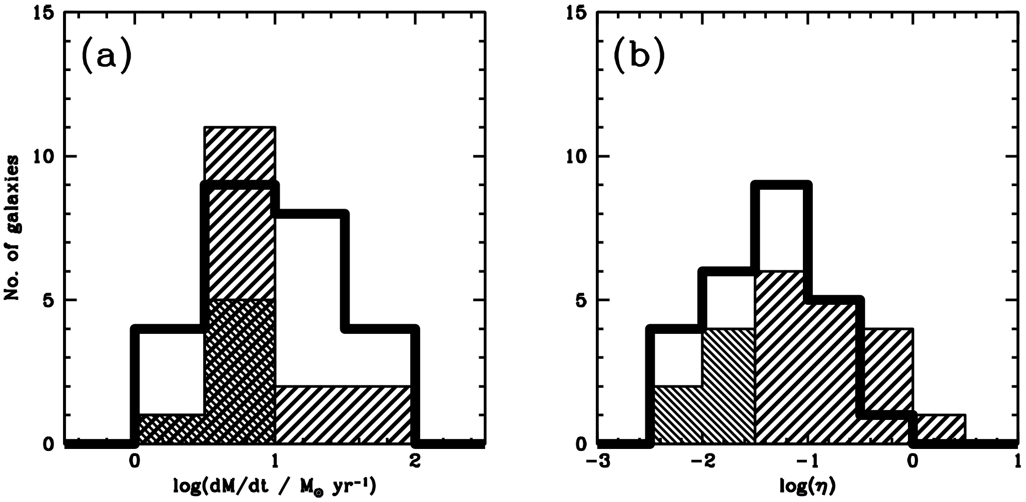

Figure 3.16: The distributions of (a) mass outflow rate and (b) mass entrainment efficiency for our three subsamples. The samples overlap in both quantities. They have similar means in dM/dt but have different means in η.

this density is averaged over the full volume of the shell, and is related to the actual cloud/filament density n by the volume filling factor f: $n_{avg} = f \times n$. We then have

$$C_{rad}^{thin\ shell} \sim \frac{r^2}{\Delta r} \sim 0.3\ f\ \left(\frac{r}{1\ \mathrm{kpc}}\right)\ \left(\frac{N(\mathrm{H})}{10^{21}\ \mathrm{cm}^{-2}}\right)^{-1}\ \left(\frac{n(\mathrm{H})}{1\ \mathrm{cm}^{-3}}\right). \quad (3.3)$$

Using our average measured column density, we thus recover $C_{rad} = 1$ kpc for a wind of radius 1 kpc, a cloud/filament particle density 10^2 cm^{-3}, and a filling factor of clouds/filaments of 1%.

We find that values of dM/dt are similar across our entire dataset, with a range of a few to ~ 20 M$_\odot$ yr^{-1} within the 1σ dispersion and an average of $5-8$. Figure 3.16(a) shows the distributions of this quantity for the three subsamples. K-S tests show that these distributions may have the same parent distribution.

3.3.4 Mass entrainment efficiency

The mass entrainment efficiency is, empirically speaking, a comparison of the amount of gas in the wind to the amount of gas being turned into stars. These two processes do not generally occur in the same place or use the same gas reservoir. The gas forming stars is in dense concentrations of molecular gas. Most of the gas in a superwind is entrained from the extended disk and halo of the host galaxy as the wind propagates outward (Suchkov et al. 1994; Strickland & Stevens 2000), which motivates the use of the phrase 'mass entrainment' efficiency. It is a useful quantitative description of how the wind's evolution is connected to its power source (the starburst).

This quantity has also been referred to as the 'reheating efficiency' (Martin 1999; Rupke et al. 2002). If its influence extends beyond its host galaxy, the superwind heats the surrounding ISM and IGM, and is thus a feedback mechanism to star formation and can have implications for galaxy formation (see Chapter 1). However, as most of the gas in the superwind is colder, entrained material, in this work we elect to use the more accurate term 'mass entrainment efficiency.'

In our calculation of star formation rate from L_{IR} (§3.1), we include a correction for AGN contribution to the infrared luminosity; α equals the fraction of the IR luminosity powered by star formation. For the IRGs in our sample we assume $\alpha = 1$. Results from *ISO* suggest that $70\% - 95\%$ of the infrared luminosity of a typical ULIRG is powered by star formation (Genzel et al. 1998). These values will certainly apply to our sample, which we have selected to include objects whose spectra indicate powerful starbursts. Thus, we assume $\alpha = 0.8$ for all of our ULIRGs. However, we assume $\alpha = 1.0$ for the IRGs.

The mass entrainment efficiency is the mass outflow rate normalized to the corresponding star formation rate for a given galaxy:

$$\eta \equiv \frac{dM/dt}{\mathrm{SFR}}. \tag{3.4}$$

Figure 3.16(b) shows the distribution of the mass entrainment efficiency in each galaxy. The distributions for our different subsamples are different at the 97% confidence level or greater.

Previous measurements of η in nearby dwarf galaxies, edge-on spirals, and nearby infrared-luminous galaxies indicate that this ratio is of order unity (Martin 1999; Heckman et al. 2000). We measure much smaller values in our galaxies, with average values of 0.15, 0.04, and 0.02 in our IRG, low-z ULIRG, and high-z ULIRG subsamples, respectively. In §3.5.4, we discuss the implications of these discrepancies. Note from the previous section that our normalization of dM/dt, and thus η, is difficult for a number of reasons, and thus the systematic uncertainty in these numbers is larger than the measurement uncertainties.

3.3.5 Spatial distribution of absorbing gas

We know from observations of local galaxies that superwind gas extends over a range of scales from sub-kiloparsec to 10+ kpc (e.g., Veilleux et al. 2003). Recent integral field spectroscopy and deep Chandra imaging and spectroscopy of the nearest ULIRG, Arp 220, show that it likely contains a superwind with velocities of 200 km s^{-1} at radii of a few kpc (Arribas et al. 2001; McDowell et al. 2003), as well as large structures at radii of $10-20$ kpc that have a symmetric velocity field which indicate a tidal origin (McDowell et al. 2003; Colina et al. 2004).

As we showed above, dM/dt is somewhat sensitive to the radial distribution of the gas. The inner radius of the wind is constrained by the size of the starburst region, and thus this radius cannot be smaller than $\sim 0.5-1$ kpc. Are there any constraints on either the inner or outer radius of the wind from measuring the size of the absorbing region across the spatially extended background continuum light?

In general, the continua of the distant ULIRGs have an angular size along the slit that is comparable to or not much greater than the seeing limit. However, there are a few nearby exceptions. F17207−0014 ($z = 0.043$) possessess extended continuum emission. Blueshifted absorption extends across the entirety of the spatial profile, meaning that this absorption occurs at projected radii of $0 - 5$ kpc. IRAS 20046−0623 ($z = 0.084$) shows variation of the Na I D profile across the $6'' \sim 9$ kpc of its continuum emission. The gradient follows that of the line emission, which has a blueshifted tail westward of the western nucleus (see also Murphy et al. 2001). This blueshifted tail in emission corresponds to the velocity of the blueshifted absorption in the west nucleus, and the absorption is extended across $\gtrsim 2$ kpc. As we discuss below, F10190+1322:E (z = 0.076) has *redshifted* absorption that is extended on scales of $5 - 6$ kpc (§3.5.1) and arises in the disk of the western nucleus. Finally, we observe blueshifted absorption across the entire continuum of F10565+2448 ($z = 0.043$), which means that the projected outer radius of the outflow is 2 kpc.

Many more of the IRGs than the ULIRGs have spatially extended continua due to their lower redshifts. Several show clear evidence for stellar rotation in their Na I D profiles; typically these rotation components are narrow. A few IRGs also show more complex structures. The blueshifted Na I D in NGC 6240 ($z = 0.024$) is constant in velocity across most of the continuum, but it becomes more blueshifted in concert with the line emission to the east of the galaxy. This suggests absorbing radii of $0 - 8$ kpc in projection. In F08354+2555 ($z = 0.018$), the blueshifted absorption extends across $22''$, which corresponds to 4 kpc in projected radius (though as we argue below, this is probably not outflowing gas; §3.5.1).

These values are consistent with our assumption above of a uniform density outflow extending from ~ 1 kpc to several kiloparsec. Furthermore, a thin absorbing shell can be ruled out from the lack of narrow absorbing components in our data. Thus, the C_{rad} factor that we use to calculate dM/dt is well-determined by observations.

3.3.6 H II galaxies vs. LINERs

Some authors have suggested that the shock-like line ratios found in the nuclei of galaxies classified as LINERs are due to the presence of shocks in outflowing gas (Veilleux et al. 1995; Lutz et al. 1999; Taniguchi et al. 1999). We can test this hypothesis by comparing the detection rate of winds in LINERs with the frequency in H II galaxies. Interestingly, we find no statistically significant difference in the detection rate of winds in LINERs and H II galaxies in each of our subsamples taken separately, or even if we consider the sample as a whole. In our entire sample, 20 of 34 LINERs host winds, versus 20 of 37 H II galaxies.

However, we do find that the median maximum velocity Δv_{max} in LINERs is higher than in H II galaxies. The distribution of maximum velocities in all LINERs in our control and low-z subsamples is different from that of H II galaxies at $>$ 98% confidence (though the difference for each subsample taken separately is not significant). The average values of Δv_{max} for LINERs in the control and low-z subsamples are -375 and -465 km s^{-1}, respectively, compared to -310 and -350 km s^{-1} for the H II galaxies.

This difference in outflow velocity could explain some or all of the physical differences between the LINER and H II optical spectral classes. As Dopita & Sutherland (1995) demonstrate, a modest increase in shock velocity can increase the [N II]λ6583/Hα line ratio and push a galaxy from having an H II galaxy classification to a LINER classification. However, other effects may also contribute to the line ratios in some LINERs, including a weak AGN.

3.4 OUTFLOW PROPERTIES AND HOST GALAXY PROPERTIES

One of the primary purposes of this survey is to look for dependence of outflow properties on the properties of the host galaxies. This allows us to (1) better understand the physics of outflows and (2) describe their properties using approximate analytic functions. The latter is especially useful as input to theoretical analysis and simulations.

3.4.1 Mass outflow rate

The two quantities that are tabulated for all of our sample are infrared luminosity and K- or K'-band magnitude. In Figure 3.17 we plot dM/dt as a function of SFR (computed from $L_{\rm IR}$) and $M_{K^{(\prime)}}$. These figures show that the mass outflow rate in our sample is uncorrelated with both star formation rate and near-infrared luminosity. Least-squares fits yield the relations $dM/dt \sim {\rm SFR}^{0.0\pm0.1}$ and log(dM/dt) $\sim (0.2 \pm 0.1)M_{K^{(\prime)}}$. Despite the slight tilt in the latter, the correlation coefficients (both parametric and non-) indicate no significance. The K-band luminosity has a contribution from the light of the old stellar mass in these galaxies; if this contribution is dominant, then mass outflow rate is independent of mass. However, the magnitude of the contribution to $M_{K^{(\prime)}}$ from warm dust emission (and thus star formation) is uncertain, which complicates this interpretation.

The lack of a correlation of dM/dt with SFR and $M_{K^{(\prime)}}$ extends over at least 2 orders of magnitude in star formation rate and 2.5 magnitudes in $M_{K^{(\prime)}}$. What of galaxies with lower star formation rates? Low-mass starbursting galaxies blow

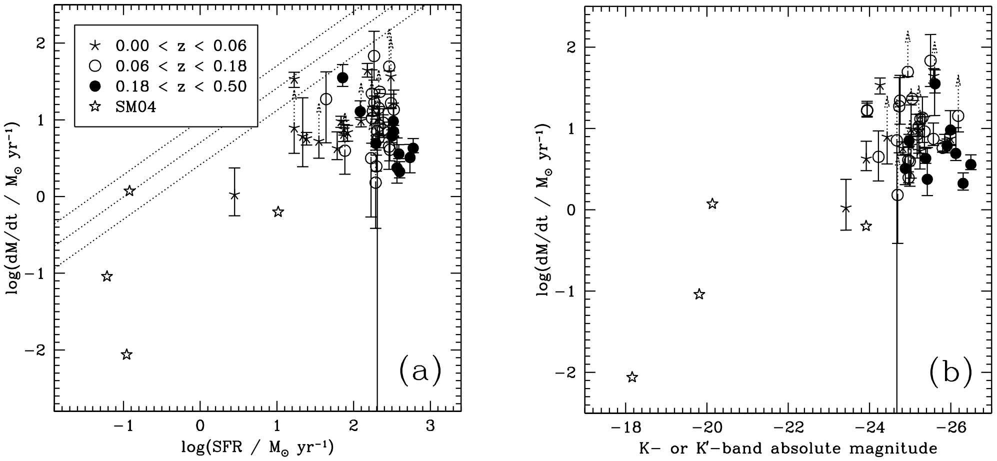

Figure 3.17: Mass outflow rate vs. (a) star formation rate and (b) K- or K'-band magnitude. dM/dt is apparently uncorrelated with either of these quantities in our data, but if dwarf galaxies are included it increases as SFR increases or the galaxy becomes more luminous in the K band over a larger range of SFR or $M_{K^{(\prime)}}$. The open stars are taken from Schwartz & Martin (2004). The dotted arrows represent lower limits for dM/dt. The diagonal dotted lines are theoretical curves from Shu et al. (2003), for different values of the interstellar medium parameter K (§3.5.3).

superbubbles and superwinds (Martin 1998), and quiescent spirals like the Milky Way may commonly host nuclear superwind activity (Bland-Hawthorn & Cohen 2003). In Figure 3.17(a), we plot points from Schwartz & Martin (2004), who surveyed the neutral gas in nearby dwarf galaxies using the Na I D feature. Their sample probes lower star formation rates and wind velocities. The addition of their data suggests that mass outflow rate does decline with star formation rate below a certain value, perhaps ∼10 $M_\odot$ yr^{-1}.

3.4.2 Mass entrainment efficiency

The consequence of dM/dt being independent of SFR is that the mass entrainment efficiency is linearly proportional to SFR:

$$\eta \sim \mathrm{SFR}^{-1.0\pm0.1}. \qquad (3.5)$$

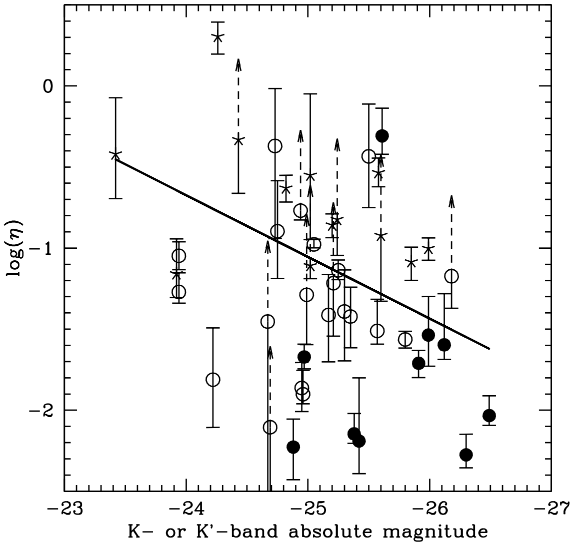

Figure 3.18: Mass entrainment efficiency vs. $M_{K(')}$. η apparently decreases as $M_{K(')}$ increases. The symbol shapes are as in Figure 3.17.

We also find that η decreases with $M_{K(')}$ according to $\log(\eta) \sim (0.3 \pm 0.1) M_{K(')}$ (see Figure 3.18). The correlation between η and $M_{K(')}$ is quite significant, at the $95 - 99\%$ level. If a significant fraction of $M_{K(')}$ comes from reprocessed starburst light, this dependence is related to that in Eq. 3.5.

Thus, the most luminous galaxies, with the largest energy reservoirs available to power outflows, are the least efficient at doing so. Starburst models suggest that the ratio of mechanical power in supernovae and stellar winds (which power superwinds) to the bolometric luminosity of a starburst is in the range $0.010 - 0.015$ (Strickland 2004). This ratio should be roughly independent of starburst luminosity, but the efficiency of thermalization of this mechanical energy, as well as the efficiency at which interstellar material is entrained by the hot free wind, may depend on environmental factors that are connected to the size of the starburst. We discuss this further in §3.5.4.

Though we do not show them in Figure 3.18, the data from Schwartz & Martin (2004) suggest that the mass entrainment efficiency may level off below some value

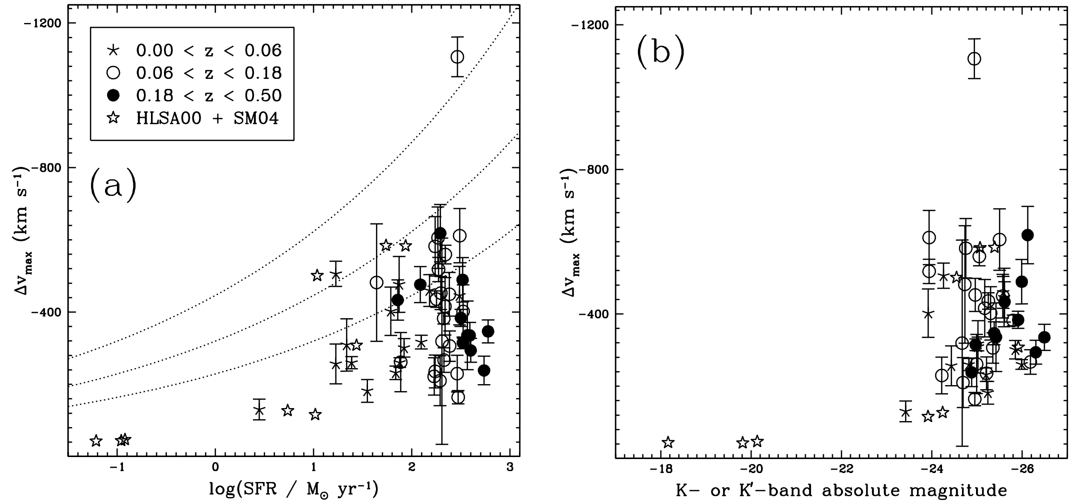

Figure 3.19: Maximum velocity ($\Delta v_{max} \equiv \Delta v + \mathrm{FWHM}/2$) vs. (a) star formation rate and (b) $\mathrm{M}_{K(\prime)}$. Δv_{max} is apparently uncorrelated with either of these quantities in our data, though declines at the lowest star formation rates. The open stars are starburst galaxies observed by Heckman et al. (2000) and Schwartz & Martin (2004). The diagonal dotted lines are theoretical curves from Shu et al. (2003), for different values of the interstellar medium parameter K (§3.5.3).

of SFR, equal to the value of SFR at which the mass outflow rate turns downward (see Figure 3.17).

3.4.3 Outflow velocity

In Figures 3.19 and 3.20, we plot for each galaxy (1) the maximum outflow velocity Δv_{max} and (2) the velocity of the gas with the highest column density as a function of (a) SFR and (b) $M_{K(\prime)}$. These figures show that the velocities in these galaxies are also independent of both star formation rate and near-infrared luminosity. However, at the lowest star formation rates, Δv does turn downwards to lower values, as evidenced by observations of dwarf galaxies (Schwartz & Martin 2004). Furthermore, in Figure 3.20(a), there is indication of an upper envelope, consistent with the significantly different distributions of Δv[max. N(H)] in IRGs and ULIRGs (§3.3.1).

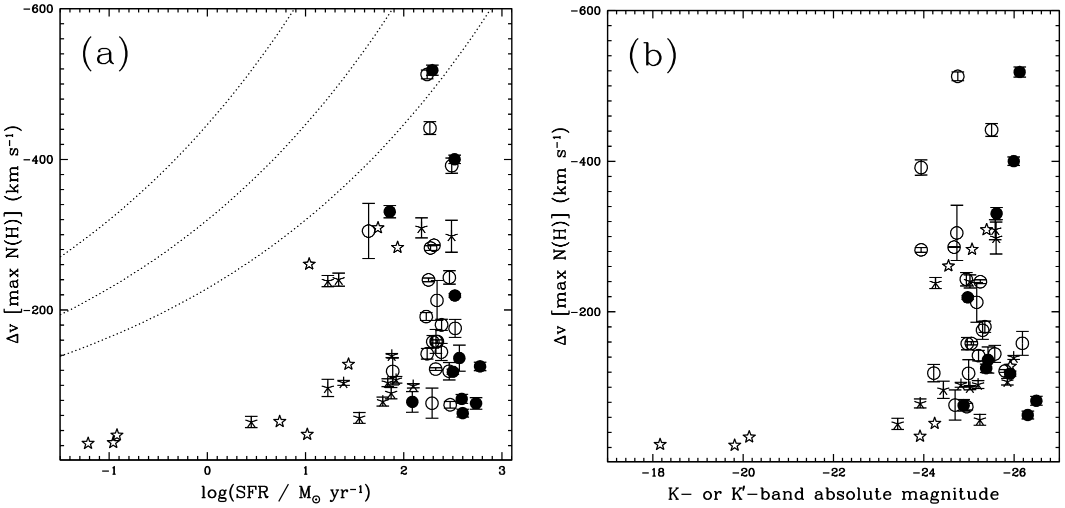

Figure 3.20: Velocity of the highest column density gas vs. (a) star formation rate and (b) $M_{K(')}$. This velocity is apparently uncorrelated with either of these quantities in our data, though declines at the lowest star formation rates. There is evidence for an upper envelope in plot (a), consistent with the signicantly different distributions of Δv[max. N(H)] in IRGs and ULIRGs. The symbol shapes are as in Figure 3.19. The diagnoal dotted lines are theoretical curves from Shu et al. (2003), for different values of the interstellar medium parameter K (§3.5.3).

3.4.4 Gas escape fraction

In our preliminary report (Rupke et al. 2002), we tentatively claimed that the fraction of gas in ULIRG superwinds that escapes the galaxy is high, perhaps up to 40 − 50%. We computed this value by estimating the circular velocity in each galaxy using a rotation curve, a velocity dispersion, or emission- and absorption-line widths, and then computing the escape velocity using a singular isothermal sphere. This estimate of v_{esc} is quite difficult, largely due to the difficulty in measuring v_c and our lack of knowledge of the large scale mass distribution and ambient environment. Furthermore, two of the galaxies which dominated this calculation of v_{esc} were Seyfert 2s, whose winds are not necessarily starburst-driven. (We discuss these galaxies further in Chapter 4.)

In analyzing our complete sample of starburst-dominated galaxies, we have chosen not to make an estimate of gas escape fraction using measurements of v_c for individual galaxies, but instead we have assumed a constant value for the whole sample and a singular isothermal sphere with $r_{max}/r = 10 - 100$. Recall from §3.3.1 that the 'maximum' velocities we measure in these galaxies are all less than 600 km s^{-1} (except for a single galaxy). Significantly, these velocities are less than the escape velocity of a galaxy with $v_c = 300$ km s^{-1}.

Our procedure to calculate f_{esc} is as follows: (a) for each galaxy, compute the mass outflow rate of gas that has a velocity above v_{esc}; (b) set $f_{esc} = 0$ if $f_{esc} <$ 1%; (c) sum dM/dt and dM/dt_{esc} over all galaxies; and (d) divide dM/dt^{total}_{esc} by dM/dt^{total}.

Assuming $v_c = 300$ km s^{-1} and ignoring halo drag (Silich & Tenorio-Tagle 2001) or acceleration of the wind, we compute that less than 3% of the material in these winds will escape the galaxy and enter the IGM. For a constant $v_c = 200$ km s^{-1}, this fraction becomes significantly non-zero, ranging from 4% for the control sample (based on 5 galaxies with $f_{esc} > 0.01$) to 18% for the low-z ULIRGs (based on 15 galaxies). Barring significant acceleration, we tentatively revise our initial estimate from Rupke et al. (2002) downward and propose that at most $10 - 20\%$ of the detected neutral gas in these winds will escape into the IGM. The hot, freely-expanding wind that drives the entrained, neutral material (and carries the majority of the metals; Martin et al. 2002) is even more likely to escape. Furthermore, if we correct for projection effects in the velocities, this escape fraction is likely to increase.

The maximum velocities that we measure are *quite close to* plausible values for v_{esc}. Is this coincidental, or rather suggestive of further physics? We would argue that there is (or was) material of higher velocites, as is seen in local starburst-driven superwinds like that in NGC 3079 at velocities of up to 1500 km s^{-1} (Veilleux et al. 1994; Cecil et al. 2001). Assuming that this gas moves radially (though it may form vortices; see Cecil et al. 2001), it will expand more quickly than the low-velocity gas and dissipate as it reaches large radius, giving it a low cross-section in the line-of-sight and making it difficult to detect using absorption-line probes. It may be that the single galaxy in our sample with $\Delta v_{max} > 1000$ km s^{-1} is an example of this, where the gas has not completely escaped to large radii. However, the Na I D feature in this galaxy is quite broad and deep, and for this reason not obviously consistent with this interpretation.

3.4.5 Morphology

The morphologies of the galaxies in our sample generally show the typical signs of interactions with a companion galaxy. Several of the IRGs possess nearby companions of small to moderate size, some of which appear on our spectroscopic slits at similar redshifts or appear connected to the infrared source by a tidal feature. Probable tidal features are visible at low surface brightness levels in the red DSS2 images of several galaxies. Finally, a number of galaxies are clearly in later stages of merging, with obviously disturbed stellar morphologies and/or long tidal tails.

As mentioned previously, the ULIRGs are in the late stages of major mergers, with long tidal tails and generally disturbed morphologies (as seen in the R- and K'-band images of Kim et al. 2002). Unfortunately, we do not have well-resolved images for the most distant LIRGs and ULIRGs in our sample, but it is a safe guess that they are involved in similar interactions. Some exhibit possible signs of tidal features or multiple nuclei in the ground-based K-band images of Stanford et al. (2000), and we have spectra of both nuclei in one double-nucleus object, F07449+3350, that show complex kinematics akin to an interaction.

In the IRG subsample, most galaxies exhibit a regular stellar disk, and we observe marginally significant correlations between the outflow detection rate and the ellipticity of the galaxy (which translates into inclination for an intrinsically thin, circular disk). We find that we are very likely to observe winds in galaxies with low inclination (i.e., almost face-on; 8 outflows in 15 galaxies) but not at all likely at high inclination (2 out of 12 galaxies). Given that superwinds in nearby disk galaxies align with the minor axis of the galaxy, one would expect to observe more winds in face-on galaxies than in edge-on galaxies, since the disk would prevent the wind from being observed in absorption in purely edge-on systems.

For any ellipticity, we are also unlikely to observe winds in galaxies when the spectroscopic slit is oriented within 15 degrees of the major axis (3 out of 14 galaxies). This may suggest that these winds are easiest to observe with this technique when the slit is oriented near the minor axis (which is again consistent with the minor-axis wind model). However, we have low statistics for the case of high inclination and slit away from the major axis, so this conclusion is not firm (and it may simply be that face-on galaxies are required and the slit position angle is irrelevant).

There are also several IRGs in which there is unambiguous evidence of a strong galaxy-galaxy interaction (based on the presence of long, bright tidal tails or obviously irregular stellar morphology). In every case except perhaps one (6 of 7 galaxies), we observe evidence of winds. This is interesting in light of the fact that ULIRGs also exhibit a high wind detection frequency, which suggests that interacting galaxies are the most likely to possess massive starburst-driven winds. Furthermore, these galaxies are brighter (on average) than the other galaxies in our IRG subsample. Given that the degree of starburst activity (and infrared luminosity) appears to be related to strength or stage of interaction, this is unsurprising.

3.4.6 Comparison with emission lines

Resolved outflows in the local universe present distinctive properties when observed in optical line emission, including limb-brightened bipolar structures and line-splitting in velocity space. The surface brightness contrast between these winds and the background galaxy is small, and it is difficult to see emission-line evidence of small superbubbles in distant galaxies. However, the massive, highly extended emission-line nebulae in nearby LIRGs and ULIRGs such as NGC 6240 and Arp 220 (Heckman, Armus, & Miley 1987; Armus, Heckman, & Miley 1990; Veilleux et al. 2003; Gerssen et al. 2004) may be powered (to an unknown degree) by starburst-driven outflows. We thus might expect to observe either morphological or kinematic evidence of winds in these galaxies in optical line emission.

Correlations with 1-dimensional emission lines

In Figures 3.5 – 3.7, we show one-dimensional plots of the [N II]$\lambda\lambda6548, 6583$ and [O III]$\lambda5007$ lines. In each case, we fitted and subtracted the continuum using a low-order polynomial. The extraction apertures for these data are the same as those for the Na I D spectra, which cover most of the visible continuum. Thus, some of the very extended emission may not be present in these spectra (and could in a few cases remove some light from the nuclear emission due to the sky-subtraction algorithm, though we tried to avoid this).

There is little information in the 1-dimensional spectra that is not also clearly displayed in the 2-d spectra. As we discuss below, there are clear cases where Na I D falls at the same velocity as an emission-line feature. There are three examples of strong blue wings in the emission lines, which are most easily visible in the 1-d spectra. In each case, there is also blueshifted Na I D. Two of these galaxies (F09539+0857 and F10378+1108) exhibit deep, broad absorption lines, while the third (F08143+3134, at a higher redshift) has a shallow, relatively narrow, absorption line. These blue emission-line wings may represent an ionized phase of the outflow.

2-dimensional emission-line morphology

For each galaxy in our sample, we display the 2-dimensional emission line morphology in Figures 3.5 – 3.7. There is a surprising amount of detailed structure in this data. Rather than discuss each object individually, we highlight some trends here and in the Discussion (§3.5.1).

A substantial number of IRGs show simple rotation. Others exhibit irregular extended emission, and in a few cases we observe no spatially resolved structures. Rotation curves of varying maximum projected velocity exist in approximately 22 of the IRGs. In 10 of these cases blueshifted Na I D is near in velocity space to the projected rotational velocity of the galaxy, but this is the case with redshifted Na I D in only 3 cases. Extended rotation curves are clearly visible in both interstellar emission and in Na I D absorption in a number of galaxies, and the sense of rotation in absorption and emission matches in each case. Finally, there are seven galaxies in which interesting extended structures are visible; all of these (except one) exhibit clear signs of an interaction, and five show blueshifted Na I D.

A notable case is NGC 6240. Our spectrum is near the minor axis of the large-scale stellar disk of this galaxy, and it shows irregular gradients in velocity, velocity dispersion, and line ratio along the slit. A number of these features can be matched with the structures observed in the emission-line and excitation maps of Veilleux et al. (2003). The Na I D feature shows gradients which match in space and velocity those of the narrow emission-line arm east of the nucleus (up to the point at which the continuum ends). Note also that there is emission-line splitting on both sides of the nucleus. NGC 1614 possesses long stellar tidal tails, and the Na I D absorption that we observe in this galaxy matches the emission-line velocities at the base and the tip of the southwest tidal tail, respectively. Finally, F02437+2122 has a faint, blueshifted emission-line blob located ~ 15 kpc above its minor axis that, assuming it is seen in [N II]λ6583, roughly matches the Na I D absorption in velocity. If this line identification is correct, this blob has a high [N II]/Hα flux ratio, indicating possible ionization by shocks.

Emission-line structures similar to rotation curves are also visible in a number of ULIRGs. In the low-z subsample, $7-9$ galaxies exhibit such structures, plus $1-4$ more in the high-z ULIRGs. In a few cases one lobe in this structure is significantly brighter than the other. In approximately all of the secure cases of rotation-like structures, there is evidence of Na I D absorption at or near the blue emission peak (see §3.5.1).

In the ULIRGs, irregular extended emission-line structures are more common than rotation-like structures, as might be expected from the large emission-line nebulae observed in bright, nearby LIRGs and ULIRGs (Heckman et al. 1987; Armus et al. 1990). We see irregular structures in ~ 16 galaxies, and they extend over scales of $5-25$ kpc. They generally exhibit flux ratios of [N II]/H$\alpha < 1$ and velocities within a few hundred km s^{-1} of systemic. These structures show a variety of shapes and sizes in position-velocity space, and are not typically indicative of simple rotation (though they may be in some cases). Correlations in velocity space between extended emission and Na I D absorption exist in several ($7-8$ galaxies); whether these correlations are coincidental or not is difficult to determine, however. Finally, in those galaxies where the clearest rotation-like structures are visible, 7 of 8 show blueshifted Na I D absorption near the velocity at which the rotation curve flattens out (see §3.5.1).

Notable cases of irregular, extended emission in ULIRGs include F08143+3134. In this galaxy, Na I D is blueshifted ~ 400 km s^{-1} from systemic, as is faint emission visible in [O III] to the north. This low signal-to-noise emission is not clearly visible in Hα or [N II], so it is conceivable (though by no means certain) that this gas is photoionized by a hidden AGN. Other interesting cases are F01462+0014, which has line-splitting north of the nucleus and other extended emission; F07449+3350, which is a double-nucleus object and has a complex emission-line structure as well as a faint emission-line blob 15 kpc from the west nucleus; F09039+0503, which has a redshifted Na I D component along with extended emission at the same velocity; F09539+0857, which has a broad plume of emission to the north of the galaxy; F10190+1322, another double-nucleus object with complex emission-line structure; and F16576+3553, which has very broad emission lobes on either side of the nucleus, one blueshifted and the other redshifted.

We also observe bright H II-region-like emission-line regions away from the systemic velocity of the galaxy in several cases. These may be bright, young star clusters that fall in our line-of-sight.

3.4.7 Comparison to H I spectra

Given the high column densities of neutral H I that we infer using the Na I D feature (10^{21-22} cm^{-2}), we might expect to also observe this gas directly in emission or absorption using the H I 21 cm line. Since such data exist for many of the objects in our control sample, we can search for direct evidence of neutral H I.

The kinematics of the H I in F10565+2448 are the most interesting. Our systemic velocity agrees with the narrow, deep absorption trough in the H I 21 cm line at ~ 12900 km s^{-1} (Mirabel & Sanders 1988). There may be a broad, blueshifted component in H I that extends to roughly the same velocities as seen in Na I D. There is also redshifted H I in emission at $\sim$ 13100 km s^{-1}. If the Na I D and possible broad H I absorption represent a bubble expanding in our direction along the line of sight, the redshifted H I emission line could indicate a counter-bubble that is expanding away from us.

Three other objects in our sample (F01417+1651, F02512+1446:S, and F03359+1523) also show H I absorption in Mirabel & Sanders (1988). The S/N of the H I spectra for these objects are comparable to that of $F10565 + 2448$, but the absorption is at systemic, and there are no obvious broad, blueshifted components.

3.5 DISCUSSION

3.5.1 Alternative explanations

The zeroth order interpretation of the blueshifted absorption lines in these galaxies is that they are produced by starburst-driven outflows. Given the interesting features noted in the emission-line spectra in §3.4.6, we can hazard other explanations for the absorption in some galaxies. However, these alternative explanations should produce velocity distributions that are symmetric about $\Delta v = 0$ km s^{-1}, for reasons we discuss below. Thus, the maximum number of blueshifted components attributable to other phenomena is a mirror reflection of the distribution of red components, and is therefore not significant.

Gas in rotation

We observe emission-line evidence of rotation in most of our IRGs and in a sizable fraction of ULIRGs, suggesting that there are ordered gas disks in most of these systems. However, we only observe the extended faint arms of the rotation curve in a subset of these cases, and sometimes the tilt of the rotation curve is quite small. In only a few cases is rotation also observed in Na I D.

In a large number of galaxies which have rotation curves visible in their spectra (~ 17 galaxies total), we see blueshifted Na I D that is at or near the blue rotation arm of the galaxy in velocity space. Rarely (in only ~ 3 cases) do we observe the Na I D near the red rotation arm. Since there is no reason for this asymmetry in a rotating disk scenario, we conclude that this gas is in general *not* in simple rotation.

Tidal debris

The red (and some of the blue) components that we observe in ULIRGs may be tidal debris, gas stirred up by vigorous interactions. The simulations of Barnes & Hernquist (1991) show that much of the gas in an equal-mass prograde merger flows suddenly to a compact region at the merger center, and large tidal arms are spun out. However, much of the extended tidal debris falls back to the merger center over Gyr time scales; in NGC 7252 radial velocities of up to ± 200 km s^{-1} are observed due to velocity gradients along tidal tails, the redshifted velocities representing gas falling back to the disk (Hibbard & Mihos 1995). A caveat is that from examination of the velocity distribution of tidal material in the simulations of Hibbard & Mihos (1995), one might typically expect a narrow velocity width from a tidal tail in projection, while we observe mostly broad profiles.

There are a few notable illustrative cases in both the IRG and ULIRG subsamples, but none are clear-cut examples. We discuss above an emission- and absorption-line feature to the east of the disk of NGC 6240; this feature lies atop a stellar structure that appears tidal in origin. However, the evidence is only circumstantial; this galaxy also has an emission-line superbubble to the east of the galaxy, and it is conceivable that the Na I D absorption and line emission to the west of the galaxy trace a counterbubble. F09039+0503 possesses a narrow (FWHM ~ 30 km s^{-1}; see Chapter 5) component that is redshifted by $180 - 190$ km s^{-1} with respect to systemic. The velocity is comparable to those measured for tidal features in NGC 7252 (Hibbard & Mihos 1995), and its small width is suggestive of a compact feature such as a tidal tail.

Multiple nuclei and overlapping disks

We observe evidence of overlapping disks in several of the double-nucleus galaxies which are present in both our IRG and ULIRG subsamples. In five of these galaxies, there is a redshifted absorbing component in the spectrum of one nucleus that is within 40 km s^{-1} of the redshift of the other nucleus; the nuclei with these components are F01417+1651:S, F02411−0353:NE, F16333+4630:W, F16474+3430:N, and F23234+0946:E. A sixth galaxy, F08354+2555, contains Na I D that is blueshifted from the H I velocity but is coincident with the emission-line peak, which also corresponds to that of a compact stellar object $5 - 10''$ S of the nucleus; the Na I D may be associated with either the galaxy nucleus or the south object. Finally, F10190+1322:E has redshifted absorption at +322 km s^{-1} with respect to systemic, which is 107 km s^{-1} higher than the velocity of the west nucleus. However, the portion of the western disk that overlaps the slit over the eastern nucleus matches the redshifted absorption in the eastern nucleus quite well in velocity space (Murphy et al. 2001).

This suggests that some of the components in our velocity distribution are due to the projection of gas disks along the line of sight. Notably, however, the seven galaxies in which these nuclei reside still contain three cases of unambiguous, high-velocity blueshifted absorption. In our analysis, we have removed the components that appear to be due to these overlapping disks, as we find this hypothesis more compelling than the outflow one for this small subset of components.

Merger-induced winds

Recently, Cox et al. (2004) have hypothesized that the shocks produced as gas funnels to the center of the merger of two equal-mass galaxies can produce outflows of hot gas. These shocks heat a large amount of gas to 10^{6-7} K, which, in analogy to a starburst-driven superwind, expands radially outward at speeds $\gtrsim 200$ km s^{-1}. This gas could potentially entrain cold gas clouds and evolve much as a starburst-driven superwind. However, the energy injection region may be on larger scales (several kpc vs. $\lesssim 1$ kpc for a superwind). Further exploration of this idea is warranted, but it is currently indistinguishable in our data from the superwind hypothesis.

3.5.2 Frequency of occurrence and global covering fraction

The detection rate of outflows D is a function of both the actual frequency of occurrence of winds F and the global covering fraction C_Ω of these winds. The latter is substantially less than unity in local galaxies ($C_\Omega \sim 0.4$ on average; Heckman et al. 1990), so we might suspect our detection rate is actually a lower limit to the actual rate of occurrence of outflows.

Suppose that all galaxies contain winds (i.e. $F = 1$). Then, the detection rate directly measures the global covering fraction of winds, and we have $C_\Omega = D$. In this scenario, C_Ω in ULIRGs is roughly twice that in IRGs. Now, suppose that $D = F$, or that our detection rate is the actual frequency of occurrence. In this case, $C_\Omega = 1$ and F in ULIRGs is roughly twice that in IRGs.

In reality, the case is likely to be somewhere in between these, such that $D < F < 1$ and $D < C_\Omega < 1$. Furthemore, we have ignored local clumping in the outflow; in starbursts, this probably will not affect the detection rate due to the relatively large background continuum sources, but in AGN (where the continuum source is point-like) it must be factored in. Local clumping also affects our definition of C_Ω; since winds in starbursts tend to be continuous structures, we assume that C_Ω ignores local clumping and describes the overall structure of the wind. Our measurements of C_f may also provide some information about F and C_Ω; they likely contain a contribution from both local and global covering fractions.

In IRGs, the detection rate of winds is suspiciously close to the average value of C_Ω as measured in local galaxies, ~ 0.4. It is also quite close to the average value of C_f in our sample, $0.35 - 0.40$. This result may suggest that winds occur in all IRGs, and that the average C_f describes the mean global covering fraction of outflows. As we showed above, however, $C_\Omega \sim 0.4$ cannot apply to ULIRGs, since a lower limit to C_Ω is set by D. Thus, C_f in ULIRGs must be more indicative of a local covering factor (or else include more contribution from a background source extended beyond the outflow).

3.5.3 Comparison with theory

A substantial number of numerical simulations of superwinds have been performed over the years (e.g., Suchkov et al. 1994; Strickland & Stevens 2000). These models do not typically make predictions about values for dM/dt in the cold gas. They do show that there are large quantities of cold gas in the superwind, distributed both in filaments and clouds entrained from the disk and as a swept-up shell surrounding the wind (which is disrupted by Rayleigh-Taylor instabilities at 'blowout'). Uncertainties in these models still exist because they treat the ISM as a continuous medium and do not include the microphysics of wind/cloud interactions (such as conduction and ablation leading to mass-loading of the wind fluid and cloud destruction, small-scale hydrodynamic instabilities, and radiative cooling). New simulations are underway (Sutherland & Bicknell 2004, in preparation) incorporating a fractal gas distribution, which will better treat the physics of entrainment and thus the cold gas mass in the wind. This should in turn lead to accurate predictions of mass outflow rates.

Silk (2003) argues that the mass outflow rate may be proportional to the porosity of the ISM. The porosity Q is related to the filling factor of hot gas by $f_{hot} \equiv 1 - e^{-Q}$. In this prescription, $dM/dt = \beta f_{hot} \times$ SFR, where β represents the amount of entrainment and is approximately equal to unity. Assuming a constant value of β, the mass entrainment efficiency is then directly governed by the porosity: $\eta \sim 0.5 - 1$ for $Q \gtrsim 1$, and η is lower for lower porosities. This applies to our sample as long as the porosity also decreases with an increase in SFR.

A more detailed analytical model that incorporates the supernova physics of McKee & Ostriker (1977) was recently developed (Shu, Mo, & Mao 2003). This model makes very specific predictions of velocities and mass outflow rates as a function of both local and global physical parameters. For a spherical system, they find that $dM/dt \sim \mathrm{SFR}^{0.71} K^{-0.29}$, where K represents local properties of the ISM in the galaxy. This is inconsistent with our finding that dM/dt is independent of SFR. In Figure 3.17, we plot dM/dt from Shu et al. (2003) for different values of K; these theoretical predictions appear to overestimate dM/dt at high star formation rates.

Shu et al. (2003) also discuss a model for winds emerging from a star forming disk. In this model they incorporate a ‘critical radius’ beyond which the disk does not contribute to the outflow, or equivalently a critical density in the (exponential) disk. The equation for the mass outflow rate in this model is

$$dM/dt = 98\left(\frac{M_g}{10^9 M_\odot}\right)\left(\frac{\mu_0}{M_\odot \mathrm{pc}^-2}\right)^{-0.3}\left(\frac{\sigma_g}{\mathrm{km\ s}^{-1}}\right)^{0.58} \times \left(\frac{M_{ps}}{125 M_\odot}\right)^{-0.71} K^{-0.29} F(\mu_0, \mu_{cr})\ M_\odot\ \mathrm{yr}^{-1}, \tag{3.6}$$

where M_g is the cold gas mass in the disk, μ_0 and μ_{cr} are the central and critical gas mass surface densities, σ_g is the linewidth of gas clouds, M_{ps} is the star formation rate divided by the supernova rate, K is a function of local ISM physics, and $F(\mu_0, \mu_{cr})$ is the fractional area of the disk contributing to the outflow. K in turn depends on the thermal conductivity relative to the classical value, ϕ_k, and the smallest cloud size, a_l. A similar equation can be derived for the SFR, which depends only on M_g and μ_0. These equations assume a porosity of unity.

Assuming $\sigma_g = 10$ km s^{-1}(i.e. thermal cloud support), $M_{ps} = 125\ M_\odot$ (as for a Salpeter mass function with limits of 0.1 and 50 $M_\odot$), and $K = 1$, we can follow theoretical values for dM/dt, SFR, and the resulting η as a function of central gas mass surface density μ_0. Figure 3.21 shows these curves along with the ranges of dM/dt, SFR, and η measured from our data. We also estimated central gas mass surface densities for LIRGs and ULIRGs from high-resolution CO observations (Sanders et al. 1988; Scoville et al. 1989; Downes & Solomon 1998; Sakamoto et al. 1999), and these ranges are shown in the figures.

Comparing the intersections of the observed quantities to the theoretical curves, we then scale the curves to match the measured mass outflow rate and star formation rate ranges from our data with the proper range of μ_0. The required gas masses M_g ($10^{9.2}\ M_\odot$ for LIRGs and $10^{9.7}\ M_\odot$ for ULIRGs) are roughly consistent with interferometer data from the above authors but lower than single-dish masses from Sanders et al. (1991) and Solomon et al. (1997) ($\sim 10^{10}\ M_\odot$ for LIRGs and $\sim$

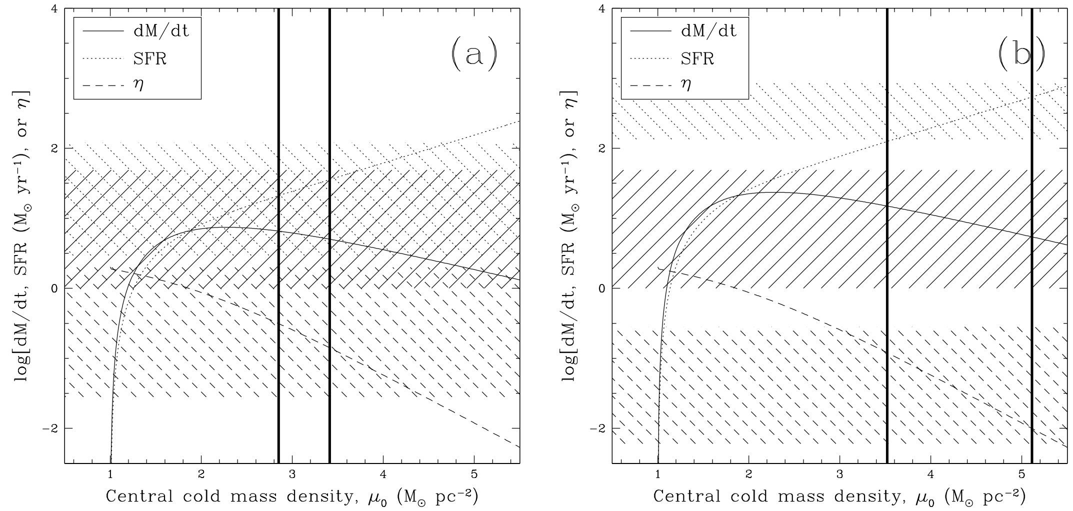

Figure 3.21: Model predictions from Shu et al. (2003) for dM/dt, SFR, and η as a function of central gas mass density μ_0; plots for LIRGs and ULIRGs are in panels (a) and (b), respectively. We assume that the cloud linewidth $\sigma_g = 10$ km s^{-1}, the thermal conductivity relative to the classical value $\phi_k = 0.01$, and that the smallest cloud size $a_l = 1$ pc. The bracketed regions on the vertical axes are determined by the limits of our data, and on the horizontal axes from molecular gas mass densities (Sanders et al. 1988; Scoville et al. 1989; Downes & Solomon 1998; Sakamoto et al. 1999). The gas masses M_g required to match the data and theoretical curves ($10^{9.2}$ $M_\odot$ for LIRGs and $10^{9.7}$ $M_\odot$ for ULIRGs) are roughly consistent with interferometer data from these same authors but lower than single-dish masses from Sanders et al. (1991) and Solomon et al. (1997) ($\sim 10^{10}$ $M_\odot$ for LIRGs and $\sim 10^{10.0-10.5}$ $M_\odot$ for ULIRGs).

$10^{10.0-10.5}$ $M_\odot$ for ULIRGs). The agreement here is quite good, suggesting that the weak dependence of mass outflow rate on central gas mass surface density in this model is correct.

We also perform the same test on the theoretical runs of velocity vs. μ_0 from Shu et al. (2003), but these curves match our data poorly; see Figure 3.22. Here we plot the ranges (median $\pm 1\sigma$) of Δv_{max} for U/LIRGs, and we find that the theoretical curves overpredict the velocities by an amount that increases with μ_0.

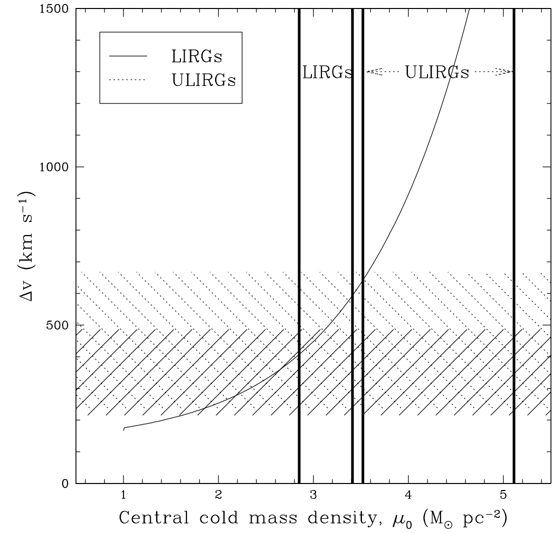

Figure 3.22: Model predictions from Shu et al. (2003) for Δv_{max} as a function of central gas mass density μ_0, compared to the ranges from our data. The models overpredict Δv_{max} for a given value of μ_0.

3.5.4 Low values of η in ULIRGs

It is clear from our data that the starbursts in ULIRGs are much less efficient in powering massive superwinds (by an order of magnitude) than those in IRGs. This discrepancy shows up as values of η in ULIRGs that are an order-of-magnitude lower than those in less luminous galaxies. What is the cause of this difference?

One obvious possibility is the large concentrations of molecular gas in these galaxies. The amount of cold gas increases roughly in proportion to infrared luminosity (Sanders et al. 1991). Furthermore, the central gas mass surface densities in ULIRGs are larger by up to 3 orders of magnitude than those in LIRGs (Sanders et al. 1988; Scoville et al. 1989; Downes & Solomon 1998; Sakamoto et al. 1999). For instance, the central gas densities in the dual nuclear disks of Arp 220 are $\sim 10^6$ $M_\odot$ pc^{-2}, vs. several hundred to a few thousand $M_\odot$ pc^{-2} for less luminous galaxies (Sanders et al. 1988; Downes & Solomon 1998; Sakamoto et al. 1999).

This cold, dense gas may take away a substantial amount of energy from the hot wind fluid by transfer of bulk kinetic energy and creation of turbulence. Furthermore, radiative losses, which scale roughly as the square of the gas density, will be highest in this gas. This will in turn reduce the wind's radius of influence and its ability to entrain and destroy gas clouds.

3.5.5 Superwinds in mergers

It has been postulated that superwinds play a role in the evolution of gas-rich mergers. ULIRGs may evolve into quasars when a buried AGN turns on and breaks the obscuring screen of dust (Sanders et al. 1988; Veilleux et al. 2002). Given their detection rate in these galaxies, outflows could easily play a role in redistributing dust and gas, increasing the escape fraction of continuum light. If most ULIRGs do evolve into ellipticals, this gas redistribution may also destroy the central gas density spikes predicted in numerical simulations of mergers (Mihos & Hernquist 1994). If left in place, these spikes would evolve into sharp upturns in the stellar surface brightness distribution in evolved ellipticals at small radii; breaks like this are not typical of elliptical surface brightness profiles (Hibbard & Yun 1999).

Many of the best-studied and clearest examples of superwinds in the local universe are found in starbursting disk galaxies with $L_{\rm IR}< 10^{11}$ $L_{\odot}$. Given that many LIRGs, and most ULIRGs, are gas-rich mergers in which the morphology and kinematics of the galaxy are highly disturbed (e.g., Veilleux et al. 2002; Arribas et al. 2004), one might suppose that the physical picture of a symmetric, bipolar superwind along the galaxy's minor axis may not apply. However, there is evidence from observations of resolved, infrared-luminous merging galaxies that these galaxies produce ordered superwind structures analogous to those in quiescent disk galaxies. Examples include (in order of increasing $L_{\rm IR}$): NGC 520 (Hibbard & van Gorkom 1996; Hibbard, Vacca, & Yun 2000), Arp 299 (Heckman et al. 1999; Hibbard et al.

2000), NGC 6240 (Heckman et al. 1987; Veilleux et al. 2003; Gerssen et al. 2004), and Arp 220 (Heckman et al. 1987, 1996; Hibbard et al. 2000; Arribas et al. 2001; McDowell et al. 2003). These galaxies all show spectacular signs of merging, including tidal tails and bridges and multiple nuclei. NGC 520, Arp 299, and Arp 220 possess large-scale rotating H I disks, and the H I data for these galaxies show gaps along the minor axis and H I-poor regions in the stellar tidal tails; this gas may have been evacuated by a superwind (Hibbard et al. 2000). Other evidence for superwinds comes from emission-line and X-ray data, which show minor-axis extensions, bubble-like and bow shock structures, kinematic broadening and/or line-splitting, shock-like emission line ratios, and/or tight correlations between optical and X-ray emitting filaments. Most recently, diffuse and extended X-ray-emitting gas has been discovered in perhaps the best-studied merger, the Antennae; this gas may have a superwind origin (Fabbiano et al. 2004).

3.5.6 Redshift evolution

One of the original purposes of this study was to explore the properties of superwinds deeper into redshift space. Given that the number density of ULIRGs evolves strongly with redshift and that there are many more earlier in the universe, we would expect that winds from ULIRGs would have a much stronger impact on the intergalactic medium and galaxy evolution at higher redshifts (if at all). However, this assumes that the properties of winds in ULIRGs do not change with z.

We have partially accomplished this goal by observing a substantial number of galaxies at redshifts up to $z = 0.5$. We do observe differences between our high-z and low-z subsamples. Notably, winds are less frequently observed in the high-z ULIRGs (with a detection rate of $46 \pm 14\%$ vs. $77 \pm 8\%$ for the low-z ULIRGs), and are less efficiently powered by the starburst at $> 95\%$ confidence (with a lower median η than the low-z ULIRGs by a factor of 2). However, the high-z galaxies have higher star formation rates (or equivalently, luminosities) than the low-z ULIRGs, on average (389 $M_\odot$ yr^{-1} and 225 $M_\odot$ yr^{-1}, respectively). This is a selection effect, since the most distant ULIRGs observed by IRAS are necessarily those with the highest intrinsic luminosities.

We suggest that the differences between the low- and high-z subsamples are primarily a result of the variation of superwind properties with star formation rate, rather than redshift evolution. In other words, the average reheating efficiency in our high-z ULIRGs is lower simply because it follows a trend of η vs. SFR that is largely independent of redshift.

The change in the frequency of wind detection is less certainly attributable to SFR variations. It is quite possible that the wind frequency drops above a certain star formation rate. Other factors may also play a role; for instance, more extended continuum light in a distant galaxy may leak into the slit and wash out the Na I D absorption line. The high-z spectra generally have lower S/N than those of nearer galaxies, as well, diminishing our ability to detect Na I D.

3.6 CONCLUSIONS

We have shown in this chapter that the properties of superwinds in infrared-selected starbursting galaxies are surprisingly constant across two orders of magnitude of star formation rate, specifically in velocity and mass outflow rate. However, their rate of detection and 'mass entrainment efficiency' increase and decrease, respectively, with star formation rate. (These trends are also seen as a function of K-band luminosity.) The velocity of the highest column density gas in these galaxies has an upper envelope that increases with SFR.

We find that superwinds are common in infrared-luminous starburst galaxies, with detection rates of 45% and 65% for our IRG ($\langle L_{\rm IR}\rangle = 10^{11.36} L_\odot$) subsample and ULIRGs, respectively. These detection rates are lower limits to the actual frequency of occurrence of outflows in these galaxies and also to the mean global covering fraction of the outflows. Thus, either winds in ULIRGs are more common than winds in IRGs or they have a higher angular covering fraction.

At the highest star formation rates, the detection rate in ULIRGs may decrease, as evidenced by a smaller detection rate in the high-z subsample than in the low-z subsample (46% vs. 77%), since the high-z subsample also has a higher median star formation rate (389 $M_\odot$ yr^{-1}) than in the low-z subsample (225 $M_\odot$ yr^{-1}). However, we cannot disentangle this potential luminosity dependence from redshift evolution or observational effects.

The maximum velocities for these winds range from 150 to 600 km s^{-1}; median values for Δv_{max} are $300 - 420$ km s^{-1}. If we make a statistical correction for projection effects, a typical Δv_{max} is in reality close to the maximum value that we measure ($500 - 600$ km s^{-1}). We also measure the velocity of the gas with the maximum column density in each galaxy; the 1σ ranges for this quantity in the IRGs and low-z ULIRGs are $60 - 300$ km s^{-1}. Our measured velocities are comparable to those found using the same technique by Heckman et al. (2000), but are larger than the deprojected velocities measured in warm, ionized gas in edge-on starbursts (Lehnert & Heckman 1995, 1996). The projected velocities in LBGs, ~ 300 km s^{-1} on average (Adelberger et al. 2003; Shapley et al. 2003), are higher than the values we measure for $\Delta v[\max N(\mathrm{H})]$ but are comparable to the maximum velocities we measure.

One consequence of these high velocities is that the fraction of gas in these outflows that escapes the galaxy is not insignificant. With reasonable assumptions about the gravitational potential (and ignoring halo drag or IGM pressure; Silich & Tenorio-Tagle 2001), we estimate a global escape fraction of neutral gas between a few percent and $\sim 20\%$. This fraction is even higher if projection effects are accounted for.

We show that LINERs have higher median values of Δv_{max} (by $50-100$ km s^{-1}) than H II galaxies. Thus, the spectral classification for these systems, based on line ratios, may simply reflect high-velocity vs. low-velocity shocks.

One of the most significant results of our analysis is that the average 'mass entrainment efficiency' of cold gas in ULIRGs is significantly less than unity, on the order of a few percent of the star formation rate. We attribute this decrease in efficiency at high star formation rates to large reservoirs of molecular and ambient gas that trap the mechanical energy of the wind (or the supernovae that power it) and dissipate this energy as radiation or turbulence. Superwind prescriptions in galaxy formation simulations typically assume η is generically equal to one; our results show that this assumption is incorrect.

The lack of correlation that we observe in dM/dt and Δv as a function of star formation rate and $M_{K(\prime)}$ do not continue to very low star formation rates or low values of $M_{K(\prime)}$ (Schwartz & Martin 2004). At low star formation rates (up to four orders of magnitudes below the upper limit of our data), dM/dt and Δv_{max} decline and η flattens out with respect to galaxies with higher star formation rates. A more extensive comparison of our data set with lower-luminosity galaixes, which would require significantly more data on dwarf galaxies, is clearly imperative. More detailed modeling of dM/dt may be necessary for a proper comparison.

There is some evidence in the IRG subsample that outflows are preferentially found in near-face-on galaxies near the minor axis, and are also much more common in galaxies with major interactions. In LIRGs with major interactions and in ULIRGs, the emission-line spatial profiles often exhibit irregular kinematics and extended faint structures, and the outflowing gas is seen with significant frequency in loose kinematic correlation with these emission-line structures.

It is clear by comparing the absorption line data to emission lines and stellar morphology, as well as considering the fact that many of these galaxies are involved in major interactions, that some of the absorption is related to overlapping gas disks in a multiple system or to tidal debris. In a handful of cases we can demonstrate that these explanations are more likely than the outflow hypothesis. However, these phenomena should produce a roughly symmetric velocity distribution, and the one that we observe in our data is quite asymmetric. Thus, the number of outflowing components that we can attribute to these alternative explanations is a mirror image of the distribution of red components, and thus minor.

There is evidence for starburst-driven superwinds in local mergers such as NGC 6240. However, the complex kinematics in these galaxies make it sometimes difficult to distinguish starburst-driven winds from tidal motions directly produced by the interaction. In this sense, our data provides the most unambiguous evidence to date for outflows in these systems.

To interpret our data more completely, we require better knowledge of local merging systems. Hydrodynamic modelling of winds in evolving environments such as these would allow comparison of observational data to numerical models, as is possible in more quiescent systems. More sensitive observations to probe the morphology and kinematics of faint structures in these galaxies, and three-dimensional kinematic observations of multiple gas phases will also help to disentangle the motions of different components (e.g., tidal tails vs. expanding superbubbles) as has been done for Arp 220 (Arribas et al. 2001; McDowell et al. 2003; Colina et al. 2004).

Chapter 4

Outflows in AGN-dominated ULIRGs

4.1 INTRODUCTION

Large-scale outflows are not limited to galaxies that have nuclear starbursts. Galaxies that host an active galactic nucleus powered by a supermassive black hole, and which are optically classified as Seyferts by their emission line and continuum properties, often show similar evidence of winds. Radio continuum, optical emission-line, and X-ray emission probes reveal extended morphological structure and kinematic evidence for winds in many local edge-on Seyfert galaxies (Colbert et al. 1996a,b, 1998). The scale of these structures is comparable to that found in starburst galaxies (i.e., $r \gtrsim 1$ kpc). Furthermore, the X-ray emission in these galaxies is likely thermal, rather than non-thermal synchrotron as expected in a relatvistic plasma that could accompany an AGN jet or wind (Colbert et al. 1998).

However, these structures are not identical to those found in starbursts. For instance, the angles with respect to the galaxy minor axis of the optical line-emitting structures, which probe warm ($T \sim 10^4$ K) gas, are not generically small, but instead range from 0 to 70° (Colbert et al. 1996b). Yet the large-scale radio structures in Seyferts do not in general align with the nuclear 'linear' radio structure (Baum et al. 1993), which implies that the jets from the supermassive black hole accretion disk do not *directly* drive the winds (though they may indirectly by injecting energy into the ISM; e.g., Schiano 1985).

In this chapter, we discuss in detail the results of a study of a sample of luminous Seyferts at redshifts up to $z = 0.5$. As in Chapter 3, we look for outflows in the Na I D interstellar absorption line. We study the unique properties of these outflows, and compare them to those found in starbursts of comparable luminosity in Chapter 3.

4.2 SAMPLE

Our AGN-dominated sample consists of 23 ULIRGs and 3 LIRGs. Four of these ULIRGs have redshifts in the range $0.25 < z < 0.50$; the others have lower redshifts, as do the LIRGs. Most galaxies are taken from the IRAS 1 Jy survey (Kim & Sanders 1998), but a few come from the FIRST/FSC survey (Stanford et al. 2000) and one is in neither. As with the starburst-dominated 1 Jy ULIRGs, we have slightly increased the published infrared luminosities to correspond to the standard cosmology. Figure 4.1 shows the distributions of L_{IR} and z for these Seyferts, and compares these distributions to those of our starburst sample from Chapter 3. Table 4.1 lists the properties of the galaxies in our sample, as well as the relevant observation information.

We selected 1 Jy galaxies which have Seyfert 1 or 2 optical spectral classifications based on low-dispersion spectroscopy (Kim et al. 1998; Veilleux et al. 1999b). These

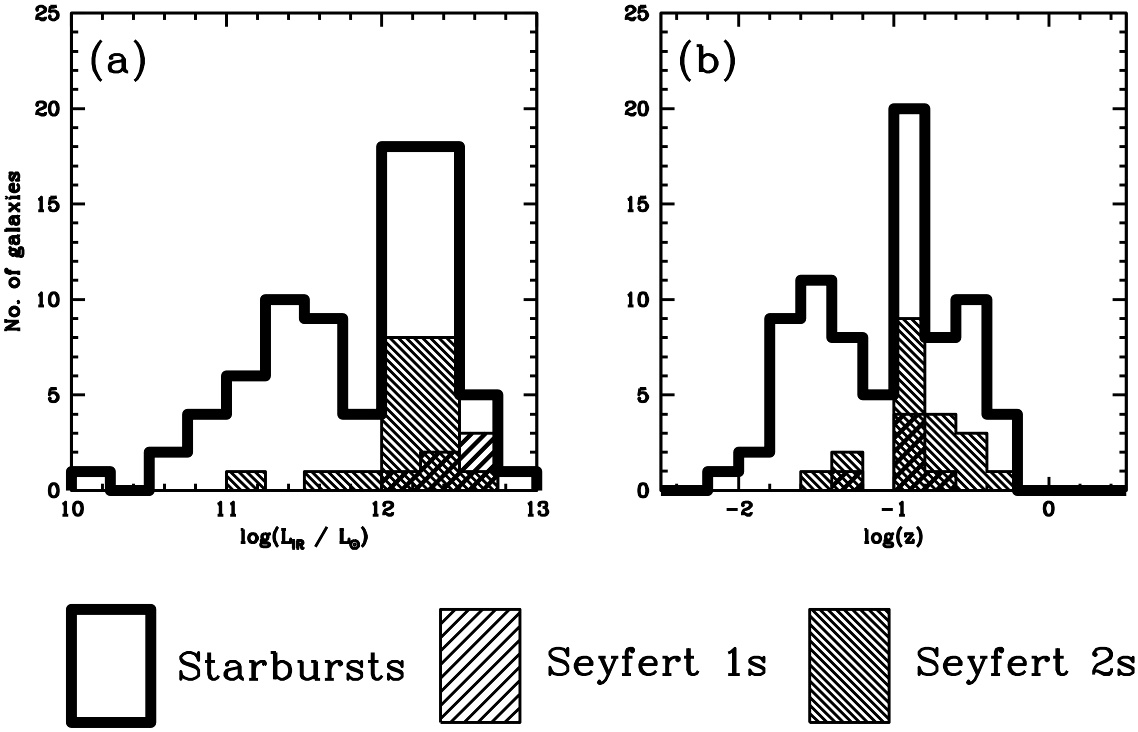

Figure 4.1: The distributions of (a) total infrared luminosity and (b) redshift for starbursts and AGN in our sample. Most of the Seyferts have $\log(L_{\rm IR}/L_{\odot}) > 12$ and $z > 0.1$.

galaxies have infrared luminosities that may be dominated by active galactic nuclei rather than star formation; however, whether or not the AGN dominates $L_{\rm IR}$ is uncertain, even in Seyferts (Genzel et al. 1998). Four of the galaxies in this subsample were observed in the mid-infrared with ISO and are classified as AGN (Lutz et al. 1999). Five to ten Seyfert 2 galaxies in our sample show evidence for an AGN in the near-infrared, either by the presence of broad lines in Paα or strong [Si VI] emission (Veilleux et al. 1999c).

We have classified the FIRST/FSC objects using our spectra. One of these, F08526+3720, possesses a faint broad-line region in Hα but not Hβ, suggesting it is a Seyfert 1.9 galaxy. We put it in the Seyfert 2 category despite the visible broad line. Another galaxy, F04210+0401, which is a radio galaxy with a jet (and which we observe with the slit aligned along the jet), also possesses a faint broad-line region in Hα, though it is classified as a Seyfert 2 in the literature. In this case, the broad-line emission may be scattered light from dust and gas in the radio jet. We treat it similarly.

A final special case is F05189−2524. This optical Seyfert 2 has an obscured broad-line region and has been shown to host a dominant AGN (Veilleux et al. 1999c). Furthermore, the strength of its 7.7 μm feature Laureijs et al. (2000) is identical to that of for Mrk 231 (Genzel et al. 1998), an optically-classified Seyfert 1. However, for the purposes of this paper we keep the optical spectral type of Seyfert 2.

In all, our sample contains six bona-fide Seyfert 1s, two Seyfert 1.9s with faint broad-line regions in Hα (which we label Seyfert 2s in this paper), and eighteen other Seyfert 2s.

Three of these Seyferts have double nuclei, and we also have one triple nucleus-system in the sample (F13443+0802). In each of these cases, one (but not both or all three) of the nuclei is a Seyfert 1 or 2, and we have derived spectral classes for the other nuclei when the [O III]λ5007 line is available. For simplicity, we subsume the absorption properties of these non-Seyfert nuclei into our analysis.

4.3 OUTFLOW PROPERTIES

In Figures 4.2 and 4.3, we display the Na I D lines in these galaxies with our analytica fit superimposed. Figures 4.4 and 4.5 show these same spectra along with 1-dimensional spectra of [N II]λ6583 and [O III]λ5007 (where available). The latter also display the spatial and kinematic variation of [O III]λ5007 (where available, or [N II] otherwise) and Hα. Tables 4.1 and 4.2 list the measured properties for the galaxies in our sample and for each velocity component, respectively.

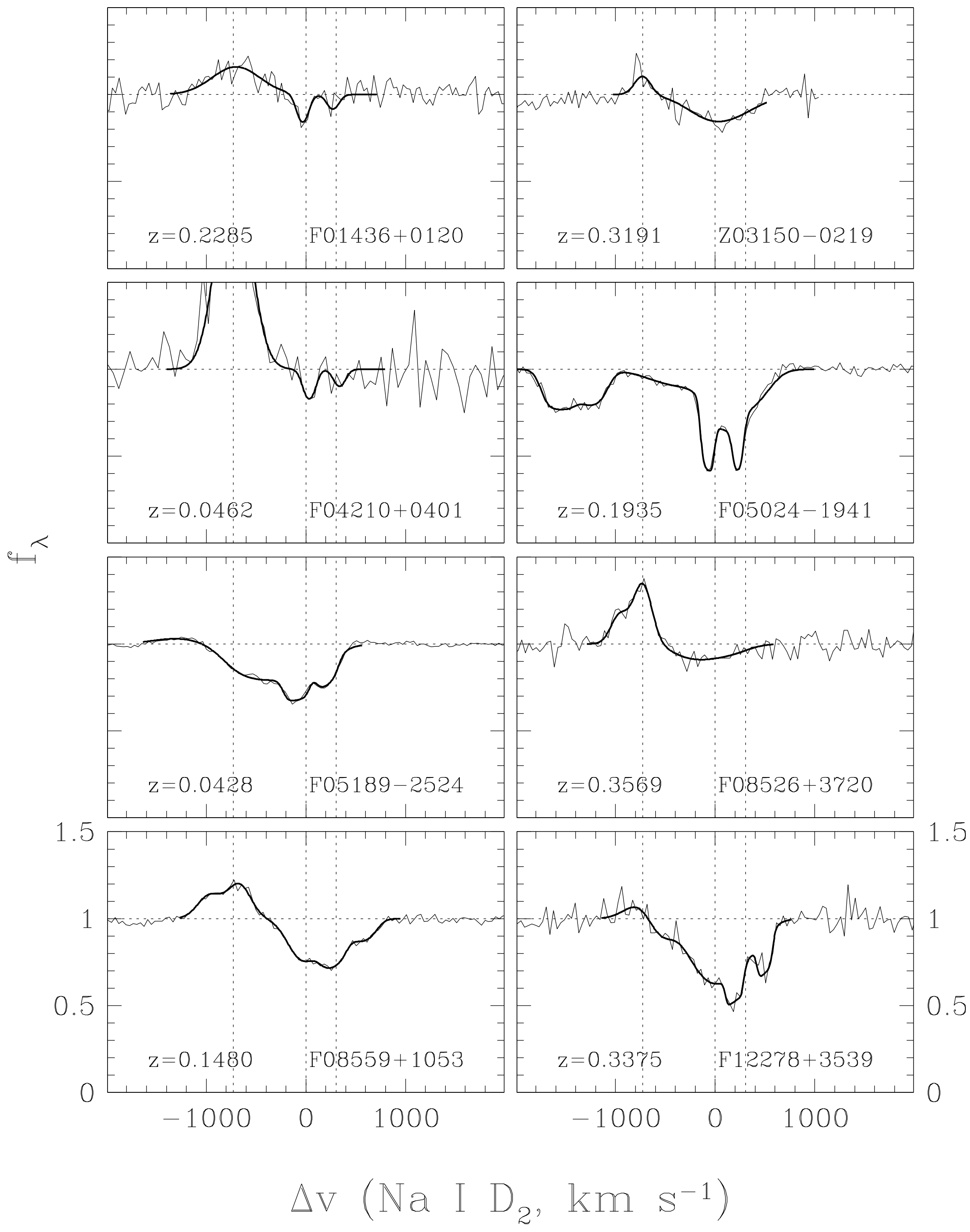

Figure 4.2: Spectra of the Na I D line in Seyfert 2 galaxies. The thin lines are the original spectra (slightly smoothed) and the thick lines are the fits to the data. The vertical dotted lines locate the Na I D$\lambda\lambda5890, 5896$ doublet and He I $\lambda5876$ emission line in the rest frame of the galaxy. The diagonal hashed lines locate atmospheric absorption from O_2.

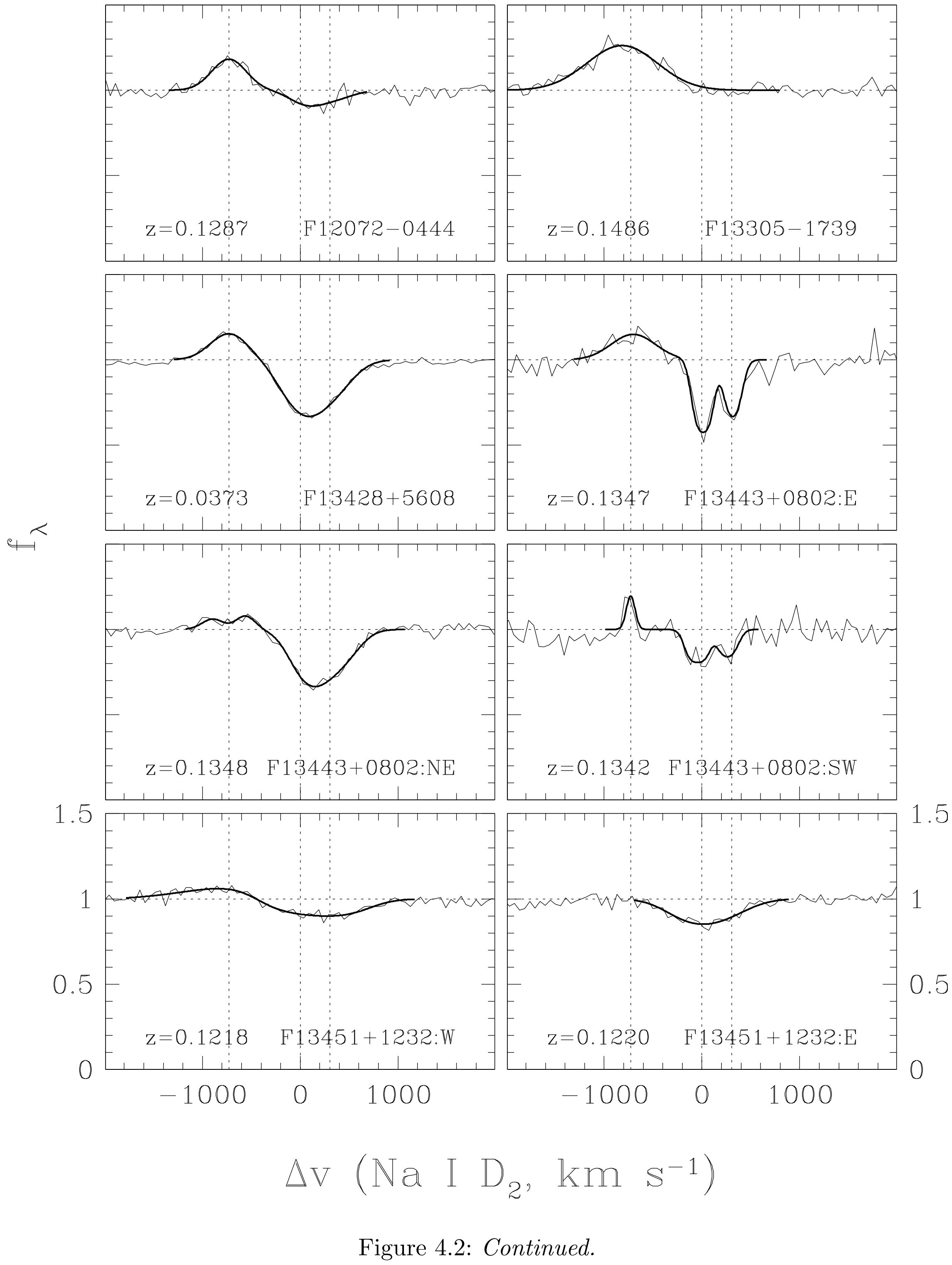

Figure 4.2: *Continued.*

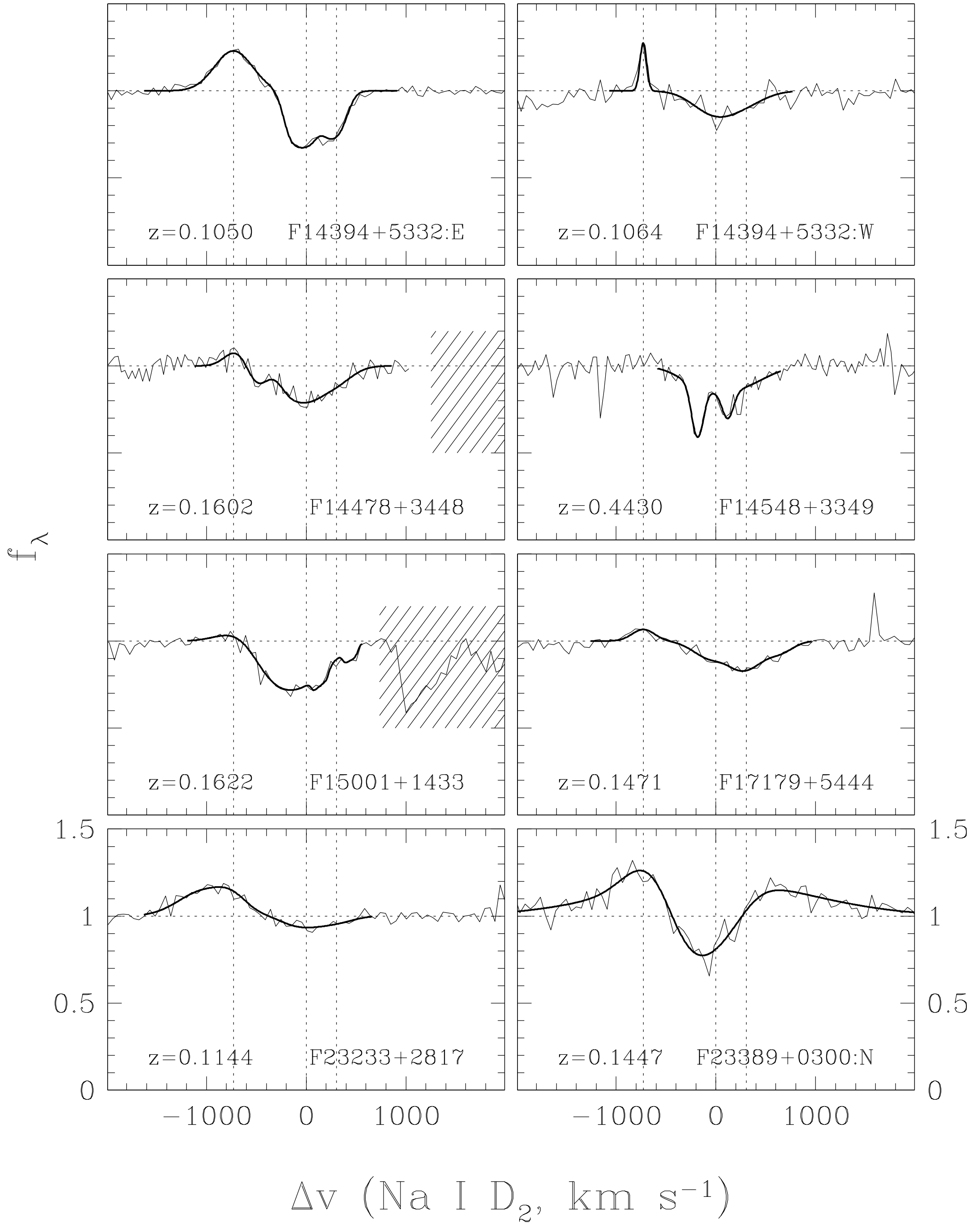

Figure 4.2: *Continued.*

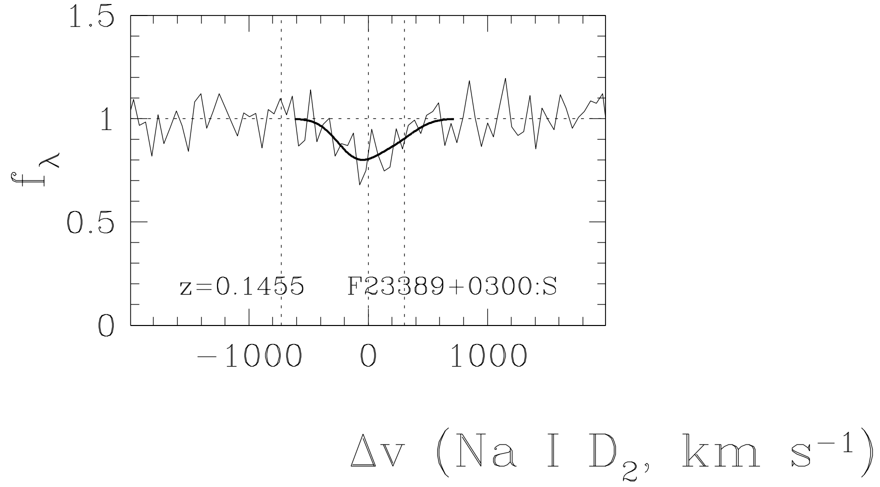

Figure 4.2: *Continued.*

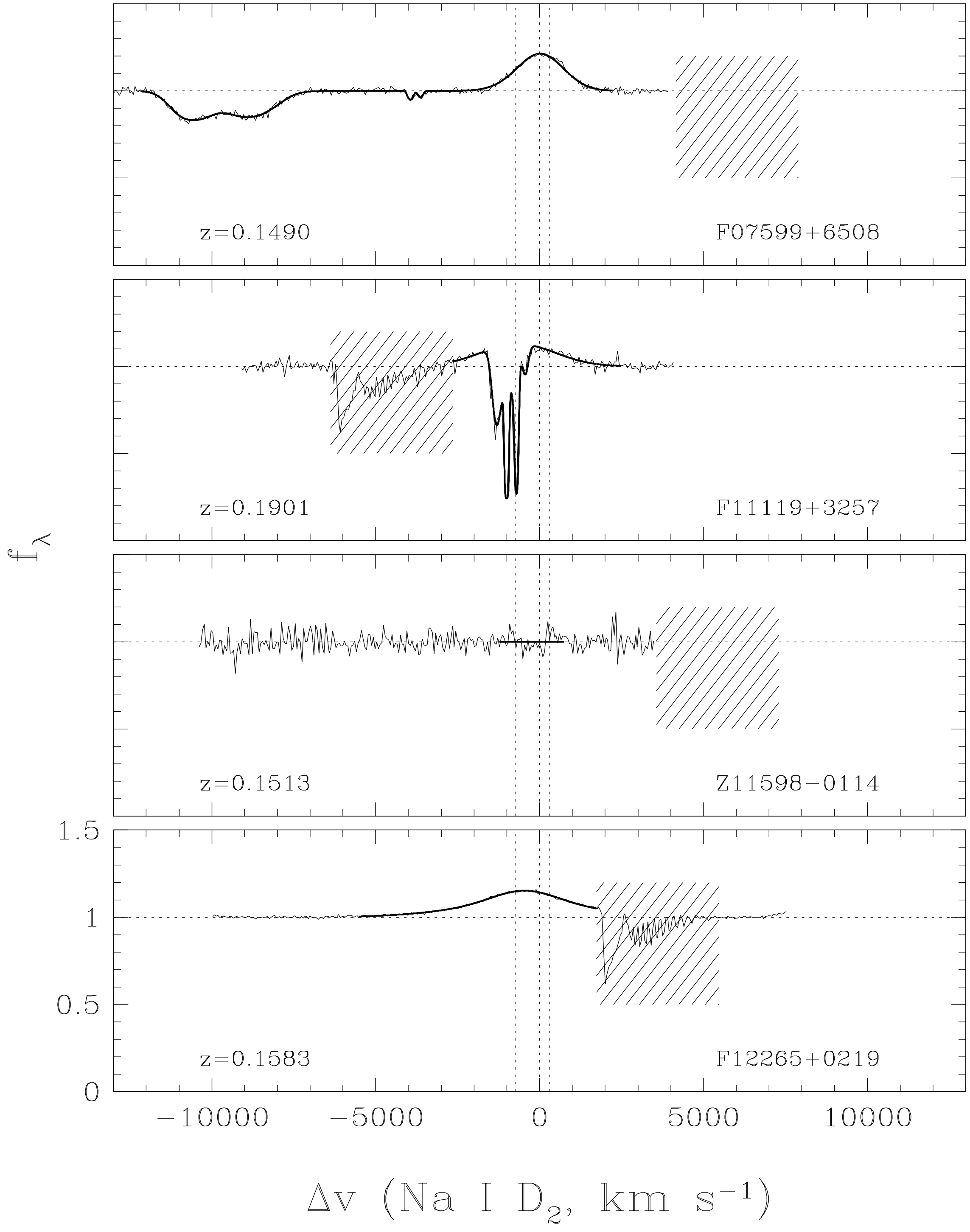

Figure 4.3: Spectra of the Na I D line in Seyfert 1 galaxies. See Figure 4.2 for more details.

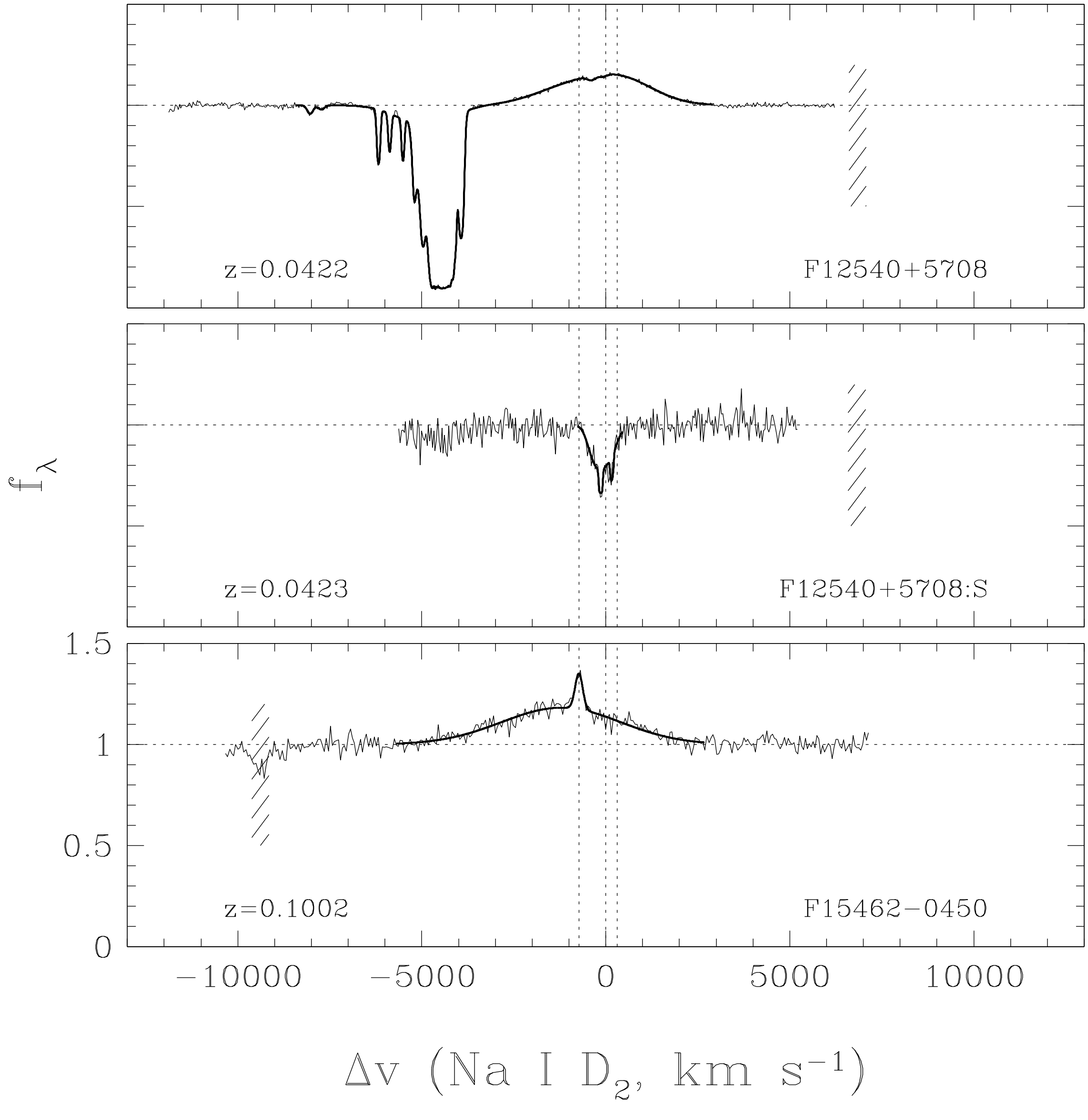

Figure 4.3: *Continued.*

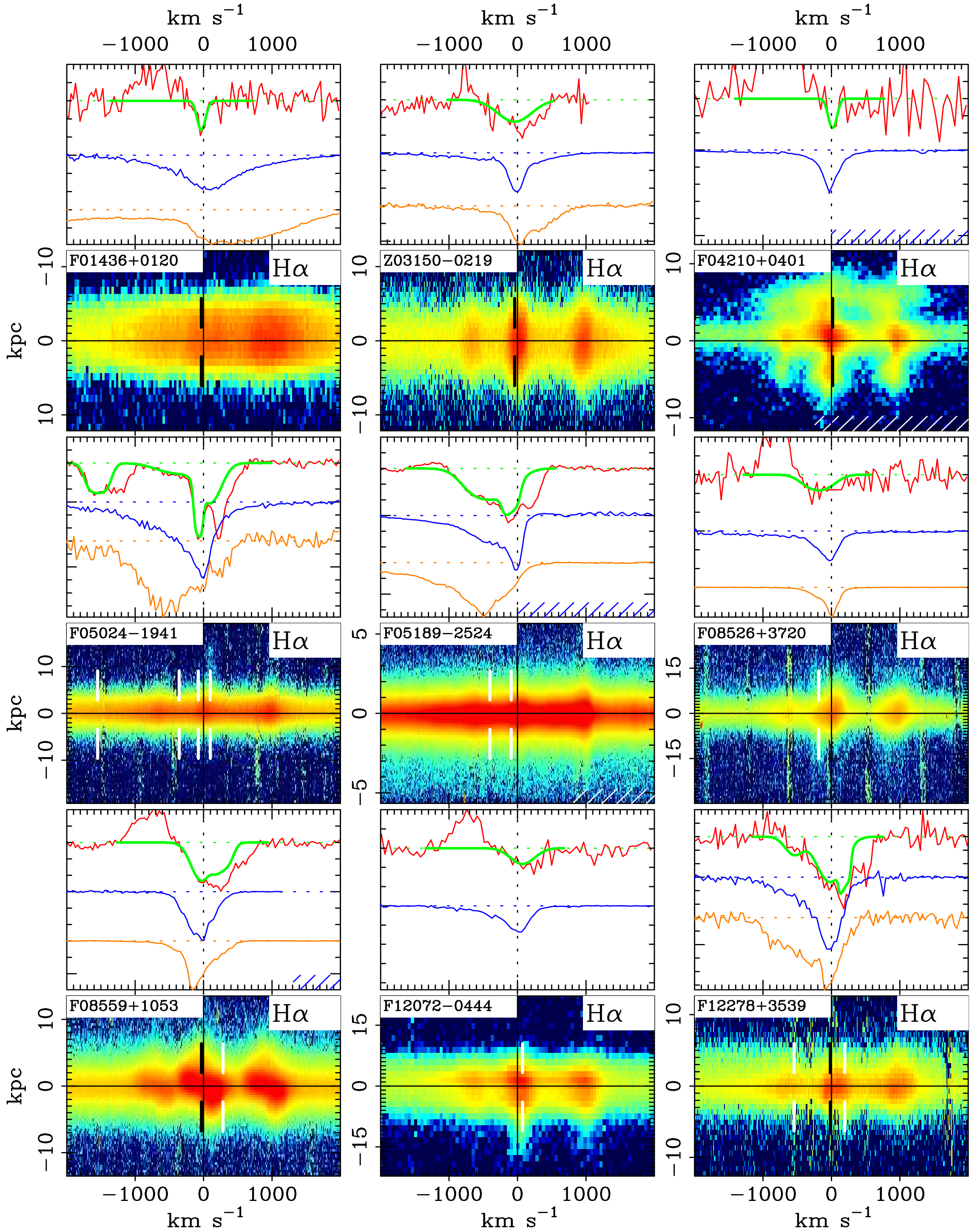

Figure 4.4: Smoothed spectra of Na I D, [N II]$\lambda\lambda 6548, 6583$, and [O III]$\lambda 5007$ for the Seyfert 2 galaxies in our sample. Below these we plot the spatial distribution of Hα. In the 1-dimensional spectra, red is the observed Na I D profile, green is a singlet realization of this profile at the expected location of Na I D$_2$, blue is the observed [N II] profile, and orange is the [O III] profile. (*Continued.*)

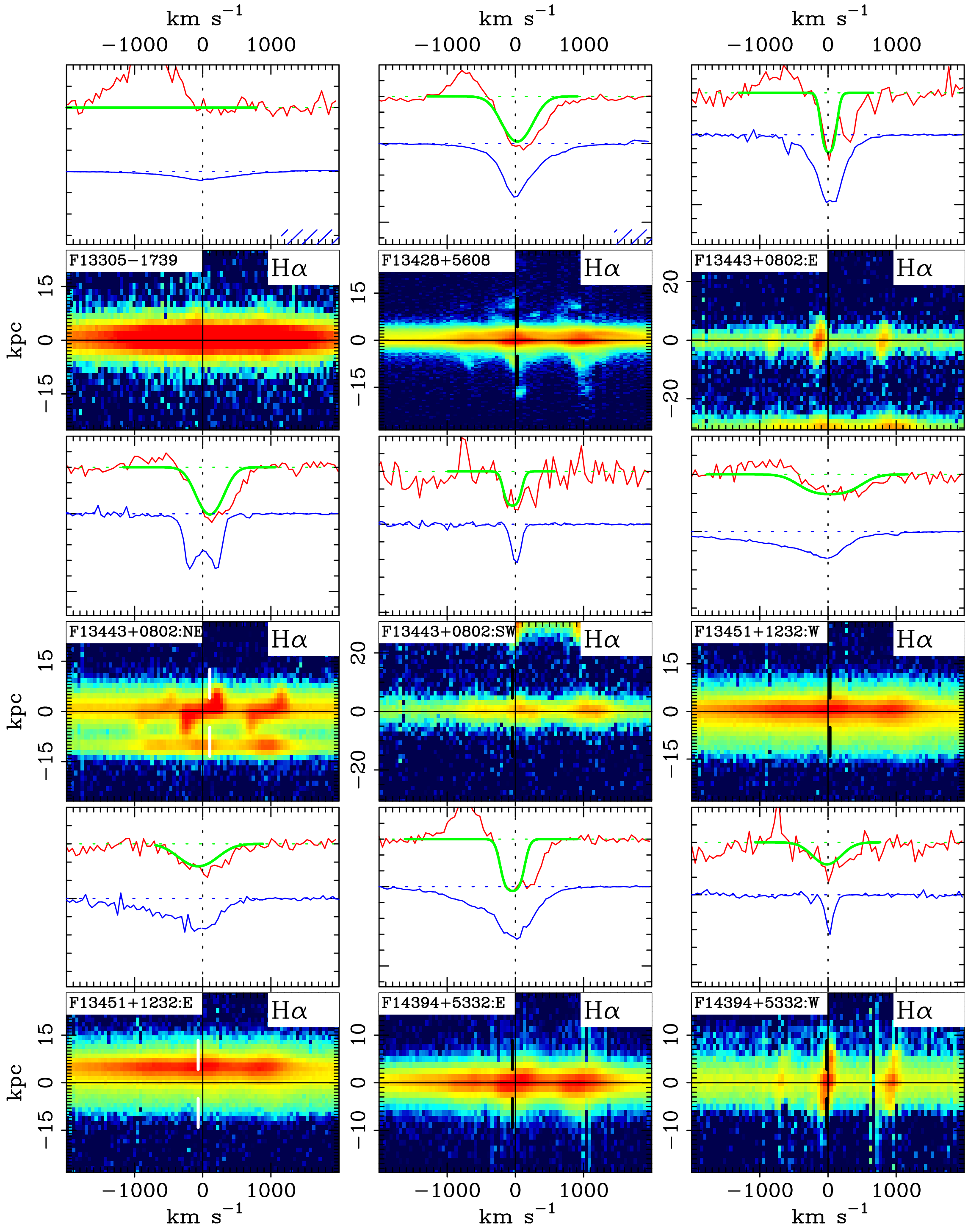

Figure 4.4: The hashed lines locate atmospheric absorption from O_2 and are color coded to match the appropriate line. In the 2-dimensional spectra, the vertical dashed lines locate the fitted velocity components in Na I D. Black represents components within 50 km s^{-1} of systemic, and white represents components blue- or red-shifted at least 50 km s^{-1} from systemic. The sense of direction is such that for a slit with PA = 0°, north is down and south is up.

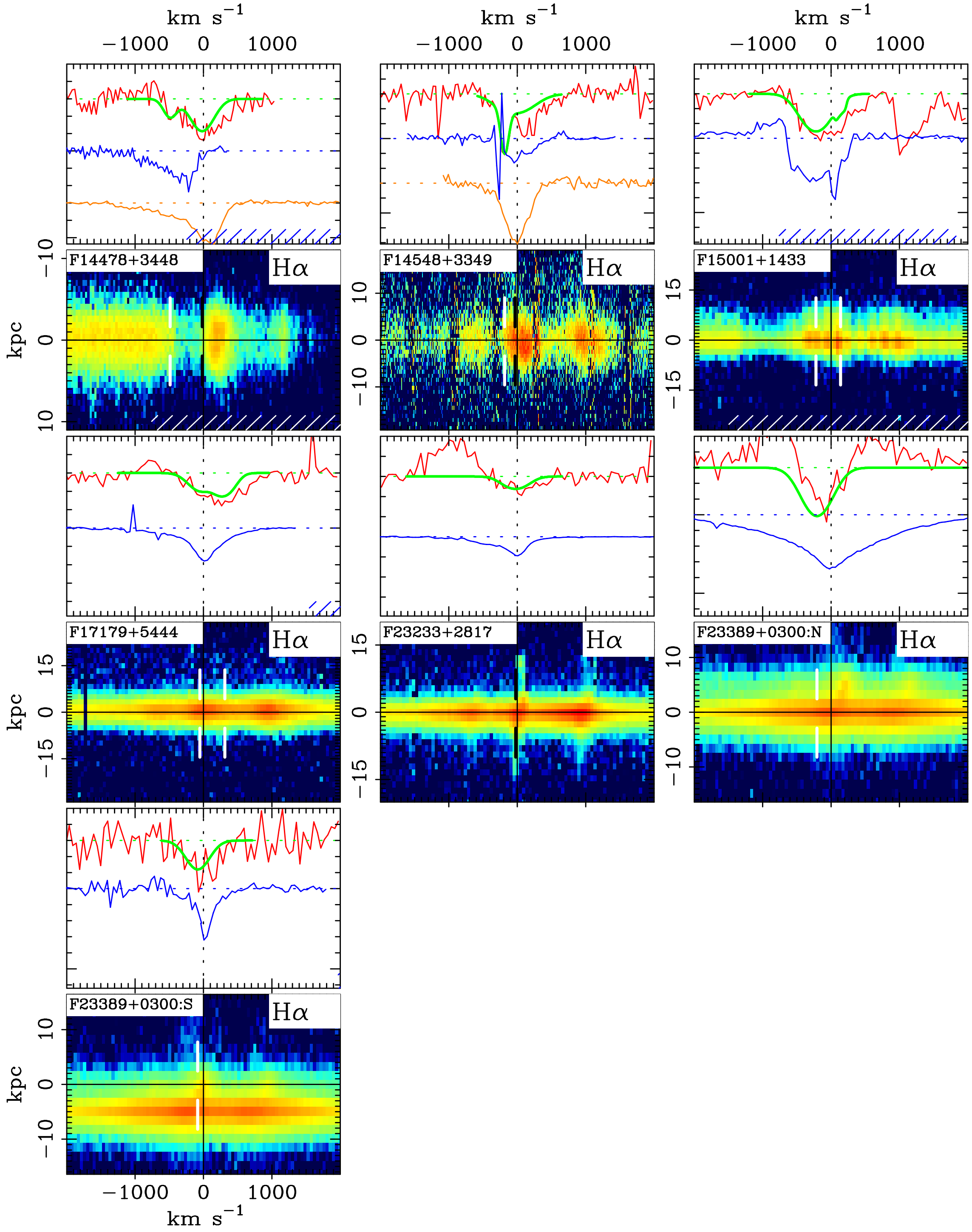

Figure 4.4: *Continued.*

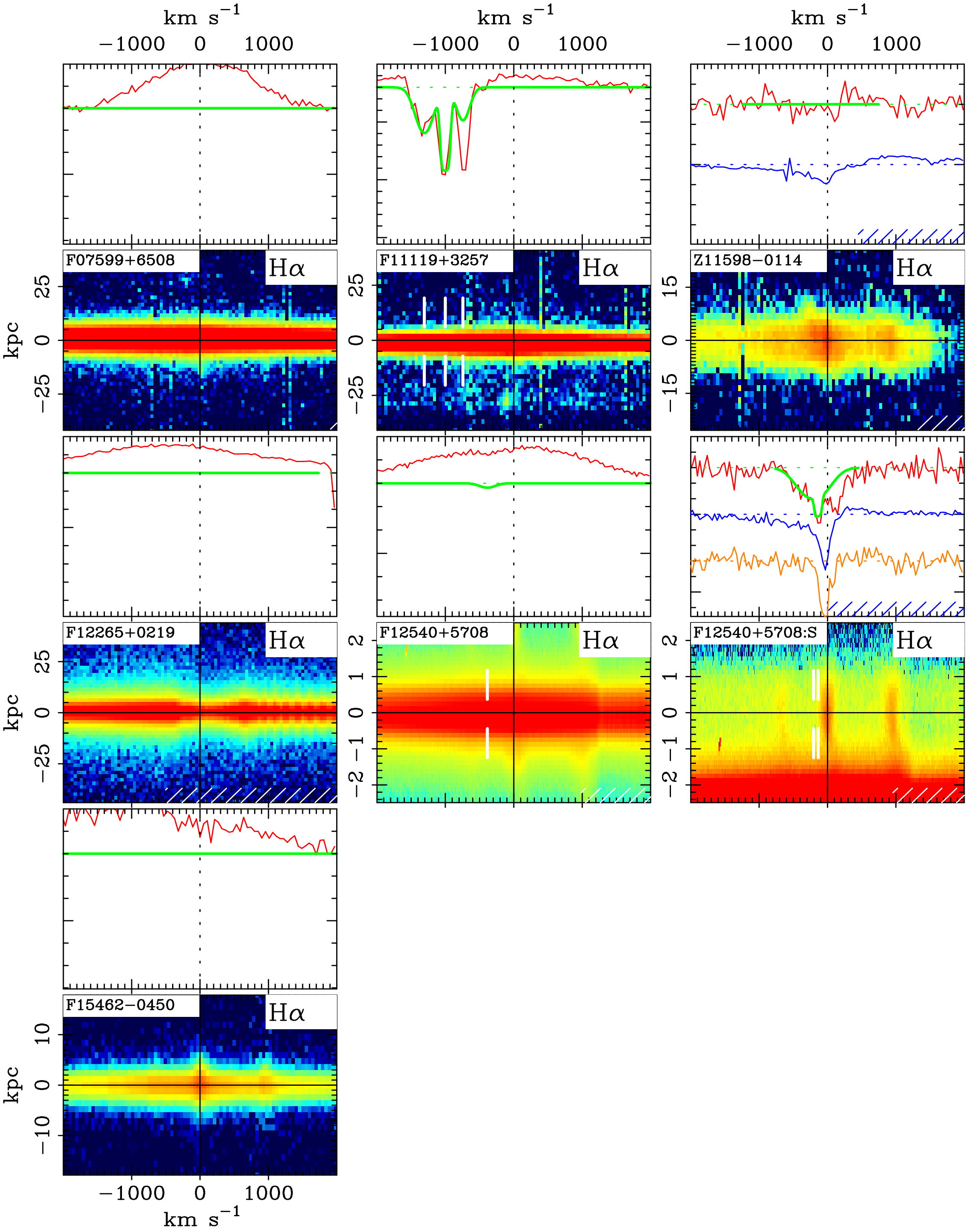

Figure 4.5: The same as Figure 4.4, but for the Seyfert 1 galaxies in our sample.

Table 4.1. Galaxy Properties

Name (1)	Other (2)	z (3)	Type (4)	$L_{\rm IR}$ (5)	$K^{(\prime)}$ (6)	dM/dt (7)	Run (8)	t_{exp} (9)	PA (10)	Refs (11)
Seyfert 1s										
F07599+6508	···	0.1490	Sy1	12.48	-28.43	4014.23	15	5400	168	1
F11119+3257	···	0.1901	Sy1	12.61	-27.79	107.06	15	9000	95	1b
Z11598−0114	···	0.1513	Sy1	12.51	-26.19	0.00	15	3600	12	1
F12265+0219	3C.273	0.1583	Sy1	12.75	-29.93	0.00	15	2400	40	1
F12540+5708	Mrk.231	0.0422	Sy1	12.50	-27.12	2251.22	2,15	5100	0	13
F12540+5708:S	···	0.0423	L	···	···	···	···	···	···	13
F15462−0450	···	0.1002	Sy1	12.17	-25.71	0.00	15	8400	30	1
Seyfert 2s										
F01436+0120	···	0.2285	Sy2	11.83	-25.96	0.00	9	3600	0	2
Z03150−0219	···	0.3191	Sy2	12.30	-25.79	0.00	4,9	9000	0	2
F04210+0401	···	0.0462	Sy2	11.14	-24.82	0.00	13	1800	0	4
F05024−1941	···	0.1935	Sy2	12.47	-25.68	107.04	2	1800	0	1
F05189−2524	···	0.0428	Sy2	12.11	-25.91	37.16	2	900	0	13
F08526+3720	···	0.3569	Sy2	12.36	-26.47	>3.04	4	1800	0	2
F08559+1053	···	0.1480	Sy2	12.24	-26.14	0.00	1	1200	0	1
F12072−0444	···	0.1287	Sy2	12.37	-25.12	0.00	15	10800	8	1
F12278+3539	···	0.3375	Sy2	12.33	-25.43	6.33	6	3600	0	2
F13305−1739	···	0.1486	Sy2	12.25	-25.82	0.00	15	3600	0	1
F13428+5608	Mrk.273	0.0373	Sy2	12.09	-25.05	0.00	15	6000	30	1
F13443+0802:E	···	0.1347	Sy2	12.20	-26.05	0.00	15	14400	166,62	1
F13443+0802:NE	···	0.1348	H	···	···	···	···	···	···	1
F13443+0802:SW	···	0.1342	L	···	···	···	···	···	···	1
F13451+1232:W	···	0.1218	Sy2	12.29	-25.87	1.72	15	10800	104	1
F13451+1232:E	···	0.1220	···	···	···	···	···	···	···	1
F14394+5332:E	···	0.1050	Sy2	12.06	-25.36	0.00	15	9000	93	1
F14394+5332:W	···	0.1064	···	···	···	···	···	···	···	1

Table 4.1 (cont'd)

Name (1)	Other (2)	z (3)	Type (4)	$L_{\rm IR}$ (5)	$K^{(\prime)}$ (6)	dM/dt (7)	Run (8)	t_{exp} (9)	PA (10)	Refs (11)
F14478+3448	···	0.1602	Sy2	11.53	-24.80	>3.15	12	7200	270	2
F14548+3349	···	0.4430	Sy2	12.66	-26.22	2.18	5	3600	0	2
F15001+1433	···	0.1622	Sy2	12.45	-25.63	11.08	15	10800	55	1
F17179+5444	···	0.1471	Sy2	12.26	-25.45	0.57	13	7200	100	1
F23233+2817	···	0.1144	Sy2	12.07	-25.28	0.00	13	7200	75	1
F23389+0300:N	···	0.1447	Sy2	12.24	-26.65	>12.71	13	7200	12	1
F23389+0300:S	···	0.1455	···	···	···	···	···	···	···	1

References. — (1) Kim & Sanders 1998; Veilleux et al. 1999b; (3) Stanford et al. 2000; (4) Sanders et al. 2003; (b) Heckman et al. 2000

Note. — Col.(1): IRAS Faint Source Catalog label, plus nuclear ID. Only 2 objects are not found in the FSC. Col.(2): Another name. Col.(3): Heliocentric redshift, in vacuum. Col.(4): Optical spectral type. Col.(5): Infrared luminosity in logarithmic units of $L_\odot$ (§4.2). Col.(6): K- or K′-band absolute magnitude (Stanford et al. 2000; Kim et al. 2002; 2MASS). 2MASS magnitudes are 'total.' Col.(7): Total mass outflow rate, in $M_\odot$ yr^{-1}. Col.(8): Observing run (from Chapter 2). Col.(9): Total exposure time in seconds. Col.(10): Position angle. Col.(11): Reference.

Table 4.2. Outflow Component Properties

Name (1)	$\lambda_{1,c}$ (2)	Δv (3)	b (4)	$\tau_{1,c}$ (5)	C_f (6)	log[N(Na I)] (7)	log[N(H)] (8)	dM/dt (9)
Seyfert 1s								
F07599+6508	6538.21	-10718	632	0.50	0.11	14.06	21.70	363.48
···	6562.50	-9608	1026	4.09	0.09	15.19	22.83	3445.24
···	6575.95	-8995	581	0.39	0.10	13.92	21.56	189.44
···	6687.84	-3939	78	0.96	0.06	13.43	21.07	16.07
F11119+3257	6988.12	-1309	167	0.25	1.00	13.18	20.82	50.29
···	6995.27	-1002	23	2.84	0.71	13.37	21.01	43.06
···	7001.29	-744	121	0.17	1.00	12.86	20.50	13.71
Z11598−0114	···	···	···	···	···	···	···	···
F12265+0219	···	···	···	···	···	···	···	···
F12540+5708	5983.92	-8031	103	0.03	0.71	12.06	19.70	16.87
···	6021.10	-6175	33	0.92	0.33	13.04	20.68	56.43
···	6034.48	-5510	21	0.81	0.28	12.79	20.43	23.98
···	6041.45	-5164	100	0.42	0.61	13.18	20.82	123.79
···	6044.39	-5019	934	0.26	0.17	13.94	21.58	188.40
···	6045.34	-4972	79	0.68	0.84	13.29	20.93	210.54
···	6049.06	-4787	80	0.42	1.00	13.09	20.73	150.65
···	6050.89	-4696	94	0.70	1.00	13.38	21.02	288.17
···	6052.66	-4609	38	1.32	0.64	13.26	20.90	138.95
···	6054.16	-4534	27	1.30	0.84	13.10	20.74	122.03
···	6056.61	-4413	45	3.04	0.74	13.69	21.33	413.42
···	6060.23	-4234	69	2.72	0.69	13.83	21.47	508.45
···	6138.53	-386	149	0.14	0.08	12.86	20.50	0.57
F12540+5708:S	6142.66	-205	282	0.51	0.32	13.71	21.35	8.45
···	6144.05	-136	9	3.23	0.15	13.00	20.64	0.52
F15462−0450	···	···	···	···	···	···	···	···
Seyfert 2s								
F01436+0120	7244.37	-32	67	0.09	1.00	12.32	19.96	0.00
Z03150−0219	7778.40	-41	338	0.07	1.00	12.90	20.54	0.00
F04210+0401	6170.61	18	63	0.32	0.36	12.85	20.49	0.00
F05024−1941	7002.50	-1547	146	2.00	0.24	14.02	21.66	97.87
···	7030.36	-357	398	0.27	0.19	13.58	21.22	6.84
···	7036.97	-75	38	1.93	0.46	13.42	21.06	2.32
···	7041.06	99	209	0.17	1.00	13.11	20.75	0.00
F05189−2524	6141.44	-402	351	1.21	0.22	14.18	21.82	34.17
···	6147.79	-92	91	2.48	0.16	13.90	21.54	2.99
F08526+3720	7997.42	-187	256	0.56	0.12	13.71	21.35	3.04
F08559+1053	6769.69	-31	197	0.15	0.92	13.01	20.65	0.00
···	6776.83	285	126	1.13	0.17	13.70	21.34	0.00
F12072−0444	6658.21	74	239	0.04	0.96	12.58	20.22	0.00
F12278+3539	7873.64	-546	178	0.07	1.00	12.66	20.30	6.33
···	7887.57	-16	246	0.31	0.72	13.44	21.08	0.00
···	7893.11	195	42	>5.00	0.23	>13.88	>21.52	0.00
F13305−1739	···	···	···	···	···	···	···	···

Table 4.2 (cont'd)

Name (1)	$\lambda_{1,c}$ (2)	Δv (3)	b (4)	$\tau_{1,c}$ (5)	C_f (6)	log[N(Na I)] (7)	log[N(H)] (8)	dM/dt (9)
F13428+5608	6118.06	29	285	0.23	0.78	13.37	21.01	0.00
F13443+0802:E	6692.21	11	89	1.28	0.46	13.61	21.25	0.00
F13443+0802:NE	6695.18	105	248	0.30	0.68	13.42	21.06	0.00
F13443+0802:SW	6687.87	-43	99	1.56	0.20	13.74	21.38	0.00
F13451+1232:W	6616.51	28	400	1.18	0.11	14.22	21.86	0.00
F13451+1232:E	6615.59	-67	357	0.27	0.29	13.54	21.18	1.72
F14394+5332:E	6515.87	-43	134	1.66	0.34	13.90	21.54	0.00
F14394+5332:W	6524.51	-17	286	0.07	1.00	12.83	20.47	0.00
F14478+3448	6831.25	-487	127	0.06	0.99	12.41	20.05	3.15
···	6841.92	-19	228	0.12	0.85	13.00	20.64	0.00
F14548+3349	8504.94	-185	66	0.20	1.00	12.66	20.30	2.18
···	8509.28	-32	347	0.37	0.25	13.66	21.30	0.00
F15001+1433	6849.10	-220	283	0.46	0.42	13.67	21.31	11.08
···	6857.30	138	21	>5.00	0.08	>13.57	>21.21	0.00
F17179+5444	6763.92	-52	232	0.06	0.80	12.73	20.37	0.57
···	6772.13	312	179	0.47	0.19	13.48	21.12	0.00
F23233+2817	6571.65	-24	231	0.47	0.10	13.59	21.23	0.00
F23389+0300:N	6746.30	-206	300	0.24	0.80	13.41	21.05	10.94
F23389+0300:S	6753.76	-84	232	0.10	0.97	12.93	20.57	1.77

Note. — Col.(2): Redshifted heliocentric wavelength, in vacuum, of the Na ID$_1$ λ5896 line; in Å. Col.(3): Velocity relative to systemic, in km/s. Negative velocities are blueshifted. Col.(4): Doppler parameter, in km/s. Col.(5): Central optical depth of the Na ID$_1$ λ5896 line; the optical depth of the D$_2$ line is twice this value. Col.(6): Covering fraction of the gas. Col.(7-8): Logarithm of column density of Na I D and H, respectively, in cm^{-2}. Col.(9): Mass outflow rate of the component, in M$_\odot$ yr^{-1}.

4.3.1 Detection rate

We detect absorption blueshifted by more than 50 km s^{-1} in half of Seyferts ($50\pm20\%$ of Seyfert 1s and $50 \pm 11\%$ of Seyfert 2s). These detection rates are similar to those measured in starburst galaxies (43% of IRGs and 63% of ULIRGs). Our measurement is identical to that of Heckman et al. (2000), who find winds with $\Delta v < -50$ km s^{-1} in 3 of 6 Seyfert 2s.

In contrast, this is larger than the detection frequency of large-scale radio/optical structures found in a distance-limited sample of 22 Seyferts (Colbert et al. 1996a). Six of these 22 galaxies host large-scale radio structures, and six host optical features indicative of superwinds, which translates to a detection rate of approximately 30%. The rate of detection of outflows in our Seyfert ULIRGs is $\sim 20\%$ larger than this, which may mean that the detection rate of superwinds depends on luminosity in much the same way as for the starburst galaxies in Chapter 3.

As we discuss in Chapter 3, these detection rates are lower limits to the actual rates of occurrence of superwinds if the global angular covering fraction of an outflow is less than unity (see also §4.4.4 below).

4.3.2 Absorption-line properties

Table 4.3 compares the average properties in these AGN with those measured in starburst galaxies from Chapter 3. Figures 4.6 – 4.11 compare the distributions of various measured quantities in AGNs and starbursts. In these plots we show the properties measured in Seyfert 1 and Seyfert 2 galaxies separately. For Doppler width, covering fraction, and optical depth, we show only Seyfert 2s, for clarity and since fitting the broad lines in Seyfert 1 galaxies carries added uncertainties (as we discuss in §4.3.3).

Table 4.3. Average Properties

Quantity	Seyfert 1s	Seyfert 2s	low-z ULIRGs
N_{gals}	6	20	30
$\langle z \rangle$	$0.150^{+0.110}_{-0.064}$	$0.148^{+0.141}_{-0.072}$	$0.129^{+0.066}_{-0.044}$
$\langle log(L_{\rm IR}/L_{\odot}) \rangle$	$12.50^{+0.19}_{-0.19}$	$12.24^{+0.34}_{-0.34}$	$12.21^{+0.15}_{-0.15}$
$\langle dM/dt \rangle$ ($M_{\odot}$ yr^{-1})	2251^{+13525}_{-1930}	4^{+17}_{-4}	8^{+15}_{-5}
$\langle \Delta v \rangle$ (km s^{-1})	4653^{+11565}_{-3318}	196^{+320}_{-122}	183^{+152}_{-83}
$\langle \Delta v_{max} \rangle$ (km s^{-1})	8117^{+16306}_{-5419}	456^{+349}_{-198}	416^{+233}_{-149}
$\langle \Delta v[\text{max. } N(\text{H})] \rangle$ (km s^{-1})	5019^{+11058}_{-3452}	213^{+368}_{-135}	176^{+131}_{-75}

Note. — For each value we include the median ± the linear 1σ dispersions under the assumption of a Gaussian distribution in the log of the quantity.

The distributions of Seyfert 2 galaxies and starbursts are quite similar, while the absorbing gas in Seyfert 1 galaxies clearly has extreme properties. The only very significant difference between starbursts and Seyfert 2s is in the distribution of Δv. Here, we briefly compare these three subsamples.

Velocities

Seyfert 2s have higher maximum velocities on average than starbursts of comparable luminosity (a median of 456 km s^{-1} vs. 416 km s^{-1} for the low-z ULIRGs), and Seyfert 1s clearly have the highest maximum velocities on average (median 8100 km s^{-1}). The range of values of Δv_{max} is shifted upward by about 100 km s^{-1} with respect to the starbursts, with lower and upper limits of 240 and 700 km s^{-1} (disregarding the one galaxy with $\Delta v_{max} > 1000$ km s^{-1}).

K-S tests show that the differences in the distribution of Δv_{max} between the Seyfert 2s and the starbursts or the Seyfert 2s and low-z ULIRGs are not significant. However, the distributions of Δv between Seyfert 2s and low-z ULIRGs are different

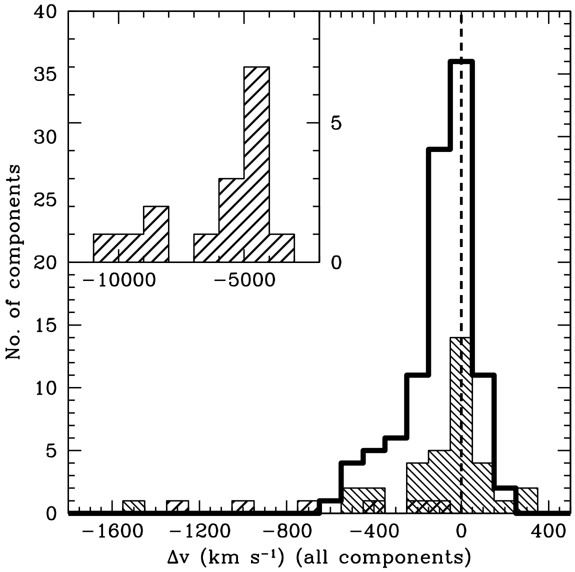

Figure 4.6: Distributions of central velocity of each component in each galaxy for starburst- and AGN-dominated galaxies. The distributions of Δv for starbursts and AGN are different at 98% confidence. The bin size is 100 km s^{-1} (and 1000 km s^{-1} for the insets). The shading follows the pattern of Figure 4.1.

at $>$ 98% confidence and have medians and standard deviations of -30 ± 315 km s^{-1} and -120 ± 180 km s^{-1}, respectively.

As with the starbursts, the velocity distribution must be corrected for projection effects. If this distribution reflects different orientations, then most values of Δv_{max} are close to the highest values of Δv_{max} that we measure.

As with the low-z ULIRGs, there is one Seyfert 2 with $\Delta v_{max} > 1000$ km s^{-1} (F05024−1941). The velocities in Seyfert 1s are in general quite large, but there are several components with velocities between -50 and -1400 km s^{-1}. Two of these components occur in the emission-line region south of the nucleus of F12540−5708 (Mrk 231).

The distribution of Doppler parameter in Seyfert 2s and starbursts are quite similar. The average value and logarithmic dispersion in Seyfert 2s and low-z ULIRGs are 183^{+180}_{-91} km s^{-1} and 178^{+165}_{-85} km s^{-1}, respectively. K-S tests show that the Seyfert 2s and starbursts could have the same parent distribution for b.

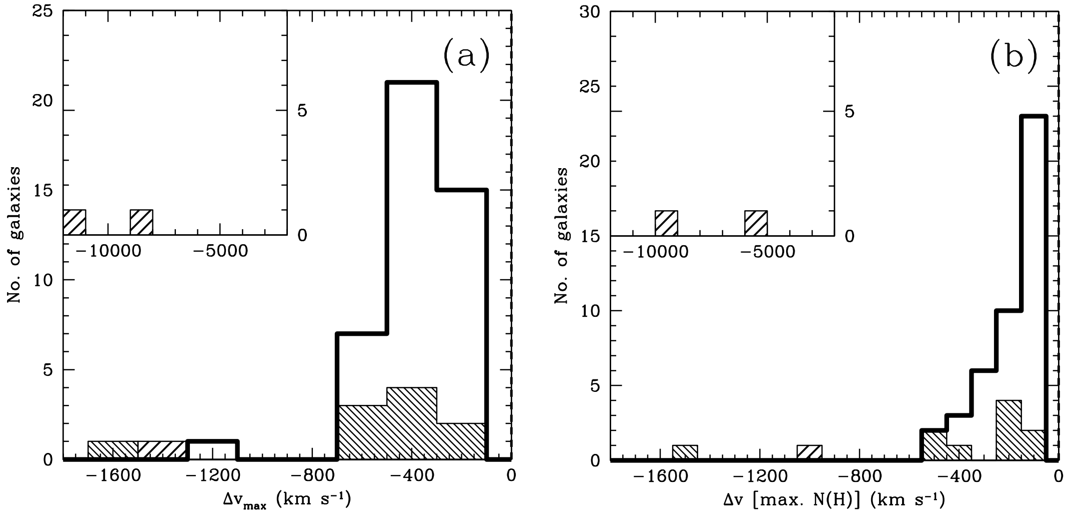

Figure 4.7: Distributions of (a) maximum velocity and (b) velocity of the highest column density gas in each galaxy for starburst- and AGN-dominated galaxies. The distributions of Δv_{max} are not significantly different, nor are the Δv[max. N(H)] distributions. However, the maximum and minimum values for Δv_{max} are larger in Seyfert 2s by $\sim$ 100 km s^{-1} at $>$ 95% confidence (disregarding the galaxies with $\Delta v_{max} > 1000$ km s^{-1}). The shading follows the pattern of Figure 4.1.

Covering fraction, optical depth, and mass outflow rate

The optical depths in outflowing components in Seyfert 2s are smaller on average than in starbursts (0.3 in Seyfert 2s vs. 0.9 in the low-z ULIRGs). However, the distributions of τ for these two samples are not significantly different. The median covering fraction for outflowing components is ~ 0.4 in each of these samples, and the covering fraction distributions are also not significantly different. However, the Seyfert 2 distribution peaks at $C_f \sim 1$ rather than $C_f \sim 0.1 - 0.4$, and it resembles the distribution of low-z ULIRGs more closely than that of the IRGs. The differences in dM/dt between Seyfert 2s and starbursts are not significant, but the mass outflow rates for Seyfert 1s are quite high (several thousand M$_{\odot}$ yr^{-1}).

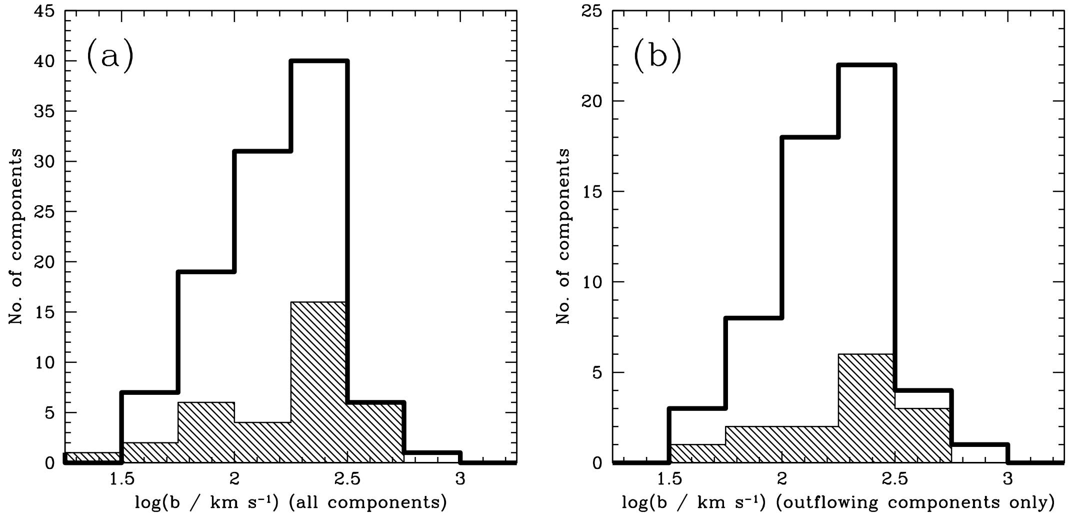

Figure 4.8: Logarithmic distributions of the Doppler parameter for (a) all and (b) outflowing components in starburst and Seyfert 2 galaxies. These distributions are consistent with arising out of the same parent distribution. The shading follows the pattern of Figure 4.1.

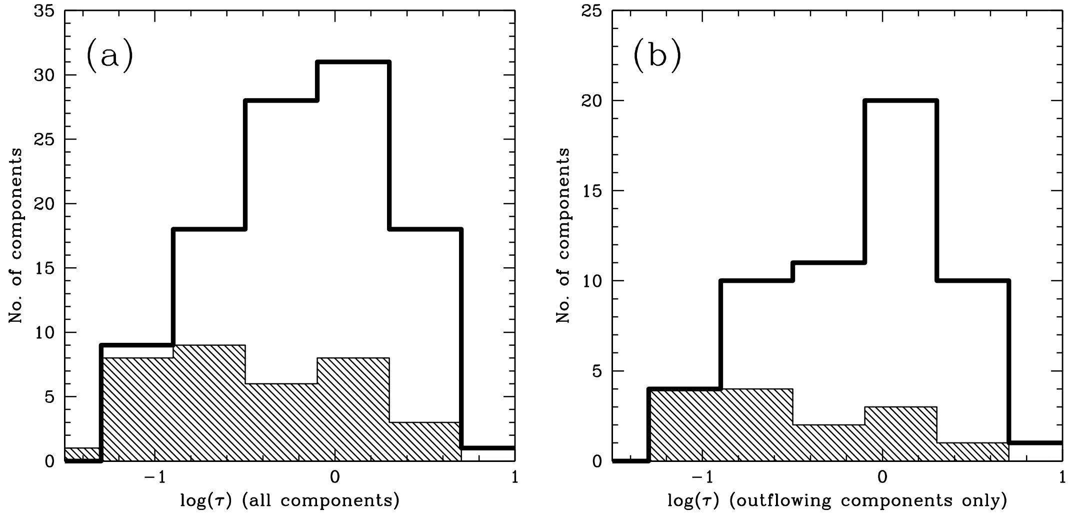

Figure 4.9: Logarithmic distributions of the central optical depth in the D_1 line for (a) all and (b) outflowing components in starburst and Seyfert 2 galaxies. The distributions are not significantly different. The shading follows the pattern of Figure 4.1.

4.3.3 Na I D in Seyfert 1s

The properties of the absorption lines in the six Seyfert 1 galaxies in our sample show clear differences from those found in the Seyfert 2 galaxies. The most obvious

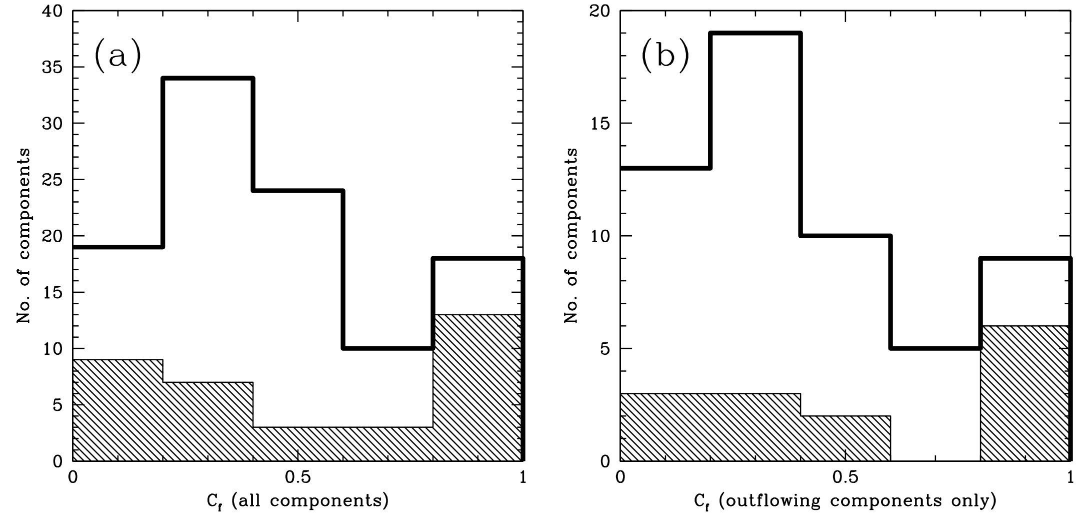

Figure 4.10: Logarithmic distributions of the covering fraction for (a) all and (b) outflowing components in starburst and Seyfert 2 galaxies. The distributions are not significantly different. The Seyfert 2 distribution most resembles that of the low-z ULIRGs, and peaks at $C_f \sim 1$. The shading follows the pattern of Figure 4.1.

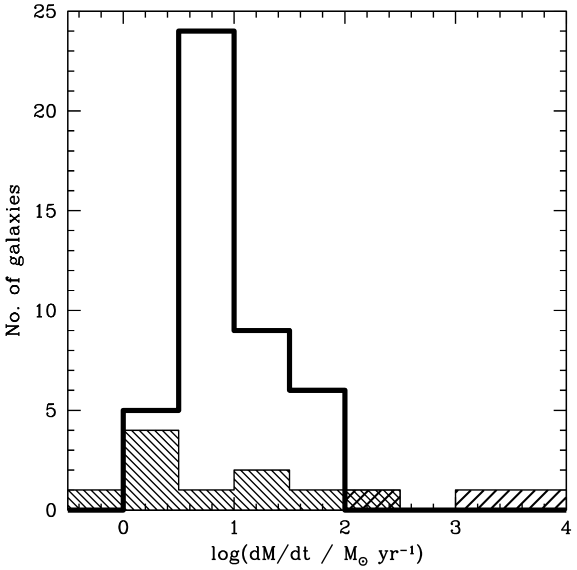

Figure 4.11: Logarithmic distribution of mass outflow rate for starburst and active galaxies. The distributions of are not significantly different. The shading follows the pattern of Figure 4.1.

is the much higher velocities observed, similar to those seen in broad-absorption-line quasars. Two Seyfert 1s (F07599+6508 and F12540+5708) show very broad ($\Delta v \gtrsim 2000$ km s^{-1}) and deep absorption complexes. A third (F11119+3257) shows a narrower profile, but the profile contrasts with those found in most Seyfert 2s and starbursts in that there are three relatively narrow ($b \lesssim 170$ km s^{-1}) components with high covering fractions ($C_f = 0.7 - 1.0$) and velocities ($\Delta v \sim 700 - 1400$ km s^{-1}), clustered together in velocity space.

In Rupke et al. (2002), we discuss in detail our method for modeling the deep absorption trough in Mrk 231. We have only slightly modified the results of this modeling for the current work. F07599+6508, however, is more difficult since it has strong Fe II lines that are complex to model and remove (and that have little or no impact on the absorption lines in Mrk 231). Rather than attempt to remove Fe II in F07599+6508, we have simply fit the continuum around the broad complex, which partially removes the emission feature seen in the blue half of the line in Boroson & Meyers (1992). However, we are insensitive to the very blueshifted absorption that Boroson & Meyers (1992) claim to see in this galaxy at ~ 16000 km s^{-1}.

The number of components that we should fit to each of the broad features is uncertain. In F11119+3257, we easily fit several narrow components ($b < 170$ km s^{-1}) with high covering fractions. In F12540+5708, we fit many narrow components to the broad profile, as suggested by Forster, Rich, & McCarthy (1995), who find the appropriate number of components by minimizing a χ^2 statistic. For F07599+6508, however, we fit only three very broad components to the deep Na I D feature; without doing a detailed analysis similar to that of Forster et al. (1995), it is unclear whether we should use few or many components.

In our current analysis, we fit an extra blueshifted component in F12540+5708 that does not appear in Rupke et al. (2002), at a velocity with respect to systemic of -386 km s^{-1}. This component is suggested by a dip atop the He I λ5876 and Na I D broad emission lines. It appears to be secure if we assume Gaussian shapes for the emission lines. However, if they deviate significantly from Gaussian this component may be spurious.

4.3.4 Emission-line properties

Similar to the starburst galaxies, the AGN display diverse emission-line properties. The emission lines tend to be broader and have a greater tendency to show structure in velocity space (especially [O III]λ5007). Three of the nine galaxies for which we have observed [O III] have peaks that are blueshifted from systemic; each of these galaxies also possesses blueshifted Na I D. Thirteen nuclei have blue wings or asymmetries in either [N II] or [O III]; three galaxies possess red wings or asymmetries. Seven of the galaxies which have blue wings have outflowing neutral gas; two of the three galaxies with red asymmetries have Na I D absorption at or near these velocities.

Only three nuclei in this sample exhibit rotation curves. Irregular extended emission exists in a number of galaxies, however, on scales up to $\sim$ 30 kpc. Some of this material appears to be AGN-illuminated and generally has non-zero velocity with respect to systemic.

The emission-line profiles in a few of these galaxies are worthy of individual mention.

Z03150−0219. This galaxy has a red emission-line component, with velocities up to +800 km s^{-1} above systemic, that has a higher [O III]/Hβ ratio than the gas at systemic by a large factor (at least 10). No detectable Hβ emission is observed at this velocity.

F04210+0401. This radio galaxy possesses a jet. We observed this galaxy with the spectroscopic slit aligned with the position angle of the jet, and observe spectacular emission-line structures that have been studied in previous works (e.g., Steffen, Holloway, & Pedlar 1996a,b). We observe a narrow and low signal-to-noise Na I D component at systemic.

F05024−1941. This Seyfert 2 has the highest absorption-line velocity with respect to systemic of all non-Seyfert 1s in this survey. A low-velocity blue wing is present, as well as an optically thick component with low covering fraction at $\Delta v = 1550$ km s^{-1}. This galaxy also has a redshifted absorbing component whose velocity is identical to that of an emission feature extending $\sim$ 15 kpc to the south. The velocities of the [O III] line do not extend as far as $\Delta v = 1550$ km s^{-1}, but those of the [N II] line do. The peak of [O III] is blueshifted from systemic by $\sim$ 470 km s^{-1}.

F05189−2524. This galaxy has numerous emission lines of various stages of ionization in its spectrum (superimposed on a continuum with deep stellar absorption lines). The high-ionization lines (e.g., [O III]λ5007, Ar III $\lambda\lambda 7137, 7752$, and S III $\lambda\lambda 9070, 9532$) are blueshifted by 510 km s^{-1} with respect to systemic (as determined by the stellar absorption lines and CO emission), while the low-ionization lines are at systemic. Some of the high-ionization lines also have blue wings extending even farther from systemic. The blue component of Na I D is close in velocity to that of the peak of the high-ionization lines.

F08526+3720. Here again we see blueshifted Na I D and [O III], this time by only a couple hundred km s^{-1}. However, the [O III] centroid is at systemic in this galaxy. There is extended emission $\sim$ 15 kpc to the N and S of the galaxy that corresponds to the outflow velocity; the high [O III]/Hβ flux ratio indicates this material may be ionized by an AGN.

F08559+1053. The peak of [O III] is located 200 km s^{-1} blueward of systemic, and [N II] also has a blue lobe at this velocity. There is extended emission about 5 kpc to the S of this galaxy at a velocity near systemic; this gas has [O III]/Hβ $\sim$ $5-6$, which implies ionization by the AGN. There are substantial variations between

[O III]/Hβ in both position and velocity space, suggesting variations in the source of ionization.

F12540+5708 (Mrk 231). This local quasar has an irregular host galaxy (Hamilton & Keel 1987; Surace et al. 1998). Our spectrum intersects a region approximately 3″ south of the Seyfert nucleus. A bright emission-line region with a LINER spectrum is visible here on top of a spatially distinct stellar continuum; the emission-line region is slightly offset towards the nucleus, however. Hamilton & Keel (1987) observe blueshifted emission in this region and at other regions within several arcseconds of the nucleus, at velocities up to 1500 km s^{-1} with respect to systemic. Our Na I D spectrum of this region shows blueshifted velocities with respect to systemic of up to ~ 300 km s^{-1}. We also observe a faint blue wing in [N II]λ6583 with velocities up to at least 600 km s^{-1}. These extranuclear regions contain numerous blue star-forming knots with a range of ages ($\sim 10^7 - 10^9$ yr); these knots are especially dense in the southern region in which we detect the outflow (Surace et al. 1998).

F13428+5608 (Mrk 273). This well-known Seyfert 2 shows irregular extended line-emitting structures on scales of up to $30 - 40$ kpc on both sides of the nucleus and complex velocity profiles (reminiscent of NGC 6240; see Chapter 3). Variations in Hα/[N II] are visible, including possibly shock-excited regions several kpc to the NE and SW that also exhibit line-splitting of $300 - 400$ km s^{-1}. Larger line-splitting (~ 500 km s^{-1}) occurs at larger radii (see Colina, Arribas, & Borne 1999).

4.3.5 Dependence on host galaxy properties

Figures 4.12 − 4.14 plot mass outflow rate and velocity as a function of total infrared luminosity and K- or K'-band magnitude for these AGN and the starburst galaxies from Chapter 3. In this chapter, we use infrared luminosity as an abscissa instead of star formation rate.

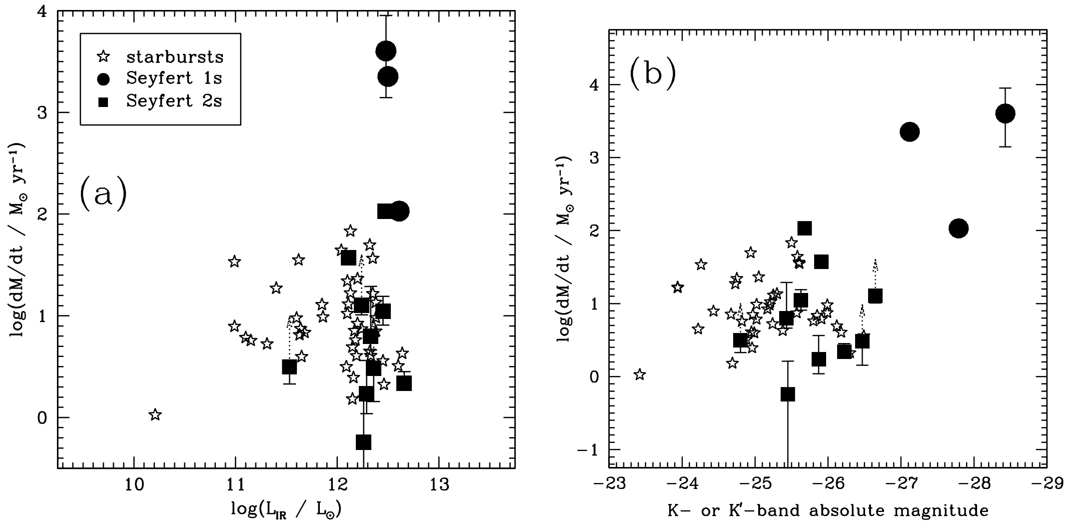

Figure 4.12: Mass outflow rate vs. (a) infrared luminosity and (b) $M_{K^{(\prime)}}$ in starburst and active galaxies. There are no obvious trends. The Seyfert 2s occupy similar, though not identical, regions to the starbursts. The symbols are described in the legend.

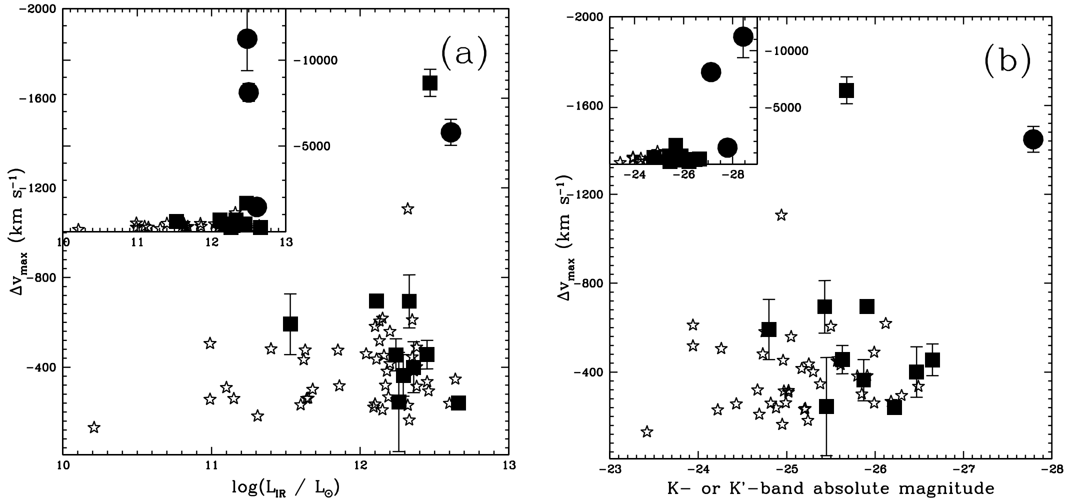

Figure 4.13: Maximum velocity vs. (a) infrared luminosity and (b) $M_{K^{(\prime)}}$ in starburst and active galaxies. There are no obvious trends. The Seyfert 2s occupy similar, though not identical, regions to the starbursts. The symbols follow the pattern of Figure 4.12.

Many of the Seyfert 2 points fall in the regions of these plots populated by starburst galaxies. As noted above in §4.3.2, the greater dispersion in mass outflow rate for Seyfert 2s (compared to starbursts) is clearly visible. There are no obvious trends in the plots, apart from those recognized in starburst galaxies and described

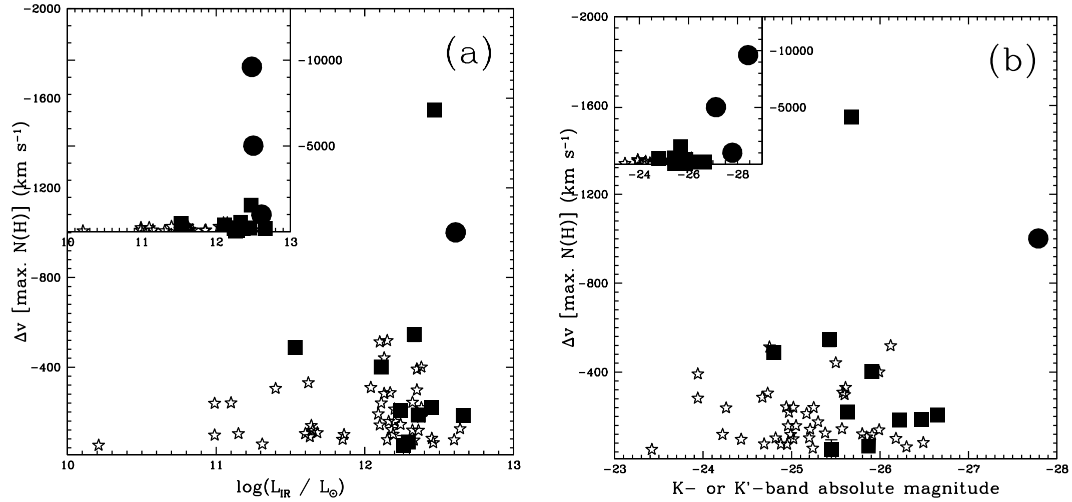

Figure 4.14: Velocity of the highest column density gas vs. (a) infrared luminosity and (b) $M_{K(\prime)}$ in starburst and active galaxies. There are no obvious trends. The Seyfert 2s occupy similar, though not identical, regions to the starbursts. The symbols follow the pattern of Figure 4.12.

in Chapter 3.

In Figure 4.15, we plot a hypothetical mass entrainment efficiency for these galaxies. Recall from Chapter 3 the relation between infrared luminosity and star formation rate (Kennicutt 1998):

$$\mathrm{SFR} = \alpha \, \frac{L_{\mathrm{IR}}}{5.8 \times 10^9 \, L_\odot}. \tag{4.1}$$

The factor α describes the fractional amount of L_{IR} that arises from dust heating by star formation. For the Seyfert 1 galaxies in our sample, and a few Seyfert 2s that show either broad lines in the near-infrared or faint broad lines in the optical, we assume $\alpha = 0.4$. For the rest of the Seyfert 2s, we assume $\alpha = 0.6$. These assumptions are based on estimates from mid-infrared spectroscopy (Genzel et al. 1998). Curiously, with this correction most (8 of 11) of these points fall on the relation established for star-forming galaxies. Three others are outliers, either above or below the region populated by starbursts. The Seyfert 1s have much higher values for dM/dt, but as we demonstrate below the assumptions used to calculate dM/dt

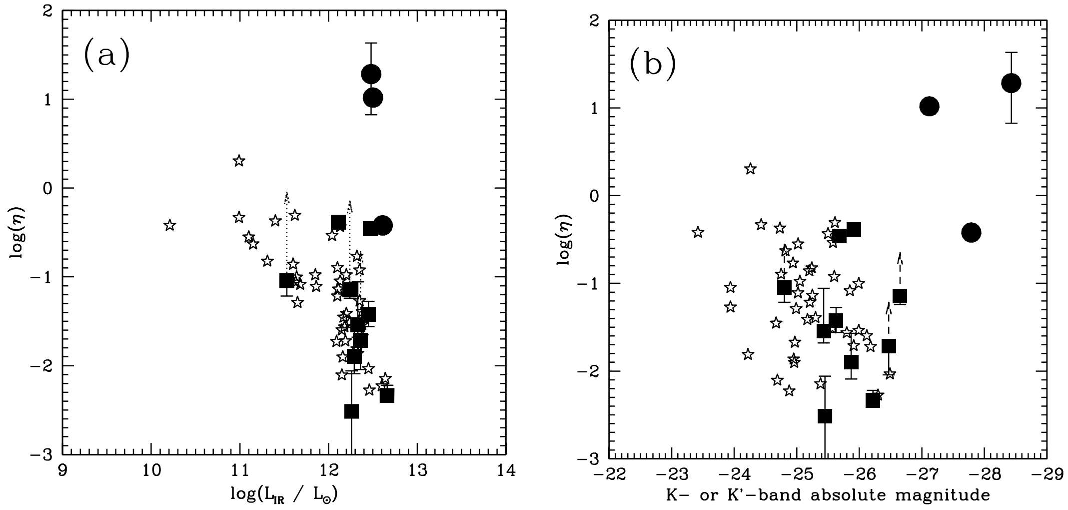

Figure 4.15: Mass entrainment efficiency vs. (a) infrared luminosity and (b) $M_{K(')}$ in starburst and active galaxies. The Seyfert 2s occupy similar, though not identical, regions to the starbursts. The symbols follow the pattern of Figure 4.12.

in Seyfert 2s and starbursts may not apply to Seyfert 1s. Note that the Seyfert 2 with the highest value of η is F05189−2524, which as we discuss earlier (§4.2) is closer to being a Seyfert 1 than the other Seyfert 2 galaxies.

4.4 DISCUSSION

4.4.1 Location of absorbing gas

Outflows in AGN are a complicated phenomenon, resulting from as-yet-uncertain physical processes and manifesting on a wide range of scales from sub-pc to kpc (as we discuss in Chapter 1). Our absorption-line data by itself contains limited information about the galactocentric radius at which the absorption occurs. However, by comparing to other data and using simple physical arguments we can make some useful statements.

One line of evidence for small-scale (i.e., inside the narrow-line region, $r \lesssim 1$ kpc) outflows in AGN is a short time-lag between changes in the ionizing flux and

Table 4.4. Time variation of blueshifted absorption in Mrk 231

Date (1)	Velocity (2)	W_{eq} (3)	Reference (4)
1984 December	⋯	⋯	Hamilton & Keel 1987
1988 May	-7760	2.1	Boroson et al. 1991
1991 April	-7830	1.7	Forster et al. 1995
1994 April	-7860	0.9	Forster et al. 1995
2001 February	-8020	0.3	Rupke et al. 2002
2004 April	-7960	0.2	this work

Note. — Col.(1): Date of observation Col.(2): Velocity relative to systemic, in km/s, assuming a redshift of $z = 0.04217$. Col.(3): Rest-frame equivalent width, in Å. Col.(4): Reference.

changes in the absorber. For instance, this technique applied to FUV data of NGC 4151 implies that the absorber radius is less than 25 pc (Espey et al. 1998). A second line of evidence is that broad absorption lines in QSOs partly or completely cover the BLR emission (Turnshek 1988), which implies a minimum distance to the quasar of 0.1 pc and a maximum distance of a few tens of pc.

In the absence of high spatial resolution spectra, perhaps the most convincing argument for small radius-outflows in Seyferts is the observation of variation in the line profile with time. Variability in column density on short timescales can imply short distances to the ionizing source (Crenshaw et al. 2003). It can also be caused by motion of the absorbing cloud across the continuum source (Crenshaw et al. 2003). The bluest component in Mrk 231 is seen to be time-variable. Non-detections and detections are listed in Table 4.4 (with the measurements from Rupke et al. 2002 revised slightly downwards).

It is useful to note that the strength and blueshifted velocity of this feature in Na I D have decreased and increased, respectively, over time (though very recently the trend is for the velocity to decrease slightly). The most likely explanation for this trend is an increasing ionizing luminosity seen by the absorbing gas, which would reduce the equivalent width by ionizing the cloud and/or decreasing the line/continuum contrast and would simultaneously accelerate the gas radially via radiation pressure. The small change in W_{eq} over the last three years and the slight deceleration of the gas could imply a recent weakening in the continuum luminosity or possibly interaction with an ambient medium.

Absorption-line evidence for large-scale outflows in AGN also exists. Dusty, 'lukewarm' absorbers have unique properties: they (a) show saturation in UV lines; (b) may cover and redden the narrow-line region, implying radii of at least 100 pc; (c) may originate in the host galaxy; and (d) have measured column densities and velocities of a few times 10^{21} cm^{-2} and less than 200 km s^{-1}, respectively (Crenshaw et al. 2001; Crenshaw & Kraemer 2001; Crenshaw et al. 2002). Ionization modeling of the broad absorption-line systems in the quasar FIRST J104459.6+365605, with velocities in the range $200 - 1200$ and $3400 - 5200$ km s^{-1}, imply that column densities are $\sim 10^{21}$ cm^{-2}, the absorbing radius is roughly 700 pc, and the mass outflow rate is 70 M$_{\odot}$ yr^{-1}(modulo the global covering factor) (de Kool et al. 2001). Finally, ionization modeling of associated absorption lines in 3C 191, which has absorbing velocities of $400 - 1400$ km s^{-1}, yields column densities of $10^{18.6}$ cm^{-2} or less in the low-ionization gas (and at least $10^{20.3}$ cm^{-2} in the high-ionization gas) and radii of ~ 28 kpc (Hamann et al. 2001).

The fact that we see emission on scales of 5 kpc or greater at or near the velocity of Na I D absorption in several of our Seyfert galaxies is suggestive of outflows on kpc scales in at least some systems. However, the correlation with high-velocity [O III] emission (§4.4.3) instead suggests smaller scales ($\lesssim$ 250 pc), since the blue wings of these lines are generally unresolved and arise in the inner narrow-line region (e.g., Veilleux 1991c, and references therein). The greater dispersion we see in dM/dt in AGN compared to starbursts may in fact reflect a larger dispersion in radii for the absorbing gas in AGN, suggesting that we see gas at both large and small scales. The peak at high covering fractions in AGN may also indicate absorption on small scales (though it could also reflect the intrinsic size of the background continuum source).

Another argument for a different radial distribution of gas in some of these galaxies compared to starbursts is the very high mass outflow rates that we compute in Seyfert 1s. Mass outflow rates of a hundred to several thousand km s^{-1} will move over 10^{9-10} $M_{\odot}$ of gas in only 10 million years, which is a substantial disruption (though note the total mass of 2×10^{9} $M_{\odot}$ in the outflow in 3C 191; Hamann et al. 2001). Furthermore, if these winds are driven by black hole accretion, they are at least 1000 times the Eddington accretion rate for a mass-to-energy conversion efficiency of 0.1 and a bolometric luminosity of 10^{46} ergs (as in Mrk 231). Lowering C_{rad} by several orders of magnitude in these galaxies will ameliorate this (though there may be other necessary adjustments, as well, such as correction for very high ionization).

In one galaxy, F05189−2524, we have a low-resolution spectrum obtained with STIS on HST that probes radii of 200 pc or less with respect to the galaxy's nucleus (Farrah et al. 2004, in preparation). Interestingly, this spectrum does *not* show the deep Na I D absorption observed in the ground-based data; we measure equivalent widths of 0.7 Å and 5.4 Å for the HST and ground-based spectra, respectively. This implies that this absorption occurs at projected radii of 200 pc or greater and that the background source for this is not the core of the Seyfert nucleus, but rather a more extended continuum source (which is also consistent with the strong stellar lines observed in the ground-based spectrum). A caveat is the bright He I λ5876 emission that is seen in the STIS spectrum but not the ground-based spectrum. In the STIS spectrum, this emission line could blend with Na I D and reduce its observed equivalent width, though there would have to be 50% more He I emission than is observed to bring the Na I D equivalent width in line with the ground-based data.

A further line of argument for an outflow at kiloparsec radii in F05189$-$2524 is slightly extended absorption in our ground-based spectrum. Roughly $2''$, or 2 kpc, to the south we observe both the narrow and broad absorption seen in the nucleus. We do *not* observe this absorption 2 kpc to the north of the nucleus, which suggests that this is not a seeing effect (which would probably be symmetric around the nucleus). Interestingly, in each of these offset spectra we also observe what appears to be redshifted Na I D *in emission*. Similar behavior is seen in an outflow in NGC 1808; this emission is interpreted as resonance scattering by the receding part of the outflow (Phillips 1993). The velocity of this emission is consistent with this interpretation, as it appears to be redshifted roughly 100 km s^{-1} from systemic (matching the velocity of the blueshifted absorbing component nearest to systemic). Another potential origin of this emission is scattered light from the broad line region of the nucleus, but such signatures are not obvious in other emission lines.

4.4.2 Luminosity dependence

A recent study by Laor & Brandt (2002) finds strong luminosity dependence in the maximum outflow velocity in AGN. They find that Δv_{max} (as measured in the UV in the [C IV] high-ionization lines) increases as visual luminosity M_V increases and that Δv_{max} decreases as the equivalent width of [O III]λ5007 increases. Many of the galaxies they study are quasars with outflow velocities up to and exceeding 10^4 km s^{-1}.

In Figure 4.13, we plot Δv_{max} as a function of $L_{\rm IR}$ and K-band luminosity, and find no obvious trends. Note that K-band luminosity is not obviously equivalent to M_V, since the latter may be a much better tracer of the ionizing continuum of the AGN. However, a similar plot of Δv_{max} vs. M_R shows no correlations, either. As for [O III] dependence, since all but one of our Seyfert 1s have weak or undetected [O III] emission, we can only look at this behavior in Seyfert 2s.

Figure 4.16 shows Δv_{max} vs. W_{eq}([O III]) for the Seyfert 2s in our sample. There is no obvious dependence, but there is a hint of a possible upper envelope in Δv_{max} that decreases as W_{eq}([O III]) increases. In this figure we also show the approximate dependence that we estimate by eye from the plot in Laor & Brandt (2002), which is $\log(-\Delta v_{max}) \sim 0.04\ W_{eq}$([O III]) (scaled so that $\Delta v_{max} = -20000$ km s^{-1}at $W_{eq} = 0$). The possible upper envelope is not consistent with this solution.

4.4.3 Emission and absorption-line correlations

Blue asymmetries in AGN emission lines, especially the high-ionization lines, are a common and well-documented phenomenon (e.g., De Robertis & Osterbrock 1984, 1986; Veilleux 1991a,b,c). There are many models for the narrow-line region in AGN, and they go beyond the scope of this work. However, suffice it to say that outflowing gas is a common (but not universal) feature (e.g., Veilleux 1991c, and references therein), which may help to explain these blue asymmetries. In emission lines, however, outflow is not always distinguishable from radial inflow.

Blueshifted absorption lines are thus useful in that they are an unambiguous indicator of outflow. Correlations with emission-line wings would be a telling indicator that emission lines also probe outflowing gas, perhaps in the narrow-line region.

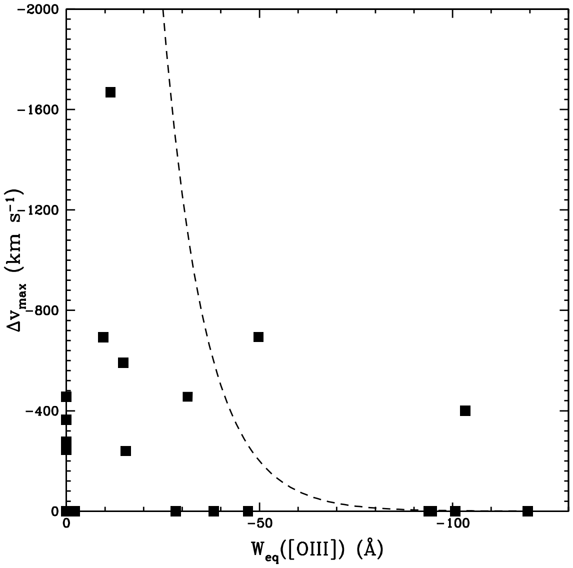

Figure 4.16: Maximum outflow velocity vs. rest-frame equivalent width of [O III]λ5007 in Seyfert 2s. We find a possible upper envelope for Δv_{max} that decreases as W_{eq}([O III]) increases, but the two quantities are not significantly correlated. The points on the axes have either no outflow or no measured [O III]λ5007 equivalent width. The dashed line is the upper envelope for quasars and Seyferts from Laor & Brandt (2002), scaled appropriately.

In Figure 4.17, we plot the maximum Na I D velocity in Seyfert 2 nuclei as a function of the full-width at half maximum and 20% of maximum of the [O III] line. We find that Δv_{max} is correlated with FWHM at $> 97\%$ confidence using the standard parametric correlation coefficient. Δv_{max} is also correlated with the full-width at 20% maximum at $> 90\%$ confidence if instead we use a non-parametric correlation coefficient (though in each case the alternate statistic yields lower confidence levels). Thus we tentatively conclude that Δv_{max} is correlated with these quantities, though the number of points is low and the statistical tests are somewhat ambiguous.

This suggests that the high-velocity neutral gas we observe in absorption is associated with high-ionization gas at both low and high velocities with respect to systemic. The implication is that the physical model that explains the ionized gas must also account for a substantial amount of neutral gas at similar velocities, and perhaps at the same physical location. If the latter is the case, clearly something

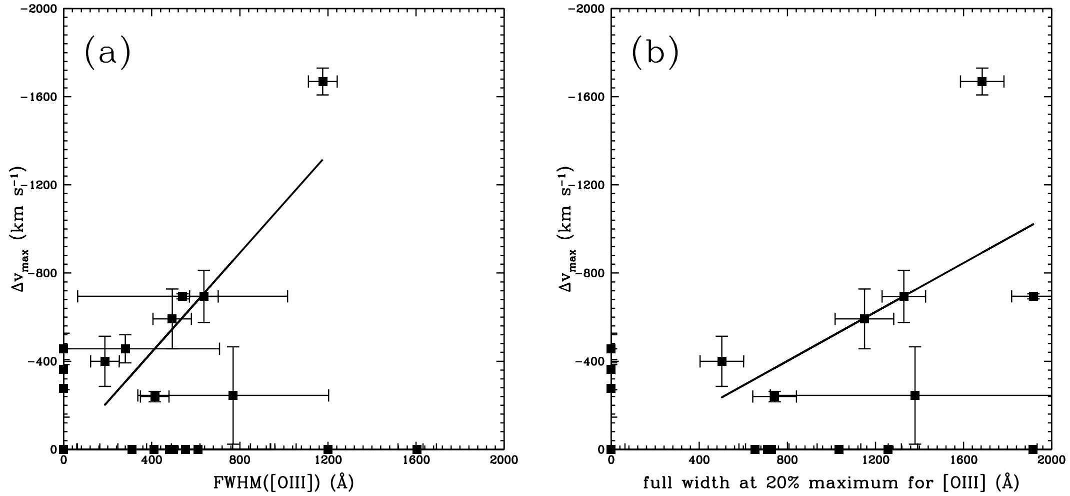

Figure 4.17: Maximum outflow velocity vs. (a) full-width at half-maximum and (b) full-width at 20% maximum of [O III]λ5007 in Seyfert 2s. Δv_{max} may be significantly correlated with FWHM and the full width at 20% of maximum, in the sense that it increases as the [O III] width increases; the confidence levels depend on the statistic used. The points on the axes have either no outflow or no measured [O III]λ5007 widths.

is necessary (e.g., high columns of gas and/or dust) to shield the neutral gas from ionizing radiation.

A caveat to this conclusion is F05189$-$2524, whose absorption apparently occurs at large scales ($\sim 0.2 - 2$ kpc), while the bulk of the highly ionized material is at smaller radii (as can be confirmed from the STIS spectrum). Thus, in at least one case this correlation may be coincidental rather than physical.

4.4.4 Frequency of occurrence and global covering fraction

As we discuss in Chapter 3, the detection rate D is a function of both the real frequency of occurrence of winds F and the global angular covering fraction of the wind, C_Ω. We can set lower limits to F and C_Ω using our detection rate: $D < F < 1$ and $D < C_\Omega < 1$.

As in the starburst case, the interpretation for our Seyfert 2 galaxies is that (a)

$C_\Omega = 0.50$ for all Seyfert 2s and every Seyfert 2 hosts a wind; (b) $C_\Omega = 1$ for all Seyfert 2s and only 50% host a wind; or (c) something in between.

For Seyfert 1 galaxies, the wind structure may be quite different; it may not be a continuous, collimated structure as is probably the case with large-scale winds. Thus, we must also consider the local clumpiness of the wind (perhaps described by C_f) in computing C_Ω. For Seyfert 1 galaxies, $C_\Omega = F \times \langle C_f \rangle$, and from observations of high-ionization absorption lines, this fraction is inferred to be high: $C_\Omega \sim 0.5$ (Crenshaw et al. 2003). Our data suggests that $C_\Omega \sim 0.3$ in Seyfert 1s, but our measurement is somewhat uncertain given the uncertainties in fitting the broad absorption lines in these galaxies.

4.4.5 BALQSOs and ULIRGs

We observe six Seyfert 1 galaxies from the 1 Jy sample, three of which possess blueshifted Na I D. Boroson & Meyers (1992) observe blueshifted Na I D in 4 of 19 infrared-selected quasars (including F07599+6508 and F12540+5708). Interestingly, all four of these are low-ionization broad-absorption line quasars (lo-BAL QSOs), which by definition have an obvious Mg II $\lambda\lambda 2795, 2802$ doublet in the UV as well as low-ionization broad absorption lines (Weymann et al. 1991). Furthermore, they are all ULIRGs; their infrared colors are intermediate between those of ULIRGs and QSOs; images of their hosts show signs of major merger; and spectra show that their hosts possess young starbursts, with ages $\lesssim 250$ Myr (see Canalizo & Stockton 2001, and references therein). Given that the four nearest lo-BAL QSOs are also ULIRGs, we expect that F11119+2357 may also turn out to be a BALQSO (though the properties of its Na I D feature are closer to those of intrinsic absorbers; see Chapter 1).

The lo-BAL QSOs as a class have a number of unique properties. These include weak [O III]λ5007 (Boroson & Meyers 1992), strong Fe II lines (Weymann et al. 1991), red continua (Weymann et al. 1991), and relatively weak X-ray flux and/or high absorbing columns (Gallagher et al. 2001). It has been hypothesized that lo-BAL QSOs have very high global covering fractions, and that IR-luminous lo-BAL QSOs may represent a stage in the life of quasar when the nucleus is enshrouded in dust and is in the process of destroying this screen via fast outflows. Thus, it may be an evolutionary stage in the proposed scenario by which some quasars are formed by major mergers. In this scenario dust-enshrouded ULIRGs are an intermediate stage between the merger and a quasar. Consistent with this idea is the much higher incidence of lo-BAL QSOs in infrared-selected quasar samples than in optically-selected samples (27% vs. 1.4%; Boroson & Meyers 1992).

4.4.6 H I gas

We claim high column densities of H I gas in these outflows, of magnitude 10^{20-22} cm^{-2}. Recently, Morganti et al. (2003) observed a weak, broad component in H I absorption in the radio galaxy 3C 293. They measure velocities blueshifted up to 1000 km s^{-1} with respect to systemic (with a full-width at zero intensity of 1400 km s^{-1}). They also estimate column densities of 10^{21} cm^{-2} or larger. Finally, evidence for outflowing gas is also seen in the blue tails of low-ionization forbidden emission lines in the same galaxy.

These velocities and column densities are comparable to those we measure in some of the galaxies in our sample. Thus, it is conceivable that blueshifted H I is detectable at low levels in these systems. It would be instructive to take a moderately-high resolution optical spectrum of 3C 293 to look for evidence of outflowing gas in Na I D. At least three of the galaxies in our sample (F04210+0401, F13451+1232, and F23389+0300) are radio galaxies, and two possess outflowing gas detected in

Na I D at velocities up to -300 km s^{-1} with respect to systemic.

Morganti et al. (2003) suggest that the outflowing gas in this galaxy is a result of the shocking of the interstellar medium by the radio jet. They consider other options such as a starburst superwind, but they dismiss this option because of the age of the starburst in the galaxy, which is $0.5 - 2.5$ Gyr.

4.4.7 Gas escape fraction

There are several Seyfert 2 galaxies with very high velocities in our sample. This means that some of this material, if it is at large enough radius and does not encounter substantial drag from interstellar gas, will escape the galaxy and enter the intergalactic medium. It is difficult to estimate precise escape velocities for these galaxies. However, we can make simplifying assumptions that allow us to calculate an 'escape fraction' of gas. We consider this illustrative rather than strictly quantitative due to the uncertainties.

As in Chapter 3, we assume a singular isothermal spherical density distribution with circular velocity v_c that truncates at a radius r_{max}. If the absorbing gas is at a radius r, then the escape velocity is parameterized uniquely by v_c and r_{max}/r. Assuming constant values for v_c of $200 - 300$ km s^{-1} and for r_{max}/r of $10 - 100$ (which is nominal for an absorbing radius of $1 - 10$ kpc and a dark matter halo of size ~ 100 kpc), we compute a range for the escape fraction of gas f_{esc} of $50 - 60\%$. To get this value we sum over the escaping mass outflow rate in the entire sample and divide by the total mass outflow rate for the sample. The value for f_{esc} is based on $1 - 8$ galaxies which individually have $f_{esc} > 1\%$ (recall from Chapter 3 that this is our criterion for including a galaxy in the calculation of $\langle f_{esc} \rangle$). The magnitude of f_{esc} is dominated by the galaxies with the highest velocities (and correspondingly, the highest mass outflow rates). Furthermore, if we correct for projection effects in the velocities, f_{esc} is likely to increase.

If this value of f_{esc} is correct to within a factor of 5 (i.e., $f_{esc} \gtrsim 10\%$), then the neutral outflowing gas in AGN-dominated ULIRGs may play a significant role in enriching the intergalactic medium at higher redshifts, where the number density of ULIRGs is high (see the Introduction to Chapter 3). Furthermore, the hot free wind that drives the expansion of the large-scale winds in starbursts may also be present in these systems. This gas has more kinetic energy and is hence even more likely to escape the galaxy and enter the IGM.

4.4.8 Comparison to starburst-dominated galaxies

Is there evidence from our data that these outflows are powered by AGN rather than starbursts? The fact that the infrared luminosities of many of these galaxies may be dominated by radiation from an AGN rather than a starburst does not a priori imply that these outflows are AGN-driven, as the star formation rates are still likely to be high ($\gtrsim 100$ $M_\odot$ yr^{-1} for the ULIRGs) and thus able to power substantial outflows on their own.

It is safe to say that the broad absorption lines in the Seyfert 1 galaxies are a unique case, as these types of profiles are not found in pure starbursts and are analogous to the broad lines found only in quasars. However, there may also be starburst-driven outflow components in the host galaxies of these quasars (e.g., the disk outflow in Mrk 231 and possibly the low-velocity component in the nucleus).

We show above that the properties of outflows in Seyfert 2s are largely statistically identical to those in starburst galaxies. The only significant difference is in the distribution of Δv (at $> 98\%$ confidence). The Seyfert 2s also have a higher upper envelope for Δv_{max} in Seyfert 2s at 700 km s^{-1} (vs. 600 km s^{-1} for starbursts). Furthermore, if we assume a conversion from L_{IR} to star formation rate such that the AGN produces roughly half of L_{IR}, the Seyferts fill the same region of the L_{IR}-η diagram that is populated by starbursts (Figure 4.15. Complicating the situation is the fact that a thermal wind from an active black hole accretion disk can have similar large-scale effects as a starburst nucleus (Schiano 1985), though admittedly the energy injection is on different scales (Strickland 2004).

The relative contribution of AGN and starbursts to outflows in the local universe is still unresolved. Our data do not distinguish between outflows in starburst and Seyfert 2 infrared-luminous galaxies, and are thus consistent with being driven by either or both power sources.

4.5 CONCLUSIONS

It is clear from this chapter and the last that outflows are a common phenomenon in both starburst- and AGN-dominated infrared-selected galaxies. In this chapter we find a 50% detection rate in infrared-luminous galaxies (mostly ULIRGs) that are optically classifed as Seyferts. This detection rate is comparable to that in starburst-dominated galaxies.

There are many similarities between the properties of outflows in most Seyfert 2s and those in starbursts. Overlap in properties such as velocity and mass outflow rate, and in the fitted profile parameters, suggest that there could be a common power source for outflows in starburst-dominated ULIRGs and at least some Seyfert 2s. Furthermore, assuming a reasonable conversion from SFR to L_{IR} for AGN, we find that starbursts and most Seyfert 2s overlap in the L_{IR} vs. mass entrainment efficiency plane.

We find few significant differences between starbursts and Seyfert 2s. Seyfert 2s have significantly different distributions of Δv, and have higher maximum values of Δv_{max} (700 km s^{-1}) than in starbursts (600 km s^{-1}). The latter is based on two galaxies with 600 km s^{-1} $<$ Δv_{max} $<$ 700 km s^{-1}. We find very high (up to $\Delta v \sim 10^4$ km s^{-1}) velocities in Seyfert 1s. Overlap in properties such as velocity and mass outflow rate, and in the fitted profile parameters, suggest that there could be a common power source for outflows in starburst-dominated ULIRGs and at least some Seyfert 2s. Furthermore, assuming a reasonable conversion from SFR to $L_{\rm IR}$ for AGN, we find that starbursts and many Seyfert 2s overlap in the $L_{\rm IR}$ vs. mass entrainment efficiency plane.

The outflow phenomenon in Seyfert 1s is likely to be powered dominantly by the central black hole engine and to emerge on small scales, based on simple physical arguments, comparison to the properties of quasar absorption lines in the UV, and time variation in the absorption properties. Furthermore, possible correlations between the velocity width of [O III]λ5007 and the maximum velocity observed in Na I D suggest that neutral gas outflows may be linked to outflows of highly ionized gas in the narrow-line region of Seyfert 2s. However, even in Seyfert 1s there may also exist starburst-powered outflows in the host galaxy, as we show to be a possibility in Mrk 231. Cases such as F05189$-$2524 also (a Seyfert 2) argue for absorption on kiloparsec scales, rather than in the inner narrow-line region where the high-ionization lines originate.

Since at least some powering of outflows in Seyfert 2 ULIRGs is likely to come from a circumnuclear starburst, it would clearly be useful to observe a sample of Seyferts in which the starburst component is minimal. Observing Seyferts selected either by nuclear X-ray or radio emission would allow a look at the absorption-line phase of outflows in a sample of Seyferts that is less biased towards starbursting galaxies. It would be especially useful to compare to a set of galaxies which have well-studied narrow-line regions in emission. Ideally, one would also want to select a sample at similar redshifts to those observed here in order to minimize aperture effects.

The total fraction of outflowing gas that escapes Seyfert 2s and enters the IGM is non-negligible, perhaps as high as 50−60% when averaged over the whole population. Thus AGN-dominated ULIRGs are more likely to pollute the intergalactic medium with gas and energy than the starburst-dominated ULIRGs. However, it is unclear whether the outflows in these galaxies will contain metal-enriched gas, as is almost certainly the case in starburst-dominated galaxies.

Chapter 5

High-Resolution Spectroscopy

5.1 INTRODUCTION

One of the primary results from the last two chapters is the measurement of the column density of outflowing neutral gas in the line of sight. This quantity, along with the measured outflow velocity and an axially symmetric, constant density model, leads to a mass outflow rate. As discussed in Chapter 3, this calculation has a number of uncertainties involving both the limitations of our measurements and the lack of a model incorporating detailed physics.

One of the measurement uncertainties lies in our inability to resolve narrow components in the absorption lines in our spectra. Any unresolved narrow components can cause us to underestimate the true column density of the absorbing gas (Nachmann & Hobbs 1973). Higher resolution spectroscopy allows us to resolve features with a smaller width in velocity space. The cost of going to higher resolution is that the photons are more finely dispersed across the detector, which decreases the signal-to-noise in each pixel. Thus, observations at high resolution are only possible with large telescopes and bright targets.

In this chapter, we discuss the results from an investigation at high spectral resolution of five galaxies from our full sample. We present the spectra and our analysis, and compare to our moderate-resolution observations. Finally, we compare this data to other high-resolution observations and discuss the constraints we can place on the outflowing absorbers.

5.2 SAMPLE AND RESULTS

5.2.1 Sample

We culled a small number of galaxies from our full sample, selected to represent a variety of interesting profile types. These galaxies and their properties are listed in Table 5.1. We observed these targets during one night of observing at the 10m Keck I telescope using the High Resolution Spectrograph (HIRES); the spectrograph and observations are fully discussed in Chapter 2.

One of these galaxies is a Seyfert 2, and the other four are LINERs. Four are ULIRGs from the 1 Jy sample (Kim & Sanders 1998), and the fifth is a LIRG from the RBGS (Sanders et al. 2003) with $\log(L_{\rm IR}/L_\odot)$= 11.10. Their redshifts range from $z = 0.02$ to 0.14.

5.2.2 Spectra

The observed spectra of these five galaxies are displayed in Figure 5.1. Overlaid on these spectra are fitted profiles. The binning in Figure 5.1 is 13 km s^{-1}, equal to the spectral resolution. In Figure 5.2, we display these spectra again, this time with the moderate-resolution spectra (presented previously in Chapters 3 and 4) plotted below. We also show the components of each fit and 1σ error bars. The binning for each spectrum is 36 km s^{-1} (except for F02437+2122, which has 57 km s^{-1} bins). Table 5.2 lists the parameters we measure for each component in our fits.

Table 5.1. Sample

Name (1)	z (2)	Type (3)	L_{IR} (4)	dM/dt (5)	t_{exp} (6)	PA (7)	Refs (8)
F02437+2122	0.0233	L	11.10	8.43	4800	55	34
F03250+1606	0.1290	L	12.13	31.17	9000	0	1
F05189−2524	0.0427	S2	12.11	25.58	3600	0	1
F09039+0503	0.1252	L	12.10	24.66	9600	0	1
F10378+1108	0.1363	L	12.32	55.68	6300	0	1

References. — (1) Kim & Sanders 1998; Veilleux et al. 1999b; (3) Sanders et al. 2003; (4) Kim et al. 1995; Veilleux et al. 1995.

Note. — Col.(1): IRAS Faint Source Catalog label. Col.(2): Heliocentric redshift, in vacuum. Col.(3): Optical spectral type. Col.(4): Logarithm of the infrared luminosity in units of $L_{\odot}$. Col.(5): Mass outflow rate, in $M_{\odot}$ yr^{-1}, computed from high-resolution data. Col.(6): Total exposure time, in seconds. Col.(7): Position angle of observation slit, in degrees east of north. Col.(7): Reference.

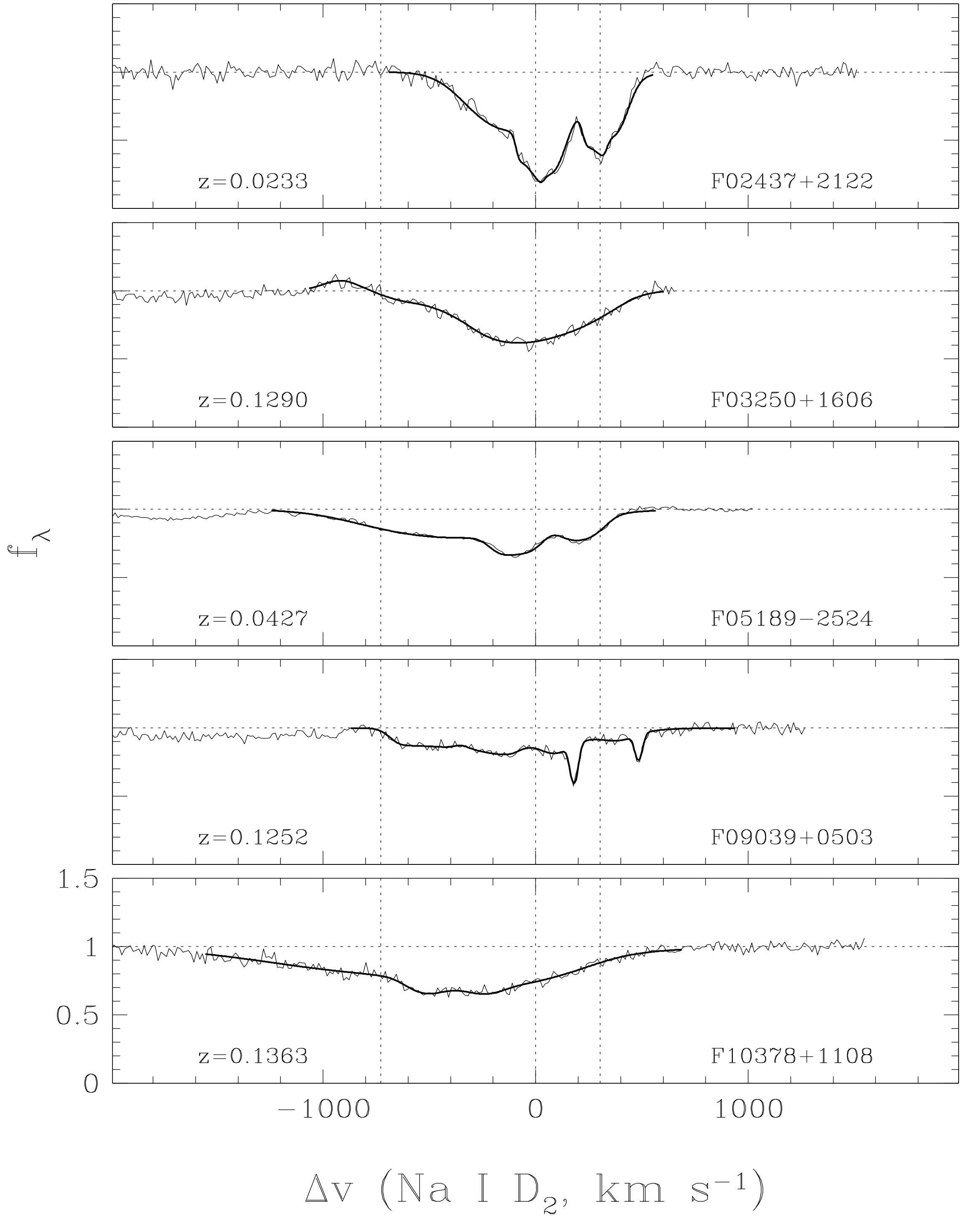

Figure 5.1: High-resolution spectra of the Na I D doublet in four ULIRGs and one LIRG. The data are displayed with only the fit superimposed.

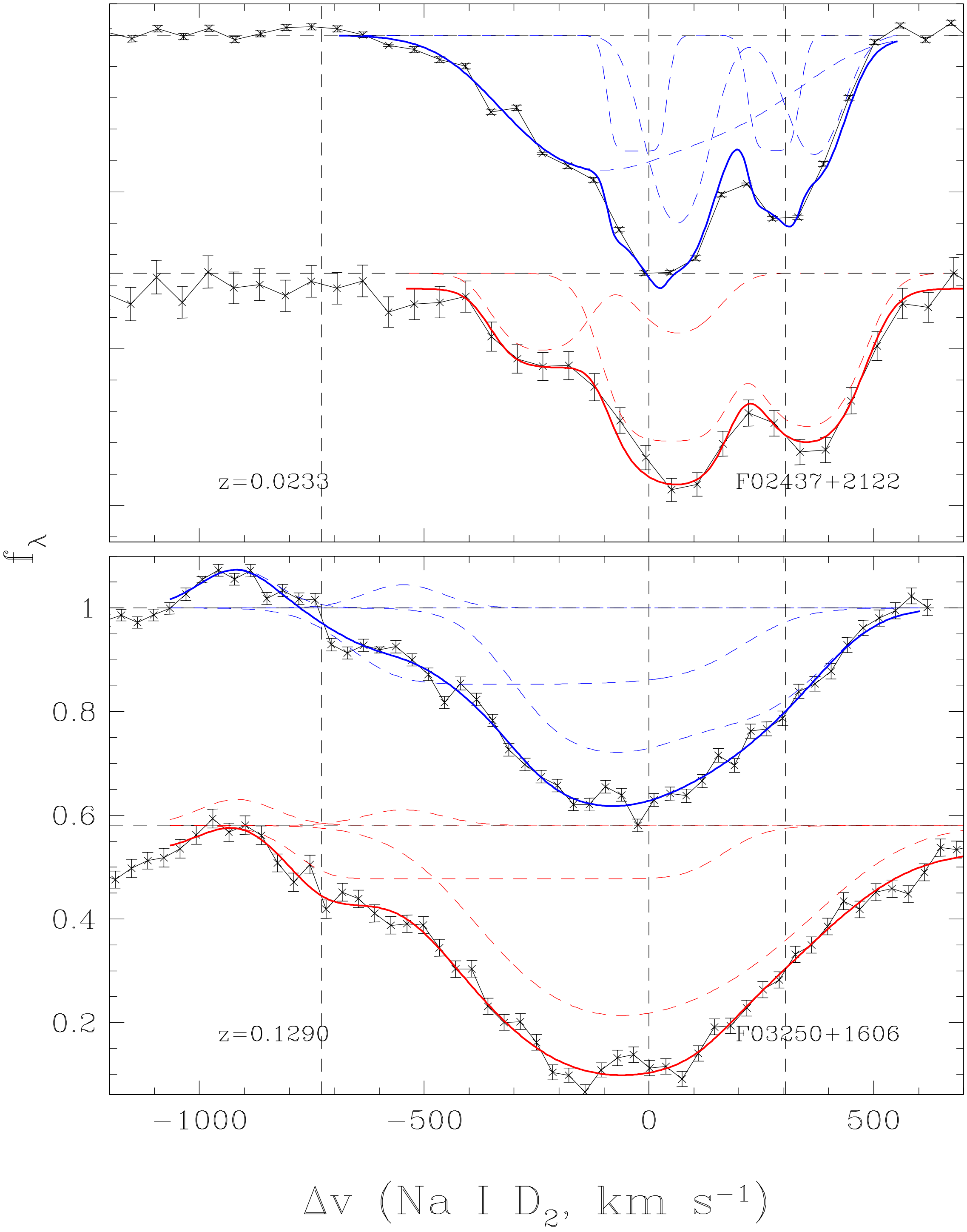

Figure 5.2: Comparison of moderate- and high-resolution spectra. For each galaxy, the high-resolution data is displayed atop the moderate-resolution data. In each case the absorption and emission components are also plotted, as well as 1σ error bars.

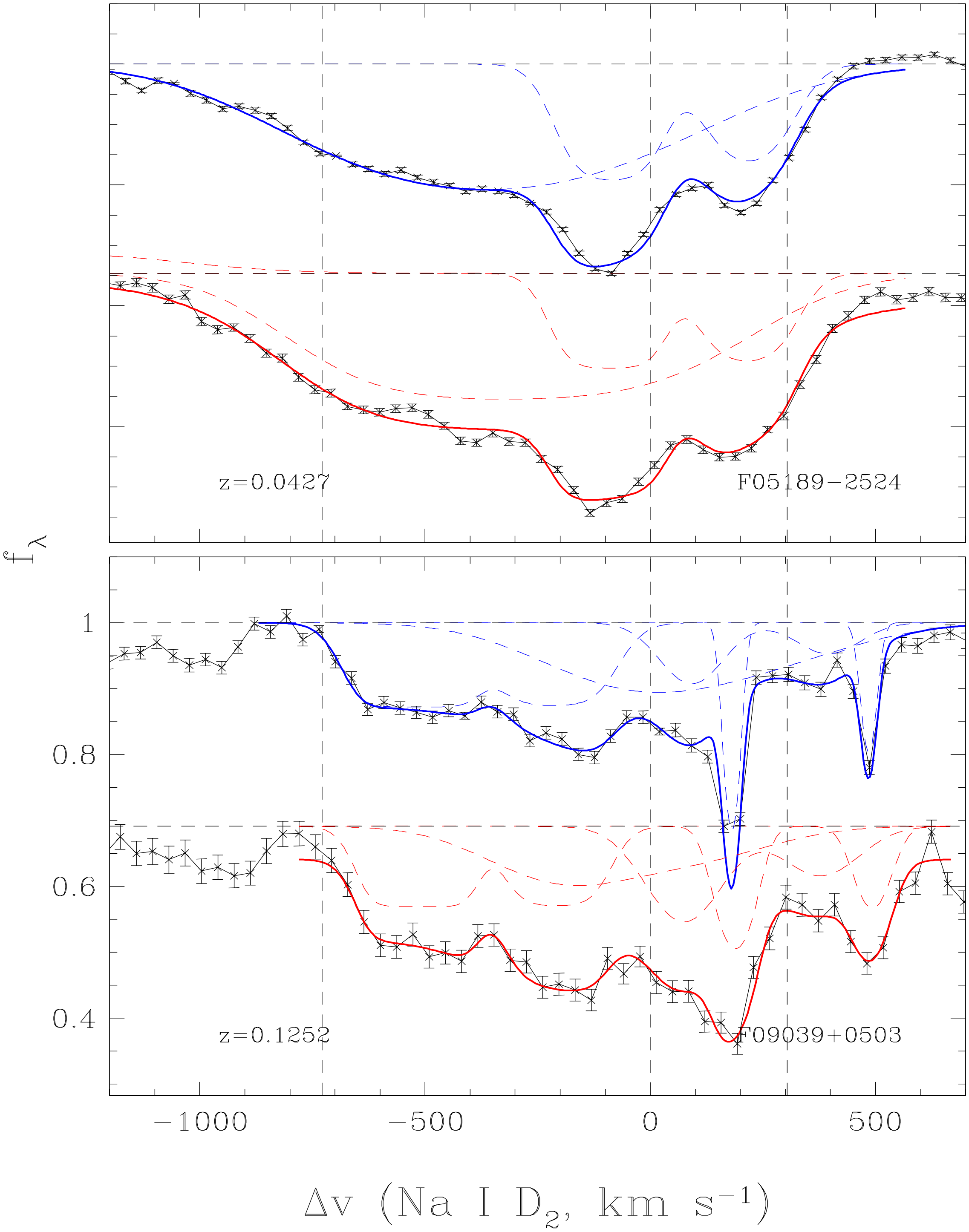

Figure 5.3: *Continued.*

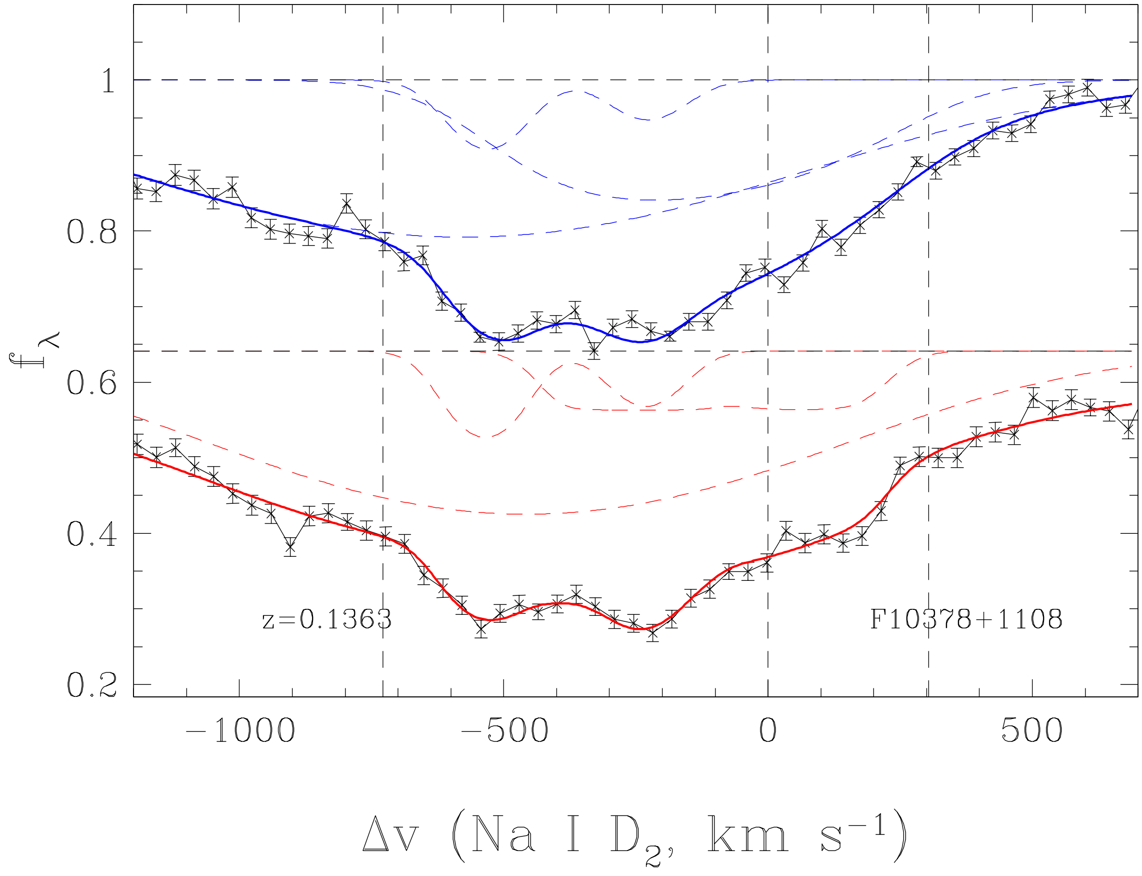

Figure 5.3: *Continued.*

Table 5.2. Outflow Component Properties from High-Resolution Data

Name (1)	$\lambda_{1,c}$ (2)	Δv (3)	b (4)	$\tau_{1,c}$ (5)	C_f (6)	log[N(Na I)] (7)	log[N(H)] (8)	dM/dt (9)
F02437+2122	6032.33	-132.79	218.65	0.48	0.66	13.57	21.21	8.43
⋯	6034.45	-27.62	8.19	6.25	0.37	13.26	20.90	0.00
⋯	6036.27	62.64	70.27	0.57	0.88	13.15	20.79	0.00
F03250+1606	6650.46	-355.04	220.35	2.49	0.15	14.29	21.93	26.44
⋯	6656.37	-89.06	194.02	0.92	0.32	13.81	21.45	4.74
F05189−2524	6140.41	-449.39	427.01	0.44	0.30	13.83	21.47	23.15
⋯	6147.86	-86.01	95.24	1.63	0.20	13.74	21.38	2.44
F09039+0503	6624.47	-518.30	101.64	4.00	0.13	14.16	21.80	24.66
⋯	6635.03	-40.58	279.15	0.10	0.50	13.00	20.64	0.00
⋯	6637.96	91.76	90.05	0.05	1.00	12.19	19.83	0.00
⋯	6639.95	181.47	23.39	0.51	0.49	12.63	20.27	0.00
F10378+1108	6686.37	-672.89	758.59	0.19	0.48	13.72	21.36	43.79
⋯	6689.54	-530.66	89.34	0.32	0.19	13.01	20.65	2.69
⋯	6695.47	-265.06	260.84	0.76	0.19	13.85	21.49	9.20

Note. — Col.(2): Redshifted heliocentric wavelength, in vacuum, of the Na I D_1 $\lambda5896$ line; in Å. Col.(3): Velocity relative to systemic, in km/s. Negative velocities are blueshifted. Col.(4): Doppler parameter, in km/s. Col.(5): Central optical depth of the Na ID_1 $\lambda5896$ line; the optical depth of the D_2 line is twice this value. Col.(6): Covering fraction of the gas. Col.(7-8): Logarithm of the column density of Na I D and H I, respectively, in cm^{-2}. Col.(9): Mass outflow rate of the component, in $M_\odot$ yr^{-1}.

We find that in all but one of these galaxies the high resolution observations reveal no obvious new narrow components. In other words, at a resolution of 13 km s^{-1}, the neutral, outflowing gas in these galaxies shows a remarkably smooth profile (though there are clearly variations on larger velocity scales). The one galaxy in which we do observe a narrow component that was unresolved by our moderate-resolution spectra is F09039+0503. The narrow component in this galaxy is redshifted by 180 km s^{-1}, and has a (resolution-corrected) Doppler width of 23 km s^{-1} (corresponding to a FWHM of 32 km s^{-1}). Since the measured FWHM is now over twice the spectral resolution, this line is resolved. The Doppler width from the moderate-resolution data is 35 km s^{-1}, larger by 50%.

Aside from the newly-resolved component in F09039+0503, the moderate- and high-resolution profiles are remarkably identical. However, in F02437+2122, we observe that, while the high-resolution data reveals no new narrow components, the high- and low-resolution data do show differences in other respects. The absorption at certain wavelengths is not quite as deep in the moderate-resolution data, and there may be a shift towards bluer wavelengths in the high-resolution data.

A closer inspection of the error bars on our data and the associated fits (Figure 5.2) indicates that there are some low-significance differences between the moderate- and high-resolution spectra. These features have a variety of characteristic scales, though these scales are not larger than ~ 100 km s^{-1}. We observe similar features in the continua of these galaxies, which suggests that these features are not due to the resolution of narrow interstellar clouds, but rather we are seeing minor flatfielding effects or (more likely) stellar features. To be more quantitative about this, we computed power spectra of the residuals from the fit with an FFT routine. These power spectra are fairly noisy, and they show nothing significant.

5.2.3 Moderate vs. high resolution

In the following section, we more carefully compare our moderate- and high-resolution data.

Aperture

The effective apertures that the observing slit subtends on the sky for the high-resolution data are $1\overset{''}{.}7 \times 1\overset{''}{.}9 - 2\overset{''}{.}3$, or approximately $4\ \square''$. The first dimension is determined by the slit width, and the second by the spatial extraction aperture during data processing (which includes most of the profile but weights the data toward high signal-to-noise pixels, i.e., the center of the profile). The apertures for the moderate-resolution data are generally only slightly different ($1\overset{''}{.}0 \times$ a few arcseconds), though for F02437+2122 the moderate-resolution aperture is significantly larger ($1\overset{''}{.}25 \times 9\overset{''}{.}7$).

The smaller extraction aperture for the high-resolution data likely explains the differences between the two data sets of F02437+2122. The physical reason for these differences is unclear, however, as multiple effects could contribute to the profile change. One possibility is that there is more continuum present in the moderate-resolution data but a similar column density of gas. The larger aperture may also probe a different overall velocity distribution of gas, since we do observe rotation in Na I D in this galaxy in the moderate-resolution data.

Continuum normalization

Because the HIRES orders are relatively short in wavelength space, only a limited amount of continuum is available for normalization (typically ~ 90 Å). We use a low-order (order $2-3$) polynomial to fit and remove the continuum. In two or three objects, this results in some subtle profile differences. This is especially true in the region just blueward of the line, which contains the He I emission line and a broad stellar feature, since both of these (along with the Na I D feature) must be avoided in the fit.

In the high-resolution spectrum of F05189−2524, the result of this discrepancy in continuum fitting is that we do not recover the faint He I emission line that is observed in the moderate-resolution data. This does not result in large discrepancies in the absorption-line fitting, however. Furthermore, we do recover the double-component He I emission lines in F03250+1606 in both data sets.

Number of components

To fit both the moderate- and high- resolution data, we increase the number of components until the properties of one or more components becomes unconstrained in the Monte Carlo data simulations. Remarkably, we find that in every case but one the same number of components is allowable at both resolutions, with the exception of F02437+2122, which has an extra component in the high-resolution data. A close examination of Figure 5.2 shows that corresponding components are in general similar in velocity and shape at different resolutions, though there are some visible differences. The biggest difference is that high resolution gives more sensitivity to high optical depths ($\tau > 5$), which allows us to relax the parameter boundaries imposed on the moderate-resolution observations.

Outflow properties

The most important test is a comparison of the fitting results for each data set. Table 5.3 lists the difference between the high- and low-resolution data for various fit parameters or computed quantities. For a given quantity, we compute the difference (high - moderate) for each component and tabulate the range and median for all components.

Overall, the differences between high and moderate resolution are not significant. However, in any given component the difference might be large. We find that the median velocity difference per component is essentially zero. The median column density difference is -0.2 dex, implying that our high resolution column densities are lower on average by 40%. This is perhaps contrary to expectation. Although we do not resolve any blueshifted narrow components, doing so should increase the column density estimate, not decrease it.

When we sum the mass outflow rates together for each galaxy, the results at different resolutions are also similar. The ratio [dM/dt(moderate) / dM/dt(high)] has a range of $0.5 - 1.4$, and the median is 1.1. Thus, the mass outflow rates measured from our high resolution data are on average only 10% lower than those measured from our moderate-resolution data, and at worst a factor of two different.

5.3 DISCUSSION

High-resolution observations of the Na I D doublet in nearby galaxies have been attempted at least twice in the past (Carter, Johnstone, & Fabian 1997; Schwartz & Martin 2004). Observations of the M87 nucleus at 9 km s^{-1} resolution reveal unresolved absorbing clouds, and at least one of these is blueshifted with respect to the nucleus (Carter et al. 1997). Schwartz & Martin (2004) observe 8 nearby

Table 5.3. Comparison of high- and moderate-resolution data

Quantity (1)	Low (2)	Median (3)	High (4)
C_f	-0.2	0.1	0.4
b (km s^{-1})	-86	19	147
τ	-4.7	-0.3	0.4
Δv (km s^{-1})	-120	6	151
$\log[N(\mathrm{Na})/\mathrm{cm}^{-2}]$	-0.8	-0.2	0.1
dM/dt (M$_\odot$ yr^{-1})	-32.8	-0.6	8.1

Note. — The difference between high and moderate resolution values of various fit parameters or computed quantities are compiled for each fitted component, and these are then used to compute the ranges and medians of these differences over all components. Positive values mean a larger value of the quantity in the high-resolution data.

starbursts at a resolution of $6 - 11$ km s^{-1}, and they find outflowing absorbing components with widths of 25 km s^{-1} and above.

The thermal linewidth for Na is 2.5 km s^{-1} in a $T = 10^4$ K gas. Thus, if clouds entrained in these outflows are dominated by internal thermal motions, we should not expect to resolve them. We observe only two components that have a FWHM smaller than 100 km s^{-1}; one of these has FWHM $=$ 32 km s^{-1} and the second has FWHM $\gtrsim$ 13 km s^{-1}. (The latter is a lower limit because this is an optically thick component whose observed width is dominated by τ, such that the resolution correction underestimates the actual velocity width.) These lower limits on FWHM are consistent with those from Schwartz & Martin (2004), though they detect many more components with FWHM $<$ 100 km s^{-1} than we do. However, many of their galaxies are dwarf starbursts.

Thus, our observations are consistent with a scenario in which individual velocity components are the superposition of many entrained clouds (of uncertain temperature) with many different velocities. The spreads in velocity of these cloud ensembles are then due to large-scale shear (and perhaps to some local turbulence within the clouds). The fact that component linewidths in these five U/LIRGs (average 235 km s^{-1} FWHM) are much larger than those in dwarf galaxies implies that (a) the outflowing gas is more disturbed in U/LIRGs than in dwarf galaxies and/or (b) due to the larger distances of these U/LIRGs, the larger effective observing aperture subtends more clouds at once, and these clouds have a larger spread in velocities due to extended structures in the line of sight.

The state of the ISM in M87 is clearly different from that in our sample galaxies, since the absorbing clouds or cloud ensembles appear to be much narrower. M87 is a giant elliptical galaxy, so it might be expected to be more gas-poor and perhaps less disturbed than the gas-rich, interacting starbursts in our sample.

This model is consistent with observations of high-velocity clouds in our Galaxy. Wakker & Schwarz (1991) find that these clouds, which have neutral hydrogen linewidths of several tens of km s^{-1} when observed over large angular scales, have much smaller linewidths (a few km s^{-1}) on smaller angular scales ($\sim 1'$). This suggests that large-scale motions exist but that an HVC complex is composed ultimately of small clouds with small individual linewidths. However, some HVCs may have a separate warm component with a larger linewidth of a few tens of km s^{-1} (vs. the cold component with FWHM of a few km s^{-1}; e.g., Brüns, Kerp, & Pagels 2001). Very high resolution (~ 2 km s^{-1}) Na I D observations of intermediate- and high-velocity clouds also exist, and resolve structures with linewidths as small as FWHM ~ 2 km s^{-1} (Lehner et al. 1999). These clouds are found in blended structures as wide as 20 km s^{-1}. A width of FWHM ~ 2 km s^{-1} is consistent with the thermal linewidth of Na at $T = 10^4$ K, but implies some turbulent broadening (or acculumation of smaller cloudlets) if the temperature is lower than this.

If we envision the absorption observed in Na I D as an ensemble of small clouds, we can make a loose estimate of the number of clouds present in the line of sight. In many cases, such an ensemble can be properly treated as a single component as we have done (Jenkins 1986). Following Daines, Fabian, & Thomas (1994), the mean number of optically thick clouds within a cloud ensemble is given by

$$\tau_{obs} = N(\gamma \Delta v / \Delta V)(1 - e^{-\tau_c}). \tag{5.1}$$

where τ_{obs} is the observed optical depth, N is the number of clouds in the ensemble, $\gamma \sim 1-2$ is a small correction factor, Δv is the width of a cloud, ΔV is the observed width of the ensemble, and τ_c is the optical depth of a cloud. Strictly speaking, this equation assumes $\tau_{obs} \ll 1$, but we will use it for illustrative purposes despite the moderate optical depths in our data.

We measure typical values of $\tau_{obs} \sim 0.8$ and $\Delta V \sim 235$ km s^{-1} within a component, or potential cloud ensemble. If we assume that $\tau_c \sim 1$, then $N \times \Delta v \sim 300$. Using the upper limit $\Delta v \lesssim 13$ km s^{-1} based on our data, we find that there are at least 25 clouds per ensemble. In reality, the number of clouds should be much larger; for instance, the number of warm ionized clouds or resolved structures seen in high-resolution HST observations of NGC 3079 is at least 230 (Cecil et al. 2001). If we assume a thermal linewidth for Na at $T = 10^4$ K (such as observed in high-velocity cloudlets), we expect many more clouds, approximately 1500. Note that N is quite sensitive to τ_c, such that these are upper limits to the actual number of clouds present if τ_c is larger than 1.

5.4 CONCLUSIONS

We show in the above discussion that our high-resolution observations do not clearly resolve any new outflowing components in these galaxies. One redshifted component is newly resolved in this data, and may be associated with tidal debris (as we discuss in Chapter 3). These results are consistent with observations of nearby dwarf starbursts (Schwartz & Martin 2004).

Our data suggest (or are at least consistent with) a model in which the absorbing gas consists of many clouds ($\sim 10 - 1000$) that fill the line of sight and form a large ensemble that enters our fits as a single absorbing 'component.' These clouds may be dominated by thermal motions, but could also have a contribution from local turbulence. Na I D observations of high-velocity clouds in our Galaxy resolve cloudlets down to a width of 2 km s^{-1}, and these cloudlets may be similar to clouds that exist in superwinds. However, large-scale turbulence or shear that separates the clouds in velocity space clearly dominates the linewidth of an individual component (FWHM $\gtrsim 200$ km s^{-1}) in U/LIRGs.

An interesting follow-up experiment would be high-spatial resolution (and velocity resolution) spectroscopy with a space-based telescope, to see if such clouds systems could be better resolved. STIS aboard HST possesses very high spatial resolution, though the spectral resolution may not be quite sufficient to resolve individual clouds. A simpler alternative would be to find a very nearby face-on galaxy that possesses an outflow and perform spectroscopy of the Na I D doublet across the face. With enough signal-to-noise and slit positions, one should be able to uncover Na I D absorption, perhaps in small cloud complexes.

Chapter 6

Summary and Prospects

6.1 SUMMARY

In this work, we have undertaken the most comprehensive study to date of superwinds in infrared-selected starbursts and AGN. Previous studies have shown that galaxy-scale outflows are common in infrared-selected galaxies (Heckman et al. 2000), edge-on starbursts (Lehnert & Heckman 1995, 1996), and Seyfert galaxies (Colbert et al. 1996a,b, 1998). However, our study has by far the most galaxies (over 100, including 78 starbursts and 26 AGN), enabling us to group them according to luminosity, spectral type, and redshift in order to look for trends with galaxy properties. We also cover very completely a range of star formation rate ($\gtrsim 100$ M$_\odot$ yr^{-1}) which other studies have neglected, and are able to directly compare starbursts and AGN of a given infrared luminosity.

Our technique is absorption-line spectroscopy of the Na I D feature, which is conveniently located in the optical regime for galaxies with redshifts of $z < 0.5$. Absorption-line spectroscopy is a simple and efficient technique for locating outflows in unresolved sources. Blueshifted absorbing gas is unambiguously outflowing, which presents an advantage over detection in emission (where a degeneracy exists between outflows and inflows). If velocity components of the Na I D feature are blueshifted by more than 50 km s^{-1} in a particular galaxy, we assume that a wind exists in that galaxy.

This project consists of three major parts; in order of decreasing sample size and observing investment, they are (a) moderate-resolution ($\Delta v = 65 - 85$ km s^{-1}) spectroscopy of starbursts; (b) moderate-resolution spectroscopy of AGN; and (c) high-resolution spectroscopy of five galaxies. The starburst sample is further subdivided into low-z ULIRGS ($0 < z < 0.25$), high-z ULIRGs ($0.25 < z < 0.50$), and a sample of less-luminous galaxies (IRGs, with $\langle L_{\rm IR} \rangle = 10^{11.36} L_{\odot}$).

In this section, we briefly summarize the major results of this work and compare these results to those of previous studies and to current models.

1. Detection Rate. The results from our starburst sample show that superwinds are found in the majority of starburst-dominated ULIRGs (with a detection rate of $\sim 65\%$) and in almost half of our IRG subsample (45%). These detection rates are lower limits to the actual frequency of occurrence of winds in these galaxies in the event that the angular covering fraction of these winds is less than unity, which it almost certainly is if local observations are any indication. Similar detection rates are found for Seyfert 1s and 2s, 50% of which host outflows seen in Na I D absorption.

Only one other study of superwinds in local galaxies can provide a quantitative comparison to our results. Heckman et al. (2000) observe 32 local infrared-luminous galaxies (both starbursts and AGN) using the Na I D absorption-line technique. Within the errors, their detection rates are comparable to ours. Applying to their sample the same velocity threshold as in our data, winds are present in 3 of 6 Seyfert 2s (50%) and 7 of 22 starbursts (32%).

At high redshift, winds are seen in almost all Lyman-break galaxies (LBGs;

Adelberger et al. 2003; Shapley et al. 2003); in this sense they are most comparable to ULIRGs. LBGs are different from ULIRGs, however, in that they have more modest star formation rates and are UV-bright (Steidel et al. 1996). Their star formation rates are more comparable to the IRG subsample. If we compare them to the IRGs, the higher detection rate of winds in LBGs implies either a higher frequency of occurrence or a larger global covering fraction. If the former is the case, then some physical factor apart from the star formation rate contributes to this higher frequency of occurrence (perhaps a lack of dense ambient gas). If the global covering fraction of the wind is instead significantly larger in LBGs than in IRGs, then the physical distribution of gas in LBGs is not the same as in the local IRGs (perhaps even indicating the lack of a simple gas disk).

There are some detections of outflows that are in fact due to other phenomena. We see convincing evidence of Na I D components that arise in other gaseous disks in $6-7$ systems with multiple nuclei. These components are removed from our analysis. We also find circumstantial evidence of Na I D absorption from tidal debris in a handful of ULIRGs. The most convincing case is a very narrow ($\Delta v \sim 35$ km s^{-1}) component in F09039+0503 that is redshifted by 180 km s^{-1} and matches the velocity of an extended line-emitting filament. A similar feature arises in F10190+1322. However, both of these features are *redshifted*. We expect that the maximum number of blueshifted tidal components that we observe is simply a mirror image of the number of redshifted components, and thus not significant.

2. Velocities. Maximum velocities for these winds range from 150 to 700 km s^{-1} in both starbursts and Seyfert 2 galaxies; typical values for Δv_{max} are $300-450$ km s^{-1}. If we make a statistical correction for projection effects, a 'typical' Δv_{max} is in reality close to the maximum value that we measure ($500-700$ km s^{-1}, depending on the sample). We also measure the velocity of the gas with the maximum column density in each galaxy; the 1σ ranges for this quantity in the IRGs and low-z ULIRGs are $60 - 300$ km s^{-1}. Our measured velocities are comparable to those found using the same technique by Heckman et al. (2000), but are larger than the deprojected velocities measured in warm, ionized gas in edge-on starbursts (Lehnert & Heckman 1995, 1996). The projected velocities in LBGs, ~ 300 km s^{-1} on average (Adelberger et al. 2003; Shapley et al. 2003), are higher than the values we measure for Δv[max N(H)] but are comparable to the maximum velocities we measure.

These velocities are suspiciously close to the escape velocities in these systems. Does this imply some conspiracy, such that the wind velocity has a priori information about the gravitational potential? A more likely scenario is that higher velocity gas once existed, as is observed in two systems (one starburst and one Seyfert 2, with maximum velocities of 1110 and 1670 km s^{-1}, respectively). However, this high-velocity gas has in most cases quickly expanded and dissipated into the galaxy halo or the IGM, making it undetectable to our technique. Velocities of this magnitude are sometimes seen in local galaxies in the warm, ionized phase of the ISM (e.g., NGC 3079; Cecil et al. 2001). In the case of NGC 3079, this high-velocity gas may be caught in vortices along the sides of the outflow (Suchkov et al. 1994).

3. Escape fraction. The precise fraction of cool, neutral gas that escapes these galaxies is uncertain, and relies on assumptions about the gas distribution in the outflow and surrounding halo, the depth and shape of the gravitational potential of the host galaxy, and the pressure of the surrounding intergalactic medium. However, by considering reasonable ranges for these quantities, we can estimate values of f_{esc}. We model the galaxy and outflow by using ranges for circular velocity ($v_c \sim 200-300$ km s^{-1}) and outflow radius ($r \sim 0.01 - 0.1$ times the size of the dark matter halo) that are based on observations of resolved outflows and galaxies in the nearby universe, and we model the gravitational potential as a singular isothermal sphere.

These assumptions yield escape fractions of a few percent to 20% for starbursts and $50 - 60\%$ for Seyfert 2s. These globally-averaged escape fractions are even larger if velocity projection effects are accounted for.

In a ULIRG with $\eta = 0.05$, $f_{esc} = 1\%$ means that the ratio of escaping gas mass to the gas mass that is forming stars is quite small, less than a tenth of a percent. However, a 20% escape fraction yields an 'ejection efficiency' of 1% in ULIRGs. A full study of the impact of IRGs and ULIRGs on the intergalactic medium depends on their relative number density and contribution to the global star formation rate density of the universe at a given redshift. Given sufficient a sufficient galaxy density, however, these numbers show that the contribution of U/LIRGs to the pollution of the IGM may be significant.

We also find that Seyfert 2s are more efficient than starbursts at ejecting outflowing gas from their hosts. However, the outflows in Seyferts are not necessarily as metal-enriched as those in starbursts, so their impact on the enrichment of the IGM is unclear.

4. Outflow properties and the host galaxy. One of the major and unique results of this project is our comparison of outflow properties with the properties of the galaxies hosting these outflows. From the outflow, we can measure velocity (Δv_{max} or Δv[max N(H)]), mass outflow rate (dM/dt), and mass entrainment efficiency (η), and the host galaxy properties to which we compare these are star formation rate (SFR) and K- or K'-band magnitude ($M_{K^{(\prime)}}$).

We show that dM/dt and Δv_{max} are constant across two orders of magnitude of SFR and several orders of magnitude of $M_{K^{(\prime)}}$. However, the distribution of Δv[max N(H)] is different in IRGs and ULIRGs at $> 98\%$ confidence, and the median value of this velocity is larger in ULIRGs by ~ 70 km s^{-1}. The plot of Δv[max N(H)] with SFR suggests the existence of an upper envelope that increases with SFR.

There is also a clear correlation between η and SFR or $M_{K(\prime)}$, in that η decreases as either quantity increases. Thus the mass entrainment efficiencies in ULIRGs are much lower than those in the IRGs.

What of galaxies with much lower star formation rates? Seven dwarf starbursting galaxies (and one LIRG) were observed by Schwartz & Martin (2004) using the Na I D technique. Four of the dwarf galaxies contain neutral outflows, and the velocities and mass outflow rates are much lower than in our sample (using the same model for dM/dt as for our data). The lower velocities in dwarfs ($\lesssim 50$ km s^{-1}) show that there is at least a weak upper envelope for Δv_{max} and Δv[max N(H)] as a function of SFR and $M_{K(\prime)}$ when galaxies over a very broad range of star formation rate are considered. The very low mass outflow rates in dwarfs are less secure, since the model parameters used in U/LIRGs to compute dM/dt may not apply to dwarfs. If they do, however, dM/dt does increase with increasing star formation rate when galaxies of both very low and very high SFR are included. Mass entrainment efficiency also decreases gently as star formation rate increases in the galaxies with lower SFR, but it decreases much more quickly with SFR in the U/LIRGs.

Few current models make any predictions about outflow properties as a function of host galaxy properties. We discuss one model for starbursts in Chapter 3 (Shu et al. 2003); there is some agreement between their predictions for outflow properties as a function of central gas mass density and our data, but the trends that they predict for Δv and dM/dt vs. SFR do not match our data. Current hydrodynamic simulations of outflows do not predict the mass in the neutral phase of the wind or how this mass depends on the properties of the host galaxy of the wind. This is largely due to the inability of these simulations to model a sufficiently clumpy medium, since most of the neutral gas likely resides in small clouds of gas. However, simulations incorporating a fractal gas distributions are underway (Sutherland & Bicknell, in prep.) and should have more bearing on our data.

5. Low values of η in ULIRGs. Simulations of galaxy formation frequently incorporate superwinds, typically using simple prescriptions based on observations rather than actually resolving the winds in the simulation. Many simulations have assumed that the mass entrainment efficiencies in all galaxies is unity (e.g., Kauffmann & Charlot 1998; Aguirre et al. 2001a), and analytic arguments have suggested the same (e.g., Silk 2003). However, our results imply that in both IRGs and ULIRGs, η is significantly less than unity by up to two orders of magnitude. This quantity is especially low in ULIRGs; thus, galaxies with high star formation rates are less efficient at redistributing gas (per unit star formation rate) than galaxies with low star formation rates.

The discrepancy between our observations and current thought on the dependence of dM/dt on SFR and on the normalization of η means that the relative impact of massive galaxies may be less significant in cosmological simulations than previously thought. These simulations often predict that winds have the strongest impact on the formation and evolution of low-mass galaxies (e.g., Theuns et al. 2002), and our observations could mean that this effect is further enhanced relative to massive galaxies. However, few (if any) simulations incorporate galaxies of the size and star formation rate of ULIRGs. Furthermore, winds in ULIRGs may be much more common and are somewhat higher in velocity (in the sense of Δv[max. N(H)]) than less-luminous galaxies, so these effects will mitigate the differences in η between these two galaxy types.

Low values of η in ULIRGs may be explained by the copious quantities of molecular gas that are observed within 1 kpc of the nuclei of these galaxies (Sanders et al. 1991; Solomon et al. 1997). This gas could easily absorb momentum and mechanical energy from the wind, decreasing its mass outflow rate. Radiative losses are higher in the molecular gas due to the higher mass density. This gas, or other unique physical conditions in ULIRGs, may also prevent the efficient thermalization of supernova mechanical energy as the superwind is generated in the starburst.

Two potential uncertainties in our measurements of dM/dt, and hence η, are uncertainty in the geometry of the wind and in the fraction of Na atoms that are ionized. The former depends on the inner and outer radii of the wind. The inner wind radius is constrained by the size of the starburst region, and thus cannot be smaller than about 1 kpc. The outer radius is constrained by our observations; in several cases we observe (projected) absorption radii of several kpc or more. Furthermore, the range of radii must be broad, rather than small, because we observe only one very narrow absorbing component (which one would expect from a very thin shell). Thus, the radial factor in dM/dt is secure. The ionization fraction is less certain; we assume N(ionized Na) / N(all Na) = 10, which is consistent with sightlines through the local Galactic ISM. The mass outflow rate scales linearly with this quantity.

6. Redshift dependence. We have surveyed ULIRGs over a large range of redshift, from $z = 0$ to $z = 0.5$. The low-z and high-z ULIRGs are quite similar, but the detection rate in the high-z bin ($46 \pm 14\%$) is smaller than in the low-z bin ($77 \pm 8\%$). The high-z bin also has a higher median star formation rate (390 $M_\odot$ yr^{-1}) than the low-z subsample (225 $M_\odot$ yr^{-1}). Thus the discrepancy in detection rate represents true redshift evolution, dependence of frequency of occurrence on SFR (i.e., it declines at high SFR), or an observational effect. The latter two are the simplest explanations and for this reason the most likely; however, we cannot rule out redshift evolution of superwinds in ULIRGs. Observations of galaxies with lower luminosities at $0.25 < z < 0.50$ are necessary to factor out luminosity effects, and higher signal-to-noise data is necessary to mitigate distance-related observational effects.

7. Starburst-driven vs. AGN-driven winds. The properties of outflows in Seyfert 2s are remarkably similar to those of outflows in starbursts. In plots of outflow properties vs. host galaxy properties, these two samples have substantial overlap. The only significant differences are in the distribution of Δv (at $> 98\%$ confidence) and in a higher upper envelope for Δv_{max} in Seyfert 2s at 700 km s^{-1} (vs. 600 km s^{-1} for starbursts). (The difference between these upper envelopes is based on only two galaxies with 600 km $s^{-1} < \Delta v_{max} <$ 700 km s^{-1}, and the envelopes exclude two galaxies, one starburst and one Seyfert 2, with $\Delta v_{max} >$ 1000 km s^{-1}.)

Thus, the degree to which outflows in Seyfert 2s are driven by the AGN or by a circumnuclear starburst is uncertain, since both are present in these systems. As we discuss in the next section, observations of active Seyfert 2s without strong circumnuclear starbursts would help to better constrain the power sources of these winds.

8. LINERs and H II galaxies. The large size of our sample allows us to subdivide the starbursts into LINERs and H II galaxies. Past authors have suggested that these two spectral classes may be differentiated either by the presence of outflows or by their velocities: LINERs may more frequently host outflows or have higher velocity outflows than H II galaxies (Veilleux et al. 1995; Lutz et al. 1999; Taniguchi et al. 1999). We find no evidence to support the first hypothesis, but we do find evidence to support the second. The median Δv_{max} in LINERs is $50 - 100$ km s^{-1} higher than that in H II galaxies, and statistical tests show that the velocity distributions of the two subsamples are significantly different at $> 98\%$ confidence.

9. Seyfert 1s. The Seyfert 1 galaxies are a unique subsample, with very high velocity gas blueshifted up to ~ 11000 km s^{-1} with respect to systemic. The lines in two Seyfert 1s are broad absorption lines, resembling those seen in the UV in other galaxies. These two galaxies are low-ionization broad absorption line quasars (lo-BAL QSOs), a unique classification with properties that suggest they may be an evolutionary link between ULIRGs with hidden AGN and unobscured quasars. A third galaxy has an absorption-line system with properties intermediate between those of the Seyfert 1 lo-BAL QSOs and the Seyfert 2 galaxies; the lines in this system may be intrinsic absorbers.

We present evidence that the host galaxy of Mrk 231 hosts a starburst-driven wind in conjunction with the AGN-driven BAL outflow. A spectrum $3''$ south of the nucleus shows blueshifted absorption and emission in a starbursting disk with a LINER spectrum. Thus, Seyfert 1s could generically host starburst-driven outflows in their host galaxies along with the AGN outflow; the physical link between these two phenomena within a single galaxy is worth further study.

10. High-resolution data. Finally, we present very high resolution ($\Delta v = 13$ km s^{-1}) spectra of five galaxies that were also observed at moderate resolution. The high resolution spectra do not clearly resolve any new outflowing components in these galaxies. One redshifted component is newly resolved in this data, and may be associated with tidal debris. Our data suggest (or are at least consistent with) a model in which the absorbing gas consists of many clouds ($\sim 10 - 1000$) that fill the line of sight and form a large ensemble that enters our fits as a single absorbing 'component.' These clouds may be dominated by thermal motions, but could also have a contribution from local turbulence. Na I D observations of high-velocity clouds in our Galaxy resolve cloudlets down to a width of 2 km s^{-1}, and these cloudlets may be similar to clouds that exist in superwinds. However, large-scale turbulence or shear that separates the clouds in velocity space clearly dominates the linewidth of an individual component (FWHM $\gtrsim 200$ km s^{-1}) in U/LIRGs.

6.2 FUTURE PROSPECTS

We have begun to scratch the surface of redshift space in studying outflows in infrared-selected galaxies. The Spitzer Space Telescope will reveal numerous sources at higher redshifts, enabling more complete studies of distant objects. However, the Na I D transition is not particularly well-suited for galaxies above $z \sim 0.5$, so one may have to resort to ultraviolet transitions, which move into the optical region of the electromagnetic spectrum at higher redshifts. Unfortunately, the UV fluxes of these galaxies are not large, so achieving the requisite signal-to-noise at an appropriate spectral resolution may be quite difficult. Thus, studying outflows in infrared-selected galaxies using absorption-line spectroscopy is currently infeasible at redshifts much above $z \sim 0.5$.

Despite the faintness of the UV fluxes of these galaxies, planned UV spectrographs (e.g., the Cosmic Origins Spectrograph, which may be mounted on the Hubble Space Telescope) may be sensitive enough to study the nearest infrared-luminous galaxies with sufficient spectral resolution to observe outflows in absorption. The advantage of UV lines is that they present a range of ionization states, which would allow the physics of these outflows to be studied in great detail, as is currently possible with galaxies hosting an AGN.

Better physical modeling would also be possible by more careful comparisons between absorption and emission lines. By studying resolved galaxies with superwinds in both the spatial and spectral dimensions, one could better understand the relation between the neutral and ionized phases of an outflow. A local, nearly face-on starbursting galaxy would be an ideal laboratory for studying the 2-dimensional kinematics of outflowing gas in absorption, though separating the superwind emission from background emission may be difficult in this case. On-going studies of molecular and H I gas in well-known superwinds will also help to elucidate their multi-phase properties. H I absorption studies may even be feasible with the new generation of large-diameter radio dishes coupled with broad-band spectrometers.

Better modeling of superwinds is an undeniable imperative. We expect these winds to be loaded with interstellar matter that is entrained as the wind moves through the ISM of the galaxy; if the ISM is treated incorrectly, the outcome of this process cannot be reliably predicted. Thus the mass outflow rates and energies that are output from these simulations are of limited use. However, new and realistic simulations of superwinds are now in progress (Bicknell & Sutherland 2004, in preparation) to incorporate for the first time a multi-phase ISM with a fractal gas distribution.

The success of our absorption-line technique for a large sample of galaxies is encouraging, and suggests that it could be applied to a broad array of galaxy types. Specifically, it would be useful to look at Seyfert galaxies which are not infrared-selected, in order to better separate the contributions from starbursts and AGN to outflows in these galaxies. It would be useful to survey galaxies over a wider range of star formation rates, in order to fully understand the trends of outflow properties with galaxy luminosity that we have begun to explore.

A new multi-object spectrograph with moderate resolution (~ 1 Å) has recently come on-line on the Keck telescope. DEIMOS is the first of a generation of multi-object spectrographs that will enable the absorption-line technique to be used to study galaxies over a substantial range of redshift in a single field. The efficiency of a multi-object spectrograph allows even greater statistical completeness, as well as searches over a variety of galaxy types.

A complementary technique to survey the sky for superwinds is to look for extended gas with shock-like line ratios (e.g., [N II]$\lambda 6583/\mathrm{H}\alpha > 1$) in individual galaxies. This technique works for single galaxies in the very local universe, and may be feasible out to at least 100 Mpc (Veilleux & Rupke 2002). Surveys of line ratios over a wide field of view will be made possible by the next generation of tunable filters on $6 - 10$m class telescopes.

Appendix A

Properties of Individual Galaxies

Here we discuss unique properties of individual galaxies based on our spectra and available images.

- **F01417+1651 (III Zw 35)**. The spectral types listed in Veilleux et al. (1995) are backwards.

- **F02509+1248 (NGC 1134)**. This galaxy has no spectral type in the literature, and we do not observe the [OIII] line in this galaxy. However, Condon, Cotton, & Broderick (2002) classify it as a starburst on the basis of (1) the radio/FIR flux ratio, (2) the 25μm/60μm flux ratio, and (3) a lack of extended radio structures.

- **F02512+1446**. Zink et al. (2000) and Surace, Sanders, & Mazzarella (2004) show that the southern nucleus is the source of the far-infrared emission. The northern nucleus in this galaxy contains no emission lines. It does, however, contain blueshifted Na I D gas in its spectrum that is at the redshift of the southern nucleus, suggesting that the S nucleus is in the foreground. If we assume this, and also that the redder Na I D component in this galaxy is the stellar systemic velocity, we compute a redshift for the N nucleus of 0.0324.

- **F1_5**. This galaxy is the only one in our sample without IRAS fluxes. (The apparent peaks in the 60 and 100 μm flux maps are from another nearby IR source.) It does have an ISO 12 μm flux, and its bolometric luminosity is estimated using a starburst SED (Clements et al. 1999, 2001). This is clearly only a zeroth-order estimate of $L_{\rm IR}$, but we have kept it in our sample due to its high redshift and the beautiful, high S/N Na I D profile evident in its spectrum.

- **F04326+1904 (UGC 3094)**. See comments on F02509+1248.

- **F05024−1941.** The blueshifted Na I D component observed at -1550 km s^{-1} is seen also in Ca II H & K.

- **F07353+2903**. There is an emission-line object located $0-2''$ south of the galaxy center. We detect an emission line at 8704.3 Å. If we assume it is [O III]λ5007, [O III]λ4959 is detected with modest significance at the expected location, and Hβ with low significance. If these line identifications are correct, the redshift of the object is 0.7380, and it is likely to be an AGN based on the flux ratio of [O III]λ5007 and Hβ.

- **F08143+3134**. Hα and [N II]in this galaxy are blended and have strong blue wings so deblending them is non-trivial. However, [O III]/H$\beta \sim 1.6$, which implies that the spectral type is H II or LINER.

- **F08559+1053.** There is an emission-line object $4''\!.9$ north of the galaxy, possibly related to the faint, compact object seen in the *R*-band image (Veilleux et al. 2002). No continuum is visible, but several emission lines (elongated and tilted) are, yielding $z = 0.253$. [N II]λ6583 is not visible but Hα is, suggesting flux(Hα) $\gg$ flux([N II]). [O III]λ5007 is also brighter than Hβ by an uncertain factor (not more than a few).

- **F08591+5248**. This galaxy has no spectral classification listed in Veilleux et al. (1999b), and we cannot classify it because Hα intersects telluric lines and we do not measure [O III]λ5007. However, a low-dispersion spectrum of this object taken with ESI in long-slit mode shows that [O III]/H$\beta \sim 0.8$, which implies it is either an H II galaxy or a LINER.

- **F09039+0503**. The narrow absorbing component in this galaxy observed in Na I D at +190 km s^{-1} is observed also in Ca II K at the same velocity.

- **F10565+2448**. This galaxy has a bright central object with one or more nearby nuclei that are interacting with the central object. For the central object, we measure an optical emission-line redshift of $v_{hel} = 12891$ km s^{-1}, and the outflowing components appear in Na I D at 12758 and 12590 km s^{-1}. Our systemic redshift is in good agreement with the RC3 heliocentric optical redshift of 12912 ± 37 km s^{-1}, the CO redshifts of 12895 km s^{-1} (Sanders et al. 1991) and $v_{lsr} = 12923$ km s^{-1}(Downes & Solomon 1998), and the deepest H I 21 cm trough at 12900 km s^{-1} (see §3.4.7). However, these differ from the optical redshifts listed in Kim et al. (1995), which are 13160 km s^{-1} for the central object and 13100 km s^{-1} for the fainter NE nucleus.

- **F11387+4116**. There is a background emission-line object 3$''\!.$8 south of the galaxy; no continuum is visible, but [O III], Hβ, and Hα are observed, yielding $z = 0.346$. This background emission-line object has [O III]/H$\beta > 3$ (suggesting the presence of an AGN).

- **F13443+0802.** The southwest nucleus of this triplet is listed in Veilleux et al. (1999b) as a Seyfert 2. The Seyfert 2 nucleus is actually the eastern nucleus (and the correct line ratios are listed in Veilleux et al. 1999b under the label of the SW nucleus), while the other two nuclei are an unknown spectral type (SW) and an H II galaxy (NE).

- **F13451+1232**. Veilleux et al. (1999c) claim to observe a broad line in the Paα line in this galaxy. We observe similar asymmetric profiles in the optical in the western nucleus (which hosts most or all of the emission line flux), but they also appear to be present in the [O I]$\lambda\lambda 6300, 6364$ lines (as $2000 - 3000$ km s^{-1} blue wings), which suggests that they do not originate in the broad line region. It is difficult to discern the situation in the east nucleus due to its small separation from the west nucleus, which makes separation of the emission lines from the two nuclei very hard.

- **F16474+3430**. We do not have individual [O III]$\lambda 5007$ fluxes for the two nuclei in this galaxy. From Veilleux et al. (1999b), [O III]/H$\beta \sim 1$ for one of the nuclei or both together. We assume that this ratio is small for both nuclei to achieve our nuclear classifications (H II for each case).

- **F21549−1206**. The redshift listed in Kim et al. (1995) for the SE nucleus in this source is incorrect; its redshift is 0.0900, not 0.051. Thus the SE nucleus is a distant background galaxy.

Bibliography

Adelberger, K. L., Steidel, C. C., Shapley, A. E., & Pettini, M. 2003, ApJ, 584, 45

Aguirre, A., Hernquist, L., Schaye, J., Katz, N., Weinberg, D. H., & Gardner, J. 2001a, ApJ, 561, 521

Aguirre, A., Hernquist, L., Schaye, J., Weinberg, D. H., Katz, N., & Gardner, J. 2001b, ApJ, 560, 599

Arav, N., Becker, R. H., Laurent-Muehleisen, S. A., Gregg, M. D., White, R. L., Brotherton, M. S., & de Kool, M. 1999, ApJ, 524, 566

Arav, N., Kaastra, J., Steenbrugge, K., Brinkman, B., Edelson, R., Korista, K. T., de Kool, M. 2003, ApJ, 590, 174

Arav, N., Korista, K. T., de Kool, M., Junkkarinen, V. T., & Begelman, M. 1999, ApJ, 516, 27

Armus, L., Heckman, T. M., & Miley, G. K. 1990, ApJ, 364, 471

Arribas, S., Bushouse, H., Lucas, R. A., Colina, L., & Borne, K. D. 2004, AJ, 127, 2522

Arribas, S., Colina, L., & Clements, D. 2001, ApJ, 560, 160

Barger, A. J., Cowie, L. L., & Sanders, D. B. 1999, ApJ, 518, L5

Barlow, T. A., & Sargent, W. L. W. 1997, AJ, 113, 136

Barnes, J. E., & Hernquist, L. E. 1991, ApJ, 370, L65

Baum, S. A., O'Dea, C. P., Dallacassa, D., de Bruyn, A. G., & Pedlar, A. 1993, ApJ, 419, 553

Beckers, J. M., Bridges, C. A., & Gilliam, L. B. 1976, A High Resolution Spectral Atlas of the Solar Irradiance From 380 to 700 Nanometers. Volume I. Tabular Form (Massachusetts: Air Force Geophysics Lab)

Blain, A. W., Barnard, V. E., & Chapman, S. C. 2003, MNRAS, 338, 733

Blain, A. W., Kneib, J.-P., Ivison, R. J., & Smail, I. 1999, ApJ, 512, L87

Bland-Hawthorn, J., & Cohen, M. 2003, ApJ, 582, 246

Bond, N. A., Churchill, C. W., Charlton, J. C., & Vogt, S. S. 2001, ApJ, 562, 641

Boroson, T. A., Meyers, K. A., Morris, S. L., & Persson, S. E. 1991, ApJ, 370, L19

Boroson, T. A., & Meyers, K. A. 1992, ApJ, 397, 442

Brüns, C., Kerp, J., & Pagels, A. 2001, A&A, 370, L26

Canalizo, G., & Stockton, A. 2001, in ASP 255, Mass Outflow in AGN: New Perspectives, ed. D. M. Crenshaw, S. B. Kraemer, & I. M. George (San Francisco: ASP), 195

Carter, D., Johnstone, R. M., & Fabian, A. C. 1997, MNRAS, 285, L20

Castor, J., McCray, R., & Weaver, R. 1975, ApJ, 200, L107

Cecil, G., Bland-Hawthorn, J., Veilleux, S., & Filippenko, A. V. 2001, ApJ, 555, 338

Chevalier, R. A., & Clegg, A. W. 1985, Nature, 317, 44

Clements, D. L., Desert, F.-X., & Franceschini, A. 2001, MNRAS, 325, 665

Clements, D. L., Desert, F.-X., Franceschini, A., Reach, W. T., Baker, A. C., Davies, J. K., & Cesarsky, C. 1999, A&A, 346, 383

Colbert, E. J. M., Baum, S. A., Gallimore, J. F., O'Dea, C. P., & Christensen, J. A. 1996a, ApJ, 467, 551

Colbert, E. J. M., Baum, S. A., Gallimore, J. F., O'Dea, C. P., Lehnert, M. D., Tsvetanov, Z. I., Mulchaey, J. S., & Caganoff, S. 1996b, ApJS, 105, 75

Colbert, E. J. M., Baum, S. A., O'Dea, C. P., & Veilleux, S. 1998, ApJ, 496, 786

Colina, L., Arribas, S., & Borne, K. D. 1999, ApJ, 527, 13L

Colina, L., Arribas, S., & Clements, D. 2001, ApJ, 602, 181

Condon, J. J., Anderson, M. L., & Helou, G. 1991, ApJ, 378, 65

Condon, J. J., Cotton, W. D., & Broderick, J. J. 2002, AJ, 124, 675

Cowie, L. L., Barger, A. J., Fomalont, E. B., & Capak, P. 2004, ApJ, 603, L69

Cox, T. J., Primack, J., Jonsson, P., & Somerville, R. S. 2004, ApJ, 607, L87

Crenshaw, D. M., et al. 2002, ApJ, 566, 187

Crenshaw, D. M., & Kraemer, S. B. 2001, ApJ, 562, 29

Crenshaw, D. M., Kraemer, S. B., Boggess, A., Maran, S. P., Mushotzky, R. F., & Wu, C. 1999, ApJ, 516, 750

Crenshaw, D. M., Kraemer, S. B., Bruhweiler, F. C., & Ruiz, J. R. 2001, ApJ, 555, 633

Crenshaw, D. M., Kraemer, S. B., & George, I. M. 2003, ARA&A, 41, 117

Daines, S. J., Fabian, A. C., & Thomas, P. A. 1994, MNRAS, 268, 1060

Dekel, A., & Silk, J. 1986, ApJ, 303, 39

de Kool, M., Arav, N., Becker, R. H., Gregg, M. D., White, R. L., Laurent-Muehleisen, S. A., Price, T., & Korista, K. T. 2001, ApJ, 548, 609

De Robertis, M. M., & Osterbrock, D. E. 1984, ApJ, 286, 171

De Robertis, M. M., & Osterbrock, D. E. 1986, ApJ, 301, 727

Dopita, M. A., & Sutherland, R. S. 1995, ApJ, 455, 468

Dopita, M. A., & Sutherland, R. S. 1996, ApJS, 102, 161

Downes, D., & Solomon, P. M. 1998, ApJ, 507, 615

Elvis, M. 2000, ApJ, 545, 63

Espey, B. R., Kriss, G. A., Krolik, J. H., Zheng, W., Tsvetanov, Z., & Davidsen, A. F. 1998, ApJ, 500, 13

Fabbiano, G., et al. 2004, ApJ, 605, 21

Forster, K., Rich, R. M., & McCarthy, J. K. 1995, ApJ, 450, 74

Furlanetto, S. R., & Loeb, A. 2003, ApJ, 588, 18

Frye, B., Broadhurst, T., & Benítez, N. 2002, ApJ, 568, 558

Gallagher, S. C., Brandt, W. N., Laor, A., Elvis, M., Mathur, S., Wills, B. J., & Iyomoto, N. 2001, ApJ, 546, 795

Genzel, R., et al. 1998, ApJ, 498, 579

Genzel, R., Tacconi, L. J., Rigopoulou, D., Lutz, D., & Tecza, M. 2001, ApJ, 563, 527

Gerssen, J., van der Marel, R. P., Axon, D., Mihos, J. C., Hernquist, L., & Barnes, J. E. 2004, AJ, 127, 75

Hamann, F. W., Barlow, T. A., Chaffee, F. C., Foltz, C. B., & Weymann, R. J. 2001, ApJ, 550, 142

Hamann, F., Barlow, T. A., Junkkarinen, V., & Burbidge, E. M. 1997, ApJ, 478, 80

Hamilton, D., & Keel, W. C. 1987, ApJ, 321, 211

Heckman, T. M., Armus, L., & Miley, G. K. 1987, AJ, 93, 276

Heckman, T. M., Armus, L., & Miley, G. K. 1987, ApJS, 74, 833

Heckman, T. M., Armus, L., Weaver, K. A., & Wang, J. 1999, ApJ, 517, 130

Heckman, T. M., Balick, B., & Crane, P. C. 1980, A&AS, 40, 295

Heckman, T. M., Dahlem, M., Eales, S. A., Fabbiano, G., & Weaver, K. 1996, ApJ, 457, 616

Heckman, T. M., Lehnert, M. D., Strickland, D. K., & Armus, L. 2000, ApJS, 129, 493

Heckman, T. M., & Leitherer, C. 1997, AJ, 114, 69

Heckman, T. M., Sembach, K. R., Meurer, G. R., Strickland, D. K., Martin, C. L., Calzetti, D., & Leitherer, C. 2001, ApJ, 554, 1021

Hibbard, J. E., & Mihos, J. C. 1995, AJ, 110, 140

Hibbard, J. E., Vacca, W. D., & Yun, M. S. 2000, AJ, 119, 1130

Hibbard, J. E., & van Gorkom, J. H. 1996, AJ, 111, 655

Hibbard, J. E., & Yun, M. S. 1999, ApJ, 522, L93

Horne, K. 1986, PASP, 98, 609

Hughes, D. H., et al. 1998, Nature, 394, 241

Hutchings, J. B. 1989, AJ, 98, 524

Jarrett, T. H., Chester, T., Cutri, R., Schneider, S., & Huchra, J. 2003, AJ, 125, 525

Jenkins, E. B. 1986, ApJ, 304, 739

Kauffmann, G., & Charlot, S. 1998, MNRAS, 294, 705

Kennicutt, R. C. 1998, ApJ, 498, 541

Kewley, L. J., Heisler, C. A., Dopita, M. A., & Lumsden, S. 2001, ApJS, 132, 37

Kim, D.-C., & Sanders, D. B. 1998, ApJS, 119, 41

Kim, D.-C., Sanders, D. B., Veilleux, S., Mazzarella, J. M., & Soifer, B. T. 1995, ApJS, 98, 129

Kim, D.-C., Veilleux, S., & Sanders, D. B. 1998, ApJ, 484, 92

Kim, D.-C., Veilleux, S., & Sanders, D. B. 2002, ApJS, 143, 277

Kriss, G. A. 1994, in ASP Conf. Ser. 61, ADASS III, ed. D. R. Crabtree, R. J. Hanisch, & J. Barnes (San Francisco: ASP), 437

Kukula, M. J., Ghosh, T., Pedlar, A., & Schilizzi, R. T. 1999, ApJ, 518, 117

Kunth, D., Mas-Hesse, J. M., Terlevich, E., Terlevich, R., Lequeux, J., & Fall, S. M. 1998, A&A, 334, 11

Laor, A., & Brandt, W. N. 2002, ApJ, 569, 641

Larson, R. B. 1974, MNRAS, 169, 229

Laureijs, R. J., et al. 2000, A&A, 359, 900

Lehner, N., Sembach, K. R., Lambert, D. L., Ryans, R. S. I., Keenan, F. P. 1999, A&A, 352, 257

Lehnert, M. D., & Heckman, T. M. 1995, ApJS, 97, 89

Lehnert, M. D., & Heckman, T. M. 1996, ApJ, 462, 651

Lequeux, J., Kunth, D., Mas-Hesse, J. M., & Sargent, W. L. W. 1995, A&A, 301, 18

Lilly, S. J., Eales, S. A., Gear, W. K. P., Hammer, F., Le Fèvre, O., Crampton, D., Bond, J. R., & Dunne, L. 1999, ApJ, 518, 641

Lutz, D., Veilleux, S., & Genzel, R. 1999, ApJ, 517, L13

Mac Low, M.-M., McCray, R., & Norman, M. L. 1989, ApJ, 337, 141

Madau, P., Ferrara, A., & Rees, M. J. 2001, ApJ, 555, 92

Marquardt, D. M. 1963, Journal of the Society for Industrial and Applied Mathematics, 11, 431

Marsh, T. 1989, PASP, 100, 1032

Martin, C. L. 1998, ApJ, 506, 222

Martin, C. L. 1999, ApJ, 513, 156

Martin, C. L., Kobulnicky, H. A., & Heckman, T. M. 2002, ApJ, 574, 663

Martin, J. M., Bottinelli, L., Dennefeld, M., & Gouguenheim, L. 1991, A&A, 245, 393

McDowell, J. C., et al. 2003, ApJ, 591, 154

McKee, C. F., & Ostriker, J. P. 1977, ApJ, 218, 148

Mihos, J. C., & Hernquist, L. 1994, ApJ, 437, L47

Mirabel, I. F., & Sanders, D. B. 1988, ApJ, 335, 104

Morganti, R., Oosterloo, T. A., Emonts, B. H. C., van der Hulst, J. M., & Tadhunter, C. N. 2003, ApJ, 593, 69

Morton, D. C. 1991, ApJS, 77, 119

Murphy, T. W., Jr., Soifer, B. T., Matthews, K., & Armus, L. 2001, ApJ, 559, 201

Nachmann, P., & Hobbs, L. M. 1973, ApJ, 182, 481

Nagar, N. M., Wilson, A. S., Falcke, H., Veilleux, S., & Maiolino, R. 2003, A&A, 409, 115

Nulsen, P. E. J., Barcons, X., & Fabian, A. C. 1998, MNRAS, 301, 168

Perault, M. 1987, Ph.D. thesis, Univ. Paris

Pettini, M., Shapley, A. E., Steidel, C. C., Cuby, J.-G., Dickinson, M., Moorwood, A. F. M., Adelberger, K. L., & Giavalisco, M. 2001, ApJ, 554, 981

Phillips, A. C. 1993, AJ, 105, 486

Press, W. H., Teukolsky, S. A., Vetterling, W. T., & Flannery, B. P. 1992, Numerical Recipes in C (New York: Cambridge)

Reichard, T. A., et al. 2003, AJ, 126, 2594

Rupke, D. S., Veilleux, S., & Sanders, D. B. 2002, ApJ, 570, 588

Sahu, M. S., & Blades, J. C. 1997, ApJ, 484, L125

Sakamoto, K., Scoville, N. Z., Yun, M. S., Crosas, M., Genzel, R., & Tacconi, L. J. 1999, ApJ, 514, 68

Sanders, D. B., & Mirabel, I. F. 1996, ARA&A, 34, 749

Sanders, D. B., Mazzarella, J. M., Kim, D.-C., Surace, J. A., & Soifer, B. T. 2003, AJ, 126, 1607

Sanders, D. B., Scoville, N. Z., Sargent, A. I., & Soifer, B. T. 1988, ApJ, 324, L55

Sanders, D. B., Scoville, N. Z., & Soifer, B. T. 1991, ApJ, 370, 158

Sanders, D. B., Soifer, B. T., Elias, J. H., Madore, B. F., Matthews, K., Neugebauer, G., & Scoville, N. Z. 1988, ApJ, 325, 74

Savage, B. D., & Sembach, K. R. 1996, ARA&A, 34, 279

Scannapieco, E., Ferrara, A., & Broadhurst, T. 2000, ApJ, 536, L11

Scannapieco, E., Thacker, R. J., & Davis, M. 2001, ApJ, 557, 605

Schaye, J. 2001, ApJ, 559, L1

Schiano, A. V. R. 1985, ApJ, 299, 24

Schwartz, C. M., & Martin, C. L. 2004, ApJ, in press (astro-ph/0404148)

Scoville, N. Z., Sanders, D. B., Sargent, A. I., Soifer, B. T., & Tinney, C. G. 1989, ApJ, 345, L25

Sedov, L. 1959, Similarity and Dimensional Methods in Mechanics (New York: Academic Press)

Shapley, A. E., Steidel, C. C., Pettini, M., & Adelberger, K. L. 2003, ApJ, 588, 65

Sheinis, A. I., Bolte, M., Epps, H. W., Kibrick, R. I., Miller, J. S., Radovan, M. V., Bigelow, B. C., & Sutin, B. M. 2002, PASP, 114, 851

Shu, C., Mo, H. J., & Mao, S. 2003, MNRAS, submitted (astro-ph/0301035)

Silich, S., & Tenorio-Tagle, G. 2001, ApJ, 552, 91

Silk, J. 2003, MNRAS, 343, 249

Simcoe, R. A., Sargent, W. L. W., & Rauch, M. 2002, ApJ, 578, 73

Smail, I., Ivison, R. J., & Blain, A. W. 1997, ApJ, 490, L5

Solomon, P. M., Downes, D., Radford, S. J. E., & Barrett, J. W. 1997, ApJ, 478, 144

Spitzer, L. 1968, Diffuse Matter in Space (New York: Wiley-Interscience)

Stanford, S. A., Stern, D., van Breugel, W., & De Breuck, C. 2000, ApJS, 131, 185

Steffen, W., Holloway, A. J., & Pedlar, A. 1996a, MNRAS, 282, 130

Steffen, W., Holloway, A. J., & Pedlar, A. 1996b, MNRAS, 282, 1203

Steidel, C. C., Giavalisco, M., Pettini, M., Dickinson, M., & Adelberger, K. L. 1996, ApJ, 462, L17

Stokes, G. M. 1978, ApJS, 36, 115

Strickland, D. K. 2004, in IAU 222, Interplay among Black Holes, Stars, and ISM, ed. T. Storchi Bergmann, L. C. Ho, & H. R. Schmitt (IAU)

Strickland, D. K., & Stevens, I. R. 2000, MNRAS, 314, 511

Suchkov, A. A., Balsara, D. S., Heckman, T. M., & Leitherer, C. 1994, ApJ, 430, 511

Surace, J. A., Sanders, D. B., & Mazzarella, J. M. 2004, AJ, in press (astro-ph/0402531)

Surace, J. A., Sanders, D. B., Vacca, W. D., Veilleux, S., & Mazzarella, J. M. 1998, ApJ, 492, 116

Sutherland, R. S., & Dopita, M. A. 1993, ApJS, 88, 253

Tacconi, L. J., Genzel, R., Lutz, D., Rigopoulou, D., Baker, A. J., Iserlohe, C., Tecza, M. 2002, ApJ, 580, 73

Taniguchi, Y., Yoshino, A., Ohyama, Y., & Nishiura, S. 1999, ApJ, 514, 660

Taylor, G. I. 1950, Proc. R. Soc. London, A201, 159

Theuns, T., Mo, H. J., & Schaye, J. 2001, MNRAS, 321, 450

Theuns, T., Viel, M., Kay, S., Schaye, J., Carswell, R. F., & Tzanavaris, P. 2002, ApJ, 578, L5

Tomisaka, K., & Ikeuchi, S. 1988, ApJ, 330, 695

Turnshek, D. A. 1988, in QSO Absorption Lines: Probing the Universe, (Cambridge: Cambridge UP), 17

Ulvestad, J. S., & Wilson, A. S. 1984, ApJ, 285, 439

Vader, J. P. 1986, ApJ, 305, 669

van Driel, W., Gao, Y., & Monnier-Ragaigne, D. 2001, A&A, 368, 64

Veilleux, S. 1991a, ApJS, 75, 357

Veilleux, S. 1991b, ApJS, 75, 383

Veilleux, S. 1991c, ApJ, 369, 331

Veilleux, S., Bland-Hawthorn, J., Cecil, G., Tully, R. B., & Miller, S. T. 1999a, ApJ, 520, 111

Veilleux, S., Cecil, G., Bland-Hawthorn, J., Tully, R. B., Filippenko, A. V., & Sargent, W. L. W. 1994, ApJ, 433, 48

Veilleux, S., Kim, D.-C., & Sanders, D. B. 1999b, ApJ, 522, 113

Veilleux, S., Kim, D.-C., & Sanders, D. B. 2002, ApJ, 143, 315

Veilleux, S., Kim, D.-C., Sanders, D. B., Mazzarella, J. M., & Soifer, B. T. 1995, ApJS, 98, 171

Veilleux, S., Sanders, D. B., & Kim, D.-C. 1999c, ApJ, 522, 139

Veilleux, S., & Osterbrock, D. E. 1987, ApJS, 63, 295

Veilleux, S., & Rupke, D. S. 2002, ApJ, 565, L63

Veilleux, S., & Rupke, D. S. 2004, PASA, in press

Veilleux, S., Shopbell, P. L., & Miller, S. T. 2001, AJ, 121, 198

Veilleux, S., Shopbell, P. L., Rupke, D. S., Bland-Hawthorn, J., & Cecil, G. 2003, AJ, 26, 2185

Vogt, S. S., et al. 1994, Proc. SPIE, 2198, 362

Wakker, B. P., & Schwarz, U. J. 1991, A&A, 250, 484

Weaver, R., McCray, R., Castor, J., Shapiro, P., & Moore, R. 1977, ApJ, 218, 377

Weymann, R. J., Morris, S. L., Foltz, C. B., & Hewett, P. C. 1991, ApJ, 373, 23

Zink, E. C., Lester, D. F., Doppmann, G., & Harvery, P. M. 2000, ApJS, 131, 413